

University of Strathclyde
Department of Chemical & Process Engineering

**Nickel Electroforming
for Large-Scale Applications:
Process Modelling & Optimisation**

Eleni Andreou

A thesis submitted to the Department of Chemical and Process Engineering, University of Strathclyde in fulfilment of the requirements for the degree of Doctor of Philosophy

2022

This thesis is the result of the author's original research. It has been composed by the author and has not been previously submitted for examination which has led to the award of a degree.

The copyright of this thesis belongs to the author under the terms of the United Kingdom Copyright Acts as qualified by University of Strathclyde Regulation 3.50. Due acknowledgement must always be made of the use of any material contained in, or derived from, this thesis.

Signed:

A handwritten signature in black ink, appearing to be 'A. P. I. O.', written over a horizontal line.

Date: 10/12/2022

Acknowledgements

Having worked together and alongside each other for the last four years, I would like to thank my supervisor, Prof. Roy, for a great PhD experience and all the opportunities she gave me. Most importantly, I would like to thank her for always being there to support me, defend me, advise me, guide me, listen to me, and argue with me, when needed. My gratitude is also extended to my second supervisors, Dr. Brightman and Dr. Green, for their continuous support and fresh perspective that they were always willing to share with me.

A big *thanks* goes out to Christine for her support and friendship; she will always have a special place in my heart. Also, to Thomas, Shaon, John, Pamela, Grace, Lewis, Russell, James, and all the other amazing friends and colleagues I had the chance to share this experience with. My appreciation goes to Michael Watt, Chris Jones and James Kelly for their help and professionalism; all three enabled, through their hard work, important novelties of this work.

On a more personal note, I would like to acknowledge my partner, family, and life-long friends for always reminding me to stand by my ethical values and ideals, no matter what the difficulties are. But also, for challenging me to be a better version of myself every time I was failing to live up to my own standards. My love and gratitude for them is deep and undeniable.

Last but not least, I would like to make a special reference to all the people who have suffered, or even lost their lives, due to our global society's deep inequalities and injustice. I dream that, in the future, the progressive parts of our world and the global scientific community, will succeed in making this world a better place for everyone. A place where no more people will have to suffer and those who already have will never be forgotten. *Venceremos!*

Abstract

Electrochemical forming is a chemical additive process to manufacture a variety of niche components. Its capability has been exploited in micro-manufacturing as well as “heavy industry”, such as aerospace. As the “Industry 4.0” era unfolds, there is a need to develop models for electroforming which are based on electrochemically sound data. To do this, physical and electrochemical parameters for modelling purposes should be determined first, followed by rigorous modelling studies. For modelling to be useful, parameters which could play a significant role in process optimisation should be examined, followed by continuous cross-validation through appropriate measurements. Through that way a model can be a valuable aid, allowing predictability in tooling, piloting, and manufacturing in a reliable manner.

In that context, during this project the effect of physical and electrochemical parameters on electroformed parts was studied and a well-informed modelling tool, using COMSOL Multiphysics[®], was developed. The model was subsequently validated through carefully designed experiments. That way, this project succeeded in bridging the gaps among electrochemistry, chemical engineering, and manufacturing.

Specifically, to meet the industrial partner’s (Radius Aerospace Bramah) vision for large-scale and large-volume manufacturing of large parts with extremely high precision, the key engineering variables which can be used to manipulate an electroformed part were identified and a 5-step systematic approach of studying the electroforming process was established. The industrial partner was provided with a well-informed and validated model of the process, as well as suggestions towards the optimisation of the electroforming reactor and auxiliary tooling (*e.g.*, “masks” and “thieves”). Upon implementation, the proposed 5-step methodology could allow for process scaling-up and volume manufacturing while minimising the number of manufacturing trials and process waste.

Table of Contents

Acknowledgements	3
Abstract	4
Chapter 1: Introduction	18
1.1 The “Industry 4.0” Concept.....	18
1.2 The electroforming process: an overview	21
1.2.1. Nickel electroforming	24
1.2.3. Applications	35
1.2.4. Sustainability.....	38
1.3 Modelling the electroforming process.....	42
1.3.1. Key modelling studies of the electroforming process	44
1.3.2. Today’s challenges	58
1.3.3. Most common commercial modelling software	62
1.4 Project Aims.....	65
References	67
Chapter 2: Electrochemical Characterisation of the Electroforming System	78
2.1 Equipment & Materials	80
2.2 Electrochemical Analysis	83
2.2.1 pH & Conductivity (σ)	83
2.2.2 Polarisation Studies (Linear Sweep Voltammetry)	84
2.2.3 System Reversibility (Cyclic Voltammetry).....	95
2.3 Deposition Experiments	98
2.4 Conclusions	104
References	106
Chapter 3: Model Foundation & Implementation.....	107
3.1 The Finite Element Method	108
3.2 Developing the RDE Model	112

3.2.1 Geometry (2-D Axisymmetric)	112
3.2.2 Mesh	113
3.2.3 Boundary and Initial Conditions Declaration - Mathematical Foundation	117
3.2.4 Implementation & Assessment	127
3.3 The 3-D RDE Model	137
3.4 Conclusions	139
References	141
Chapter 4: Results on Modelling the Scaling-Up of the Nickel Electroforming Process	143
4.1 Introduction	143
4.3 Control simulations.....	150
4.4 Mesh Sensitivity Studies	159
4.5 Geometry Sensitivity Studies	165
4.5.1 RDE System Model.....	168
4.5.2 Electroforming Reactor.....	173
4.6 Conclusions	178
References	180
Chapter 5: The Case of the Mechanical Vane	181
5.1 Mechanical Vanes in Gas Turbine Engines	181
5.2 The Vane Geometry	185
5.3 Experimental Results	189
5.4 Model & Validation	193
5.5 Deposit Structural Characterisation	205
5.6 Conclusions	212
References	215
Chapter 6: Electroforming Process Model Assessment	221
6.1 “Masks” & “Thieves”.....	222
6.1.1 “Masks”	223
6.1.2 The “Shell Mask” - “Ring Thief” Configuration	239

6.1.3 “Masks” alongside the Mechanical Vane Mandrel	244
6.2 Primary, Secondary & Tertiary Current Distribution.....	248
6.3 Conclusions	263
References	266
Chapter 7: Conclusions.....	268
References	284

Table of Figures

Figure 1. 1: Generalized model of an industrial revolution developed by E. G. Popkova, Y. V. Ragulina and A. V. Bogoviz [4].	20
Figure 1. 2: (a) Non-conductive, silicone rubber (by CIR Electroplating) and (b) conductive, stainless steel (by V.M. Moulds and Dies) electroforming mandrels.	27
Figure 1. 3: Cell voltage (in black) and current (in red) as a function of time during electrochemical deposition from a sulphamate electrolyte of composition stated in Table 1.1. Applied current density at start was 20 mAcm^2 (2 ASD) and was applied for a period of 2 h. Solution temperature 50°C .	33
Figure 1. 4: Alex Fradkin. The copper pieces created by studio Akoaki through electroforming can be arranged into a sculptural installation. [73]	36
Figure 1. 5: Global nickel reserves 2000-2021 [79] [80]	39
Figure 1. 6: Global consumption volume of nickel between 2010 and 2021 [82]	40
Figure 1. 7: Average nickel price, globally, between 2014 and 2021. Estimates for years 2022-2025 are also shown. [83]	41
Figure 1. 8: The electroforming process.	42
Figure 1. 9: 2-D cell geometry used by Alkire et al. for their study of a shape evolution problem using the finite element method. [90]	46
Figure 1. 10: Simulation of electrodeposition result in a Hull cell for Wagner number at (a) $W = 0.005$ and (b) $W = 500$. [92]	47
Figure 1. 11: Computational domain used for the studies of Oh et al. [94]	49
Figure 1. 12: Schematic of the electroforming cell studied by Yang et al.. [95]	51
Figure 1. 13: (a) The experimental setup used by Behagh et al. and (b) its representation in a 2-D axisymmetric model. [96]	52
Figure 1. 14: Experimental setups and their representation in modelling software studied by Belov et al. [97]. Specifically, (a) lab-scale setup Assaf panel, (b) 3-D model of half of the Assaf panel in modelling software, (c) Industrial-scale complex component for telecom application and (d) 3-D model of the industrial-scale component.	54
Figure 1. 15: (a) Schematic of the experimental rotating cone electrode setup used by Heydari et al. (b) 2-D axisymmetric model of the experimental rotating cone electrode setup [103]	57
Figure 2. 1: Proposed strategy for approaching the vision of implementing digitalisation for large-scale / high-volume electroforming.	79
Figure 2. 2: The rotating disk electrode (RDE) setup used in laboratory experiments.	82
Figure 2. 3: (a) Comparative pH data for the freshly and aged electrolytes at room temperature ($\sim 25^\circ\text{C}$), (b) Comparative conductivity (σ) data for the freshly and aged electrolytes at room temperature ($\sim 25^\circ\text{C}$).	85
Figure 2. 4: (a) Comparative pH data for the freshly and aged electrolytes at working temperature ($\sim 50^\circ\text{C}$), (b) Comparative conductivity (σ) data for the freshly and aged electrolytes at working temperature ($\sim 50^\circ\text{C}$).	85

Figure 2. 5: Overlap of cathodic polarisation curves of a freshly prepared electrolytic solution, scan was taken up to $(-1) V$, at different scan rates, under stagnant conditions, at $50\text{ }^{\circ}\text{C}$	87
Figure 2. 6: Cylindrical polar coordinates for the rotating disk electrode.	87
Figure 2. 7: Overlap of cathodic polarisation curves of a freshly prepared electrolytic solution, scans were taken up to $(-1.35) V$, at a scan rate of $0.005 V/s$, under various agitation conditions, at $50\text{ }^{\circ}\text{C}$	88
Figure 2. 8: Cathodic polarisation curve of the freshly prepared electrolytic solution. Scan was run from $0 V$ to $(-1.1) V$ at a rate of $0.005 V/s$, under agitation at 1500 rpm . A current range of 100 mA was chosen for the measurement and the results were being corrected in real time for ohmic drop.	90
Figure 2. 9: Cathodic Tafel slope for the freshly prepared electrolytic solution, extrapolated by the LSV data of Figure 2.8. $OCP = -0.254 V$ (vs. SCE), slope 1: -51 mV/dec (defines b_1), slope 2: -314 mV/dec (defines b_2).	94
Figure 2. 10: Cyclic voltammetry curves of freshly prepared electrolytic solution, starting at $(+0.8) V$, going down to $(-1.4) V$ and returning to $(+0.4) V$, under stagnant conditions, with a scan rate of $0.005 V/s$ - 5 cycles.	96
Figure 2. 11: Laboratory deposition RDE set-up.	98
Figure 2. 12: Nickel deposit formed using the RDE setup. Deposition ran at 44 ASD , under agitation at 1000 rpm , for 1800 s and at $50\text{ }^{\circ}\text{C}$	101
Figure 2. 13: Total system potential (black line) “break-down” for a (a) deposition experiment at 3.98 ASD and (b) deposition experiment at 19.71 ASD . Both depositions ran for 1800 s , at 1000 rpm and $50\text{ }^{\circ}\text{C}$. Cathode reactions potential (red line), anode reactions potential (blue line).	103
Figure 3. 1: Representative example of the mesh of a 2-D domain when the finite element method analysis is used. In this case, the domain spacing consists of 2-D triangular elements. [14]	109
Figure 3. 2: Representative mesh spacing in COMSOL Multiphysics® of (a) a 1-D domain consisting of elements appearing as intervals, (b) a 2-D domain consisting of triangular elements and (c) a 3-D domain consisting of elements in the form of tetrahedrons.	110
Figure 3. 3: Example of a “hanging node” [14].	110
Figure 3. 4: Simplified 2-D Axisymmetric RDE Geometry used for modelling purposes.	113
Figure 3. 5: (a) Cathode and (b) anode surface of the simplified 2-D Axisymmetric RDE model.	114
Figure 3. 6: (a) Mesh spacing of the 2-D axisymmetric RDE model domain. (b) Close view of the mesh around the cathode boundary and recess point (in circle), showing the transition from the domain mesh sizing to a much finer mesh around these areas.	116
Figure 3. 7: Model Builder in COMSOL Multiphysics®	118
Figure 3. 8: (a) “Electrolyte” and (b) “Initial Values” nodes within the COMSOL Multiphysics® Model Builder. The domain equations are shown.	119
Figure 3. 9: (a) “Nondeforming Boundary” and (b) “Insulation” nodes within the COMSOL Multiphysics® Model Builder. The boundary equations are shown.	120

Figure 3. 10: “Deforming Boundary” node within the COMSOL Multiphysics® Model Builder. The boundary equations are shown.....	121
Figure 3. 11: (a) “Cathode” and (b) “Anode” nodes within the COMSOL Multiphysics® Model Builder. The boundary equations are shown. (c) The “Electrode Reaction” sub-node appearing as part of both the “Cathode” and “Anode” nodes and including exactly the same information for both.....	123
Figure 3. 12: Comparison of the experimental current density - potential curve, constructed based on data collected in the laboratory using linear sweep voltammetry (red curve), against the theoretical B-V curve for use in nickel electroforming models, “shifted” B-V curve (blue line). The corresponding linear sweep voltammetry was conducted with a scan rate of 0.005 V/s, at 50 °C and under agitation at 1500 rpm. The kinetic parameters used to plot the theoretical B-V curve were the ones presented in Table 3.2.	129
Figure 3. 13: 2-D representation of (a) the potential distribution, (b) the current distribution in the electrolytic volume and (c) the current distribution on the cathode surface. The results simulate potential and current distributions after 1800 s at 50 °C. The current streamlines are also shown in figure (b) emanating from the anode (at higher potential) and being collected at the cathode (at lower potential). The vertical distance between the electrodes’ geometrical centres is also noted in figure (a) alongside the local average cathode surface potential and current after the final converged step.....	131
Figure 3. 14: (a) 2-D representation of the thickness distribution on the cathode surface. The results simulate the current distribution after 1800 s at 50 °C. (b) Total cathode thickness change with time. The thickness profiles at the four converged simulation steps are shown.....	134
Figure 3. 15: Sectioning of the RDE nickel disk deposit for thickness measurements. The white arrows indicate the side face of the section measured under the microscope, following this being mounted in a resin specimen.....	134
Figure 3. 16: Comparative graph of the experimentally achieved and the simulated thickness profiles for the RDE setup. The RDE deposit was produced at $-5 V$ and $-0.565 A$, for 1800 s. These conditions allowed for a thick enough deposit to be sectioned, mounted in resin, and measured under the microscope without deforming. The arc length depicted corresponds to the RDE disk radius.	135
Figure 3. 17: (a) Mesh spacing of the 3-D RDE geometry domain. (b) The blue line highlights the “recess”, transition edge of the stainless-steel disk electrode in the RDE model.....	138
Figure 4. 1: The industrial scale (18L), prototype electroforming reactor setup used for the practical experiments against which the validity of the results, of both models presented in this chapter, were validated.....	146
Figure 4. 2: (a) CAD design of the prototype electroforming tank developed for the purposes of the project, (b) in scale (1:3) top view schematic of the tank’s interior including equipment, (c) in scale (1:3) side view schematic of the tank’s interior including equipment.	147
Figure 4. 3: (a) The anode basket filled with nickel pellets and fitted in the prototype electroforming tank, (b) The 304 stainless-steel, scaled-up, disk mandrel.	148

Figure 4. 4: Complete scaled up electroforming setup; titanium anode basket filled with Ni pellets and stainless-steel disk mandrel immersed in nickel sulphamate electrolyte. 149

Figure 4. 5: (a) Mesh spacing of the 3-D, laboratory-scale (0.2 dm^3), RDE geometry domain and (b) mesh spacing of the 3D, industrial-scale (18 dm^3), prototype electroforming reactor domain. The blue line in the zoom-in capture of figure (a) highlights the “recess”, transition edge of the stainless-steel disk electrode in the RDE model. Highlighted in blue, the deposition (cathode) areas of (c) the laboratory-scale setup and (d) the scaled-up setup are also shown. The RDE and scaled-up deposition areas present a ratio of 1:28. 151

Figure 4. 6: 3-D representation of potential distribution in the electrolyte volume of (a) the RDE and (b) the electroforming reactor. 3-D representation of current distribution on the cathode surface for (c) the RDE and (d) the electroforming reactor. The results simulate potential and current distributions after 3h at $50 \text{ }^\circ\text{C}$. The current streamlines in both electrolytic volumes are also shown in figures (c) and (d) emanating from the anode (at higher potential) and being collected at the cathode (at lower potential). The vertical distance between the electrodes’ geometrical centres is also noted in figures (a) and (b). Current distribution on the cathodes’ surface is shown in the cathode surface close ups provided in figures (c) and (d). 153

Figure 4. 7: Comparative graphs of the experimentally achieved and the simulated thickness profiles for (a) the laboratory-scale RDE setup and (b) the prototype electroforming reactor setup. The RDE deposit was produced at -5 V and -0.565 A , for 1800 s , while the reactor deposit was formed at -2.5 V and -1 A , for 10800 s . These conditions allowed, in both cases, for thick enough deposits to be sectioned, mounted in resin, and measured under the microscope without deforming. 156

Figure 4. 8: Sectioning of nickel disk deposits formed (a) in the tank system and (b) in the RDE system for thickness measurements. The white arrows indicate the side face of its section measured under the microscope, following these being mounted in a (c) resin specimen. 157

Figure 4. 9: Real-life nickel electroform produced in the prototype electroforming reactor at -2.5 V and -1 A , for 10800 s , at $50 \text{ }^\circ\text{C}$, under agitation. 158

Figure 4. 10: (a) Control mesh density (red), (b) mesh spacing finer than the control by 50% (green), (c) mesh spacing finer than the control by 75% (blue). Figure (d) shows an overlap of the thickness profiles predicted by the RDE model for the different mesh densities. The results simulate a 3 h process at $50 \text{ }^\circ\text{C}$ 162

Figure 4. 11: (a) Control mesh density (red), (b) mesh spacing finer than the control by 50% (green). Figure (c) shows an overlap of the thickness profiles predicted by the scaled-up model for the different mesh densities. The results simulate a 3 h process at $50 \text{ }^\circ\text{C}$ 163

Figure 4. 12: Overlap of thickness profiles predicted by the RDE model following (a) an increase of the element size parameters by various percentages and (b) a decrease of the element size parameters by various percentages. Figure (a) shows the change in the results’ quality for meshes coarser than the control mesh while, figure (b) shows the change in the results’ quality for meshes finer than the control mesh. The results simulate a 3 h process at $50 \text{ }^\circ\text{C}$ 166

Figure 4. 13: Overlap of thickness profiles predicted by the scaled-up model following (a) an increase of the element size parameters by various percentages and (b) a decrease of the element size parameters by various percentages. Figure (a) shows the change in the results' quality for meshes coarser than the control mesh while, figure (b) shows the change in the results' quality for meshes finer than the control mesh. The results simulate a 3 h process at 50 °C.....	167
Figure 4. 14: (a)-(c) Variations of anode position along the z-axis, with a fixed x-axis position. (d) Effect of anode position on the predicted thickness profile for anode position at 10 mm (red); 25 mm (green); and 40 mm (blue).....	169
Figure 4. 15: (a)-(c) Variations of anode position along z-axis, with a fixed x-axis position at the centre of the cell. (d) Effect of anode position on the predicted thickness profile for anode position at 10 mm (red); 25 mm (green); and 40 mm (blue).	170
Figure 4. 16: 3-D representation of the potential distribution in the electrolyte volume of the RDE model when the anode is placed at (a) 7 mm and (b) 43 mm from the cathode surface. 3-D representation of the current streamlines on the cathode surface of the RDE when the anode is placed at (c) 7 mm and (d) 43 mm from the cathode surface. (e) Thickness profiles predicted for the geometries shown in figures (a) and (b). The results simulate potential and current distributions after 3 h at 50 °C. Anode distances are provided with reference to its geometric centre.	172
Figure 4. 17: 3-D representation of the potential distribution in the electrolyte volume of the RDE model when the cell boundaries are double than the control simulations and the anode is placed off-centre, at (a) 25 mm and (b) 48 mm from the cathode surface. 3-D representation of the current distribution on the cathode surface for the two cases when the anode is placed at (c) 25 mm and (d) 48 mm from the cathode surface. (e) Thickness profiles predicted for all anode positions. The results simulate potential and current distributions after 3 h at 50 °C. Distances are provided with reference to the anode's geometric centre.....	174
Figure 4. 18: (a)-(c) 3-D representation of the potential distribution in the electrolyte volume of the tank system model for anode positions at different distances from the cathode surface. Current streamlines in the electrolyte are also shown. (d) Effect of anode position on the predicted thickness profile. The local cathodic potential and current density values are provided for each case. The results simulate potential and current distributions after 3 h at 50 °C. Distances are provided with reference to the anode's geometric centre.	176
Figure 4. 19: (a)-(c) 3-D representation of the potential distribution in the electrolyte volume of the tank system model for anode positions at different distances from the cathode surface when cell boundaries are doubled. Current streamlines in the electrolyte are also shown. (d) Effect of anode position on the predicted thickness profile. The local cathodic potential and current density values are provided for each case. The results simulate potential and current distributions after 3 h at 50 °C. Distances are provided with reference to the anode's geometric centre.	177
Figure 5. 1: Gas turbine components and principle. (Figure produced by engineeringlearn.com [1]).....	182

Figure 5. 2: (a) Impellers for centrifugal compressors, (b) air entry to the diffuser and diffuser vanes guiding the flow, (c) stator vanes in an axial flow compressor [2]	183
Figure 5. 3: (a) Representative turbine schematic showing the position of nozzle guide vanes, (b) nozzle guide vanes detailed schematic [2]	184
Figure 5. 4: Vane mandrel made of 304 stainless steel provided by Radius Aerospace for research and development of a real-life product. The area in red is always electroformed, the area in green may be masked or electroformed, the area in blue is always masked.	186
Figure 5. 5: Schematic of the vane mandrel geometry profile showing (a) the thickness target and (b) the tolerance for all five sections of the part.	187
Figure 5. 6: Thickness profiles of the minimum (dotted line), nominal-target (straight line) and maximum (dashed line) acceptable thicknesses for each section.	188
Figure 5. 7: Nickel mechanical vane electroforms R5, R6 and R7. The difference in the dendrites size is highlighted, with R5 presenting the thinnest dendrites around its leading edges and R7 the thicker ones. Electroforms R5, R6 and R7 were produced at 7.22 A/dm^2 after deposition for 3.5 h, 5 h and 6 h, respectively, at $50\text{ }^\circ\text{C}$.	190
Figure 5. 8: Nickel mechanical vane electroforms R1, R2, R3 and R4. The gradual change in surface finishing is highlighted. Electroforms R1, R2 and R3 were produced at 1.11 A/dm^2 , 2.44 A/dm^2 and 4.89 A/dm^2 , respectively, after deposition for 5 h at $50\text{ }^\circ\text{C}$. Electroform R4 was produced at 4.89 A/dm^2 after deposition for 2.5 h at $50\text{ }^\circ\text{C}$.	192
Figure 5. 9: 3-D geometry of the mechanical vane mandrel used in COMSOL Multiphysics®. (a) Front and (b) back views of the deposition area. (c) Side view of the mandrel revealing the challenging profile of the tool. The “nose” of the mandrel indicated in the circle.	193
Figure 5. 10: Mesh spacing of (a) the whole 3-D mechanical vane model domain and (b) the whole mandrel area.	194
Figure 5. 11: 3-D representation of (a) the potential and (b) the current distribution in the electrolyte volume of the mechanical vane model. The results simulate potential and current distributions after 5h at $50\text{ }^\circ\text{C}$. The vertical distance between the electrodes’s geometrical centres is noted in figure (a). Current distribution on the cathode surface is shown in the cathode surface close up provided in figure (b).	196
Figure 5. 12: Simulated deposit thickness distribution on the mechanical vane deposition area. Only the “front” face is shown. The simulated non-uniform thickness distribution follows the previously simulated non-uniform current distribution, with higher currents at the edges and lower at the centre.	197
Figure 5. 13: Mechanical vane deposit R3. The deposit was formed of pure nickel and deposition was conducted at -5.4 V and -4.4 A , for 18000 s, at $50\text{ }^\circ\text{C}$. “Front” indicates the mandrel side closer to the anode. The dendrites formed at the leading edges are also shown here.	198
Figure 5. 14: (a) The three strips deposit R3 was sectioned in as seen from the “back” face of the mandrel. (b) Mandrel sections mounted in resin specimen. (c) Corresponding boundaries along which simulated thickness results were retrieved. Section length is measured from point I to points II and III shown in figure (c).	199

Figure 5. 15: Comparative graphs of the experimental and simulated thickness profiles for (a) strip 1, (b) strip 2 and (c) strip 3 of the mechanical vane deposit R3. Deposition of R3 was conducted at $-5.4 V$ and $-4.4 A$, for $18000 s$, at $50 ^\circ C$. “Front” indicates the mandrel side closer to the anode. Circles highlight thicknesses that correspond to dendritic growth.	200
Figure 5. 16: Overlaps of (a) the experimental and (b) the simulated thickness profiles for strips 1, 2 and 3 of the mechanical vane deposit R3. Deposition of R3 was conducted at $-5.4 V$ and $-4.4 A$, for $18000 s$, at $50 ^\circ C$. “Front” indicates the mandrel side closer to the anode.	202
Figure 5. 17: Comparative graphs of the experimental and simulated thickness profiles for (a) strip 1, (b) strip 2 and (c) strip 3 of the mechanical vane deposit R6. Deposition of R6 was conducted at $-6.5 V$ and $-6.5 A$, for $18000 s$, at $50 ^\circ C$. “Front” indicates the mandrel side closer to the anode.	204
Figure 5. 18: The Hitachi S3700-N Scanning Electron Microscope used for the purposes of this project. The equipment is located at the Advanced Materials Research Laboratory (AMRL) at the University of Strathclyde.	206
Figure 5. 19: Scanning electron microscopy imaging of the strip 2 section surface of the etched R3 electroform at magnification $\times 3,000$. The red triangles indicate the boundaries of what believed to be pyramid-shaped nickel grains evolving during deposition. The red dots within the red triangles indicate the “tip” point of the pyramid-shaped grains indicating growth on the z -direction (outwards from the page level).	207
Figure 5. 20: Electronic microscope imaging of the strip 2 “nose” section surface of the etched R3 electroform at magnification $\times 50$. The growth mechanism presents a periodicity which leads to “necklace”-like zones of $\sim 72 \mu m$ in thickness.	209
Figure 5. 21: Spots of elemental analysis under the scanning electron microscope using the backscattered-electron beam alongside energy dispersive spectroscopy.	210
Figure 6. 1: (a) 2-D axisymmetric geometry of the RDE setup including a “ring mask” placed between the electrodes at $d_{wall} = 1.5 cm$ from the cell walls. (b) Top view of the “ring mask”; $w_{ring} = 1.5 cm$, $r_{outer} = 2 cm$, $r_{inner} = 0.5 cm$	224
Figure 6. 2: Different “ring mask” distances from the cathode surface. Position 1 at $0.05 cm$, position 2 at $0.5 cm$ and position 3 at $1.4 cm$ from the cathode surface. Radius of the “exposed” cathode area ($r_{exp} = 0.5 cm \equiv r_{inner}$) indicated in orange.	225
Figure 6. 3: 2-D representation of the potential and current distribution in the electrolytic volume for the case when the “ring mask” is placed at (a) $0.05 cm$, (b) $0.5 cm$ and (c) $1.4 cm$ from the cathode surface.	226
Figure 6. 4: Simulated thickness profiles for the different positions of the “ring mask”	227
Figure 6. 5: 2-D representation of the thickness distribution on the cathode surface for the case when the “ring mask” is placed at (a) $0.05 cm$, (b) $0.5 cm$ and (c) $1.4 cm$ from the cathode surface. For clarity, the colour code indicates lower thicknesses with blue (starting at 0 in the deep blue part of the scale) and higher thicknesses with red.	229

Figure 6. 6: (a) 2-D axisymmetric geometry of the RDE setup including a “shell mask” placed between the electrodes at $hshell = 5.4\text{ cm}$ from the bottom of the cell. (b) Top view of the mask’s base hole; $rhole = 0.5\text{ cm}$. The mask is essentially a hollow cylinder with wall thickness $\tau_{cyl.wall} = 0.1\text{ cm}$ and a hole at the base. The base of the mask is indicated by the green arrow. 230

Figure 6. 7: Different “shell mask” base distances from the cathode surface. Position 1 at 0.05 cm , position 2 at 0.5 cm and position 3 at 1.4 cm from the cathode surface. Radius of the mask’s base hole at $rhole = 0.5\text{ cm}$. The orange dash line indicates the optimal position of the mask base at $hshell = 5.5\text{ cm}$ or 0.4 cm from the cathode. 232

Figure 6. 8: 2-D representation of the potential and current distribution in the electrolytic volume for the case when the base of the “shell mask” is placed at (a) $hshell = 5.85\text{ cm}$ or 0.05 cm from the cathode surface, (b) $hshell = 5.4\text{ cm}$ or 0.5 cm from the cathode surface and (c) $hshell = 4.7\text{ cm}$ or 1.4 cm from the cathode surface. 233

Figure 6. 9: Simulated thickness profiles for the different distances of the “shell mask” base from the cathode surface. 235

Figure 6. 10: 2-D representation of the thickness distribution on the cathode surface for the case when the base of the “shell mask” is placed at (a) $hshell = 5.85\text{ cm}$ or 0.05 cm from the cathode surface, (b) $hshell = 5.4\text{ cm}$ or 0.5 cm from the cathode surface and (c) $hshell = 4.7\text{ cm}$ or 1.4 cm from the cathode surface. For clarity, the colour code indicates lower thicknesses with blue (starting at 0 in the deep blue part of the scale) and higher thicknesses with red. 236

Figure 6. 11: 2-D representation of (a) the potential and current distribution in the electrolytic volume and (b) the thickness distribution on the cathode surface for the case when the base of the “shell mask” is placed at its optimal position ($hshell = 5.5\text{ cm}$, or 0.4 cm from the cathode surface). (c) Comparative graph of the simulated thickness profiles for the cases when the “shell mask” base is placed at its optimal position, position 1, position 2 and position 3. High current accumulation at the leading edge highlighted in circle in (b). 238

Figure 6. 12: 2-D representation of (a) the potential and current distribution in the electrolytic volume and (b) the thickness distribution on the cathode surface for the case when the base of the “shell mask” is placed at its optimal position ($hshell = 5.5\text{ cm}$, or 0.4 cm from the cathode surface) and the hole at its base is decreased by 0.1 cm ($rhole = 0.4\text{ cm}$). (c) Comparative graph of the simulated thickness profiles for two different sizes of the “shell mask” base hole; $rhole = 0.5\text{ cm}$ vs. $rhole = 0.4\text{ cm}$ 240

Figure 6. 13: (a) 2-D axisymmetric geometry of the RDE setup including the “shell mask” at its optimal position and a “ring thief” placed between the “mask” and the cathode at $hthief = 5.85\text{ cm}$, or 0.05 cm from the cathode surface. (b) Top view of the “ring thief”; $rinner = 0.5\text{ cm}$, $router = 0.8\text{ cm}$. The “thief” has a width $wthief = 0.3\text{ cm}$ and is indicated by the green arrow. 241

Figure 6. 14: 2-D representation of (a) the potential and current distribution in the electrolytic volume and (b) the thickness distribution on the cathode surface for the case when the “shell mask” - “ring thief” configuration is used. (c) Comparative graph of the simulated thickness profiles for the case when the “shell mask” - “ring

thief” configuration is used vs. the case when only the “shell mask” is used placed at its optimal position.	243
Figure 6. 15: (a) 3-D geometry of the mechanical vane setup including a “shell”-type “mask” at $h_{mask} = 23\text{ cm}$ from the flat bottom of the prototype tank. (b) Side view of the “shell”-type “mask”. The dimensions of the “mask” are also shown. The circle indicates the “nose” area of the mandrel.	245
Figure 6. 16: (a) 3-D representation of the current distribution in the electrolytic volume, (b) current streamlines’ behaviour close to the mandrel surface and (c) thickness distribution on the cathode surface for the case when the a “shell”-type “mask” is used alongside the mechanical vane mandrel. The arrows in (a) and (b) indicates the current reaching the mandrel sides indirectly “from the top” while, (c) indicates the exposed “nose” area of the mandrel which the current reaches directly.	246
Figure 6. 17: Comparative graphs of the experimental and simulated thickness profiles for (a) strip 1, (b) strip 2 and (c) strip 3 of the mechanical vane deposit R6. Green line represents the simulated thickness for R6 alongside a “shell”-type “mask”, while the blue line represents the simulated thickness for R6 without the use of a “mask”. “Front” indicates the mandrel side closer to the anode.	247
Figure 6. 18: 3-D representation of (a) the potential distribution in the electrolyte, (b) the current distribution at the cathode surface and (c) the thickness distribution at the cathode surface for the PCD RDE model.	254
Figure 6. 19: Comparative graphs of the experimentally achieved (red data points) and the simulated thickness profiles by the PCD (black line), SCD (blue line) and TCD (magenta line) RDE setup models. The RDE deposit was produced at -5 V and -0.565 A , for 1800 s at $50\text{ }^\circ\text{C}$	256
Figure 6. 20: 3-D representation of (a) the potential distribution in the electrolyte, (b) the current distribution at the cathode surface and (c) the thickness distribution at the cathode surface for the PCD scaled-up disk model.	257
Figure 6. 21: Nickel ion concentration distribution at the cathode surface for the TCD RDE model when assuming two ionic species. The results simulate a deposition process conducted at -1 A (16 Adm^2) and -2.5 V , for 1800 s at $50\text{ }^\circ\text{C}$	258
Figure 6. 22: 3-D representation of (a) the potential distribution in the electrolyte, (b) the current distribution at the cathode surface, (c) the thickness distribution at the cathode surface and (d) the nickel ion concentration distribution at the cathode surface for the TCD scaled-up disk model when assuming four ionic species. The results simulate a deposition process conducted at -1 A (16 Adm^2) and -2.5 V , for 10800 s at $50\text{ }^\circ\text{C}$	260
Figure 6. 23: Comparative graphs of the experimentally achieved (red data points) and the simulated thickness profiles by the PCD (black line), SCD (blue line), TCD assuming two ionic species (magenta line) and TCD assuming four ionic species (green line) scaled-up disk setup models. The scaled-up disk deposit was produced at -2.5 V and -1 A , for 10800 s at $50\text{ }^\circ\text{C}$	261
Figure 7. 1: A 5-step methodology for systematically studying the electroforming process.	269
Figure 7. 2: The three geometries modelled for the purposes of the project using COMSOL Multiphysics®. (a) 3-D, laboratory-scale RDE geometry, (b) 3-D, industrial-	

scale disk geometry and, (c) 3-D, industrial-scale mechanical vane geometry. Samples of the deposits obtained using the three different cathode geometries are also shown here: (I) laboratory-scale nickel disk ($ARDE = 0.0113 \text{ dm}^2$), (II) industrial-scale nickel disk ($A_{disk} = 0.31 \text{ dm}^2$), (III) industrial-scale mechanical vane ($A_{vane} = 0.9 \text{ dm}^2$). 271

Figure 7. 3: Inside view of the custom, 18 L prototype electroforming reactor designed for the purposes of the project. The stainless-steel disk mandrel and anode basket filled with nickel pellets are shown here, immersed in the nickel sulphamate electrolytic bath. The level and temperature controllers, as well as the eductor and heater deployed, in the reactor for the large-scale experiments, are also shown lying in position in the empty tank during maintenance, with the plexiglass lid raised. 272

Figure 7. 4: Comparative graphs of the experimentally achieved (red data points) and the simulated thickness profiles by the PCD (black line), SCD (blue line) and TCD (magenta and green lines) models of (a) the laboratory-scale RDE setup and (b) the industrial-scale disk setup. The RDE deposited at -5 V and -0.565 A , for 1800s at $50 \text{ }^\circ\text{C}$. The scaled-up disk was deposited at -2.5 V and -1 A , for 10800s at $50 \text{ }^\circ\text{C}$ 274

Figure 7. 5: 2-D representation of the when the effect of (a) the “ring mask” and (b) the “shell mask” was studied deploying the 2-D axisymmetric RDE model. (c) 3-D representation of the current distribution in the electrolytic volume when the effect of a “shell”-type “mask” alongside the mechanical vane mandrel was studied using the 3-D mechanical vane model. In (d) a close up of the current behaviour close to the cathode surface is provided, showing the current streamlines reaching the “nose” directly and the mandrel sides “from the top” of the “shell”-type “mask”. 281

Chapter 1: Introduction

1.1 The “Industry 4.0” Concept

The term “industrial revolution” was introduced by the French economist J.-A. Blanqui in 1837 [1] to describe the quick and deep economic and social changes taking place in that period in England, caused by the transition of society from the pre-industrial to the industrial era. In 1840s, the term was mainly used by Marxists to describe the phenomena that were taking place around the world during capitalism’s transition from the manufacturing stage to the stage of industrial capitalism [2]. The term was adopted by the majority of (non-Marxists) economists in 1884 when the English historian A.-J. Toynbee published his *“Lectures on the Industrial Revolution”* [3], in an impactful attempt to record Britain’s radical shift to industrial-based economy. Since then, the term has been used to describe three highly influential industrial transitions.

The First Industrial Revolution is widely distinguished by the invention of the steam engine in 1784 however, it lasted for decades during the late 18th - early 19th century marking the transition from manual to machine labour. The positive impact of this first industrial transition started to show during the second half of the 19th century. Electrification led to the development of mass industrial production, while an increase in labour efficiency was being observed and business management was evolving to the new requirements. This new era of technological advances, including, but not limited to, the invention of dynamo by E. Siemens in 1867 and the Edison lamp by T. Edison in 1879, is nowadays known as the Second Industrial Revolution. As it was only reasonable, the new technological advances which were triggered by these two consecutive transitions in industry, economy, and society, have been continuously creating aspirations for a modernisation of the traditional means of

productions, breakthroughs in manufacturing and profit enhancement. This long-awaited transition, the Third Industrial Revolution, finally took place in the early 21st century, with transformations in technology, the traditional centralised business models, infrastructure, production, consumption, and communication infrastructure taking place. People started getting involved in production, labour efficiency grew rapidly, scientific research was now carried out by both private companies and the state, design, production, and distribution of products were split as the market, and eventually the financial system, turned global, while transport and telecommunication advances kept decreasing the cost [4].

All three industrial revolutions so far present common characteristics which distinguish them from common, evolutionary changes of the industrial sector (Figure 1.1). The main requirement for them to take place is the accumulation of various novel advances in the industrial production. The competition among the new technological advances would ease quickly as, inevitably, quality will overtake quantity. This is when an industrial revolution starts. Updated infrastructure is then needed, the state and societies evolve around the transformed economy sector, new products and opportunities, production is reorganised. As a result, the required resources and cost for production are reduced, product quality improves, niche products are developed. Finally, the real sector of economy reaches a new development level [4].

Any industrial revolution to follow will not deviate from the general idea that this model suggests either. In fact, the concept of the Fourth Industrial Revolution which was introduced to public in 2011 [5], and published as a strategic plan for industrial development by two German Ministries in 2012 [6], requires the accumulation of innovations in the sector of Internet of Things and Robotics, transition to fully automated production lines, the development of new infrastructure able to support ultra-fast internet connections, the design and development of high-end robotic equipment, niche and cheap materials, significant decrease of the human factor in production, followed by an increased demand for highly specialised employees [4].

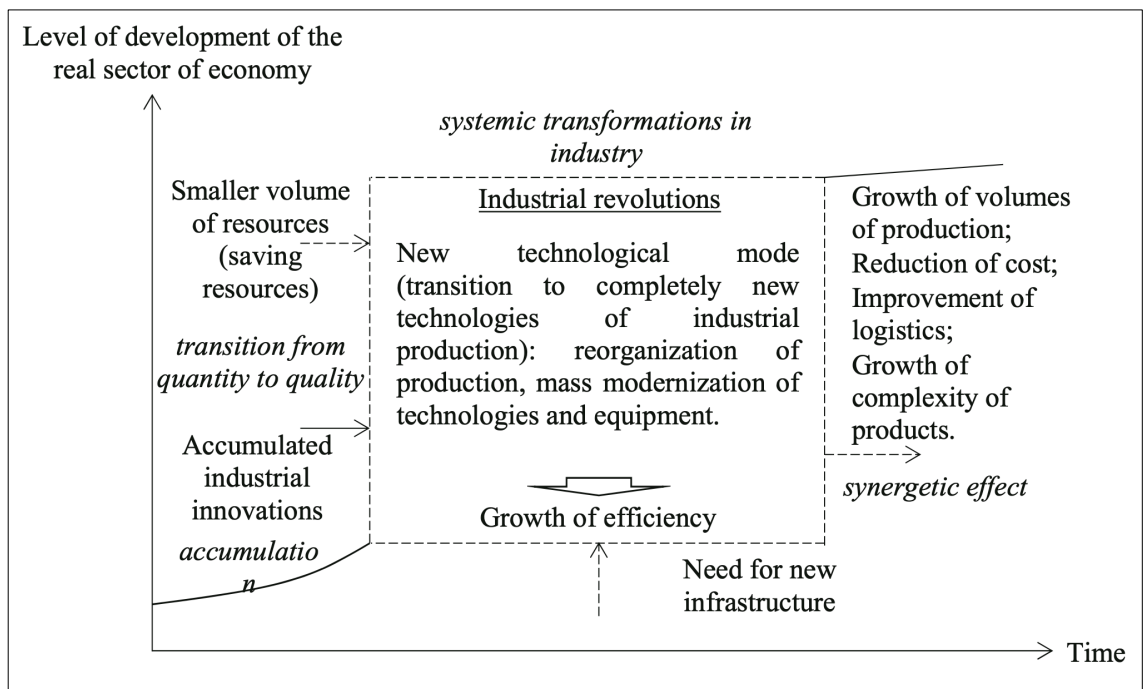


Figure 1. 1: Generalized model of an industrial revolution developed by E. G. Popkova, Y. V. Ragulina and A. V. Bogoviz [4].

Even though “Industry 4.0” is not due soon, since the concept was introduced, the most competitive industrial manufacturers around the world have been trying to secure the sustainability, high quality, and low cost of the fast technological developments of today. Using the continuously evolving and developing benefits that cyber-physical systems, the internet of things and artificial intelligence have to offer, the total computerisation of manufacturing and fabrication has been set as the greater aim [7]. For such a transition to actually take place, breakthrough developments in machine learning and machine communication are required. To achieve that, research in the fields of the Internet of Things (IT), Industrial Internet of Things (IIT), Cloud and Smart Manufacturing has been intense [8]. While the pillars of *Industry 4.0* concept mentioned so far take care of the conversion of experimental data into digital format, to establish the smart factories of the future, processes themselves need to enter a new era. New manufacturing technologies arise every day aiming to replace traditional production lines with more flexible ones, able to support the evolved industrial needs during the next industrial transition.

Among those technologies, additive manufacturing (AM) processes are gaining ground [9] due to their potential to transform production of parts for the "low-volume / high-value" industrial sectors, such as the aerospace and marine industries. According to ASTM additive manufacturing is *"a process of joining materials to make objects from 3-D model data, usually layer upon layer, as opposed to subtractive manufacturing methodologies"* [10]. One of the most appealing characteristics of AM techniques is the producer-client relationship that could be enabled through data transfer. The extensive use of software tools provides both customers and producers with the ability to digitally preview the customised product, enabling efficient design of tooling and production [11] - [15]. Moreover, the development of new products could move at a faster pace, providing industry with the ability to manufacture novel products of complex shapes and geometries [9], such as those encountered by electroforming.

1.2 The electroforming process: an overview

Electroforming was first introduced to the scientific society by the Prussian engineer and physicist, Moritz Hermann von Jacobi, in 1838. His discovery took place during his efforts to use an engraved copper printing plate as the cathode, immersed in a copper sulphate solution, upon which he was aspiring to electrodeposit copper. Even though he managed to accurately reproduce the engraved details of the cathode, he faced a difficulty in separating the electrodeposit from the original plate [16]. Following that, electroforming was used again successfully in 1842, by the Böttger of Germany to electroform nickel. During the 19th century, iron (in most of the projects) electroforming was mainly used for the reproduction of art pieces (e.g., sculptures, statues, jewellery) and the duplication of engraved plates for money printing [17].

Nowadays, every day, we encounter electroformed products many times and on several occasions. Being used in applications from micro-components for the medical and electronics industries to aircrafts and various aerostructures, this AM process impacts our daily life [18]. However, it remains, up to this day, a manufacturing process that scientists, researchers, and engineers do not know much about, mostly because the majority of the scientific investigations are only conducted by companies that already use it in their production lines and, consequently, the results remain confidential for years (or even forever).

If someone wanted to quickly describe what electroforming is, Paunovic's and Schlesinger's definition [19] of the process would be the simplest way to do it:

“Electroforming is a process in which electrodeposition is performed on a mandrel in a given pattern”. However, even though this is a comprehensive definition, it reveals neither any information of the process's mechanism nor the main reason why electroforming is considered a different process compared to electrodeposition. Therefore, to wholly define it, ASTM B 832-93 definition [20] would be the most appropriate choice:

“Electroforming is the production or reproduction of articles by electrodeposition upon a mandrel or mould that is subsequently separated from the deposit.”

In general, as every method, process and technique, electroforming demonstrates both advantages and disadvantages. These aspects were put together in the proceedings of the, only wholly dedicated, ASTM symposium on electroforming, in 1962 [21]. Using this as a basis, but not limited to that list, electroforming's pros and cons can be critically summed up as follows:

Advantages:

1. Process conditions, bath composition and considerate choice of the metals involved can control the metallurgical properties of the electrodeposited metal.

2. Dimensional accuracy is highly achievable if the proper cathode material is chosen; any limitations in that can only be implied by defects machined during the mandrel's development.
3. Fine detail reproduction compared to no other mass production process.
4. No limitations to the sizes of the products that could, potentially, be electroformed.
5. Niche shapes and geometries that cannot be developed by any other fabrication method.
6. Applicable to both low- and high-volume production lines.
7. Low-cost infrastructure required.
8. Low waste generation and satisfactory recyclability can be achieved through process optimisation.
9. Electrodeposition can be achieved in all surfaces, not just "on the line of sight" which limits the physical and vapour deposition processes.
10. The process can be used to fabricate thick (*mm*-scale) parts which cannot be achieved by physical or vapour deposition methods.

Disadvantages:

1. Relatively high cost of consumables (electrolytic bath, raw materials etc.); it can be competitive compared to other methods for high-volume production.
2. Comparatively slower production rates for parts of high thickness.
3. Limitations in product design when curves, edges or sudden changes in cross-section or thickness are required; up to this day, such requirements are reached at a second stage, by additional machining of the final electroformed part.
4. Defects on the mandrel could affect the product's appearance and/or properties.
5. Dendritic growth along leading edges can significantly affect deposition processes as in some cases of nickel electroforming, increasing process waste and minimising process efficiency.

6. Possible deposition under internal stress renders the maintenance of dimensional accuracy a challenging task.

At the same time, the disadvantages above make up the list of the challenges that an electroforming project would face and need to overcome. Since 1962, no other review -to the author's knowledge- has managed to update this catalogue and, this has been one of the goals of this project; to contribute to the scientific and engineering society, not only through our experimental and technical observations but, also, through up-to-date literature resources.

1.2.1. Nickel electroforming

Nickel is the fifth most common metal in nature and can be distinguished by its silver-white colour and shine. It is mainly found in the earth's crust in a concentration of 80 *ppm*, as well as the earth's core as a nickel-iron alloy. Annually, the consumption of nickel worldwide reaches the 100,000 metric tons [22] [23]. Other properties, its high melting point at 1435 °C, high ductility, mechanical strength, as well as anti-corrosion and anti-oxidation properties, render it a versatile material to work with for various applications [24]. As an electroforming material, nickel's popularity derives both from its ability to be used for either functional or decorative applications (or even functional ones with high aesthetics standards), and its mechanical and anti-corrosion properties.

Based on the definition provided earlier, electroforming is an electrochemical fabricating method, directly comparable to electroplating, at the end of which stand-alone parts are produced. As an electrochemical process, it requires at least two electrodes, an anode and a cathode immersed in an electrolytic solution and a power supply (DC). Due to voltage difference between the two electrodes, current travels through the electrolyte leading to the conversion of metallic ions into atoms on the cathode surface. These atoms are being built up, layer by layer, until the desirable

thickness of the electroformed part is achieved. In an industrial process, the anode consists of the metal that is to be deposited on the mandrel, while the mandrel itself plays the role of the cathode. In terms of applicability, the most electroformed metals are nickel, copper, and iron. During the last years, special alloys have also been added to the list of the “able to be electroformed materials”. However, nickel and its alloys still occupy the first place on that list [25].

Two are the most commonly used electrolytes in nickel electroforming; nickel sulphamate solutions and Watts solutions (nickel sulphate based) (Table 1.1). Nickel sulphamate is usually preferred over the latter as it presents good ductility, heat-resistance properties, high current-resistance properties and provides low intrinsic stress in the formed part [26].

Table 1. 1: Process parameters and properties for nickel sulphamate and sulphate electrolytes.

Chemicals	Units	Sulphamate Electrolyte	Sulphate Electrolyte (Watts Electrolyte)	Role
Nickel Sulphamate	$g L^{-1}$	300 – 780	150 – 300	Ni^{2+} source
Nickel Chloride	%	~1.3	20	Depassivator
Boric Acid	%	~6.7	~13.3	Buffering agent**
Parameters				
pH	N/A	4.0 ± 0.36	2 – 4	
Temperature	°C	45 – 65	45 – 70	
Current Density	ASD	0.5 – 30	5 – 30	
Current Efficiency	%	99 – 100 %	95 – 96 %	
Rate of Growth	$\mu m/hr$	25 – 61	23 – 58 ***	
Limiting Current	ASD	208.1	~150***	
Dissolved Oxygen	$g L^{-1}$	Present	Present	
Ammonium Ions	$g L^{-1}$	Avoided	N/A	
Sulphate	$g L^{-1}$	Avoided	Present	
Additives	$g L^{-1}$	Many	Many	

* If higher, then risk of hydrolysis of sulphamate increases.

** The role mentioned in most literature.

*** Estimate if compared to sulphamate bath.

Molecular weight for $Ni(SO_3NH_2)_2$ is 250.86, $NiCl_2 \cdot H_2O$ is 237.69 and H_3BO_3 is $61.83 g mol^{-1}$.

An electroformed part is fabricated using a mould (termed as mandrel) and has to be easily detachable without deformation whilst retaining its shape. Most electroformed parts are thick ($> 250 \mu m$ and often $> 1 mm$) for mechanical strength. Forming thick deposits without deformation imposes a requirement of low internal stress on the material. This unique functionality is achieved when nickel is reduced from an electrolyte containing almost only nickel sulphamate and boric acid (Table 1.1).

The recipes may vary for these two types of electrolytes; however, both can affect the final products characteristics and properties, through small changes in composition and/or process conditions. Except from their main compounds, nickel chloride and boric acid are also present in both types. The involvement of various (organic) additives can provide different product quality as well. In general, nickel sulphamate/sulphate and nickel oxide are the nickel ion carriers; however, nickel chloride is also used because of its ability to promote anode dissolution.

Table 1.1 shows the chemical constituents of a sulphamate electrolyte [27] [28]. As a comparison [29], the main constituents of a sulphate electrolyte are also included, which at first glance look similar. However, the first difference between the two solutions is the concentration of Cl^- , which is much lower in the sulphamate bath. A second difference is that sulphamate systems are additive free, whereas sulphate electrolytes use a variety of addition agents. Furthermore, surface adsorption by ions such as $[Cl]^-$, $[SO_4]^{2-}$, $[OH]^-$ are strictly avoided in sulphamates [30] - [33] because they increase internal stress. A fourth difference is that the operational current during electroforming is low; typically, between 5 and $20 mA/cm^2$ ($0.5 - 2 ASD$) vs. $50 mA/cm^2$ ($5 ASD$) for sulphate systems. At these low currents, hydrogen evolution is low and current efficiency for *Ni* deposition is consistently close to 100 % [27] [32] [34]. *Ni* content in the bath is replenished via the dissolution of specialised *Ni* anodes, which again, operate close to 100 % current efficiency. These myriad differences set the two electrolyte systems apart, and their electrochemical and chemical reactions should be viewed in this perspective.

Cathode reactions

Cathodes are actually the mandrels against which nickel is deposited to produce the final electroforms. The mandrel's conditioning and preparation are of the utmost importance as a neat electroforming result is highly dependent on them, since the final product will eventually obtain the shape, geometry, and detail of the mandrel's surface (Figure 1.2).

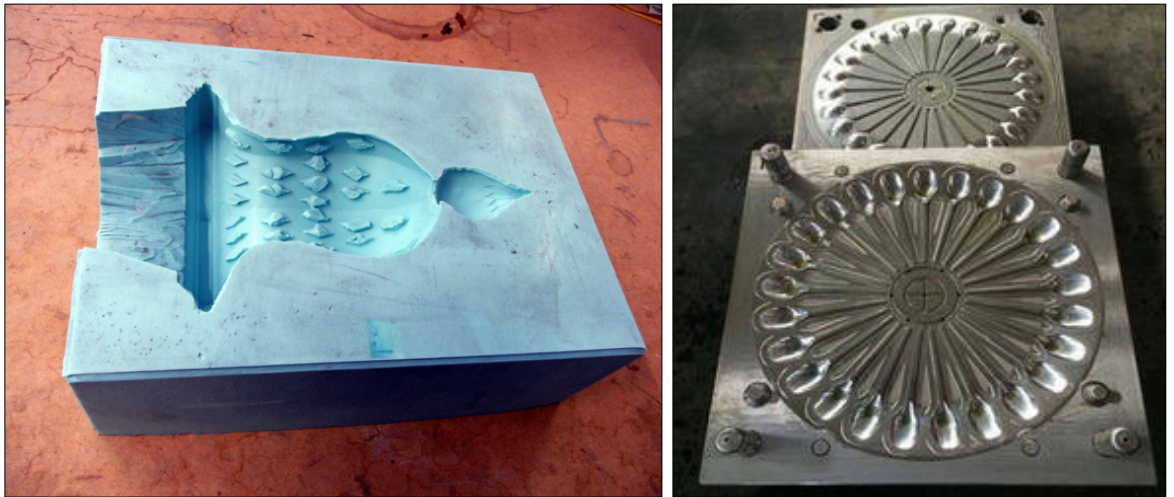


Figure 1. 2: (a) Non-conductive, silicone rubber (by *CIR Electroplating*) and (b) conductive, stainless steel (by *V.M. Moulds and Dies*) electroforming mandrels.

Material-wise, the range of candidate materials for mandrel development varies from pure metals and metal alloys to wood and fabrics. As it turns out, mandrels can be built by either conducting or non-conducting materials. Different types of stainless steel are most commonly used as mandrel material for nickel electroforming. Conductive mandrels provide sufficient adherence throughout the process and allow the relatively easy separation of the electroform at the end. On the other hand, the main disadvantage of the non-conductors is that they need to be coated over with a thin conducting film before use, adding one more stage to the already challenging enough mandrel preparation procedure. The decision on which type is the best to use is mainly dependent on the production volume; conducting mandrels can be used at a permanent basis, thus they are preferred for high-volume production [18].

Table 1. 2: Chemical and electrochemical reactions expected to occur in sulphamate systems.

Reaction	Possible reactions at the cathode	Reference
<i>Nickel Deposition</i>		
1.1	$Ni^{2+} + H_2O \rightleftharpoons Ni(OH)^+ + H^+$	[39-42]
1.2	$Ni(OH)^+ + e^- \rightleftharpoons Ni(OH)_{ads}$ [Rate Determining Step]	
1.3-a	$Ni(OH)_{ads} + e^- \rightleftharpoons Ni + OH^-$	[45,46]
1.3-b	$Ni(OH)_{ads} + Ni^{2+} + 2e^- \rightleftharpoons Ni + Ni(OH)_{ads}^*$	
<ul style="list-style-type: none"> • Note that Cl^- replaces OH^- in electrolytes where significant amounts of chloride is present. • Note that $Ni(OH)_{ads}^*$ in 1.3-b is used so that the reaction is correctly balanced, nevertheless, it denotes the continuous presence of the $Ni(OH)_{ads}$ active intermediates in the electrolytic solution. • For the purposes of this work, 1.2 is assumed to be the rate determining step however, this might not always be the case (refer to Tafel analysis in <i>Chapter 2, pages 92-94</i>). 		
<i>Proton Reduction</i>		
1.4	$Ni + H^+ + e^- \rightarrow Ni - H_{ads}$	
1.5-a	$2 Ni - H_{ads} \rightarrow 2Ni + H_2$	
1.5-b	$Ni - H_{ads} + H^+ + e^- \rightarrow Ni + H_2$	
1.6	$Ni - H_{ads} \rightarrow Ni(H_{ads})$	
Reaction (1.6) allows the formation of β -Ni phase. In effect two different Ni phases are formed which have been detected by cyclic voltammetry [47].		
<i>O₂ Reduction</i>		
1.7	$O_2 + 2H_2O + 4e^- \rightleftharpoons 4OH^-$	
<i>H₂O Electrolysis</i>		
1.8	$2H_2O + 2e^- \rightarrow H_2 + 2OH^-$	
Reaction	Chemical hydrolysis reaction in the bulk solution	Reference
1.9	$[H_2NSO_3]^- + H_2O \rightarrow [NH_4]^+ + [SO_4]^{2-}$ [Driven by temperature]	
Reaction	Possible reactions at the anode	Reference
<i>Ni Dissolution (Active): This reaction can only take place in the presence of Cl⁻ ions or when sulphur-depolarised Ni is used or when pure Ni anodes are used.</i>		
1.10	$Ni \rightarrow Ni + 2e^-$	[22,24]
<i>Anode reactions involving sulphamate</i>		
1.11	$2 [H_2NSO_3]^- \rightarrow [O_3SNH = HNSO_3]^{2-} + 2H^+ + 2e^-$ (Proposed intermediate)	[23]
1.12	$[O_3SNH = HNSO_3]^{2+} \rightarrow [O_3SN = NSO_3]^{2-} + 2H^+ + 2e^-$ (Azodisulphonate)	[23]
1.13	$2[H_2NSO_3]^- \rightarrow 2[O_3SN = NSO_3]^{2-} + 4H^+ + 4e^-$ (Overall reaction)	[23]
1.14	$2[H_2NSO_3]^- + H_2O \rightarrow N_2 + 2[SO_4]^{2-} + 8H^+ + 6e^-$ (High anode overpotentials)	[23]
1.15	$2[SO_4]^{2-} \rightarrow [S_2O_3]^{2-} + 2e^-$	[22]
<i>Reactions involving Cl⁻</i>		
1.16	$2Cl^- \rightarrow Cl_2 + 2e^-$	
1.17	$2[NH_2SO_3]H + 3Cl_2 + 2H_2O \rightarrow N_2 + H_2SO_4 + 6HCl$	[24]

As reviewed before by the authors [29], the debate around the mechanism of nickel electro-reduction has mainly centred on sulphate and chloride-based electrolytes [35] - [37], where $NiSO_4$ and $NiCl_2$ are the source of nickel ions, respectively. The proposed sequence of reactions for nickel reduction for those electrolytes is shown in Table 1.2 (c.f. Reactions 1.1 - 1.3). The key points are that the second reaction step is rate determining, although it has been argued that either $[OH]^-$ [38] [37] or $[Cl]^-$ [36] [39] can be the active intermediate. This mechanism has been tested experimentally, where possible. It has been shown that either $Ni(OH)_{ads}$ or $NiCl_{ads}$ could be the adsorbed intermediate [36] - [42] depending on Cl^- concentration. Analysis of Tafel slopes have revealed that Reactions 1.3-a & 1.3-b, involving a single or two electron transfer are favoured at low and high overpotentials [38] - [43]. Electrochemical Impedance spectroscopy (EIS) data have provided indirect support to these Tafel slope measurements [40] [41]. The generality of this mechanism has also been tested using perchlorate and methane-sulphonic acids [42]. One could argue that since sulphamate ion is a poor complexant [28], that nickel discharge follows a similar mechanism to that shown in Table 1.2 and since $[Cl]^-$ concentration is low, $Ni(OH)_{ads}$ is the adsorbed intermediate.

However, there are some major differences between cathodic processes in sulphamate and sulphate systems. For example, sulphate systems encounter co-reduction of protons and oxygen during nickel deposition leading to cathode passivation [37] [41]. This issue has been countered by maintaining high levels of chloride ions, as opposed to sulphamate systems. Other researchers have also attributed hydrogen evolution to catalysis by nickel [37] [39] [43] via Reactions 1.4 - 1.6 in Table 1.2, since none of the reactions increase the pH at the vicinity of the electrode. While these reactions can lead to low current efficiencies, it remains unclear why they should lead to oxidised nickel. One explanation offered is that this is due to co-adsorption of species such as $[OH]^-$, $[SO_4]^{2-}$, which is supported somewhat by impedance data to [41]. However, sulphamate systems have low $[Cl]^-$ concentration, no addition agents, and avoids the formation of $[SO_4]^{2-}$. The current efficiency too is nearly 100 % within the operational range cited in Table 1.1. This means that Reactions 1.4 - 1.8 are suppressed during nickel electroforming by other means.

Direct measurement of mass and charge using an electrochemical quartz crystal nano balance (EQCN) [44] for sulphate and chloride electrolytes, on the contrary, show that most of the hydrogen formed via [Reaction 1.5](#) is out-gassed, and very little β -nickel is deposited. Their results also show that that $Ni(OH)_2$ forms at the electrode surface right from the beginning of Ni deposition leading to oxidised nickel, indicating that the pH near the electrode is always high. Another independent experimental investigation using cyclic voltammetry shows that low current efficiencies and nickel oxides are obtained in only aerated solutions [45]. These data point towards [Reaction 1.7](#) (and [1.8](#) at high overpotentials) being the main cause of high surface pH. These EQCN results provide evidence that the other bath constituent, namely boric acid, may be blocking these reactions.

The role of boric acid

Because the formation of $[OH]^-$ is undesirable, boric acid (H_3BO_3) is added to nearly all nickel electrodeposition solutions [37] - [41], [44]. The use of boric acid was recorded in 1954 [46], and process descriptions of sulphamate electrolytes recommend the use of boric acid as a buffering agent to obtain current efficiencies of 100 % [27], [30] - [32], [47] - [49]. The buffering action of boric acid near the electrode surface, however, has been contested by other researchers [50] [51] since pK_a of the boric acid was calculated to be 9.3 [52], and nickel precipitation occurs at pH exceeding 5.5. The role of boric acid in sulphamate electrolytes has been examined by collecting polarisation data [53]. Tafel behaviour was found to be qualitatively similar to those in sulphate systems and current efficiency for nickel deposition remained high almost up to the limiting current (180 mA/cm^2), showing that hydrogen evolution was suppressed even at high currents. In addition, microsensor measurements close to the electrode (between 10 and $100 \mu\text{m}$) showed that the pH value remained close to that in the bulk when boric acid was present in the electrolyte.

These results build on the EQCN findings [44] mentioned in the previous section showing that *Ni* deposition is facilitated by H_3BO_3 . This also compares well with electrochemical impedance spectroscopy (EIS) analysis of sulphate-based systems which propose that a single reaction, identified as *Ni* reduction, proceeds in the presence of boric acid, [40] [41]. Further evidence can be found in cyclic voltammetry and chronopotentiometry measurements by Hoare [50] [51], whose data show the suppression of both oxygen as well as proton reduction reactions when boric acid is present. The mechanism for maintaining pH at the electrode surface, therefore, is not via classic solution side buffering, but through modification of surface and reactions, which has never been investigated for a sulphamate electrolyte.

Anode reactions

Regarding the anode electrodes, these consist of a proper nickel metal form which can be efficiently dissolved during the process and under the specific anodic conditions applied each time. Since nickel anodes present a tendency towards the formation of a resistive passive film on their surface, in most cases, sulphur is added in low quantities (*e.g.*, 0.02 wt %) to boost dissolution [54] [55]. In the case that high positive anodic potentials are applied during the process, anode passivity can be increased. As such an increase could lead to changes in pH, high power costs and even the decomposition of the sulphamate ion, halide compounds have been used in support.

The use of appropriate anodes for *Ni* electrodeposition from sulphamate electrolytes was recognised as early as 1965 [32]. It was demonstrated that depending on the choice of anode, the internal stress of the deposit could vary. Specifically, sulphurised anodes, where *Ni* dissolves at low potentials, have been observed to produce products of low internal stress. Other anodes such as platinised *Ti* and pure *Ni* have been correlated with increased amount of $[SO_4]^{2-}$ in the solution as well as incorporation of sulphur in the deposit. Because the bulk decomposition of sulphamate is slow [30] [33] [49], formation of $[SO_4]^{2-}$ is assumed to be via anodic

reactions. A detailed study by Greene [49] proposed that several electrochemical reactions can occur at the anode, depending on the potential; these reactions are listed in Table 1.2. Greene [49] identified this compound by UV-Vis analysis as azo-disulphonate, $[O_3SN = NSO_3]^{2-}$, although other authors have suggested other compounds [56] [57].

The rate of generation (and consumption) of this product is what controls the internal stress of the deposit [27] [30] [58]. Therefore, one needs to tailor and control anodic reactions such that *Ni* dissolution is the main reaction (Reaction 1.10), and small amounts of $[O_3SN = NSO_3]^{2-}$, are coproduced (Reaction 1.13).

Although the first reaction replaces Ni^{2+} ions consumed at the cathode, the latter enters the electrolyte as a stress reducer. A polarisation analysis suggests that the stress reducer is formed only at intermediate potentials [59]; this cannot be attained at de-sulphurised *Ni* but were produced using pure *Ni* anodes where the electrode partially passivated [59]. However, Reactions 1.14 and 1.17 may also occur on *Ti*, *Ti – Pt* or *Pt*, which are deleterious to process operation. However, during a process, one needs to control the production and consumption of the stress reducer in the solution to optimise the internal stress. This would require the quantification of product generation and consumption, which is lacking. As an example, Figure 1.3 shows the overall cell potential gathered in authors' laboratory during nickel electroforming, where pure *Ni* electrodes were used. The cell potential is low for the first 400 s sustaining a current of 20 mA/cm² (2 ASD) after which passivation of the anode begins. Once passivation has occurred, the cell potential “shoots up” to 10 V (compliance voltage) and the current drops to < 0.3 ASD or 3 mA/cm². Presumably these currents correspond to the formation of a myriad of products shown in Reactions 1.12 - 1.17. One needs to identify and monitor the products formed and rates of formation, which, in practice, is difficult, owing to their low concentrations. However, since these chemical changes govern deposit stress (which has often been measured), quantification of these reactions is needed if one were to develop a controllable process.

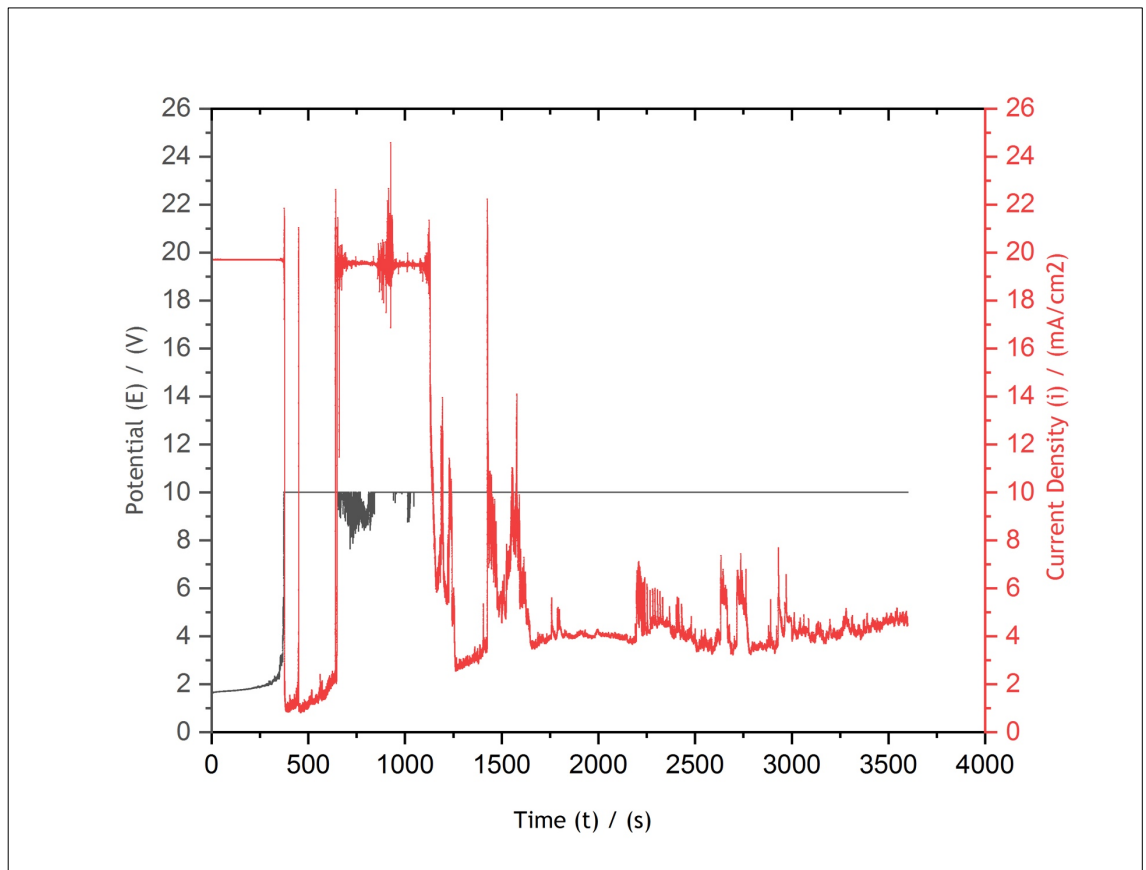


Figure 1. 3: Cell voltage (in black) and current (in red) as a function of time during electrochemical deposition from a sulphamate electrolyte of composition stated in [Table 1.1](#). Applied current density at start was 20 mA/cm^2 (2 ASD) and was applied for a period of 2 h. Solution temperature $50 \text{ }^\circ\text{C}$.

1.2.2. Nickel electroforms' properties

Hardness is one important parameter that renders nickel electroforms the best choice for a significant variety of applications; especially nickel electroforms developed in sulphamate solutions. As it was first presented in 1960s, for electroforms of thickness between $0.69 - 2.4 \text{ mm}$, developed in nickel sulphamate solutions, hardness measurements vary between $192 - 207 \text{ VHS}$, with the thinnest specimens presenting higher hardness values. The corresponding measurements for electroforms developed in a Watts bath were $128 - 135 \text{ VHS}$ [21]. Even though this is not recent

data, it is the only direct comparison between sulphamate and Watts baths up to this date. However, it is in good agreement with Kendrick's study four years later but, still, in the 1960s [27]. Since then, several more recent studies on electroforms' thickness and hardness have been published, suggesting hardness values even up to 400 *VHS*, however, they are mainly focused on the determination of the mechanisms and parameters that affect hardness and thickness distribution rather than actually measuring them [60] [61] [62]. Alternative routes have also been explored in recent years to increase hardness, including the development of Ni-Co alloys.

On another front, to express the relationship between the factors that influence current distribution, hence thickness and hardness, the concept of throwing power was introduced. Generally, the higher the throwing power, the higher the thickness uniformity in both recessed and prominent areas would be. Nickel sulphamate solution baths present an average throwing power among various electrolytes. However, its values are improved in relatively low current densities and are easily controlled by adjustments of different process parameters such as the pH, temperature, anode-cathode distance etc. [63]. This property provides engineers with the ability to control working parameters depending on the application the electroforms are developed for, rendering nickel maybe the most versatile metal that can be used for both functional and decorative purposes; as a general observation, lower current densities (leading to improved throwing power) produce brighter nickel electroforms. The reasons and mechanisms under the influence of which this kind of properties are observed is something that existing literature does not answer sufficiently, if at all.

Last but not least, internal stress is probably the most important parameter that needs to be controlled and remain under specific limits based on an application's requirements. The concept of internal stress describes the forces created within the deposit due to the electro-crystallisation process and/or the co-deposition of impurities caused by hydrogen, sulphur, or other elements [64]. Electroforms can be either tensively or compressively stressed. Tensively stressed deposits, present an average distance between nickel atoms greater than the equilibrium value while, compressively stressed deposits behave in the exact opposite way in the atomic level. As

a result, tensile stress causes the final electroformed parts to contract (bend or curl), after its separation from the mandrel while, compressive stress causes expansion [63]. Dislocation theory provides the most acceptable explanation of the origins of internal stress [65] [66]. The presence of halides in the electrolyte solutions seems to affect the extent of internal stresses. A study by Tsuru et al. [67] have suggested that, by increasing the amount of any halide in a nickel sulphamate bath, the internal stress first increases and then reaches a minimum value. As internal stresses can lead to cracks in the final product, it is of vital importance that stress is reduced when the electroforms are specifically meant for aerospace and aviation applications. Since stress is more often observed in nickel alloy electroforming, nickel alloys have been under close investigation in order to confirm whether they can provide the same quality standards as pure nickel, presenting reduced or even minimised internal stresses when used in the production of aerospace parts [68].

1.2.3. Applications

As mentioned above, electroforming finds applications in many aspects of our lives, which are well recorded in review papers over the years [21] [69] - [71]. Just to mention the most interesting of electroforming applications, we should refer to several sectors: from arts and crafts to the energy and aerospace industry.

Jewellery and art pieces were the very first products to be electroformed. The Minerva statue electroformed out of bronze in 1920 [21] and Prince Charles' Coronet was electroformed gold in 1960 [72], showcasing that the process has played an important part in the development of metal arts; electroforming is even winning art prizes, like the "Electroform(alism)" project (Figure 1.4) of the design firms "Anya Sirota + Akoaki" and "Ann Arbor, Mich." that won a "2013 R+D" award from the American Institute of Architects [73]. Even the textile industry has used electroformed rotary screens for printing textiles [18]!

Electronics and data storage industries have also benefited from the process [71] [74]. Compact disks (CDs) are maybe the most famous products that involve electroforming in their production process. Even though the main body of the product is produced by injection moulding of polycarbonate resin in nickel moulds, the pit pattern in the finished disks is actually a result of the high precision surface detail of these moulds which need, for this reason, to be prepared by electroforming.

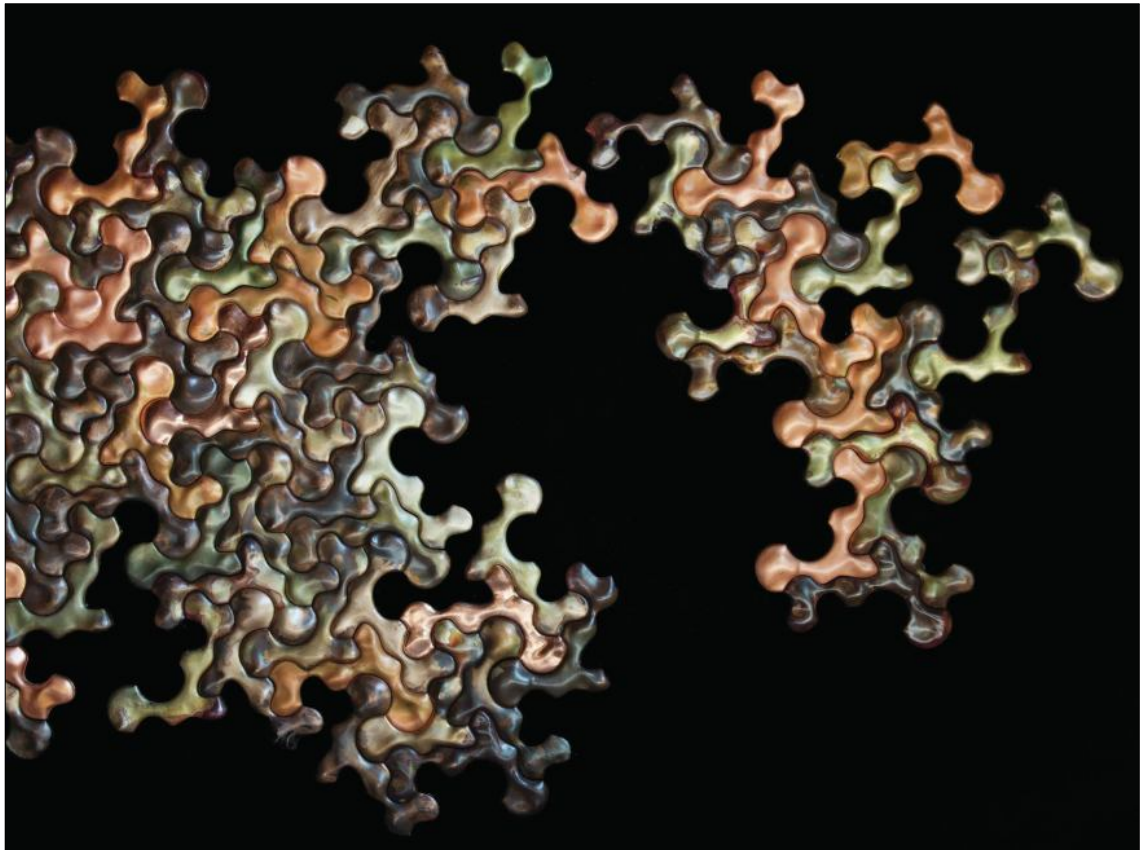


Figure 1. 4: Alex Fradkin. The copper pieces created by studio Akoaki through electroforming can be arranged into a sculptural installation. [73]

Since 1930, when electroforming was first introduced to the record industry, 78-rpm disks, 45s and LPs has been developed in electroformed nickel moulds with no other approach to have been proved better until our days. In electronics applications,

electroformed nickel stencils used in solder paste printing for fine-pitch devices remain the best alternative to date [75].

Electroforming is also to be found in the “heavy” industries’ production lines, such as the automotive and aircraft/aerospace ones. In both these sectors, electroforming is most usually used to fight corrosion, alongside wear-resistance and durability improvements. Nickel is the most electroplated metal in these industries, due to its significant mechanical and anti-corrosion properties. From functional aluminium plating to increase corrosion resistance in wheels and plated steel bumpers, to decorative plating on plastics to improve durability, design, flexibility and recyclability, electroforming serves the automotive industry as efficiently as possible [70] [71].

In aerospace the various types of metal deposition have been proved to be the most promising of the AM processes to meet the quality challenges of the industry [68], with the most famous among them being the electroforming of nickel. Therefore, their continuous study, characterisation and optimisation is of the utmost importance; airworthiness and air transport safety must be guaranteed with no space for errors of any kind. Corrosion-resistance at high temperatures, protection against abrasion and erosion [76], development of advanced tooling and increase of repairability rates are only few of the reasons which justify the viable role that electroforming plays for this industrial sector. In some cases, (nickel) electroforming is even the only practical and cost-efficient way to produce specific parts such as, parts used in electromagnetic interference shielding, volume compensators and temperature and pressure sensors [18]. Nickel electroforming has also, significantly, contributed to space aviation. From the production process of waveguides, antennae, and thrust chambers, to the development of the slit wheel segments on the Hubble Space Telescope Imaging Spectrograph (STIS) [77] nickel electroforming is present.

1.2.4. Sustainability

Nickel is an element and as such it can neither be produced nor destroyed. It occurs naturally, mainly in the form of sulphides, oxides, and silicates. Annually, more than two million tonnes of either new or primary nickel (e.g., nickel oxides, ferro-nickel) are produced and used. The production of nickel involves multiple steps and presents high energy requirements for heating during extraction and refining. Mainly sulphide and laterite-type nickel deposits are of financial interest. Lateritic ores are mined from various depths requiring large earth-moving equipment while, sulphide ores are usually found underground alongside copper ores [78].

Nickel extraction from a lateritic ore takes place by extractive metallurgy, through roasting which removes the moisture from the ore. As a next step, the nickel oxide is removed by reduction furnace which further reduces the chemical bound water. The final product is nickel of 75% purity. Nickel extraction from sulphide ores results in 45% purity and follows a more challenging process. The ore is first placed in a furnace containing pre-heated oxygen and, through this smelting process, the iron and sulphide present in the ore are removed via oxidation. A final step requires more oxygen to be injected in the molten bath eliminating any remaining iron and sulphide traces [78].

Following the mining process, nickel matte is gathered. Nickel 95% in purity can only be obtained through further refining, using either the fluid bed roasting technique or by deploying electric cells which are quickly becoming the industry standard. These cells are equipped with inert cathodes which help removing the final impurities and their use leads to better refining results if compared to the conventional roasting technique [78].

Currently global nickel reserves are estimated at 95 million metric tons (Figure 1.5) [79] [80]. Nickel ores can be found in more than 25 countries around the world among which Indonesia, Philippines, Russia, Australia, and Canada hold more than 50 % of the reserves.

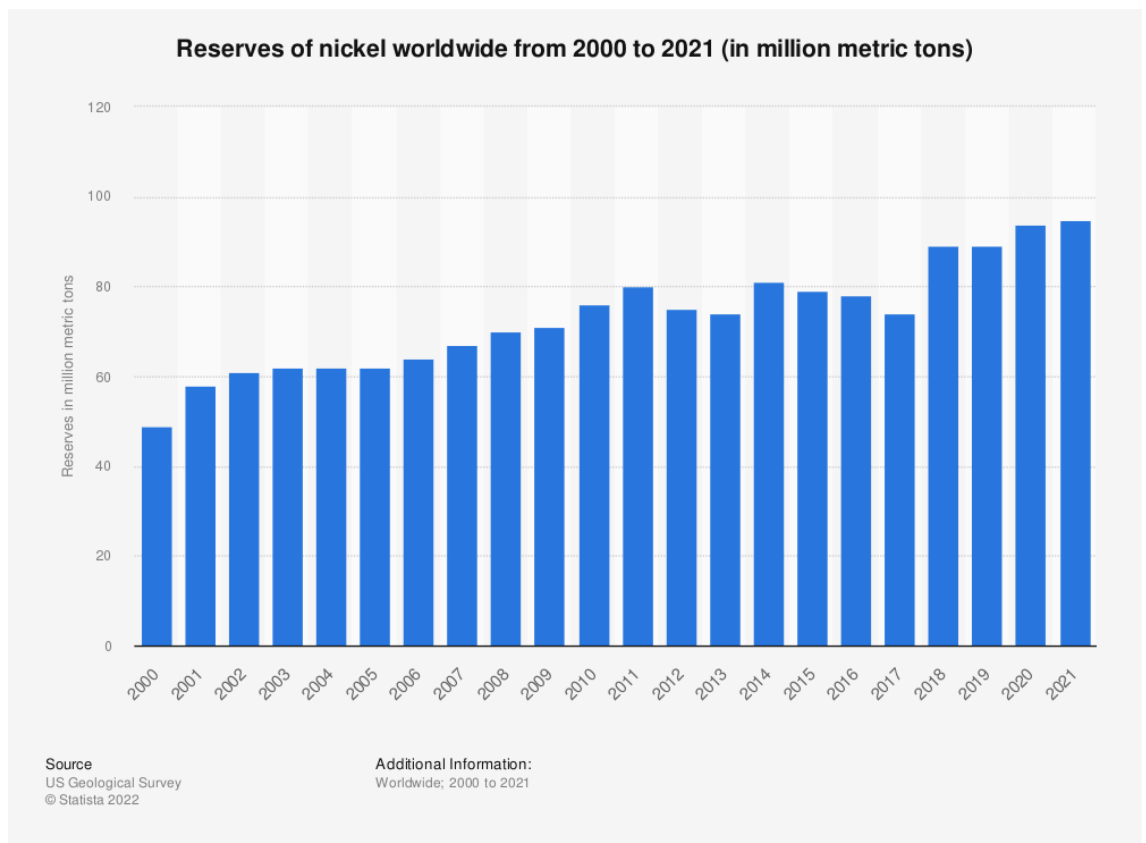


Figure 1. 5: Global nickel reserves 2000-2021 [79] [80]

Like many other metals, nickel can be recycled indefinitely without losing its quality and it does not impose a significant health hazard to humans and nature. However, nickel is toxic and therefore it needs to be handled as such [81]. Nowadays, most of the environmental issues have been addressed by the industry. The main objectives of industries that use nickel have been to reduce nickel-bearing waste and to introduce recycling or reclamation programs. Several methods, including evaporation, reverse osmosis, and ion exchange, are currently in use. At the same time, most researchers and engineers involved in nickel plating processes agree that the environmental benefits deriving from electrodeposition, as an alternative to traditional production techniques, are not to be questioned; conservation of resources, fuel efficiency and recyclability are to name a few [71].

As it can be seen in [Figure 1.6](#), nickel demands have been steadily increasing over the last decade with the global nickel consumption in 2021 reaching 2.851 million metric tons ([Figure 1.6](#)) [82], at an average price of \$18,500 per metric ton ([Figure 1.7](#)) the same year [83]. At this consumption rate, global nickel reserves, the quantities that have been already discovered, are currently recoverable, and commercial, will last for ~ 33 years. A potential increase of annual global consumption by 5% (2.991 million metric tons) or 10% (3.141 million metric tons) will lead to current nickel reserves being available for ~ 32 and ~ 30 years respectively. Even though these numbers do not seem optimistic, according to the U.S. Geological Survey Of 2019 [84] nickel resources, the quantities that have not been discovered yet and could be technically recoverable, are estimated to exist in huge volumes based on geologic knowledge and theory. It is believed that deposits like the manganese nodules, which can be found in the deep sea, contain significant amounts of nickel with recent estimates suggesting a value of 290 million tons [24].

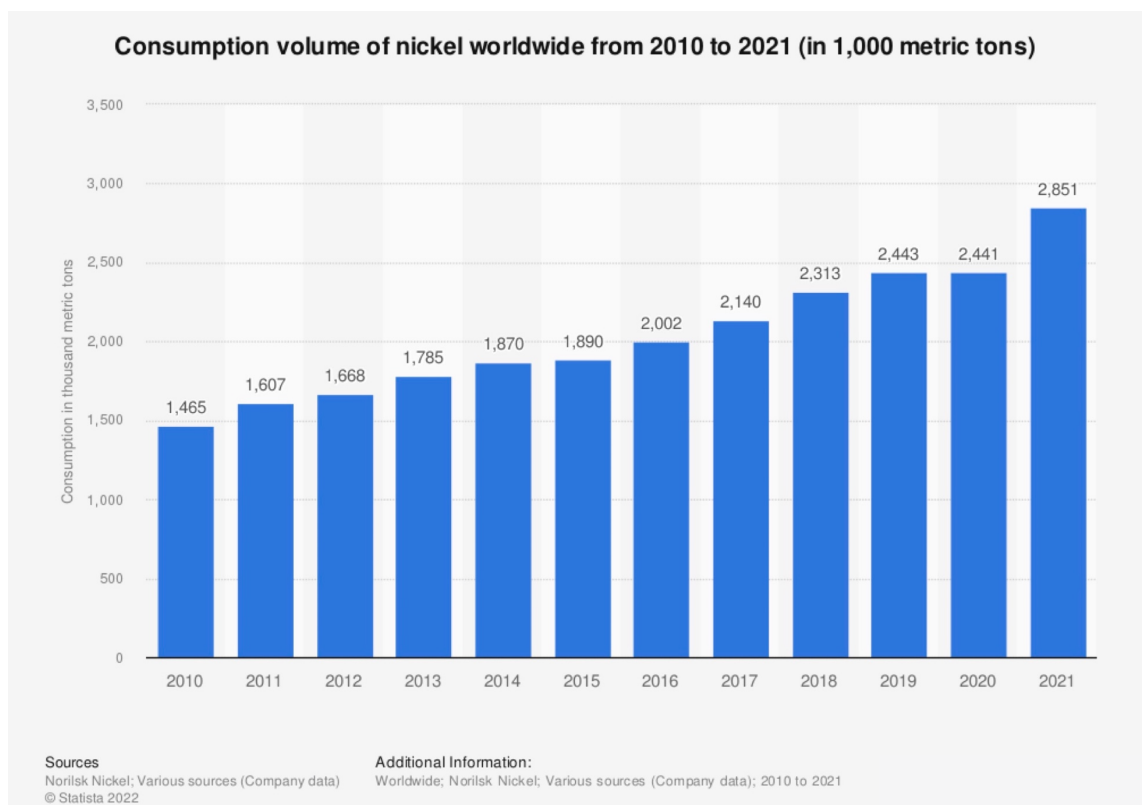


Figure 1. 6: Global consumption volume of nickel between 2010 and 2021 [82]

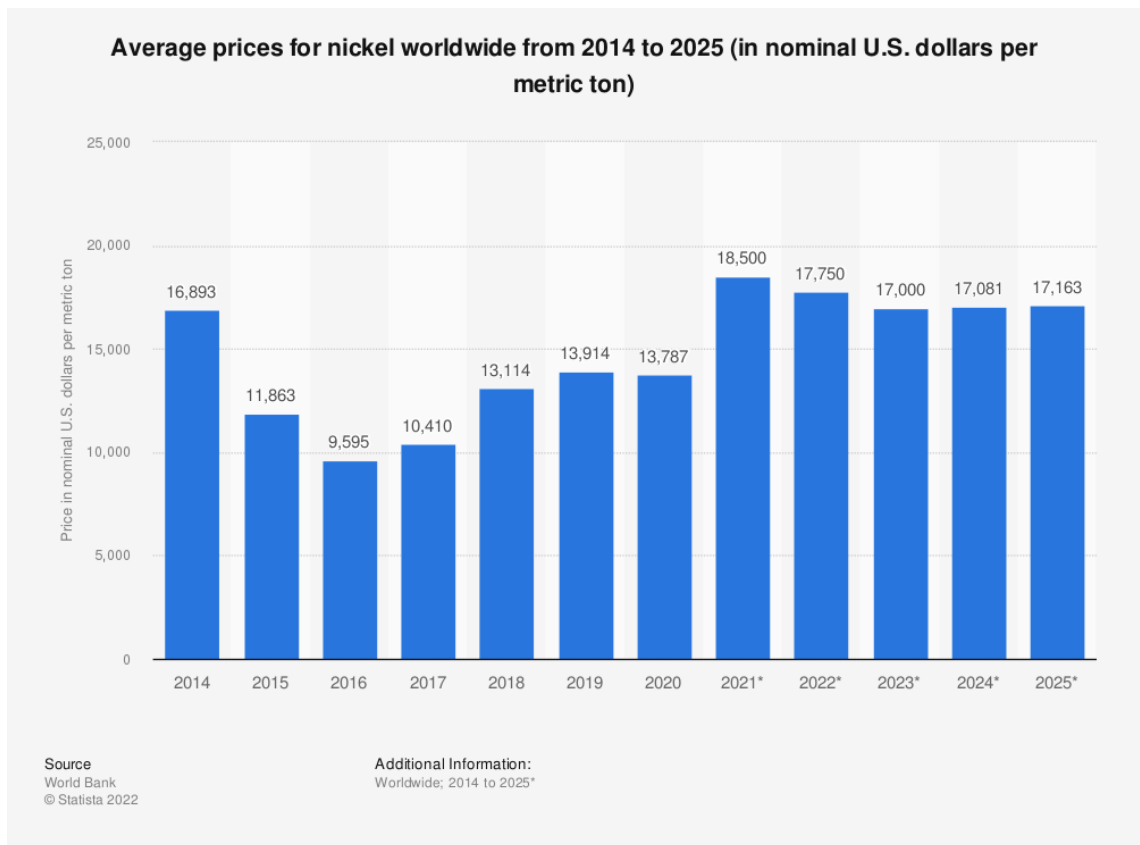


Figure 1. 7: Average nickel price, globally, between 2014 and 2021. Estimates for years 2022-2025 are also shown. [83]

Nevertheless, to the author’s opinion, a rationale of “keep consuming irrationally, just because the resources (might) exist” is not in line with a sustainable approach in modern manufacturing and resources management. Especially when the mining and refining process presents high energy requirements, produces considerable waste, and involves highly intrusive machinery (e.g., blasthole drills, bucket-wheel excavators, dozers, dragline excavators) which can significantly disturb the balance of ecosystems around the mining sites.

Therefore, optimised processes and modelling are crucial to improve economic performance and minimise the environmental footprint of modern additive manufacturing.

1.3 Modelling the electroforming process

Up to this date, the optimisation of the electroforming processes (Figure 1.8) mostly relies on empirical knowledge, which currently constrains transformation into high volume manufacturing. However, the construction of reliable modelling tools to simulate electroforming processes could enable this to happen. Starting from the study of the system's geometry, developing an accurate picture of process chemistry and electrode kinetics, and including other transfer phenomena could provide a reliable model to reveal the process's inherent weaknesses and strengths. Such a tool could also play an important role in understanding the critical mechanistic steps during electroforming, which, for many metals e.g., nickel, have still to be thoroughly studied and understood [29]. Thereby, well-designed modelling tools can prove to be a significant asset in the effort to optimise electroforming. In the forthcoming section the authors identify some of the key modelling investigations in this regard. Although key studies -as per the authors' opinion- are presented here in an effort to follow the developments and progress that has been made in modelling the electroforming process, discussion focuses on more recent studies, while some key earlier investigations are discussed for chronological coherence.

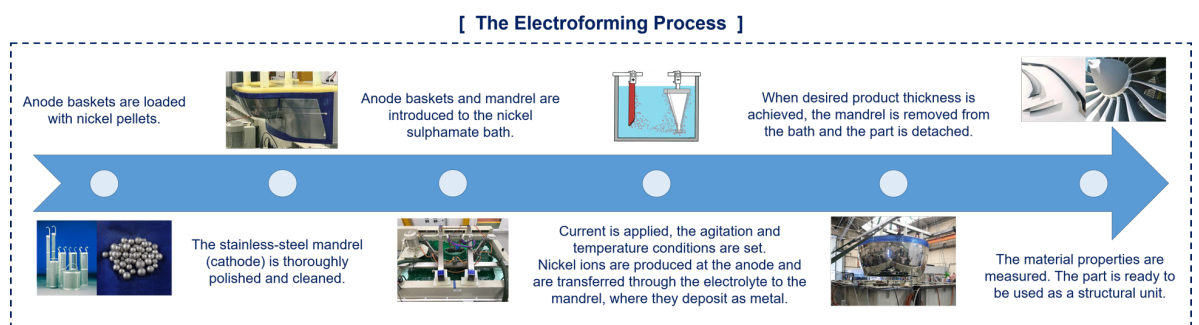


Figure 1. 8: The electroforming process

The interest in simulating the electroforming process is not a demand of modern times. The first numerical studies of the process made their appearance in the 1970s.

Since then, electroforming has only been studied occasionally, in parallel with the rapid developments in computational sciences. However, an increase in interest in this process, its applications, and the ability to model more rigorously has been observed only during the last decade. In particular, electroforming leads to a change in shape of the reacting surface and modelling these changes can be challenging. In the interim, experimental studies of this process have been carried out in a more systematic manner, providing data that allow the development of well-educated modelling tools.

To allow for a better understanding of the studies presented in this work, three concepts need to be briefly explained. There are three classes of current distribution that need to be considered during the design of any electrochemical process: the primary, secondary and tertiary current distributions. Each one of these describe different approximations regarding the solution resistance, electrode kinetics and mass transport.

The first one, primary current distribution, occurs in a system where reaction kinetics and mass transfer are fast, and the process therefore is controlled solely by issues arising within the bulk solution. Consequently, primary current distribution considers potential losses due to solution resistance which is solely dependent on the cell geometry. Secondary current distribution is the case where the effect of electrode kinetics start hindering the reaction rate. In this case, reaction kinetics are added on to that described by primary case. Lastly, tertiary current distribution, which accounts for variations in electrolyte composition due to mass transfer effects incorporates all three aspects. This necessitates the inclusion of other ions and electro-active species in the electrolytic volume, as well as the ionic strength of the electrolyte.

In effect, these three levels capture the controlling influences during reaction at a surface, the first being where reaction rates and material transfer do not hinder, the second where kinetic impediments are experienced, and the third where transport limitations are encountered. Although, it is true that a full model should

always include all three limitations, more often than not, one of the three processes can be dominant. In addition, it is difficult to predict which of these effects dominate at a particular current density. A full analysis often builds the model layer by layer, which reveal the effect of each of these reactor and reaction aspects. Some of the key modelling studies of the electroforming process discussed below have attempted to understand these very aspects in practical terms.

1.3.1. Key modelling studies of the electroforming process

In one of the first models ever proposed, J.A. McGeough and H. Rasmussen [85] investigated problems with thickness uniformity during the production of thin metal strips. Their research focused on the description of sinusoidal irregularities on the mandrels' surface, which are of small slopes and present small amplitudes when compared to the average inter-electrode gap width. A series of plating cycles consisting of a period of deposition of metal on the mandrel, followed by a shorter time of dissolution to remove any extra metal deposited (the application of periodic cathodic and anodic currents), was studied as a solution to the problem. They suggested that thickness uniformity is achieved when the current efficiency for the deposition part is different and less than that for the dissolution one. Even though longer electroforming processes seemed to favour more uniform deposits, it was also highlighted that there is a threshold in the maximum thickness that can be achieved each time since that depends on the ratio between deposition time and dissolution time needed to achieve good uniformity. Introduction of Fourier series analysis for the description of more complicated geometries was proposed while, since the electroforming process presents complex thermodynamics, the authors suggested that more experimental studies on the effects of overpotentials should be carried out before numerical solutions can describe the actual process.

Regardless of the various approaches tested in the following years, two numerical techniques have been employed successfully: the level set method (LSM) [86] - [89]

and the finite element method (FEM). The latter has been the favoured by researchers due to its flexibility in combining different theoretical models to solve various boundary problems.

In 1978, Alkire et al. [90] published a systematic study of a shape evolution problem using the finite element method to conclude that this numerical approach proves to be reliable, rather limitless, and flexible in modelling current distribution problems during electrodeposition. By studying the geometry of the 2-D cell shown in [Figure 1.9](#) and assuming secondary current distribution, for the first time to the author's knowledge, a step-by-step computational approach, consisting of eight stages, was suggested: (1) determine an efficient meshing of the domain, (2) determine initial parameters, (3) solve the problem and obtain data matrices (stationary studies), (4) determine the error range and optimise the data accordingly, (5) the current distribution at the cathode boundary, (6) introduce the variable of time in the computation to predict the final shape after a determined period (time-dependent studies), (7) optimise the mesh accordingly to contribute for the geometry deformation taking place over time and, finally, (8) repeat the calculations for every time step. For this computational approach the researchers assumed a uniform composition of the electrolyte, single reaction at the cathode boundary obeying the Butler-Volmer model, an unpolarised, non-deforming anode, fixed kinetic and transport parameters as well as a slow change in shape with respect to the electrical double layer.

Among others, their results suggested that the finite element method is not sufficient any more in cases where potential changes are highly localised, while parameters such as the anode position and transfer coefficients seemed to not affect the results. They also suggested that thickness uniformity increases with time, since the uniformity of current distribution becomes more uniform as a new surface is deposited and the deposit grows towards every direction.

Finally, and despite the two main reported difficulties in modelling the potential field and outward growth close to a singularity, the researchers suggested that the

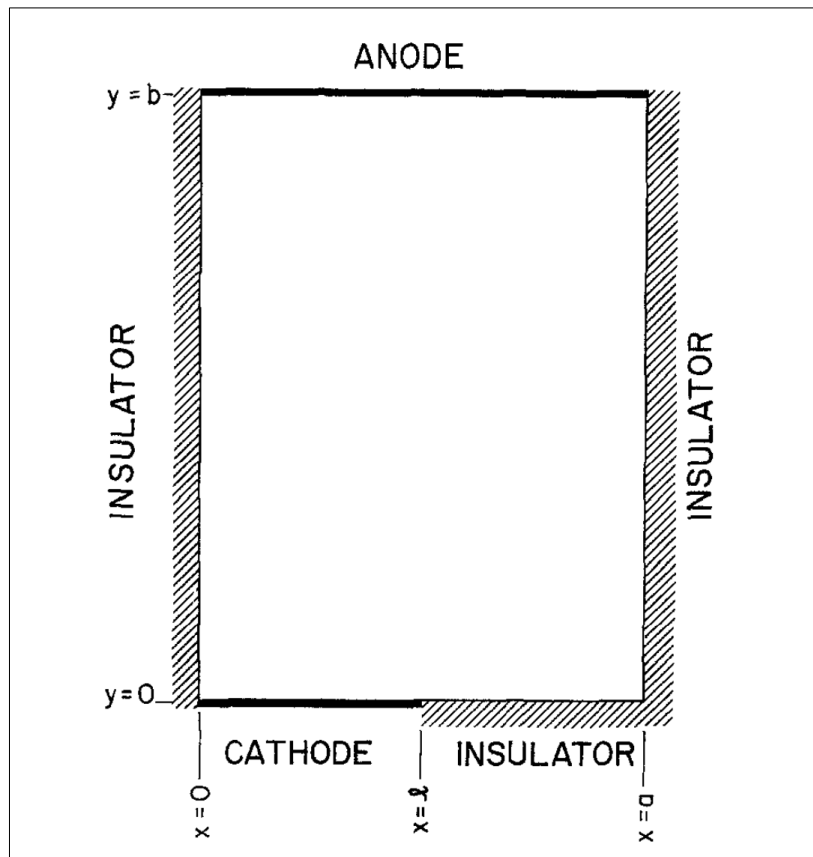


Figure 1. 9: 2-D cell geometry used by Alkire et al. for their study of a shape evolution problem using the finite element method. [90]

use of the finite element method could play an important role in solving complex electrochemical boundary problems.

Almost twenty years later, Deconinck [91] [92] introduced the boundary element method (BEM) to model evolving electrode profiles when non-linear boundary conditions are in place, focusing mainly on variations around singularities. Deconinck worked on trying to simulate electrodeposition in a Hull cell like the one shown in [Figure 1.10](#) paying significant attention to the transition point A between the cathode boundary and an insulating wall which are assumed to remain connected throughout the process and represent a real-life singularity point. For this study the Wagner number (Wa) was introduced which is defined as the polarisation resistance divided by the electrolyte resistance:

$$Wa = \mathcal{R}_{activation} / \mathcal{R}_{electrolyte} = \frac{\sigma}{L} \left(\frac{\partial \eta_a}{\partial i} \right) \quad [1.18]$$

where, σ is the electrolyte conductivity, $\frac{\partial \eta_a}{\partial i}$ is the slope of the activation overpotential (η_a) - current (i) dependence under secondary current distribution conditions and L is the characteristic length of an electrode system.

As it can be seen, the simulation results suggested that for Wagner number close to zero (Figure 1.10-a), meaning that a very small overpotential is present there, the shape evolution is only affected close to the singularity point A since primary current distribution is dominant. On the other hand, for high Wagner number (Figure 1.10-b), which represents secondary current distribution, uniform shape evolution is observed around point A since, in that case, the high overpotential favours uniformity. This showed that dendritic growth can occur near singularity points, which could be reduced (or controlled) by slow reaction kinetics. The simulation results were confirmed through practical experiments.

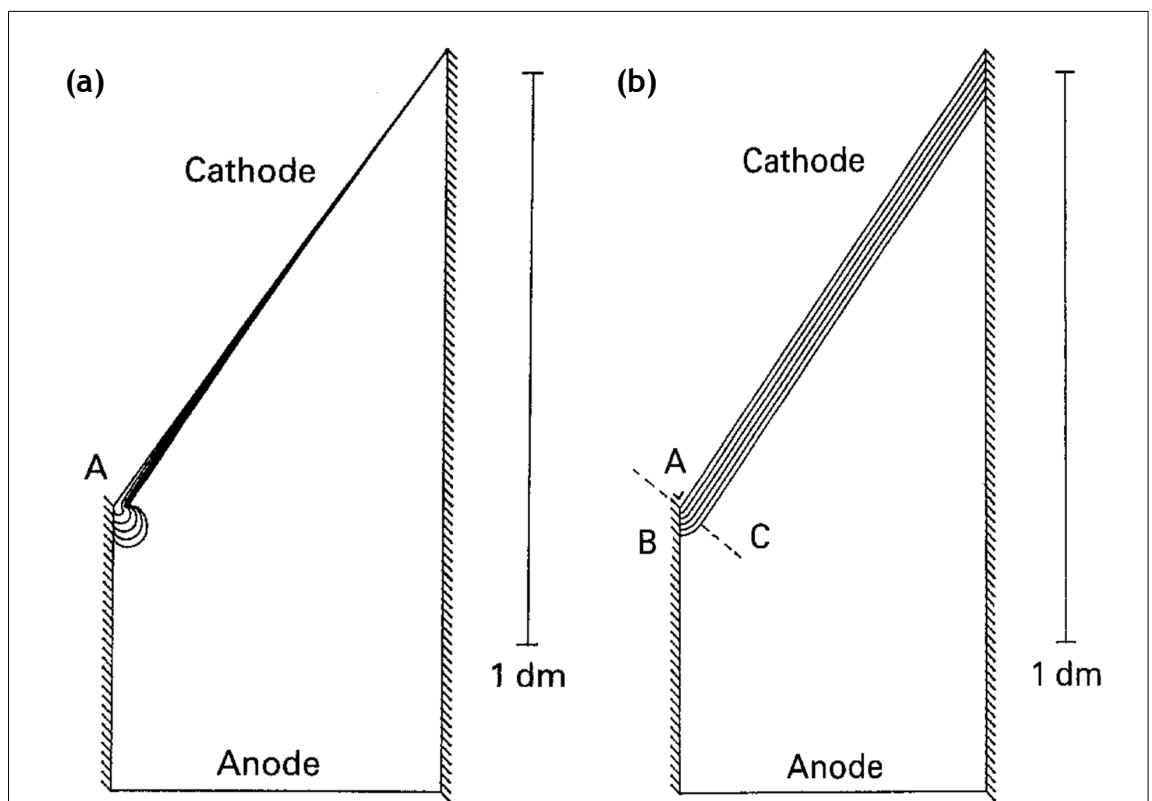


Figure 1. 10: Simulation of electrodeposition result in a Hull cell for Wagner number at (a) $W = 0.005$ and (b) $W = 500$. [92]

To the author's opinion, the above two studies of Alkire et al. and Deconinck established the applicability of FEM and BEM in simulating the electrodeposition process and laid the foundation for the development of the FEM modelling software to follow.

Masuku et al. [93] applied FEM in 2002, to develop, compare and validate 2-D and 3-D models of an electroplating process based on industrial data using ANSYS simulation software. Maybe the most significant finding from their studies was the 3-D nature of the current flow between the electrodes, which, in turn, reduced the electrical resistance in the electrolyte and increased the current (for the same applied potential) when compared to the 1-D and 2-D models. By validation through experiments, they established that 2-D modelling is not reliable when it comes to simulation modelling of industrial processes.

The direct dependence of thickness uniformity on current distribution was clearly proposed by two studies in 2004 [94] and 2008 [95], where the effect of the system's geometry on the current uniformity was the main parameter linked to the current's distribution profile.

Oh et al. [94] studied how changes in the electrodes' sizes, the distances between them, as well as the agitation velocity in the electrolyte affect the uniformity of a deposition in a computational domain as the one shown in [Figure 1.11](#). The calculations were based on the discretisation and solution of the Laplace's equation (1.18) using the finite element method. Modelling results were also validated by experiments in a system consisting by a copper anode, a titanium cathode, a titanium auxiliary electrode, and a $\text{CuSO}_4 \cdot 5\text{H}_2\text{O}$ electrolyte. Modelling and experimental results were in good agreement. The process was studied under agitation, at 25 °C while an applied current density of 200 A/m^2 was chosen for providing the best thickness uniformity at the most practical deposition rate.

As a first observation, the auxiliary electrode proved necessary for achieving high thickness uniformity, while its width, as well as the distance between itself and the cathode, played an important role in thickness distribution.

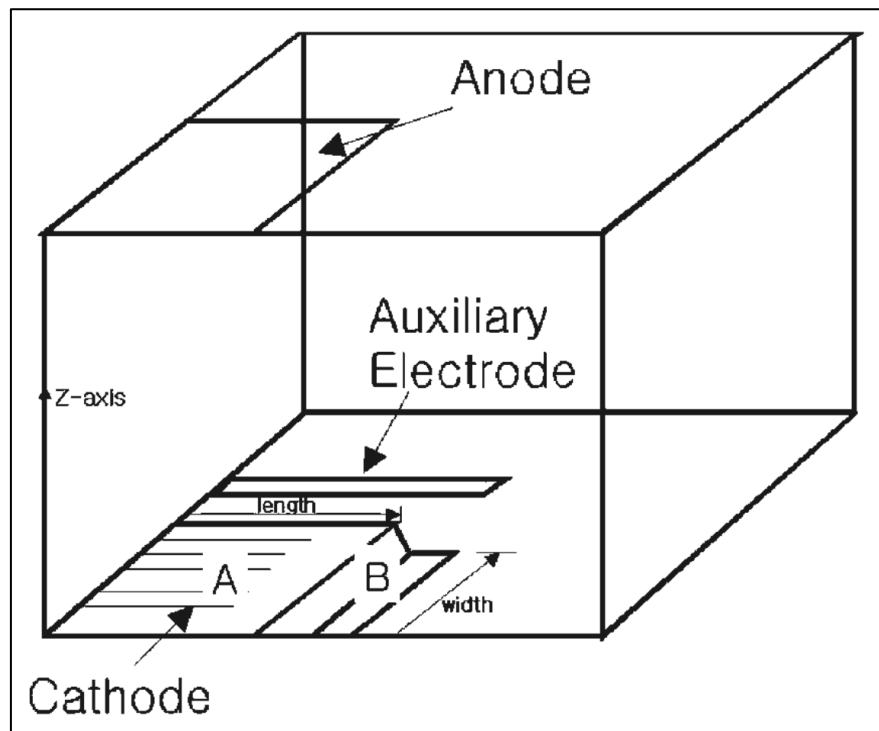


Figure 1. 11: Computational domain used for the studies of Oh et al. [94]

Specifically, it was observed that the width of the auxiliary electrode was affecting the potential distribution locally, with smaller widths leading to higher deposition rates at the edges compared to the ones developed at the middle of the cathode surface. Changes in the distance between the cathode and the auxiliary electrode also seemed to affect the results in a different way: an increased distance between the two would mean that the auxiliary electrode would not influence the deposition taking place at the cathode boundary, allowing for deposition rate to spontaneously increase at the cathode's edges and resulting in higher thicknesses there compared to the rest of the electrode's surface. The optimum gap between the cathode and the auxiliary electrode was determined at 0.4 cm . In terms of the anode and cathode sizes, the greatest uniformity was achieved when the two electrodes were the same size. Decrease in the anode length led to higher non-uniformity compared to a similar decrease in the anode width since there was no auxiliary electrode placed at the

right side of the cathode. In case no auxiliary electrode is used, a decrease in the anode's total size favoured a more uniform deposition. The distance between the two electrodes also played a role. As a general observation, a large distance between the anode and cathode allows for the flow to fully develop in the area between the two, resulting in a more uniform current distribution which leads to higher thickness uniformity. Taking into consideration the optimum distances between the electrodes, the study also suggested that an optimum agitation velocity lies above the value of 0.075 m/s .

Yang et al. [95] also investigated how geometry optimisation could help towards high thickness uniformity during an electrodeposition or electroforming process, working under the principle that uniform current distribution could be linearly translated to uniform thickness distribution. Through the study of the Ni-Mn alloy electroforming of the nozzle shown in [Figure 1.12](#), they tried to address the uniformity issues arising when curved parts need to be electroformed. They mainly focused on how the use of a conformal anode could provide a solution to the problem and, using the ANSYS software, an optimised profile for the conformal anode was determined. The optimised anode profile was developed by implementing modifications in the shape of the initial, simple conformal anode design which practically follows the cathode's profile. These modifications were mainly focused on the throat area and improved, indeed, the uniformity of current distribution between the top of the cathode and the throat. The researchers, however, suggested that current distribution studies must continue for optimum results to be achieved.

The first of the recent studies to model the nickel electroforming of a revolving part ([Figure 1.13-a](#)) using a modern software tool was the one of Behagh et al. [96]. They developed a 2-D Axisymmetric model ([Figure 1.13-b](#)) which could simulate the primary and secondary current distribution, as well as thickness distribution on the mandrel, and they validated their modelling results experimentally. Their electroforming cell consisted of a nickel anode, an aluminum mandrel of complex geometry and a nickel sulphate solution as the electrolyte. The process was run at $55 \text{ }^\circ\text{C}$, under agitation and direct current, at 2 V . The results confirmed that secondary conditions

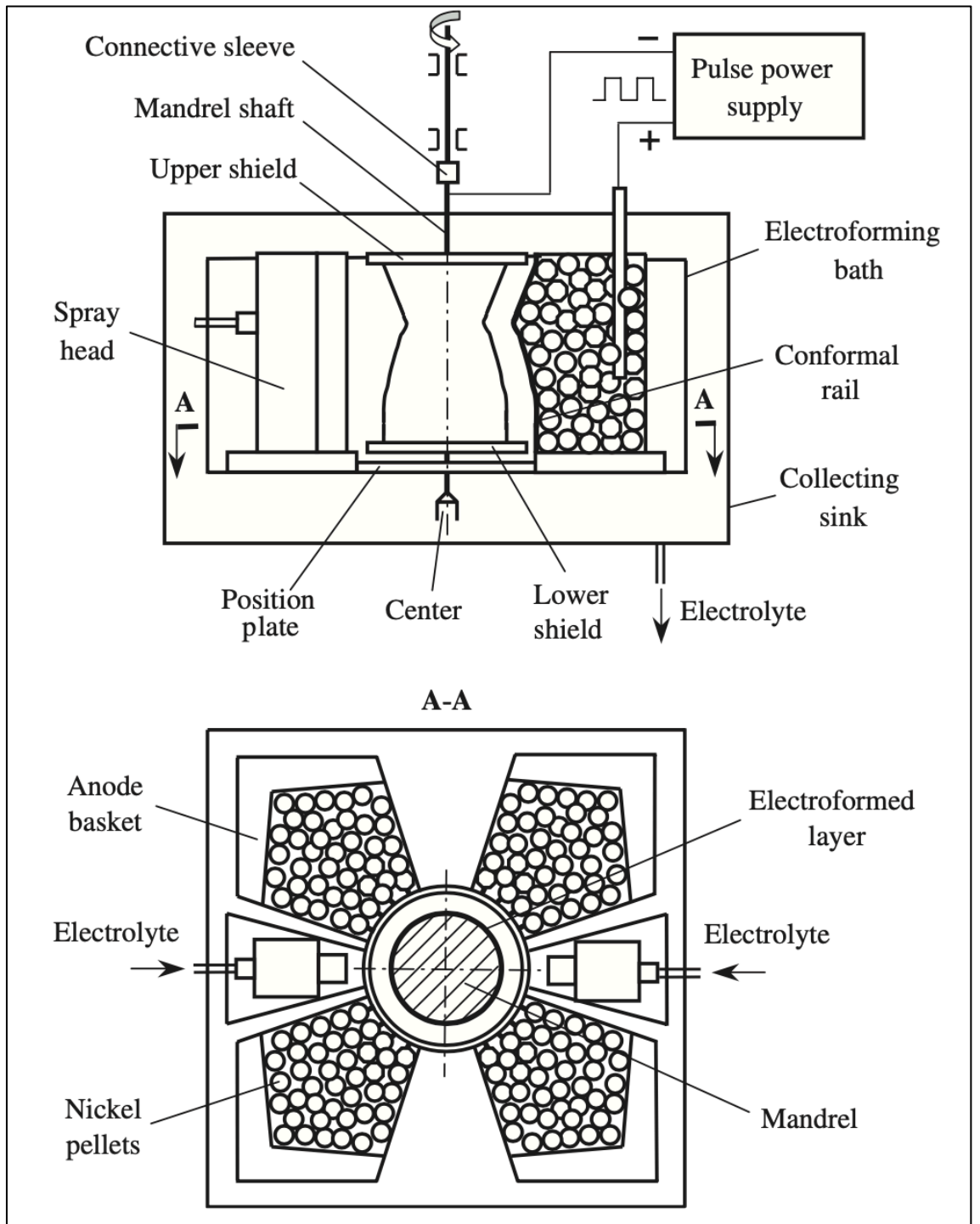


Figure 1. 12: Schematic of the electroforming cell studied by Yang et al.. [95]

describe the real process in a more efficient way compared to the primary ones while showing a linear correlation between current density and thickness. A difference in thickness uniformity was observed between the “valleys” and the “peaks” of the mandrel’s geometry, with the latter to present higher thicknesses compared to the former. Even though it is clearly stated and discussed that the finite element method was used for the simulations, it should be noted that no mention is made to the modelling software used for those and so one would assume that the computational methods were the authors’ own. Also, no quantitative data are provided to support the observations presented above. However, the qualitative results discussed are of importance since they present a systematic approach of modelling an electroforming process using modern simulation software.

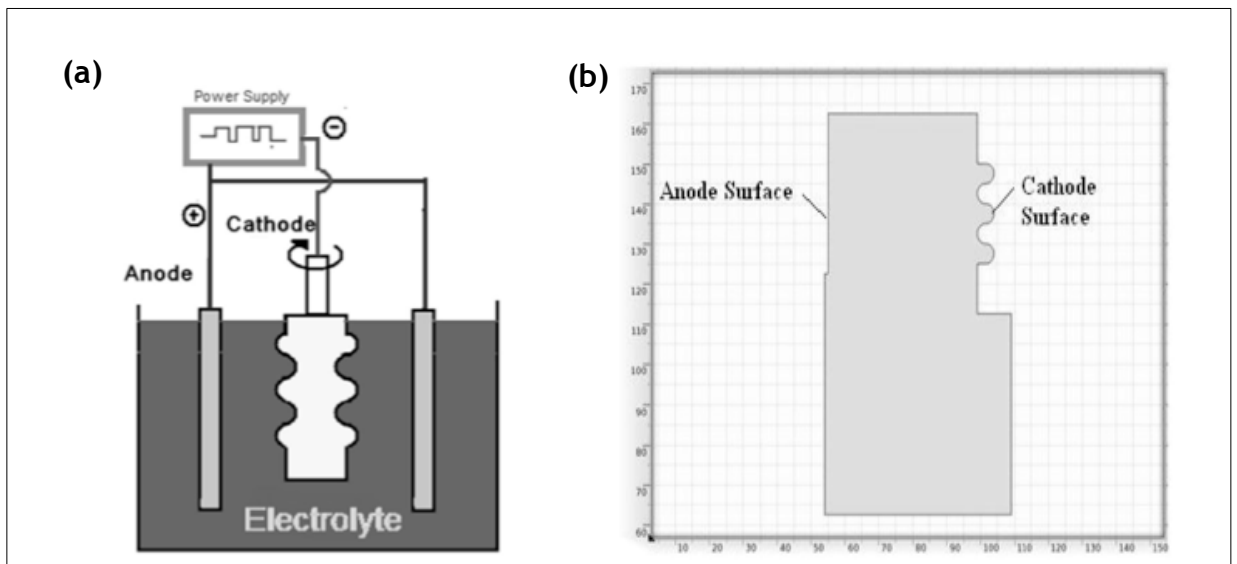


Figure 1. 13: (a) The experimental setup used by Behagh et al. and (b) its representation in a 2-D axisymmetric model. [96]

A year later, a comprehensive modelling study of a silver electroplating process was presented by Belov et al. [97]. Two finite element models, one at lab-scale (Figure 1.14-a & Figure 1.14-b) and one at industrial-scale (Figure 1.14-c & Figure 1.14-d), were studied to determine the effect of charge transfer coefficients on the process’s throwing power.

For these studies, tertiary conditions and Butler-Volmer kinetics, combined with computational fluid dynamics (CFD) at low flow rates, were used to describe the problem's physics. Additionally, a simplified version of the lab-scale model assuming secondary conditions was used to investigate how throwing power is also affected by electrolyte conductivity. The lab-scale cell, in which the modelling data were validated experimentally, consisted of a silver anode, a circular Assaf panel (Figure 1.14-a) acting as the cathode and a cyanide bath. The Assaf panel arrangement is a common tool for studying the throwing power of a system and its use has been reported in several studies before [98] - [101].

The experiments were run at 30 A/m^2 , 60 A/m^2 and 82 A/m^2 for under stagnant conditions. On the other hand, experiments in the industrial-scale setup were run at 51 A/m^2 under agitation of 0.05 m/s . The duration of each experiment was pre-calculated to result in the plating of the same amount of electric charge, chosen at 240 C for all cases.

For the lab-scale geometry and the tertiary model, a 12 % agreement was observed between the predicted thicknesses and the ones achieved experimentally, while the corresponding agreement lay at 20 % for the secondary model. The tertiary model predicted high uniformity in thickness across the cathode's surface.

The secondary model was proven more accurate in its thickness predictions in the middle of the mandrel, with the results being of a lower quality close to the edges. Also, even though concentration dependent kinetics were assumed to be negligible in the model, experimental results showed that mass transport phenomena affect the process kinetics at the edges. Predicted and experimentally obtained thicknesses were in agreement for the industrial-scale setup, too. The thickness seemed to decrease against the back wall of the industrial component's cavities, while the throwing power of the process was determined to be low, affected by the complexity of the geometry.

The study also revealed that variations of the anodic and cathodic charge transfer coefficients, as well as bulk conductivity, affect deposit thickness.

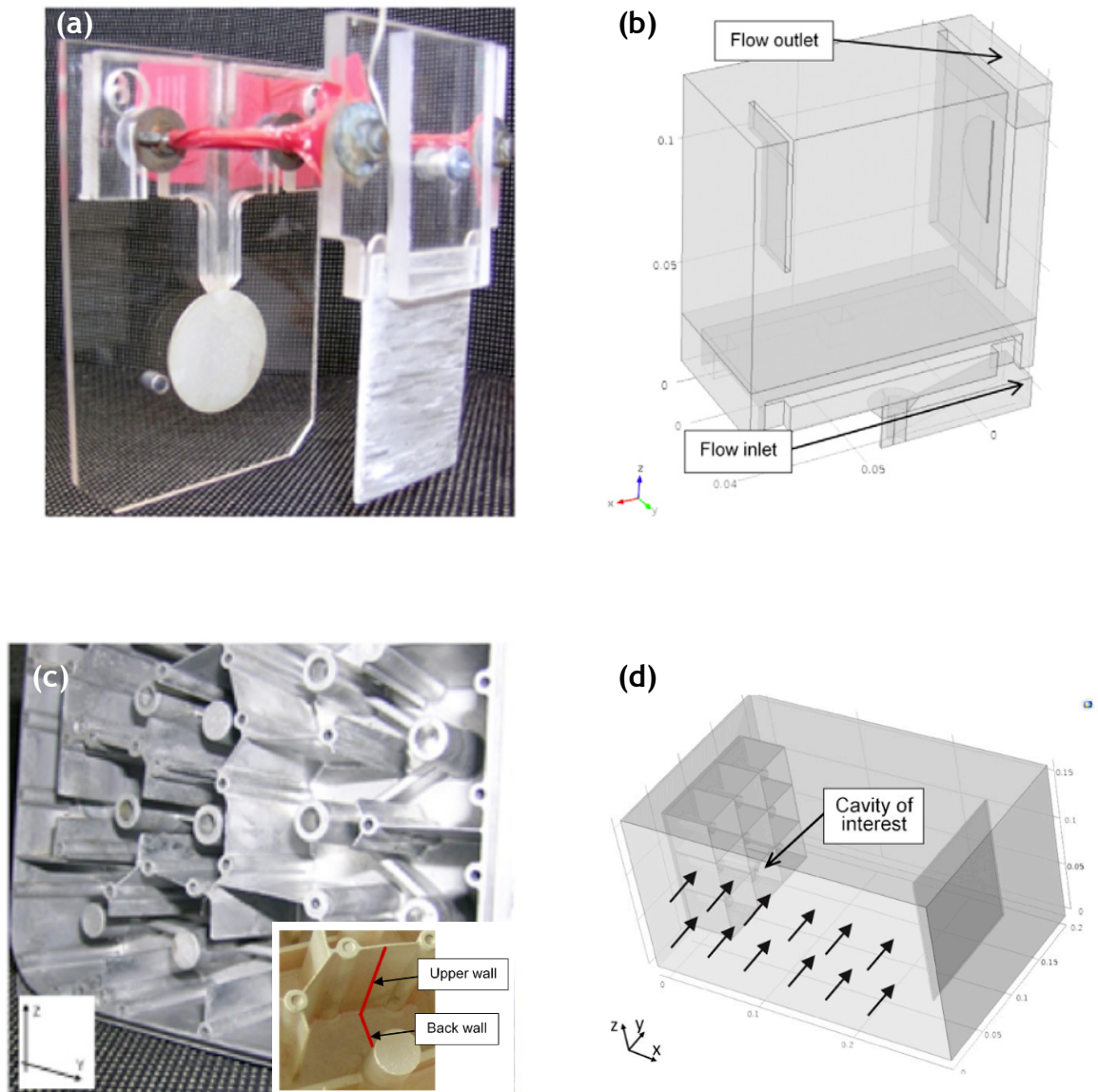


Figure 1. 14: Experimental setups and their representation in modelling software studied by Belov et al. [97]. Specifically, (a) lab-scale setup Assaf panel, (b) 3-D model of half of the Assaf panel in modelling software, (c) Industrial-scale complex component for telecom application and (d) 3-D model of the industrial-scale component.

An increased cathodic charge transfer coefficient was found to result in higher thickness at the edges, with no significant loss to be observed at the cathode's side facing the anode. On the other hand, the same increase led to a significant decrease in thickness at the other side of the cathode ("back side"). This effect led to a degradation of the process's throwing power, with an increase of either the electrolyte conductivity or the anodic charge transfer coefficient to be proposed as ways to balance that degradation. Even though the transfer coefficients were determined to significantly affect the throwing power, electrolyte conductivity and exchange current density were also found to play a role. However, the throwing power was proven to be less sensitive to variations of those parameters. This is because an increase in cathodic charge transfer coefficient results in a more primary-type current distribution.

As a general comment, regardless of how sensitive the throwing power of the process was found to be against variability of the different electrochemical parameters, this study proved that careful experimental design, including polarisation experiments, is necessary for the gathering of reliable data which could be used as input parameters in models.

More recently, Mahapatro et al. [102] developed a 2-D *COMSOL Multiphysics*[®] model to study copper electrodeposition on cobalt-chrome alloy in an aqueous $H_2SO_4 - CuSO_4$ electrolyte, aiming to determine how variations of the applied current density and electrolyte conductivity affect the system. No further specifics were given for any applied kinetic conditions or problem physics; however, it is stated that electrolyte concentration was assumed to remain stable while the general approach indicate the application of secondary conditions for the modelling studies.

In general, they reported good agreement between their experimental and modelling results. For the thickness studies, electrolyte conductivity was set at $4.23 S/m$, the current density at $3.57 \times 10^2 A/m^2$ and the experiments were run for 1800 s. The final deposit thickness was predicted at $11.7 \mu m$ while experimentally was measured at $9.445 \pm 1.79 \mu m$ by scanning electron microscopy (SEM) and at $12.375 \pm 1.36 \mu m$

by a thickness gauge. The greater deviation between the modelling and SEM results, compared to the deviation between the modelling and gauge ones, was attributed to difficulties in using SEM.

To study the effect that current density has on the thickness, the electrolyte conductivity was set at 4.23 S/m while current density values of $2.52 \times 10^2 \text{ A/m}^2$, $3.57 \times 10^2 \text{ A/m}^2$ and $6.12 \times 10^2 \text{ A/m}^2$ were applied for 2760 s . For these cases, the experimentally observed thicknesses were found to be lower than the simulated ones when lower current densities were applied, while they were found to be higher than the simulated ones for the cases when higher current densities were studied. This was attributed to the formation of an electrochemical double layer (presumably a diffusion layer) which, even though it affects ion diffusion, was not taken into account by the model. Also, the model was found to underpredict thickness for deposition longer than 1500 s at the highest current density value compared to the corresponding experimental results. At the same time, for the lowest current density value the model overpredicted thicknesses regardless the process duration. Lastly, a decrease in deposit thickness was observed with decrease in the electrolyte's conductivity, probably due to lower energy left to drive the electrode reactions. Simulations at $3.57 \times 10^2 \text{ A/m}^2$ for 2760 s were run for conductivity values at 4.23 S/m , 1.9 S/m , 0.93 S/m and 0.54 S/m . Experimentally, only the 4.23 S/m value allowed the formation of a copper deposit while the rest of the values resulted in either deposits of poor quality or no deposits at all. This meant that the validity of these results remains untested.

Finally, the most recent electroforming study, is the one published by Heydari et al. [103] discussing the modelling of copper deposition on an aluminum conical rotating electrode, using *COMSOL Multiphysics*[®]. Once more, the effect of current density, electrolyte conductivity, and electrode placement on the process were investigated. Modelling predictions were validated against experiments.

For these experiments six pure copper plates were positioned around the aluminum

conical cathode as shown in Figure 1.15-a. The electrodes were immersed in a $H_2SO_4 - CuSO_4 \cdot 6H_2O$ electrolyte and the cathode was rotating at 100 rpm. Copper was plated under a cell voltage of 1.2 V for 48 h. The model was developed in a 2-D axisymmetric environment (Figure 1.15-b) by assuming tertiary current distribution and turbulence (Reynolds number for the conical electrode at $\sim 3.6 \times 10^4$).

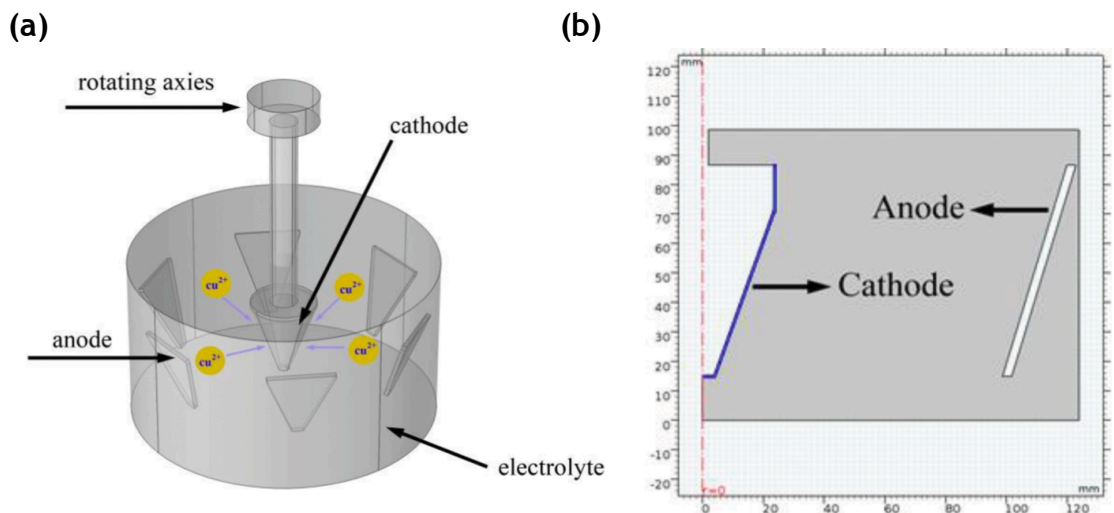


Figure 1. 15: (a) Schematic of the experimental rotating cone electrode setup used by Heydari et al. (b) 2-D axisymmetric model of the experimental rotating cone electrode setup [103]

The turbulence assumption meant that diffusion should be assumed dominant in the boundary layer and, thus, the results of the developed model are reliable for low rotating speeds. Kinetics were described by the Butler-Volmer model.

For model validation, experiments were run at $460 A/m^2$ for 48 h and electrolyte conductivity was set at $12 S/m$. Modelling and experimental results were in good agreement with average deposit thickness measured and predicted around 1.7 mm. Once more, an increase in current density was found to speed up the electroforming process and lead to increased thicknesses. However, high current densities resulted in deposits of low surface quality and purity. For current density sensitivity studies,

the values of 125 A/m^2 , 600 A/m^2 and 850 A/m^2 were tested and resulted in average thicknesses around 0.6 mm , 2 mm and 4 mm respectively. The effect of the electrolyte conductivity on thickness uniformity was predicted to be negligible. However, it was experimentally observed that increased electrolyte conductivity is related to a dendritic deposit structure. Conductivity was determined at 10 S/m during a validation experiment. Finally, it was reported that the distance between the electrodes as well as their sizes significantly affect thickness uniformity. Specifically, the process was determined to be more efficient and the thickness more uniform when the anode and cathode were the same size. At the same time, the distance between the electrodes affected both process efficiency and deposit quality. Therefore, the need to determine an optimum distance among the electrodes was concluded.

1.3.2. Today's challenges

The main challenges in modelling a process are to determine the critical parameters and key steps needed to describe a process. Recent developments in computational sciences and rapid increase in computational power allows both academia and industry to develop models - which may not be representative of the process due to incorrect use of parameters as well as inadequate validation. The authors of *"Useless Arithmetic: Why Environmental Scientists Can't Predict the Future"* [104] point out, *"...there is more to models than mathematics. There are parameters such as ..., and many other factors that make natural processes work. And each of the parameters is represented in a model by simplifications and assumptions. This is the point at which the mathematically challenged among us can evaluate models and even question the modelers."* In other words, a model will always be able to calculate a result; the important question any researcher or engineer should ask themselves is, whether the input parameters are the correct ones, and how would the results be validated against independent experiments. Without such rigour models may turn out to be sterile.

The usefulness of electroforming models is to capture the geometry, shape, and size at full scale, whilst retaining the near-surface phenomena occurring at the boundaries. In effect, on one hand, for models to represent the simulated systems and processes as closely as possible, the size of a system must be modelled at the mandrel or reactor scale. On the other hand, reactions at the electrodes and growth behaviour at surfaces, which may be controlled by processes at the micron or nano-meter scale, must be included. Especially, when the numerical methods used are dependent on space discretisation, like the boundary and finite element methods, geometry can play a significant role. The challenge for an industrially applicable model is dependent on the use of optimised mesh spacing and using appropriate convergence criteria and routines. In the following sections we delineate the task breakdown for the formulation of electroforming model.

When an electroforming process has to be modelled, obtaining the system's physical and electrochemical parameters from experiments should be attempted first. The electrochemical properties of the system need to be mapped and their effect on the chemistry of the process needs to be analysed. Model input parameters include electrolyte characteristics such as pH, electrolyte conductivity, reactions occurring at the cathode and anode, their kinetic behaviour, as well as reversible (or open circuit) potential and transport information such as limiting current and mass transfer coefficients.

The second step for modelling purposes is describing electrode kinetics. While there are several methodologies, for accurate modelling secondary or tertiary current distributions are needed (in almost all cases). The mathematical description of electrochemical systems for complex, non-linear problems, can only be numerically solved by applying strict boundary conditions and approximations. The most commonly used approach is the potential theory, according to which Laplace's equation governs the potential behaviour:

$$\nabla^2\Phi = 0 \quad [1.19]$$

where, $\nabla = i \frac{d}{dx} + j \frac{d}{dy} + k \frac{d}{dz}$. The inverted del operator (∇) in Equation 1.19 represents differentials in the i , j and k directions, where i , j and k are vectors, and Φ is the electric potential.

For insulators and symmetry axes, the boundary conditions are described by Equation 1.20 below:

$$\frac{\partial \Phi}{\partial y} = 0 \quad [1.20]$$

where, y is the distance from the boundary's surface. In the basic case of primary current distribution, both the anode and cathode are unpolarised, and the boundary conditions on the electrodes' surfaces are described by Equations 1.21 & 1.22:

$$\Phi_A = \Phi \quad [1.21]$$

$$\Phi_C = 0 \quad [1.22]$$

Electroforming of nickel usually takes place under kinetic control, and hence a secondary current model, incorporating accurate nickel deposition kinetics is needed. Although several mechanisms have been proposed for nickel deposition [35] [36], [37], [39] - [46], it is unclear if they are valid for nickel electroforming. For example, most kinetic studies focus on the initial stages of Ni^{2+} reduction, whereas electroforming of nickel proceeds at much higher current densities. Our own earlier review highlighted a variety of unresolved issues regarding nickel [29].

The lack of clarity around such specifics also doesn't allow one to understand if the results of a model describe a particular electrochemical process. Often, modellers use kinetic data from literature which may not be relevant to the process. This can affect further use and interpretation of the model results. The norm is to use electrochemical models using standard libraries of parameters accepting their applicability to any system under investigation. As a result, rough assumptions are usually introduced regarding the kinetics affecting a process. Indeed, only a limited number

of already widely studied electrochemical systems are repeatedly discussed (*e.g.*, sulphate baths but rarely sulphamate baths for nickel electroforming) and it is common that variations between experimental and modelling data go unexplained.

A complete model would provide how the system's electrochemical properties and the process parameters would affect the surface or mechanical property of the deposited material. Even though it has been reported that mechanical characteristics of electroformed parts [105] or tensile strength are influenced by current density [106], as well as by increasing translational speed of moving mandrels [107], these aspects have yet to be incorporated into models. Although there is a recognition that additives can change deposit grain size and texture (and thereby mechanical properties) [108] - [112] there are no governing equations correlating them with deposit kinetics and growth.

Nickel electroforming from sulphamate electrolytes, even though carried out far below diffusion limitations, is also characterised by the formation of dendrites. Although mathematical models can describe the growth of dendrites under diffusion limiting conditions [113] - [117] and their shape evolution [118] - [121], for Ni electroforming it may be important to determine how the situation can be ameliorated. For example, (a) if one were to identify if there is a particular current density where dendrite growth commences, (b) if this current density could be changed by using additives, and (c) how these model results can be validated, better deposits could be obtained. In addition, the scale-up of such models, which are set at the micron level, to the reactor level, which is 10^6 times larger, needs focus on multi-scale modelling and experimental validation.

1.3.3. Most common commercial modelling software

Although models for electrodeposition have been developed by several groups, ANSYS, *Elsyca*[®] and *COMSOL Multiphysics*[®] are some of the better-known commercial software for simulating electrochemical systems and processes. The goal here is to provide a brief presentation of what the authors, as software users, believe to be the advantages and disadvantages of these off-the-shelf systems. *Elsyca*[®] was founded in 1997, with the aspiration to “leverage the electrochemical knowledge through software simulation tools and engineering services” (<https://www.elsyca.com/about>, 28 January 2021). The software brought together the advantages of computing power and the underlying principles of electrochemical systems [122] - [127]. In the earlier versions, geometries of significant complexity could be created using the built-in design tools. Current versions of *Elsyca*[®] provides the facility of dropping a 3-D CAD drawing of a mandrel into an electrochemical reactor allowing one to calculate current density and thereby, the shape evolution during electrodeposition under primary, secondary, and tertiary current conditions [128]. However, the robustness of the results depends on the accuracy of input parameters, which needs laboratory data, which apparently can also be determined by the company as a service (<https://www.elsyca.com/solutions/material-characterization>, 28 January 2021).

COMSOL Multiphysics[®] is a simulation software that uses finite element analysis to solve numerical and design problems deriving from any engineering sector, especially those involving modelling of physics, acoustics, and fluid dynamics. It includes an electrodeposition module which can be employed for electroforming simulations. *COMSOL Multiphysics*[®] retains the reactor “creation” by the user or via importation of CAD models. The software interface makes it easy to declare the reactor’s boundaries and initial parameters, insert material characteristics, as well as monitor and control various parameters.

The desirable user freedom is also provided when it comes to setting up the discretisation of the problem since controlling the mesh for each problem is straightforward.

Users can use either one of the default meshing options provided or define their own mesh from scratch. The ability to customise the mesh allows the user to control the number, size, shape, and quality of elements. Detailed, fine discretisation can be applied locally only on areas of the geometry which are of interest, allowing that way the minimisation of the total elements used throughout the domain and thereby, the time needed for the calculations to be completed. As a general comment, whether different meshing approaches affect the convergence of a model and/or change, more or less, the duration of the calculations, depends on the geometrical characteristics and the electrochemical behaviour of each application. From experience, simpler geometries and processes can be less affected by a non-optimised mesh than complex ones.

As for the core calculations, *COMSOL Multiphysics*[®] provides the user with complete physics interfaces and equation libraries while, the ability to link different physics interfaces can significantly increase the computational efficiency of a model. Every time a new interface is added to the model the user must determine specific physical parameters and boundary conditions related to the corresponding physics. Then the interfaces are automatically related through a “link” command.

Regarding post-processing, the generated results can be presented in a tangible manner rendering *COMSOL Multiphysics*[®] ideal for use by industrial teams due to its user-friendly interface and comprehensive way of data presentation. The software can generate graphs, tables, images and 2-D or 3-D representations ready to be implemented in reports, or even produce whole reports ready to be circulated amongst colleagues. At the same time, numerical data can be exported and be imported to data analysis software for further manipulation by the user. One other important aspect of the software is its ability to visualise the shape evolution during electro-deposition through a “deformed geometry” interface. When this is applied to solid domains, any deformation of the boundary is assigned to material addition or removal along that boundary. The addition or removal of mass is recognised through corresponding changes in the total volume of the domain.

Therefore, through appropriate use of this software, thickness uniformity of deposits can be predicted and undesirable dendritic growth during electroforming could be reduced through modifications of reactor geometry. Simple changes in the geometry of a production setup are often preferable in industry compared to adjusting electrodeposition and/or other transfer phenomena. This way, problems which are considered complex to solve, practically and computationally, could be converted to more manageable, tangible design problems.

The prominent challenge for a new user is the steep learning curve of using such software. Since COMSOL Multiphysics® is a commercial software, it is reasonable that every user is dependent on the documentation available by the software provider and training provided. Focused full-time attention for six to five months may be necessary for a user to develop in-depth understanding and proficiency needed to implement an informed process tool. The electrodeposition module has limited documentation, even though there is an impressive tutorial library providing models for a variety of case studies. Notably, there is limited information about the steps to be taken by a user leading to those models. If this is considered in combination with the fact that the user does not have access to the actual computational solver (“the code”), reaching a reasonable level of confidence can be a challenge.

The second issue is the fact that this software is a multiphysics software and including solution and electrode chemistry can be an issue. Since input parameters need physico-chemical and kinetic data, good results are dependent on the availability of good electrochemical knowledge and facility. Even though the model and principles for including chemical principles are incorporated, the problem is that using untested and inappropriate input data can provide an incorrect result.

Last but not least, it is important to mention that neither of the modelling software discussed above, were developed to focus solely on electroforming processes. In *COMSOL Multiphysics*® the user has to work within the general *Electrodeposition Module*, approaching the modelling of the electroforming process as that similar to other electrodeposition processes. With *Elsyca*®, on the other hand, the user is

allowed to work more freely, given the ability to build the mathematical model themselves and modify it according to their needs. In effect, both software provide a route to compute electrodeposition rates at different points of the cathode; the computations are then used to calculate thickness at those points, and the shape evolution is calculated from those values.

Even though both these approaches can be used to model an electroforming process, having a modelling software or module dedicated to electroforming would be more efficient. Since the main difference between electroforming and any other electrodeposition process is that electroforms products require differing thicknesses at different points, a modelling software with good visualisation of shape evolution and geometry evolution throughout the duration of the simulation would be needed. In addition, electroforming requires longer duration, and therefore models need to be able carry out long term calculations, which needs intelligent ways for changing boundaries, re-meshing strategies, and track the evolution of deposition rates and corresponding shape changes.

1.4 Project Aims

Electrochemical forming is a chemical additive process to manufacture a variety of niche components. Its capability has been exploited in micro-manufacturing as well as “heavy industry”, such as aerospace. As the “Industry 4.0” era unfolds, there is a need to develop models for electroforming which are based on electrochemically sound data. To do this, physical and electrochemical parameters for modelling purposes should be determined first, followed by rigorous modelling studies. For modelling to be useful, parameters which could play a significant role in process optimisation should be examined, followed by continuous cross-validation through appropriate measurements. Through that way a model can be a valuable aid, allowing predictability in tooling, piloting, and manufacturing in a reliable manner.

In that context, the vision of this project's industrial partners (Radius Aerospace Bramah) has been to use electroforming to volume up the manufacturing of large parts with extremely high precision ($10^{-8} : 1$). Consequently, the aim of this collaboration has been the bringing of the gaps among electrochemistry, chemical engineering, and manufacturing. Specifically, the objectives have been identified to be:

- the study of the effect of physical and electrochemical parameters on electroformed parts,
- the development of a well-informed modelling tool based on these data and the validation of the model through carefully designed experiments,
- the identification of key engineering variables which can be used to manipulate an electroformed part,
- the optimisation of the electroforming reactor through the design of mandrels and reactor parts/tools to control the deposit growth rate,
- the efficient scaling up of the industrial process for volume manufacturing, using informed tool and mandrel design, minimising the number of manufacturing trials and producing conforming parts in volume production, is thought to be possible.

References

- [1] J.-A. Blanqui, History of political economy in Europe, T. b. E. J. Leonard, Ed., New York: Putnam, 1880.
- [2] F. Engels, The condition of the working class in England, D. McLellan, Ed., Oxford: Oxford University Press (Original work published 1845), 1993.
- [3] A. Toynbee, Lectures on the Industrial Revolution in England: popular addresses, notes and other fragments, New York: Cambridge University Press (Original work published 1884), 2011.
- [4] E. G. Popkova, Y. V. Ragulina and A. V. Bogoviz, Industry 4.0: Industrial Revolution of the 21st Century (Studies in Systems, Decision and Control), vol. 169, Springer International Publishing AG, 2019.
- [5] B. Slusarczyk, "Industry 4.0 : are we ready?," *Polish Journal of Management Studies*, vol. 17, no. 1, pp. 232-248, 2018.
- [6] "Platform Industrie 4.0," German Federal Ministry of Economic Affairs and Energy, German Federal Ministry of Education and Research , 2012. [Online]. Available: <https://www.plattform-i40.de/PI40/Navigation/EN/Home/home.html>. [Accessed 29 July 2021].
- [7] J. Müller, O. Buliga and K. Voigt, "Fortune favors the prepared: How SMEs approach business model innovations in Industry 4.0," *Technological Forecasting and Social Change*, vol. 132, pp. 2-17, 2018.
- [8] S. Vaidya, P. Ambad and S. Abhosle, "Industry 4.0 - A Glimpse," *Procedia Manufacturing*, vol. 20, pp. 233-238, 2018.
- [9] S. Ford and M. Despeisse, "Additive manufacturing and sustainability: an exploratory study of the advantages and challenges," *Journal of Cleaner Production*, vol. 137, pp. 1573-1587, 2016.
- [10] *ASTM F2792-12a, Standard Terminology for Additive Manufacturing Technologies*, vol. 10.04..
- [11] B. Berman, "3-D printing: The new industrial revolution," *Business Horizons*, vol. 55, pp. 155-162, 2012.
- [12] D. Chen, S. Heyer, S. Ibbotson, K. Salonitis, J. Steingrimsson and S. Thiede, "Direct digital manufacturing: definition, evolution, and sustainability implications," *Journal of Cleaner Production*, vol. 107, pp. 615-625, 2015.

- [13] S. Huang, P. Liu, A. Mokusdar and L. Hou, "Additive manufacturing and its societal impact: a literature review," *International Journal of Advanced Manufacturing Technology*, vol. 67, pp. 1191-1203, 2013.
- [14] I. Petrick and T. Simpson, "3D Printing Disrupts Manufacturing: How economies of one create new rules of competition," *Research-Technology Management*, vol. 56, no. 6, pp. 12-16, 2013.
- [15] V. Petrovic, J. Gonzalez, O. Ferrando, J. Gordillo, J. Puchades and L. Grinan, "Additive layered manufacturing: sectors of industrial application shown through case studies," *International Journal of Production Research*, vol. 49, no. 4, pp. 1061-1079, 2011.
- [16] J. McGeough, "Electroforming," in *CIRP Encyclopedia of Production Engineering*, Berlin, Heidelberg: Springer, 2014.
- [17] P. Spiro, *Electroforming: a comprehensive survey of theory, practice and application*, Teddington, UK: Draper, 1968.
- [18] R. Parkinson, "Electroforming-a unique metal fabrication process," Nickel Development Institute, London, UK, 1998.
- [19] M. Paunovic and M. Schlesinger, *Fundamentals of electrochemical deposition*, Hoboken, New Jersey: John Wiley & Sons, Inc., 2006, p. 348..
- [20] A. International, "Standard guide for electroforming with nickel and copper," ASTM International, West Conshohocken, USA, 2003.
- [21] A. Special Technical Publication No. 318, *Electroforming - applications, uses and properties of electroformed metal*, Philadelphia, USA: American Society for Testing and Materials, 1962.
- [22] G. DiBari, "Nickel Electroplating Applications and Trends," *Plating and Surface Finishing*, vol. 83, no. 10, p. 10, 1996.
- [23] G. DiBari and S. Watson, "A review of recent trends in nickel electroplating technology in North America and Europe," *NiDI Reprint Series*, vol. 14024, 1992.
- [24] "About Nickel," Nickel Institute, [Online]. Available: <https://nickelinstitute.org/about-nickel/>. [Accessed 19 July 2021].
- [25] N. V. Myunga, D.-Y. Park, D. E. Urgiles and T. George, "Electroformed iron and FeCo alloy," *Electrochimica Acta*, vol. 49, pp. 4397-4404, 2004.
- [26] D. Baudrand, "Nickel sulfamate plating, its mystique and practicality," *Metal Finishing*, pp. 15-18, 1996.

- [27] R. J. Kendrick, "High speed nickel plating from sulphamate solutions," *Transactions of the IMF*, vol. 42, no. 1, pp. 235-245, 1964.
- [28] A. Hankin and G. .. Kelsall, "Electrochemical recovery of nickel from nickel sulphamate plating effluents," *Journal of Applied Electrochemistry*, vol. 42, pp. 629-643, 2012.
- [29] S. Roy and E. Andreou, "Electroforming in the Industry 4.0 Era," *Current Opinion in Electrochemistry*, vol. 20, p. 108-115, 2020.
- [30] R. A. F. Hammond, "International Nickel Limited," 1971. [Online]. Available: <https://www.hartmaterials.com/images/documents/Electrodeposition-Report-LOW-RES.pdf>. [Accessed 03 07 2022].
- [31] J. L. Marti, "The effect of some variables upon internal stress of nickel as deposited from sulphamate electrolytes," *Plating*, vol. 53, pp. 61-67, 1966.
- [32] O. Klingenmaier, "The effect of anode efficiency on the stability of nickel sulphamate solutions," *Plating*, vol. 52, pp. 1138-1141, 1965.
- [33] M. Halmdienst, W. E. G. Hansal, G. Kaltenhauser and W. Kautek, "Pulse plating of nickel: influence of electrochemical parameters and composition of electrolyte," *Transactions of the IMF*, vol. 85, pp. 22-26, 2007.
- [34] N. Mannion, *Personal communication*, Doncasters - Bramah, 2019.
- [35] J. Yeager, J. P. Cels, E. Yeager and F. Hovorka, "The electrochemistry of nickel," *Journal of the Electrochemical Society*, vol. 106, pp. 328-336, 1959.
- [36] A. Saraby-Reinjes and M. Fleischmann, "Kinetics of electrodeposition of nickel from Watts baths," *Electrochimica Acta*, vol. 29, pp. 557-566, 1964.
- [37] R. Orinaková, A. Turonová, D. Kladeková, M. Gálová and R. M. Smith, "Recent developments in the electrodeposition of nickel and some nickel based alloys," *Journal of Applied Electrochemistry*, vol. 36, p. 957 - 972, 2006.
- [38] J. Yeager, P. Cels, E. Yeager and F. Hovorka, "The electrochemistry of nickel," *Journal of the Electrochemical Society*, vol. 106, p. 328 - 336, 1959.
- [39] M. Supicová, R. Rozik, L. Trnková, R. Orinaková and M. Galová, "Influence of boric acid on the electrochemical deposition of Ni," *Journal of Solid State Electrochemistry*, vol. 10, p. 61-68, 2006.
- [40] I. Epelboin and R. Wiart, "Mechanism of the electrocrystallisation of nickel and cobalt in acidic solution," *Journal of the Electrochemical Society*, vol. 118, p. 1577 - 1582, 1971.

- [41] M. Holm and T. J. O'Keefe, "Evaluation of nickel deposition by electrochemical impedance spectroscopy," *Journal of Applied Electrochemistry*, vol. 30, p. 1125-1132, 2000.
- [42] F. I. Danilov, I. V. Sknar and E. Y. Sknar, "Kinetics of nickel electroplating from methanesulfonate electrolyte," *Russian Journal of Electrochemistry*, vol. 47, p. 1035-1042, 2011.
- [43] E. Gomez, C. Muller, W. G. Proud and E. Valles, "Electrodeposition of nickel on vitreous carbon: influence of potential on deposit morphology," *Journal of Applied Electrochemistry*, vol. 22, p. 872-876, 1992.
- [44] K.-D. Song, K. B. Kim, S. H. Han and H. K. Lee, "A study on effect of hydrogen reduction reaction on the initial stage of Ni electrodeposition using EQCM," *Electrochemistry Communications*, vol. 5, p. 460 - 466, 2003.
- [45] C. Q. Cui and J. Y. Lee, "Nickel deposition from unbuffered neutral chloride solutions in the presence of oxygen," *Electrochimica Acta*, vol. 40, p. 1653 - 1662, 1995.
- [46] H. Reiser and H. Fischer, "Electrolytische abscheidung und elektrokrystallisation von metallen," Berlin, Springer Verlag, 1954, p. 623 - 628.
- [47] G. H. Bush and D. G. Higgs, "The analysis of nickel sulphamate plating solutions," *Transactions of the IMF*, vol. 36, pp. 43-47, 1959.
- [48] H. S. C. E. Rao Z, "The effects of plating current, grain size and electrolyte on stress evolution in electrodeposited Ni," *Journal of the Electrochemical Society*, vol. 166, pp. D3212-D3218, 2019.
- [49] A. F. Greene, "Anodic oxidation products in nickel sulfamate solutions," *Plating*, vol. 55, pp. 594-599, 1968.
- [50] J. P. Hoare, "On the role of boric acid in the Watts bath," *Journal of the Electrochemical Society*, vol. 133, pp. 2491-2494, 1986.
- [51] J. P. Hoare, "Boric acid as a catalyst in nickel plating," *Journal of the Electrochemical Society*, vol. 134, pp. 3102-3103, 1987.
- [52] B. V. Tilak, A. S. Gendron and M. A. Mosoiu, "Borate buffer equilibria in nickel refining electrolytes," *Journal of Applied Electrochemistry*, vol. 7, pp. 495-500, 1977.
- [53] Y. Tsuru, M. Nomura and F. R. Foulkes, "Effects of boric acid on hydrogen evolution and internal stress in films deposited from a nickel sulphamate bath," *Journal of Applied Electrochemistry*, vol. 32, pp. 629-614, 2002.

- [54] G. D. Bari and J. Petrocelli, "The effect of composition and structure on the electrochemical reactivity of nickel," *Journal of the Electrochemical Society*, vol. 112, p. 99, 1965.
- [55] I. Bear, R. Flann, K. McDonald, L. Rogers and R. Woods, "Activated basket anodes from nickel powder Part II: Fabrication of anodes by a liquid phase sintering process," *Journal of Applied Electrochemistry*, vol. 22, p. 8, 1992.
- [56] H. Zhang and S.-M. Park, "Studies on the anodic decomposition products of sulphamate," *Journal of Applied Electrochemistry*, vol. 24, pp. 1182-1187, 1994.
- [57] J. Jiazhu, Z. Haiyan and Z. Lianyu, "Investigation on the anodic decomposition products in sulfamate solutions," *Plating and Surface Finishing*, vol. 77, pp. 54-58, 1990.
- [58] A. C. Hart, W. R. Wearmouth and A. C. Warner, "The anodic behaviour of nickel in nickel sulphamate electroplating solutions," *Transactions of the IMF*, vol. 54, pp. 56-60, 1976.
- [59] H. Nakano, S. Oue, S. Kobayashi, T. Akiyama, H. Fukushima, A. Kubota and T. Inoue, "Anodic oxidation of sulfamate ions in sulfamate baths and its effect on nickel deposition.," *Denki Kagaku*, vol. 54, pp. 533-537, 2003.
- [60] H. Yang and S.-W. Kang, "Improvement of thickness uniformity in nickel electroforming for the LIGA process," *International Journal of Machine Tools & Manufacture*, vol. 40, pp. 1065-1072, 2000.
- [61] K. Wong, K. Chan and T. Yue, "A study of hardness and grain size in pulse current electroforming of nickel using different shaped waveforms," *Journal of Applied Electrochemistry*, vol. 31, pp. 25-34, 2001.
- [62] K. Wong, K. Chan and T. Yue, "Influence of spike current in different shaped waveforms on the hardness and grain size of nickel electroforms," *Journal of Materials Processing Technology*, vol. 117, pp. 97-104, 2001.
- [63] G. D. Bari, "Electrodeposition of nickel," in *Modern Electroplating*, Hoboken, New Jersey, John Wiley & Sons Inc., 2010.
- [64] M. Popereka, "Internal stresses in electrolytically deposited metals," National Bureau of Standards and the National Science Foundation, Washington, DC, 1970.
- [65] R. Weil, "The origins of stress in electrodeposits," *Plating*, vol. 57, no. 1231; 137, 1970; , 1971.

- [66] J. Dini, *Electrodeposition-The materials science of coatings and substrates*, Park Ridge, NJ: Noyes, 1993, pp. 279, 331.
- [67] Y. Tsuru, M. Nomura and F. Foulkes, "Effects of chloride, bromide and iodide ions on internal stress in films deposited during high speed nickel electroplating from a nickel sulfamate bath," *Journal of Applied Electrochemistry*, vol. 30, pp. 231-238, 2000.
- [68] A. Uriondo, M. Esperon-Miguez and S. Perinpanayagam, "The present and future of additive manufacturing in the aerospace sector: A review of important aspects," *Journal of Aerospace Engineering*, vol. 229, no. 11, pp. 2132-2147, 2015.
- [69] S. Watson, "Modern Electroforming," *Transactions of the IMF*, vol. 67, no. 1, pp. 89-94, 1989..
- [70] S. Silaimani and S. John, "Review on recent advances in electroforming during the last decade," *Bulletin of Electrochemistry*, vol. 17, no. 12, pp. 553-560, 2001.
- [71] R. Parkinson, "Nickel plating and electroforming: Essential industries for today and the future," Nickel Development Institute, London, UK, 2001.
- [72] B. Group, "BJS Group-Electroforming," BJS Group, [Online]. Available: <https://bjSCO.com/electroforming/>. [Accessed 5 September 2019].
- [73] G. Shapiro, "2013 R+D Awards Winner: Electroform(alism)," *ARCHITECT: the magazine of the American Institute of Architects*, 2013.
- [74] L. Romankiw, "Electroforming of Electronic Devices," *Plating & Surface Finishing*, 1997.
- [75] G. Marks, "An electroformed stencil for fine-pitch surface mount technology," in *AESF Conference*, Anaheim, June 1993.
- [76] S. Watson, "Applications of Electroforming," Nickel Development Institute, 1990.
- [77] M. Levy, "Max Levy Autograph, Inc. Philadelphia," *PA. Bulletin*, no. 2100.
- [78] "Nickel," Agiboo, [Online]. Available: <https://www.agiboo.com/nickel/#:~:text=Nickel%20mined%20from%20lateritic%20ore,is%20extracted%20through%20extractive%20metallurgy..> [Accessed 22 10 2022].
- [79] M. Garside, "Reserves of nickel worldwide from 2000 to 2021," Statista, 8 3 2022. [Online]. Available:

<https://www.statista.com/statistics/1003284/nickel-reserves-worldwide/>.
[Accessed 22 10 2022].

- [80] M. C. S. U.S. Geological Survey, "Nickel," 1 2022. [Online]. Available: <chrome-extension://efaidnbmnnnibpcajpcglclefindmkaj/https://pubs.usgs.gov/periodicals/mcs2022/mcs2022-nickel.pdf>. [Accessed 22 10 2022].
- [81] R. Eisler, "Nickel Hazards to Fish, Wildlife, and Invertebrates: A Synoptic Review," U.S. Geological Survey, 1998.
- [82] M. Garside, "Consumption volume of nickel worldwide from 2010 to 2021," 12 7 2022. [Online]. Available: <https://www.statista.com/statistics/273635/consumption-of-nickel-since-2007/>. [Accessed 22 10 2022].
- [83] A. O'Neill, "Average prices for nickel worldwide from 2014 to 2025," 23 2 2022. [Online]. Available: <https://www.statista.com/statistics/675880/average-prices-nickel-worldwide/>. [Accessed 22 10 2022].
- [84] D. Bernhardt and J. F. R. II, "Mineral commodity summaries 2019," U.S. Geological Survey, Reston, Virginia, 2019.
- [85] J. McGeough and H. Rasmussen, "A perturbation analysis of the electroforming process," *Journal of Mechanical Engineering Science*, vol. 18, no. 6, pp. 271-278, 1976.
- [86] V. Topa, M. Purcar, C. Munteanu, L. Grindei and C. Pacurar, "Electrode shape change simulation technique based on the extended finite element and level set method," *Acta Electrotehnica*, vol. 50, no. 4, pp. 295-301, 2009.
- [87] J. Sethian, "Level set methods and fast marching methods: evolving interfaces in computational geometry," in *Fluid Mechanics, Computer Vision, and Materials Science*, Cambridge, Cambridge University Press, 1999.
- [88] M. Purcar, J. Deconinck, B. Van den Bossche and L. Bortels, "Electroforming simulations based on the level set method," *The European Physical Journal of Applied Physics*, vol. 39, pp. 85-94, 2007.
- [89] M. Purcar, V. Topa, C. Munteanu, R. Chereches, A. Avram and L. Grindei, "Optimisation of the layer thickness distribution in electrochemical processes using the level set method," *IET Science, Measurement and Technology*, vol. 6, no. 5, pp. 376-385, 2012.
- [90] R. Alkire, T. Bergh and T. Sani, "Predicting electrode shape change with use of finite element methods," *Journal of the Electrochemical Society*, vol. 125, p. 1981, 1978.

- [91] J. Deconinck, "Current distribution and electrode shape change in electrochemical systems: a boundary element approach," in *Lecture Notes in Engineering No. 75*, Springer-Verlag, 1992.
- [92] J. Deconinck, "Mathematical modelling of electrode growth," *Journal of Applied Electrochemistry*, vol. 24, p. art. 212, 1994.
- [93] E. Masuku, A. Mileham, H. Hardisty, A. Bramley, C. Johal and P. Detassis, "A finite element simulation of the electroplating process," *CIRP Annals*, vol. 51, no. 1, pp. 169-172, 2002.
- [94] Y. Oh, S. Chung and M. Lee, "Optimisation of thickness uniformity in electrodeposition onto a patterned substrate," *Materials Transactions*, vol. 45, no. 10, pp. 3005-3010, 2004.
- [95] J.-M. Yang, D.-H. Kim, D. Zhu and K. Wang, "Improvement of deposition uniformity in alloy electroforming for revolving parts," *International Journal of Machine Tools & Manufacture*, vol. 48, pp. 329-337, 2008.
- [96] A. Behagh, A. Fadaei Tehrani, H. Salimi Jazi and O. Behagh, "Simulation of nickel electroforming process of a revolving part using finite element method," *Iranian Journal of Materials Science & Engineering*, vol. 12, no. 1, pp. 20-27, 2015.
- [97] I. Belov, C. Zanella, C. Edström and P. Leisner, "Finite element modeling of silver electrodeposition for evaluation of thickness distribution on complex geometries," *Materials and Design*, vol. 90, pp. 693-703, 2016.
- [98] P. Leisner and C. Zanella, "Application of Assaf panel for evaluating throwing power of pulse reverse electroplating on complex geometries," *Transactions of the Institute of Metal Finishing*, vol. 96, no. 5, pp. 258-264, 2018.
- [99] P. Leisner, G. Bech-Nielsen and P. Møller, "Throwing power in pulse reverse plating from an acid copper bath," in *Surface Finishing*, Atlanta, 1992.
- [100] D. R. Gabe, M. Ward and Y. Assaf, "Throwing Power Measurement: The Assaf Cell," *Plating and Surface Finishing*, vol. 88, no. 5, pp. 127-130, 2001.
- [101] P. Leisner, C. Zanella, I. Belov, C. Edström and W. Hui, "Influence of anodic pulses and periodic current reversion on electrodeposits," *Transactions of the Institute of Metal Finishing*, vol. 92, no. 6, pp. 336-342, 2014.
- [102] A. Mahapatro and S. K. Suggu, "Modelling and simulation of electrodeposition: effect of electrolyte current density and conductivity on electroplating thickness," *Advanced Materials Science*, vol. 3, no. 2, pp. 1-9, 2018.

- [103] H. Heydari, S. Ahmadipouya, A. S. Maddah and M.-R. Rokhforouz, "Experimental and mathematical analysis of electroformed rotating cone electrode," *Korean Journal of Chemical Engineering*, vol. 37, no. 4, pp. 724-729, 2020.
- [104] O. H. Pilkey and L. Pilkey-Jarvis, *Useless Arithmetic: Why Environmental Scientists Can't Predict the Future*, Columbia University Press, 2006.
- [105] D. Davies and S. Jenkins, "Mechanical and metallurgical characterisation of electroformed nickel for helicopter erosion shield applications," *Materials Science & Engineering A*, vol. 607, pp. 341-350, 2014.
- [106] R. Jianhua, Z. Zengwei and Z. Di, "Effects of process parameters on mechanical properties of abrasive-assisted electroformed nickel," *Chinese Journal of Aeronautics*, vol. 29, no. 4, pp. 1096-1102, 2016.
- [107] A. Li, X. Tang, Z. Zhu and Y. Liu, "Basic research on electroforming of Fe-Ni shell with low thermal expansion," *The International Journal of Advanced Manufacturing Technology*, vol. 101, pp. 3055-3064, 2019.
- [108] X. Zhan, Q. D. Cao, K. Trieu and X. Zhang, "Microstructure and mechanical properties of copper microtubes fabricated via the electroforming process," *Journal of Materials Engineering and Performance*, vol. 29, pp. 1741-1750, 2020.
- [109] F. Yang, W. Tian, H. Nakano, H. Tsuji, S. Oue and H. Fukushima, "Effect of current density and organic additives on the texture and hardness of Ni electrodeposited from sulfamate and Watt's solutions," *Materials Transactions*, vol. 51, no. 5, pp. 948 - 956, 2010.
- [110] Y. C. Wang, D. P. Zhao, S. K. Li, J. X. Liu and F. C. Wang, "The heat treatment effect on microstructure and dynamic mechanical properties of electroformed nanocrystalline Ni-W alloy," *Materials Science and Engineering A*, vol. 547, pp. 104 - 109, 2012.
- [111] A. M. Rashidi and A. Amadeh, "The effect of saccharin addition and bath temperature on the grain size of nanocrystalline nickel coatings," *Surface & Coatings Technology*, vol. 204, pp. 353-358, 2009.
- [112] J. H. Lim, E. C. Park, J. Joo and S.-B. Jung, "Effect of additives on microstructure and mechanical properties of nickel plate/mask fabricated by electroforming process," *Journal of the Electrochemical Society*, vol. 156, pp. D108-D112, 2009.

- [113] R. Akolkar, "Modeling dendrite growth during lithium electrodeposition at sub-ambient temperature," *Journal of Power Sources* , vol. 246, pp. 84-89, 2014.
- [114] L. Chen, H. W. Zhang, L. Y. Liang, Z. Liu, Y. Qi, P. Lu, J. Chen and L.-Q. Chen, "Modulation of dendritic patterns during electrodeposition: A nonlinear phase-field model," *Journal of Power Sources*, vol. 300 , pp. 376-385, 2015 .
- [115] C. Lupo and D. Schlettwein, "Modeling of Dendrite Formation as a Consequence of Diffusion-Limited Electrodeposition," *Journal of the Electrochemical Society*, vol. 166, p. D3182 , 2019 .
- [116] K. Wang, Y. Xiao, P. Pei, X. Liu and Y. Wang, "A Phase-Field Model of Dendrite Growth of Electrodeposited Zinc," *Journal of the Electrochemical Society*, vol. 166, no. 10, p. D389, 2019.
- [117] D. A. Cogswell, "Quantitative phase-field modeling of dendritic electrodeposition," *Physical Review E*, vol. 92, p. 011301(R), 2015.
- [118] A. M. Behagh, A. R. F. Tehrani, H. R. S. Jazi and S. Z. Chavoshi, "Investigation and optimization of pulsed electroforming process parameters for thickness distribution of a revolving nickel part," *Journal of Mechanical Engineering Science*, vol. 10 , p. 2306-2314, 227.
- [119] H. Yang and S.-W. Kang, " Improvement of thickness uniformity in nickel electroforming for the LIGA process," *International Journal of Machine Tools & Manufacture* , vol. 40 , p. 1065-1072, 2000 .
- [120] Z.-W. Zhu, D. Zhu, N.-S. Qu, K. Wang and J.-M. Yang, "Electroforming of revolving parts with near-polished surface and uniform thickness," *The International Journal of Advanced Manufacturing Technology*, vol. 39, no. 11-12, pp. 1164-1170, 2008.
- [121] C.-W. Park and K.-Y. Park, "An effect of dummy cathode on thickness uniformity in electroforming process," *Results in Physics* , vol. 4, p. 107-112, 2014 .
- [122] J. Deconinck, G. Maggetto, P. Versyck and J. Vereecken, "The boundary element method (BEM) for calculation of current distributions in electrochemical systems," in *Extended abstracts of the 34th ISE Meeting*, Erlangen, BRD, 1983.
- [123] G. Finoly, A. Gernay and A. Giroud, "Application and validation of the boundary element method to cathodic protection designs on vessels," in *XIVth International Conference on Boundary Element Methods*, Sevilla, 1992.

- [124] F. Brichau and J. Deconinck, "A numerical model for cathodic protection of buried pipe lines," *Corrosion (NACE)*, vol. 50, no. 1, pp. 39-49, 1994.
- [125] N. G. Zamani and J. M. Chuang, "Electroplating," in *Topics in Boundary Element Research*, Vols. 7, Electrical Engineering Applications, Springer-Verlag, 1990.
- [126] G. A. Prentice, Modeling of changing electrode profiles (PhD thesis), U. o. California, Ed., California: Lawrence Berkeley Laboratory, 1980.
- [127] J. O. Dukovic and C. W. Tobias, "Simulation of Leveling in Electrodeposition," *Journal of The Electrochemical Society*, vol. 137, no. 12, pp. 3748-3755, 1990.
- [128] B. De Bossche, J. Deconinck, G. Nelissen and M. Purcar, "Benefits of modelling for the electroplating industry," in *SUR/FIN Proceedings*, 2006.

Chapter 2: Electrochemical Characterisation of the Electroforming System

Keeping in mind our industrial partner's vision for "large-scale / high-volume" electroforming, we first had to identify the challenging obstacles. Following the detailed study of the literature available and presented in [Chapter 1](#), as well as extensive discussions with the Radius Aerospace Bramah team, it was clear that these challenges commence all the way from the design of the forms that can be electroformed and escalate in the digitalisation process.

The traditional way for industry to investigate the possibility of electroforming new parts of novel and complex shapes is to invest time and resources to create mandrels for these parts, fill with electrolyte industrial-scale reactors (tanks with capacity of 20 L to 1000 L) and run trial electrodeposition processes. Only if these trials are successful the electroforming of a part is moved to production, while all failed attempts lead to abandoned tooling and significant amounts of wasted resources. Since electroforming itself can be considered a sustainable process, such industry practices detract from both economy as well as the process environmental footprint.

While the challenges related to tool design and "green transition" can be easily understood, the challenges are more intricate in the context of the "Industry 4.0". "Industry 4.0" caught everyone's attention because it described and put into words, for the first time, the fact that the industrial developments which anyone could see by critically following the industry trends around the world during the last decade would be of great benefit to manufacturing. Therefore, new concepts were soon adopted to distinguish among the different aspects of the main, wide concept. Among these concepts, *digitalisation* stands a prominent position. Digitalisation should include the investigation of modern control systems which would help with

controlling electrode electrochemistry, the transformation of production to allow for manufacturing of any part through automation, as well as well-informed models which should relate specific electrochemical parameters to structural and mechanical properties, suggest optimised process parameters for faster production times and higher efficiency, and propose process modifications for sustainability through energy efficiency. Optimising agitation conditions, determining the most efficient working temperature, adjusting the system's geometry, and retrofitting equipment like “masks” and “thieves”, so that current distribution is optimised, are only some of the benefits that simulation studies could offer.

Having identified the above challenges, the next reasonable task was to devise a strategic plan and lay out our proposal of how to implement such a vision for electroforming. As it can be seen in [Figure 2.1](#), the proposed strategy practically included the process scaling down before scaling up.

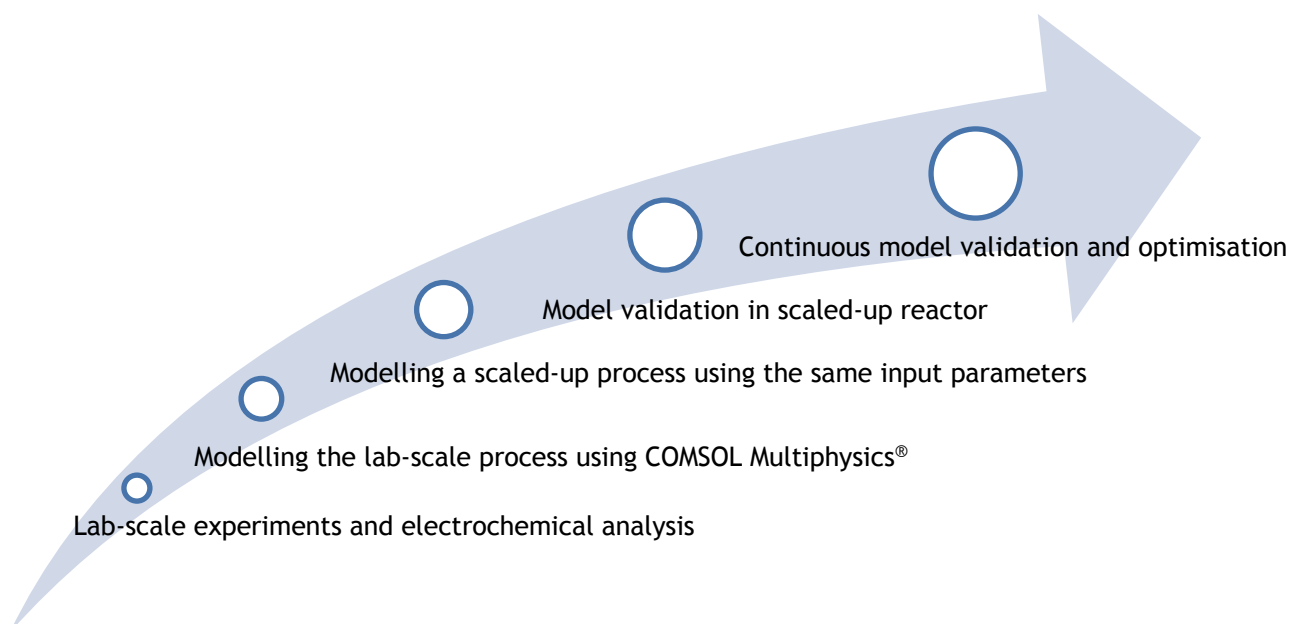


Figure 2. 1: Proposed strategy for approaching the vision of implementing digitalisation for large-scale / high-volume electroforming.

Starting from laboratory-scale experiments to electrochemically characterise the electroforming system and determine all important physical and electrochemical parameters (pH, electrolyte conductivity, limiting current, reversible and irreversible potentials, mass transfer coefficients), we moved on to building an informed model of the laboratory-scale process before, eventually, start modelling a scaled-up version of it. Both models were to be validated through deposition experiments at both scales, while a continuous cross-validation process throughout the duration of the project was to be expected.

In the following sections of this chapter, the first phase of the plan, the electrochemical characterisation of the nickel electroforming system, is discussed. Since the project's final goal is the development of a solid and efficient simulation model that could predict the electroforming process's outcome, it is vital to extract the right values of the electrochemical properties that would be used as input parameters in the model we were aiming to develop.

2.1 Equipment & Materials

For the polarisation related experiments conducted throughout the project the *PGSTAT302 Metrohm Autolab Potentiostat/Galvanostat* was used. The machine was used in a regular grounded mode and data were recorded by the *NOVA*® software. A recessed rotating disk electrode (RDE) with 304 stainless steel (main non-iron compounds, chromium at 15 – 20%, nickel at 2 – 10.5%) [1] was used as the working electrode (WE, cathode/mandrel), INCO nickel pellets (≥ 99.98 wt. % Ni) drilled and screwed through a titanium wire were used as the counter electrode (CE, anode). All measurements were recorded against a SCE reference electrode (RE). The $(\text{anode surface})/(\text{cathode surface})$ ratio was being kept greater than $2/1$ throughout the experiments, with the surface area of the nickel anode being $A_{\text{anode}} =$

0.0804 dm^2 and the cathode one, $A_{\text{cathode}} = 0.0113 \text{ dm}^2$ ($D_{RDE} = 0.12 \text{ dm}$). The laboratory-scale reactor was a 0.2 L double-wall electrolytic cell. The electrolytic solution was prepared according to the recipe summarised in [Table 2.1](#).

Table 2. 1: Electrolytic solution composition

Addition Chemical	Chemical Concentration (g/L or g/kg)	Amount to add per 1 L of solution (mL/L or g/L)		
		Min	Max	Mid
Ni(NH ₂ SO ₃) ₂ (aq)	180	416.7	611.1	513.9
NiCl ₂ · 6 H ₂ O (s)	300	5	8.3	6.7
H ₃ BO ₃ (s)	1000	30	40	35
PBN1 (s)	1000	1	2.5	1.75
Nimac 89 UNW (l)	1000	~ 1	~ 1	~ 1

To make-up 1 L of solution (2 M), 514 mL of aqueous nickel sulfamate solution [Ni(NH₂SO₃)₂ (aq)] were initially added to a conical flask, alongside de-ionised water, up to a total volume of ~ 900 mL. The solution was heated up to ~ 45 °C, under agitation by a magnetic stirrer bar. Next, 6.7 g of nickel chloride hexahydrate [NiCl₂ · 6 H₂O], 35 g of boric acid [H₃BO₃] and 1.75 g of PBN1 (trade name for 1,3,6 or 1,3,7 naphthalene tri-sulphonic acid, used as leveller) were gradually introduced to the solution, under continuous agitation at ~ 50 °C. As a final step, ~ 1 mL of Nimac 89 UNW wetting agent was added, before the solution was left under agitation, at ~ 50 °C, for 2 h before use. The components and complete RDE laboratory experimental setup are shown in [Figure 2.2](#).

For coherence, it is important to note here that, even though there is a wide range of chemicals that act as useful additives in nickel electroforming, for electroforms

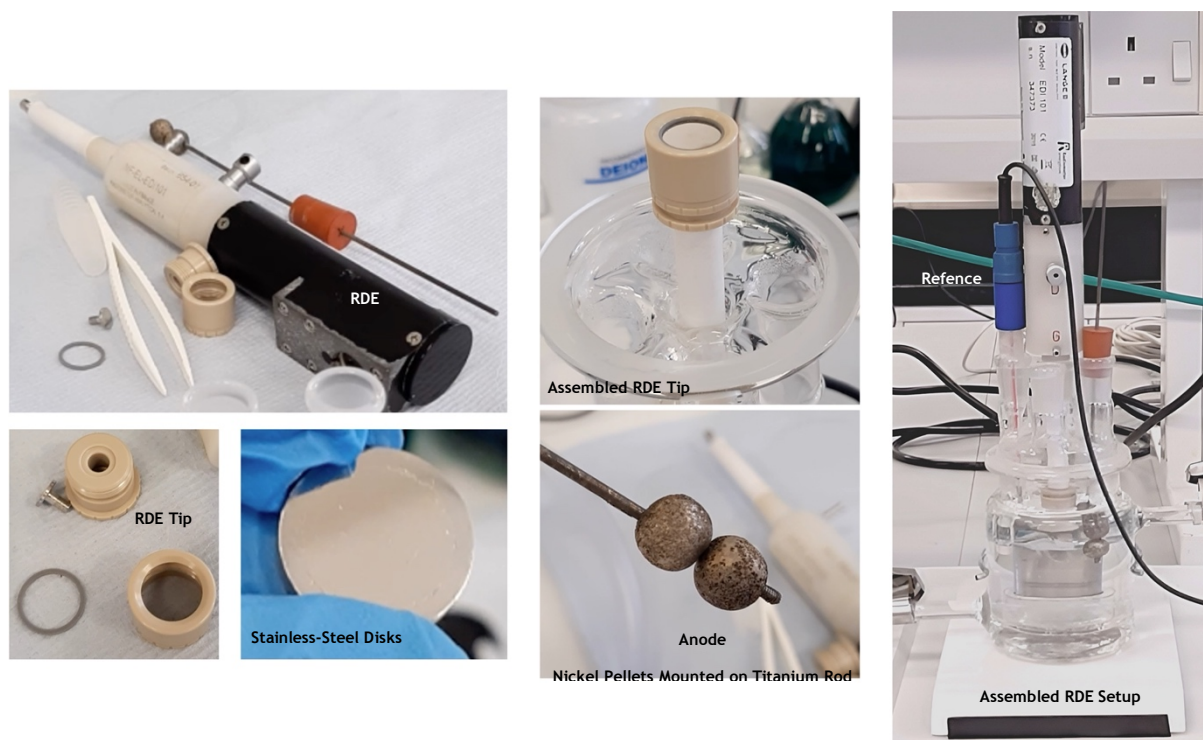


Figure 2. 2: The rotating disk electrode (RDE) setup used in laboratory experiments.

manufactured for aerospace applications the intention is to use as less as possible to avoid any negative additive-related effects to the internal stresses of the products since the extended use of additives has been empirically associated with the increase of internal stresses above the industry's strict tolerances.

When used for in the nickel electroforming of applications other than aerospace products, additives can roughly be divided into three main groups: levellers, brighteners, and wetting agents. Levellers are usually added in relative high concentrations ($1 - 10 \text{ g/l}$) to improve deposit smoothness and reduce internal stresses. They also permit brighteners to be present in suitably high concentrations without having to much effect on the mechanical properties. Brighteners are present in much smaller concentrations ($1 - 10 \text{ mg/l}$) and are responsible for mirror-like levelling effects. Nevertheless, they increase internal stresses and brittleness therefore they are usually used in nickel electroforming of decorative applications. Last but not least, wetting agents have no direct effect on the properties of the deposit but

prevent pitting holes from hydrogen bubbles formed on the cathode during the deposition.

Prior to each experiment, the stainless-steel disks that were used in the (RDE), the stainless-steel disks were carefully polished up to a “mirror-like” surface finishing against three different grades of *SiC* grinding paper (US #1200, #2400, #4000), using the *Struers Dap-7* polishing machine.

2.2 Electrochemical Analysis

For the electrochemical analysis of the RDE system, alongside initial pH and conductivity (σ) measurements, three analytical techniques were applied: linear sweep voltammetry (LSV), cyclic voltammetry (CV) and electrochemical impedance spectroscopy (EIS). The purpose of employing each one of these techniques will be discussed in detail in the sections to follow. In the experiments, a traditional, two-electrode, galvanostatically controlled, electrodeposition process was followed.

2.2.1 pH & Conductivity (σ)

The values of pH and conductivity (σ) were directly measured by *Mettler M800(1)* pH and conductivity probes. The equipment was calibrated before every set of measurements. The pH probe was calibrated using three different buffer solutions, for three different pH values (4, 7 and 9), according to the environmental temperature at the day of the measurements. The built-in module for calibration was used for the conductivity probe [2].

A freshly prepared electrolytic solution was studied in terms of its pH and conductivity (σ), both at room temperature and at 50 °C (working temperature). The same

was done for an aged electrolyte sample, of the same composition as the freshly prepared one, provided by our industrial partners; this electrolytic solution has been in use for 5 – 10 years within the company’s production line.

At room temperature, the pH value for each sample was measured at ~ 4 , with no significant differences observed between the two electrolytes. This value agrees with the relevant literature for nickel sulphamate solutions [3] and lies within the limits expected due to the boric acid’s buffering role. Conductivity values were recorded between 55 – 61 mS/cm . Again, no important variation was observed among the fresh and aged solutions. The comparative data for both the pH and conductivity at room temperature are presented in [Figure 2.3](#).

The two parameters were also measured at 50 °C, the temperature of the electrolyte during common electroforming processes. pH values for each sample were recorded at ~ 4 , as expected and, once more, in agreement with literature for nickel sulphamate solutions [4]. Following the proposed by literature behaviour [5], conductivity values were increased at a value range of 88 – 104.5 mS/cm . The comparative data for both the pH and conductivity at 50 °C are summarised in [Figure 2.4](#).

The above pH and conductivity data suggest that the age of the electrolyte and the different environmental conditions, under which they are used (controlled laboratory environment vs. industrial plant), do not affect (at least, not significantly) the values of the two parameters. This observation is attributed to the presence of boric acid as a significant stabilising parameter of the solution pH while, the excess of nickel in the electrolyte guarantees stability in conductivity.

2.2.2 Polarisation Studies (Linear Sweep Voltammetry)

Following the pH and conductivity measurements, linear sweep voltammetry (LSV) studies were conducted to determine the system’s electrochemical behaviour. For the experiments presented here, a wide voltage range ($2 V \leftrightarrow (-2) V$), different scan rates and, agitation conditions where the RDE was either stagnant or set at ro-

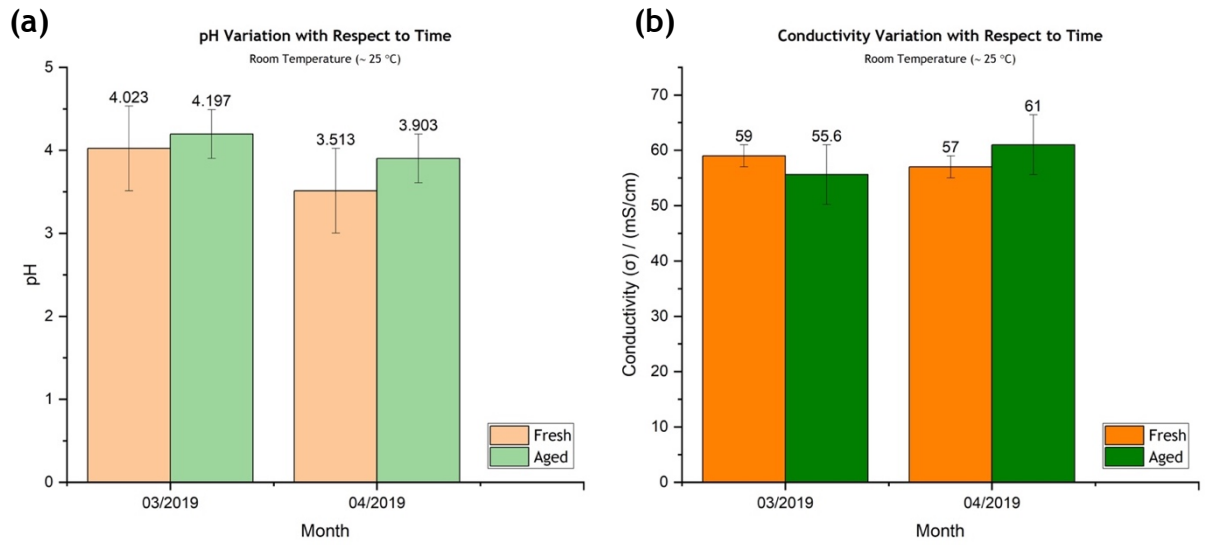


Figure 2. 4: (a) Comparative pH data for the freshly and aged electrolytes at room temperature (~ 25 °C), (b) Comparative conductivity (σ) data for the freshly and aged electrolytes at room temperature (~ 25 °C).

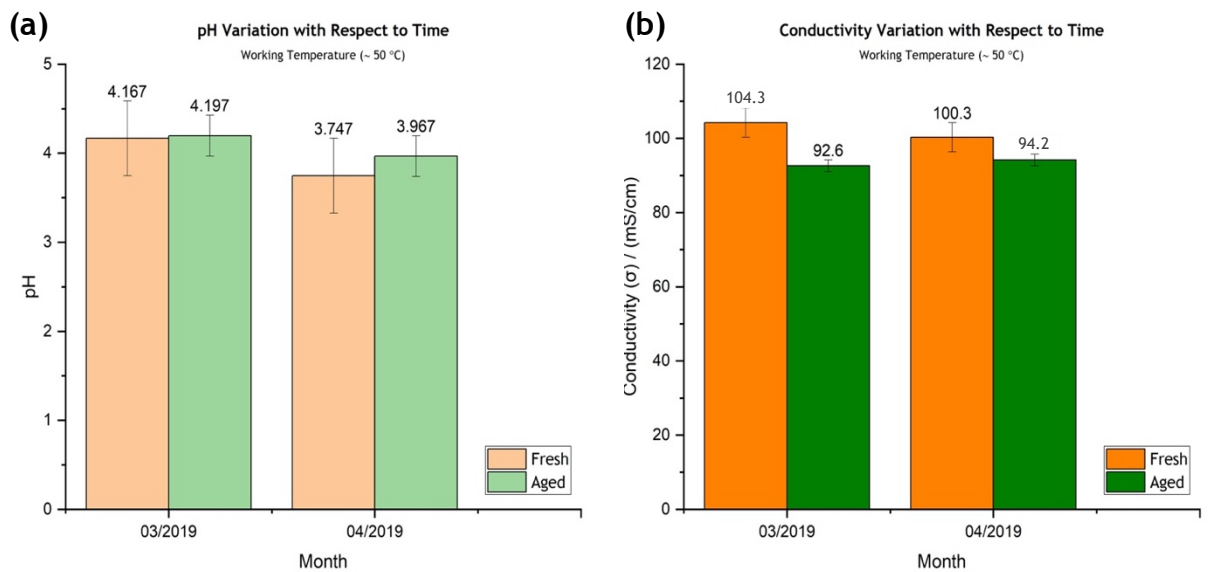


Figure 2. 4: (a) Comparative pH data for the freshly and aged electrolytes at working temperature (~ 50 °C), (b) Comparative conductivity (σ) data for the freshly and aged electrolytes at working temperature (~ 50 °C).

tation speeds of 200 rpm, 500 rpm, 1000 rpm, 1500 rpm and 2000 rpm, were investigated.

During LSV studies the potential applied to the working electrode (cathode/mandrel) is varied linearly through time. LSV is probably the most efficient electrochemical method for mapping the behaviour of an electrochemical system since a series of steps/scans can be obtained by using different scan rates and applying various potential ranges. As an output, current-potential plots are drawn; these are usually referred to as polarisation curves. LSV is conducted either cathodically or anodically; a cathodic polarisation curve is obtained when potentials are swept from positive to negative values while, an anodic polarisation curve is obtained following a reverse sweep, from negative to positive potential values. The interpretation -or even the accumulation in some cases- of this data can be challenging, especially when stationary electrodes are used. Additionally, it is difficult sometimes to recognise the presence of different species present or reactions taking place because LSV is a pretty sensitive technique that needs to be carried out under carefully and accurately chosen conditions [6].

Figure 2.5 shows how the results look when obtained at different scan rates. A scan rate describes the speed with which the LSV experiment gathers data over a given potential range. To better understand how the technique work for the RDE case, let's consider the Levich equation (2.1), giving the mathematical expression for limiting current (i_{lim}), which is the highest current that can be carried by the cupric ion in a specific solution and geometry [7]:

$$i_{lim} = 0.62nFAD^{2/3}\omega^{1/2}\nu^{-1/6}C_0^* \quad [2.1]$$

where, n is the participating number of electrons, $F = 96485.3 \text{ C/mol}$ is the Faraday constant, A is the area of the deposition surface, D is the diffusion coefficient, ω is the RDE angular velocity, ν is the kinematic viscosity and C_0^* the electrolyte initial concentration.

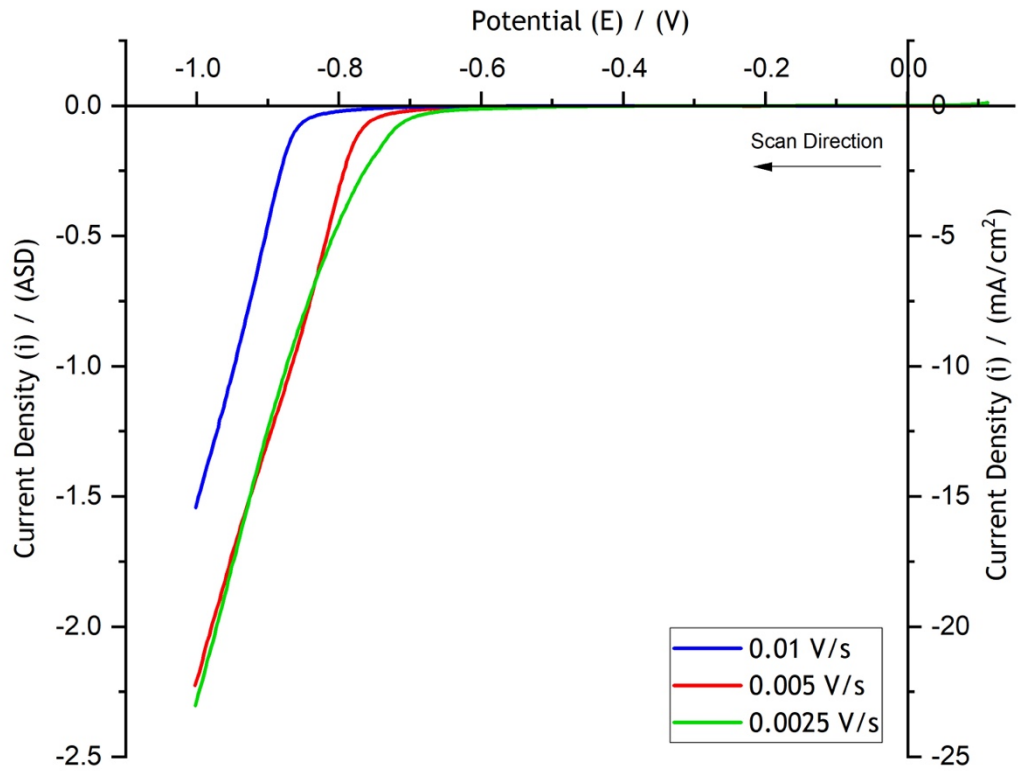


Figure 2. 6: Overlap of cathodic polarisation curves of a freshly prepared electrolytic solution, scan was taken up to $(-1) V$, at different scan rates, under stagnant conditions, at $50\text{ }^{\circ}\text{C}$.

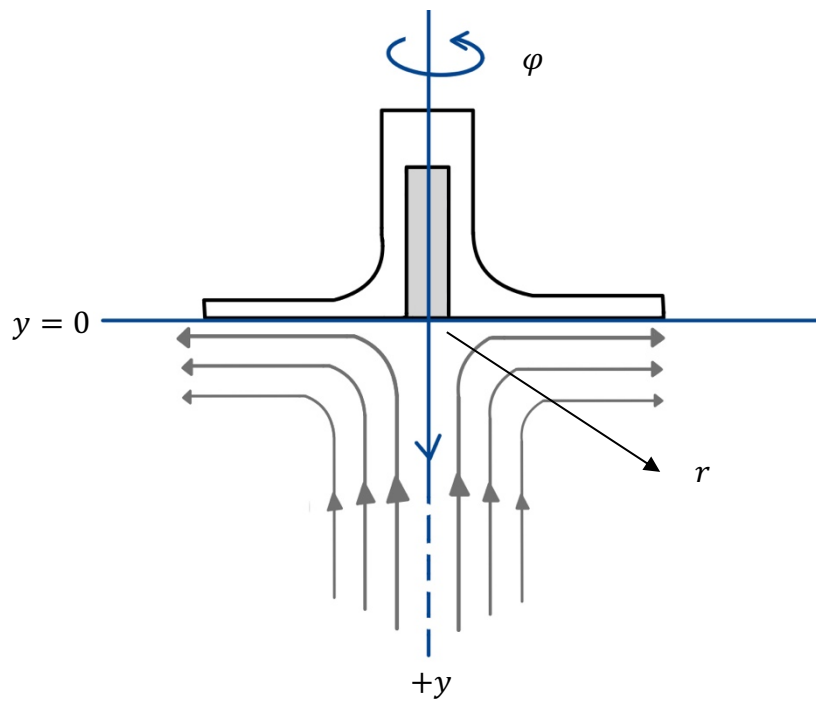


Figure 2. 6: Cylindrical polar coordinates for the rotating disk electrode.

As it can be understood, since i_{lim} varies with ω , the current density i , at any potential will also vary with ω . Therefore, it becomes obvious that the RDE agitation speed can significantly affect the quality of the LSV data. In general, the equations describing the RDE behaviour do not apply at very small or only for very large values of ω . If the cylindrical polar coordinates for the RDE are declared as shown in Figure 2.6, at low agitation speeds, the hydrodynamic boundary layer, $y_h \approx 3(\nu/\omega)^{1/2}$, becomes large, causing any approximations to break down when the RDE radius is approached. Among the approximations to break down is the one derived from the assumption of steady-state concentration conditions at the RDE surface. Therefore, when $i - E$ curves are recorded at the RDE, the LSV scan rate must be slow enough, with respect to ω , so that the above steady-state condition is satisfied [6].

Figure 2.7 shows how the system behaves under different agitation intensities.

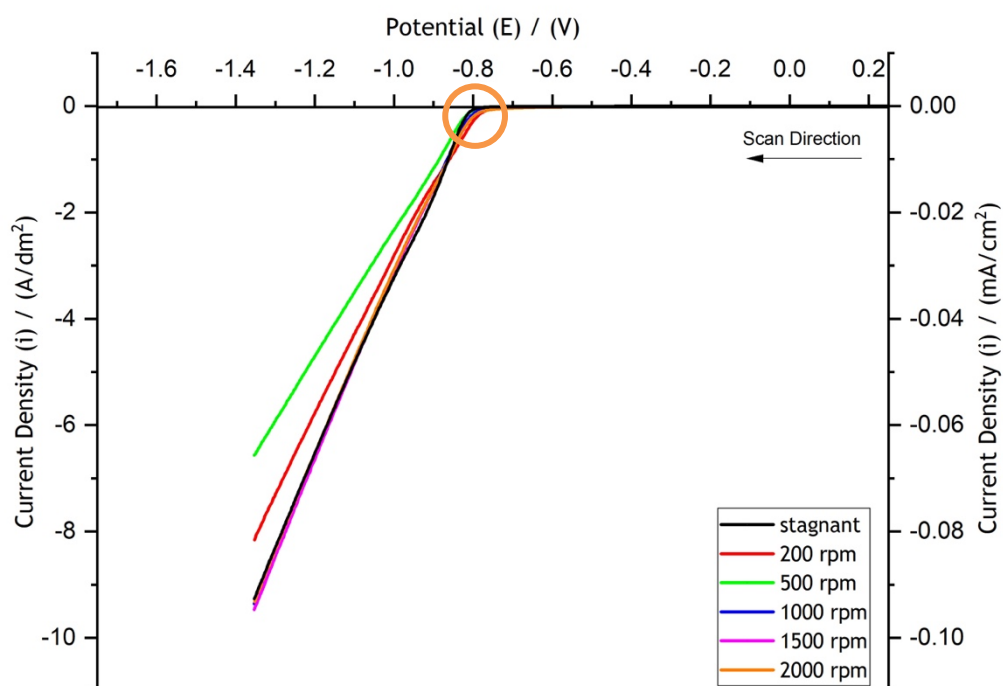


Figure 2. 7: Overlap of cathodic polarisation curves of a freshly prepared electrolytic solution, scans were taken up to $(-1.35) V$, at a scan rate of $0.005 V/s$, under various agitation conditions, at $50\text{ }^{\circ}C$.

The first important observation here is that deposition starts at the same potential [$\sim(-0.82\text{ V})$], regardless the agitation conditions, as indicated by the circled area. The second important observation confirms that more intense agitation increases the steepness of the plot slope, indicating an increased reaction rate (speed).

Following several trials under different and various experimental conditions and keeping in mind the sensitivity of the scan rate-agitation relation, a scan rate of 0.005 V/s under agitation at 1500 rpm was determined as the most efficient for the laboratory experiments. Each experiment was conducted at $50\text{ }^\circ\text{C}$ using the freshly prepared electrolyte to represent the industrial conditions. LSV experiments were systematically designed aiming to determine an efficient range of potentials and current densities within which nickel deposition efficiently occurs.

Based on these results, future deposition experiments were to be designed accordingly. The polarisation curves obtained here would, most importantly, found to be very useful for the determination of key electrochemical parameters, such as the exchange current density (i_0) and the anodic and cathodic transfer coefficients (α_a , α_c), which would have to be used as input in the models to be discussed later.

As a first approach, various deposition potentials were applied in order to investigate within which potential range we can achieve current density values of $2 - 5\text{ ASD}$ ($20 - 50\text{ mA/cm}^2$) which correspond to the working current density range in industry. Following numerous LSV experiments, it was found that the potential range lies between $(-0.86)\text{ V}$ and $(-0.92)\text{ V}$. The cathodic polarisation curve of the freshly prepared electrolytic solution is shown in [Figure 2.8](#). Scan was run from 0 V to $(-1.1)\text{ V}$ at a rate of 0.005 V/s and under agitation at 1500 rpm .

A current range of 100 mA was set for the measurements within the *NOVA*® software and the results were being corrected in real time for ohmic drop. Following this observation, a decision was made to focus on a potential window close to the deposition potentials that correspond to industry's working current density values. Consequently, linear sweep voltammetry scans up to $(-1.1)\text{ V}$ were determined to be sufficient for the electrochemical analysis to follow.

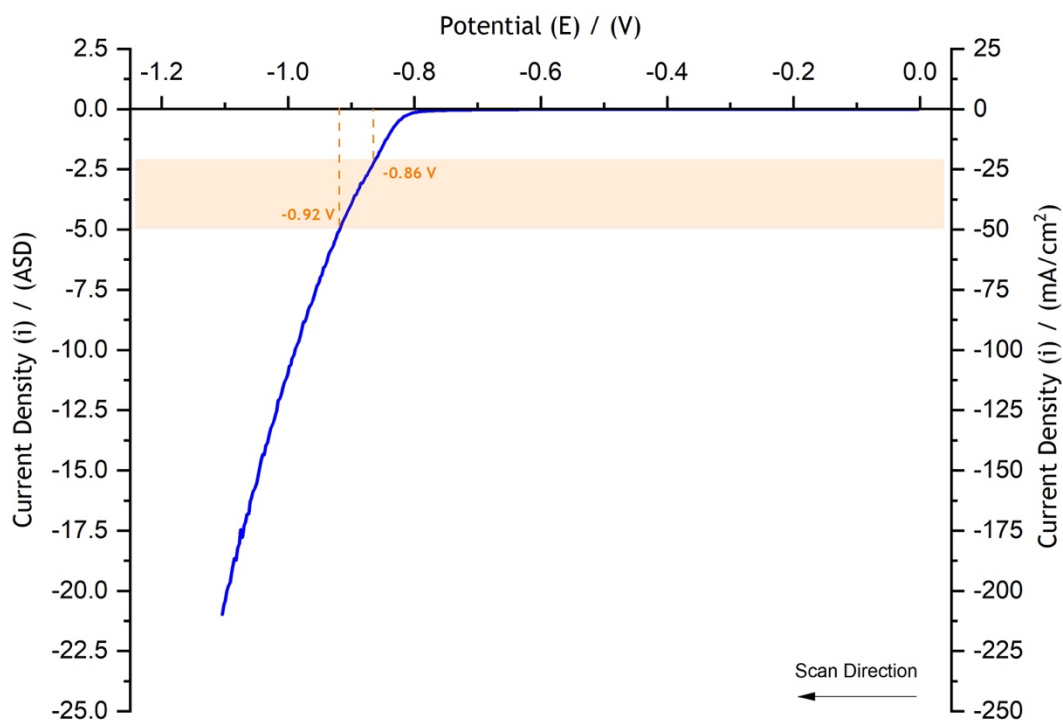


Figure 2. 8: Cathodic polarisation curve of the freshly prepared electrolytic solution. Scan was run from 0 V to (-1.1) V at a rate of 0.005 V/s, under agitation at 1500 rpm. A current range of 100 mA was chosen for the measurement and the results were being corrected in real time for ohmic drop.

Before moving forward, it is considered important to clarify what “correcting the LSV data for ohmic drop” means, as well as how this happens in practice. Due to the flow of current (I) through the electrolyte being affected by its resistance (\mathcal{R}) a voltage drop ($V_{drop} = I \times \mathcal{R}$) occurs. As a result, if someone wanted to mathematically depict the cell’s total potential, they should write:

$$E_{cell} = E_A + E_C + I \times \mathcal{R} \quad [2.2]$$

where, E_{cell} is the total cell potential, E_A is the potential of the anode electrode, E_C is the potential of the cathode electrode and $I \times \mathcal{R}$ is the energy that needs to

be consumed by the system in order to overcome the electrolyte's intrinsic resistance.

As it is obvious from Equation 2.2, in order to depict the “clean” potential that is used for the chemical process which takes place between the anode and the cathode, *i.e.*, the nickel deposition, someone should remove the $I \times \mathcal{R}$ contribution. To do so, the value of the electrolyte's resistance needs to be measured and electrochemical impedance spectroscopy (EIS) is the technique for this.

During an LSV process, the total potential and current which describe the system's state each time are measured through time. By adding the electrolyte's resistance as an input parameter, the NOVA[®] software can remove the $I \times \mathbf{R}$ contribution based on the simple concept of Ohm's law (Equation 2.3):

$$\mathcal{R} = V/I \quad [2.3]$$

It is important to note that up to 80 % of the \mathcal{R} value determined by EIS can be input to NOVA[®]. Above this limit the data tends to experience significant distortion. For the EIS measurements, the *PalmSens4* impedance analyser was used in a three-electrode setup for direct resistance measurements.

Having clarified how the LSV data were corrected for ohmic drop, the extrapolation of Tafel plots from the obtained LSV data is discussed.

Since RDE can be considered to satisfy the condition of a well-stirred electrolytic solution, creating no concentration gradients between the deposition surface and the bulk electrolyte, the Butler-Volmer model can be employed to describe the physics of the problem. Equation 2.4 is the Butler-Volmer equation:

$$i_{loc,m} = i_{0,m} \left(e^{\frac{\alpha_{a,m} F \eta_m}{RT}} - e^{\frac{-\alpha_{c,m} F \eta_m}{RT}} \right) \quad [2.4]$$

where, for a given reaction m , $i_{loc,m}$ represents the local charge transfer current density, $i_{0,m}$ is the exchange current density, $\alpha_{a,m}$ and $\alpha_{c,m}$ are the anodic and

cathodic charge transfer coefficients and, η_m is the activation overpotential. $R = 0.082 \text{ m}^3 \cdot \text{atm}/\text{K} \cdot \text{kmol}$ is the universal gas constant and T the temperature under which the problem is studied. The term $e^{\frac{\alpha_{a,m}F\eta_m}{RT}}$ is the anodic component of the B-V equation, and $e^{\frac{-\alpha_{c,m}F\eta_m}{RT}}$ is the cathodic component.

Since Equation 2.4 does not account for any mass-transfer contributions, the overpotential at any given current works only towards building up the activation energy required to drive the electrodeposition. A low exchange current density indicates slow kinetics, meaning that activation overpotential should be higher for any given current applied. In other words, the exchange current density could be considered as the charge delivered across the system at equilibrium. The role of the overpotential is to disturb the balance between the exchange rates at equilibrium, causing the current exchange to move towards one of the two directions. As a general rule, the appearance of currents lower than the exchange current would require just a small overpotential (*i.e.*, slight equilibrium disturbance) while, currents higher than the exchange current would appear only if significantly high overpotentials are applied (*i.e.*, higher activation energy is required to disturb the equilibrium balance). As a matter of fact, the exchange current could be considered as an electrochemical system's measure of its ability to deliver a net current without significant energy losses during activation [6].

For large negative values of η , as is the case in nickel deposition, the positive bracketed term in Equation 2.4 becomes negligible, providing the Tafel approximation form of the Butler-Volmer equation (Equation 2.5).

$$i_{loc,m} = i_{0,m} e^{\frac{-\alpha_{c,m}F\eta_m}{RT}} \quad [2.5]$$

The empirical Tafel constants can then be identified from theory [6] as:

$$\alpha = \frac{2.3RT}{\alpha_a F} \log(i_0) \quad [2.6]$$

and,
$$b = -\frac{2.3RT}{a_c F} \log(i_0) \quad [2.7]$$

The Tafel approximation holds when the anodic reaction, if a net reduction is considered, contributes less than 1 % of the current. For the case of nickel deposition, presenting slow electrode kinetics and requiring significant activation overpotentials, good Tafel relationships can be seen.

A Tafel plot is a plot of η vs. $\log(i)$, usually presenting an anodic branch with slope equal to a and a cathodic branch with slope equal to b . The transfer coefficients and exchange current density values can be determined via these plots.

From the cathodic polarisation curve shown in [Figure 2.8](#), the cathodic Tafel plot for the nickel electrodeposition system under investigation was extrapolated. As it can be seen in [Figure 2.9](#), two linear areas were observed. This may indicate a change in the reaction mechanism rather than an approach to limiting current conditions, as the second linearity appears far below the mass transfer limiting current value, $\log(|i_{lim}|) = 3.32 \text{ mA/cm}^2$.

The limiting current for the system was calculated at 2081.38 mA/cm^2 by [Equation 2.8](#):

$$i_{lim} = \frac{zFD_{eff}}{\delta} \times C_{Ni} \quad [2.8]$$

where, $z = 2$ is the number of ions exchanged, $D_{eff} = 5.55 \times 10^{-6} \text{ cm}^2/\text{s}$ is the diffusion coefficient for nickel sulphamate solutions [8], $C_{Ni} = 2.07 \text{ M}$ is the nickel concentration in the solution and δ is the distance between the electrodes.

To calculate the electrode distance, [Equation 2.9](#) was used:

$$\delta = 1.61 \times D_{eff}^{0.3333} \times \nu^{0.1666} \times \omega^{-0.5} \quad [2.9]$$

To complete the electrochemical characterisation of the system, the cathodic charge

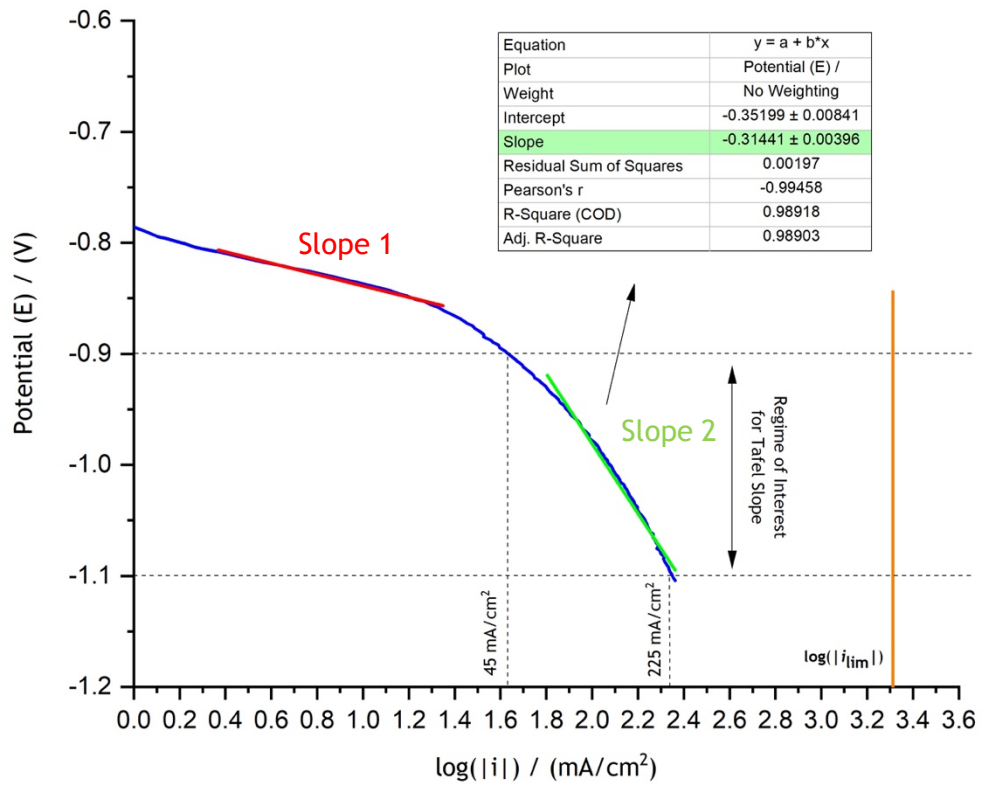


Figure 2. 9: Cathodic Tafel slope for the freshly prepared electrolytic solution, extrapolated by the LSV data of Figure 2.8. $OCP = -0.254 V$ (vs. SCE), slope 1: $-51 mV/dec$ (defines b_1), slope 2: $-314 mV/dec$ (defines b_2).

transfer coefficient was calculated using Equation 2.10 and the second slope value of the Tafel plot in Figure 2.9:

$$Tafel\ slope = \frac{-2.3RT}{a_c} \quad [2.10]$$

Since,

$$\alpha_c + \alpha_a = n \quad [2.11]$$

the anodic charge transfer coefficient was determined from Equation 2.11 and not

measured independently.

The calculations were carried out for the results presented in [Figure 2.9](#), as well as two more identical experiments to confirm repeatability. As a result, the cathodic charge transfer coefficient was determined at $\alpha_c = 0.194$ and the anodic at $\alpha_a = 1.806$. Using [Equation 2.6](#) and the experimental Tafel slope values (highlighted in green in [Figure 2.9](#)), the exchange current density was also determined at $i_0 = 0.42 \text{ A/dm}^2$.

It is important to note here that Slope 2 was chosen to calculate the values above because it lies within the region of interest. It is, however, recognised that its value is very high, and the polarisation curve is continuously bending. Based on the definition of the Tafel approximation, which assumes that a reaction is dominated by the slower chemical reaction rate, Slope 1 simulates a Tafel approximation much more sufficiently. Therefore, it is more accurate to state that the chosen Slope 2 is used here as a “sufficient linear approximation” rather than a “Tafel approximation”. Consequently, this linear approximation of the curve in [Figure 2.9](#) can be used as input for modelling, but it is not representing a specific rate determining reaction.

2.2.3 System Reversibility (Cyclic Voltammetry)

CV experiments were finally conducted in order to establish the system’s reversibility and investigate the reduction and oxidation reactions taking place.

Cyclic voltammetry (CV) is a reversal, electrolytic method during which the potential is scanned from a starting positive value to a minimum negative value and back. CV measurements are only conducted in unstirred solutions so as the measured current to be limited solely by the analyte diffusion at the electrode surface. The forward scan produces current peaks which correspond to any analyte that can be reduced while, (ideally) symmetrically positioned peaks appear as the backward branch is

being shaped for the analytes that are oxidised [6]. However, this is less applicable to metal deposition, especially, when a metal such as nickel can passivate.

Based on the LSV results, CV experiments were carried out under the same experimental parameters and stagnant conditions, starting at $(+0.8) V$, going down to $(-1.4) V$ and returning to $(+0.4) V$, with a scan rate of $0.005 V / s$.

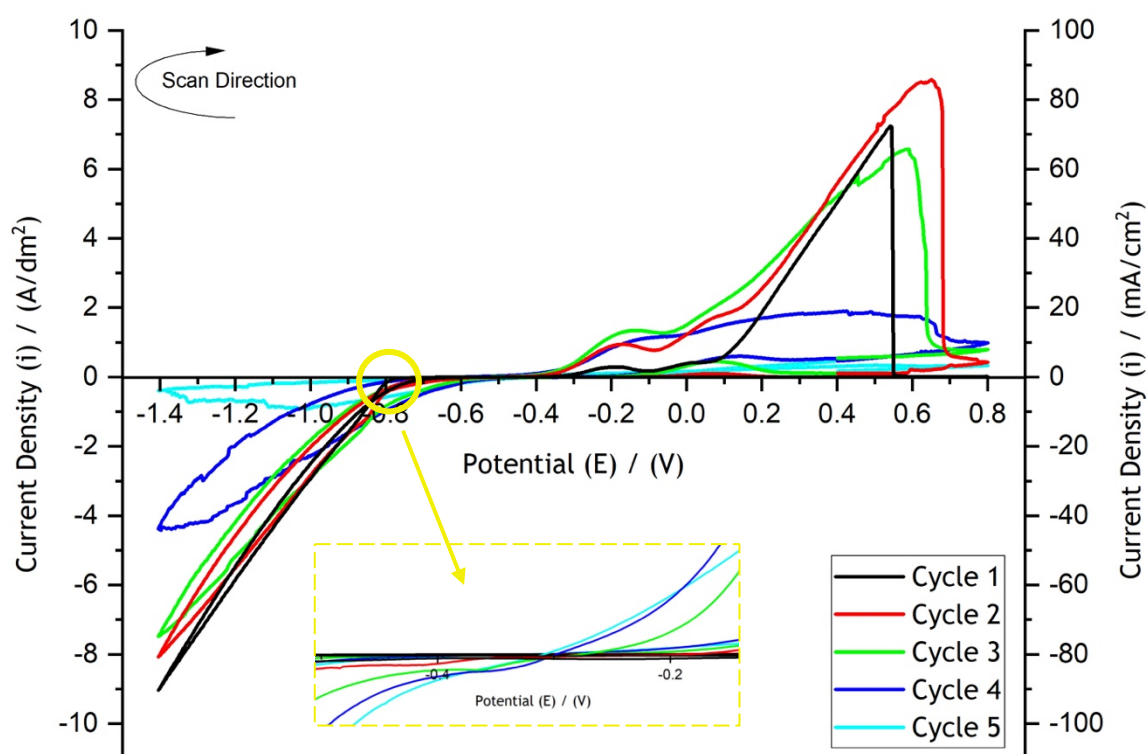


Figure 2. 10: Cyclic voltammetry curves of freshly prepared electrolytic solution, starting at $(+0.8) V$, going down to $(-1.4) V$ and returning to $(+0.4) V$, under stagnant conditions, with a scan rate of $0.005 V / s$ - 5 cycles.

Five cycles were repeated to confirm whether and how the system's behaviour stabilises through time. The results are shown in [Figure 2.10](#).

The results suggested that nickel remains “active” for three cycles, before completely passivating. The CV data confirm, however, the stability of the system in terms of both the reduction peaks’ positions and the cathodic region’s starting potential (indicated in circle), which shows progressive passivation of nickel. This result is important since it shows that electrodeposited nickel does not etch off and will remain in the deposit. [Table 2.2](#) summarises the data and parameters derived from the experiments so far.

Table 2. 2: Parameters determined via physico-chemical analysis of the RDE system and polarisation experiments.

pH \approx 4		Conductivity $\sigma = 0.9165 \text{ S/dm}$	
Exchange Current Density	Limiting Current Density	Anodic Transfer Coefficient	Cathodic Transfer Coefficient
$i_{0,m} = 0.42 \text{ A/dm}^2$	$i_{lim,m} = 208.138 \text{ A/dm}^2$	$\alpha_{a,m} = 1.806$	$\alpha_{c,m} = 0.194$
Reversible Potential			
$E_{eq} = -0.52 \text{ V}$			

2.3 Deposition Experiments

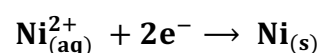
Electrochemical deposition is the process during which metal ions are reduced from an electrolytic solution, according to the general chemical equation (2.12)



with the number of z electrons (\mathbf{e}^{-}) to be provided by an external power supply [9].

Practically, electrodeposition is the growth of a metallic coating onto (electro-plating) or against (electro-forming) on a substrate or mandrel. In the case of nickel

deposition, the chemical equation (2.13) that describes the reduction of the nickel anode is



[2.13]

For the experiments presented here, a *TTI, Inc. EL301R* (30 V, 1 A) power supply (PSU) was used with the three-electrode setup described in [Section 2.1](#) ([Figure 2.11](#)). The power supply was set to the maximum allowed current value of 1 A while, the potential value was being adjusted accordingly, to achieve the (real) current magnitude desired for each experiment. The set current value (of 1 A) and potential value (different each time) were displayed on the

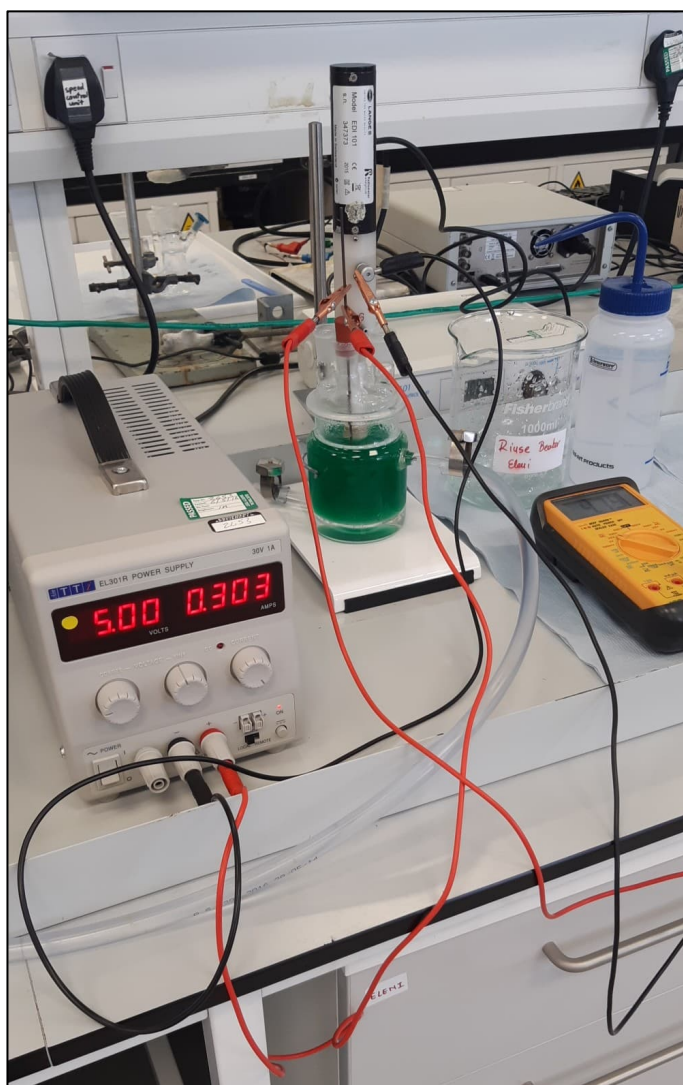


Figure 2. 11: Laboratory deposition RDE set-up.

power supply's screen. As soon as the deposition process was initiated, the power supply screen was displaying the real current and potential values during the process; these values were lower than the set ones. All deposition experiments were carried out for 1800 s, at 50 °C and under agitation at 1500 rpm.

It is important to note that, every minute, the potential reading on the power supply screen was the corresponding total potential of the cell (E_{cell}) or, in other words, the potential difference between the anode (CE) and the cathode (WE). In order to record the real cathode potential, a multimeter was used to measure the potential difference between the cathode and a SCE reference electrode. That way, it was possible to measure how much of the total cell potential (displayed on the power supply's screen) was consumed for the deposition reaction that takes place on the cathode surface almost exclusively.

Table 2.3 lists the deposition experiments conducted at various current densities and summarises the results. The deposition current densities were chosen to include the working values applied in industry (2 – 5 ASD), as well as higher and lower values than those. The RDE stainless-steel disks (mandrels) were weighed both before and after deposition to determine the deposited nickel mass. The experimentally achieved deposit masses were compared to the theoretical ones.

Using Faraday's law, the theoretical mass (m) and thickness (s) were calculated using Equations 2.14 & 2.15, respectively:

$$m = \frac{I \times t \times Mr_{Ni}}{n \times F \times \Phi} \quad [2.14]$$

and,

$$s = \frac{m}{A_{mandrel} \times \rho_{Ni}} \quad [2.15]$$

Table 2. 3: Pivot table of deposition results at various current densities, using the RDE setup. For all cases, deposition ran for 1800 s, under agitation at 1500 rpm, at 50 °C.

Potential (V) (PSU Reading)	Current (A) (PSU Reading)	Current Density (ASD)	Mandrel Weight before Deposition (g)	Theoretical Thickness (μm)	Mandrel Weight after Deposition (g)	Achieved Mass (g)	Achieved Thickness (μm)	Current Efficiency
5	0.565	50	4.2436	307.2127	4.5616	0.318	315.8428	102.81%
3.5	0.194	17.17	4.2575	105.4854	4.3541	0.0966	95.9447	90.96%
2.75	0.095	8.41	4.1183	51.6552	4.1708	0.0525	52.1439	100.96%
2.5	0.059	5.22	4.3254	32.0806	4.35	0.0246	24.4331	76.16%
2.25	0.049	4.34	4.4143	26.6432	4.4393	0.025	24.8304	93.28%
2	0.04	3.54	4.1187	21.7496	4.1352	0.0165	16.3881	75.34%
1.5	0.008	0.71	4.4446	4.3499	4.4455	0.0009	0.8939	20.45%

where, I is the applied current, $t = 1800 \text{ s}$ is the duration of deposition, $Mr_{Ni} = 58.69 \text{ g/mol}$ is the molar mass of nickel, $\Phi = 1$ is the process efficiency (assumed to be 100 %), $A_{mandrel} = 1.13 \text{ cm}^2$ is the mandrel's deposited area and $\rho_{Ni} = 8.91 \text{ g/cm}^3$ is the mass density for nickel.

Following each deposition's completion, the experimentally achieved thicknesses were also calculated using Equations 2.14 & 2.15 and the experimentally achieved mass values. As it is shown in Table 2.3, the process presents high current efficiency for current densities above 5 ASD. Borrowing Paunovic's [9] definition, "...current efficiency (CE) is the ratio between the actual amount of metal deposited, m_{act} , to that calculated theoretically from Faraday's laws, m_{th} , in percent":

$$CE = \frac{m_{act}}{m_{th}} \times 100 \quad [2.16]$$

Nickel deposition processes are expected to present current efficiencies near 100 %, nevertheless cathode efficiency is generally dependent on a series of key electrolyte parameters, such as chemical component concentrations, pH, agitation, and current density. As a matter of fact, the current density over the cathode will vary from

point to point. Since current tends to be accumulated at the leading edges and protruding points of mandrels, deposit thicknesses tend to vary over the surface of a mandrel, usually observed to be thicker at the aforementioned edges and points. Thickness distribution is significantly influenced by variation of the current efficiency with current density. In some cases, current efficiency increases with current density (e.g., chromium plating baths), resulting in high non-uniformities of thickness, while sometimes the opposite is happening (e.g., cyanide metal baths) [9].

For the nickel sulphamate bath investigated here, a proportional relationship between the applied current density and calculated current efficiency is observed; the current efficiency was calculated to be higher when higher current densities were applied. Thickness uniformity follows the expected behaviour as well, with the deposits being seemingly thicker towards the leading edge compared to the centre of the nickel disks. Up to that stage of the project, the growth of dendritic formations around the edge (Figure 2.12) constituted the only confirmation of that fact. Thickness measurements were conducted later in the project, for model validation, and will be discussed in detail in the chapters to follow.

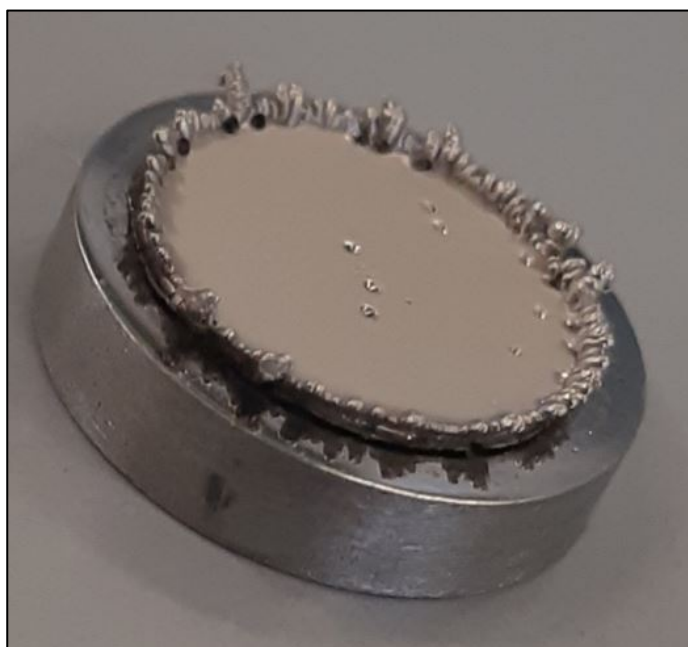


Figure 2. 12: Nickel deposit formed using the RDE setup. Deposition ran at 44 ASD, under agitation at 1000 rpm, for 1800 s and at 50 °C.

Even though the deposition process was found to generally present high current efficiencies under the various applied current densities, a deviation from that behaviour was observed for very low deposition currents. As it can be seen in [Table 2.2](#), nickel deposition at current densities lower than 1 ASD presented very poor current efficiency (20 %).

According to literature, this is something to be expected as hydrogen evolution might interfere with the nickel deposition reaction at the cathode surface [9] [10]. Nickel deposits produced in sulphamate baths at low current densities have also been found to present high contents of hydrogen and sulphur or other impurities [9]. These data might indicate the occurrence of more than one deposition reaction at the cathode when deposition is carried out at very low currents, leading to poor current efficiencies and deposit impurities. Since these current density values are much lower than the usually applied ones during industrial electroforming, no further investigations were conducted on that matter.

However, a qualitative analysis to obtain a “break-down” of the total process potential was considered interesting. During deposition, part of the energy (potential) provided to the system is consumed for the main reactions which take place on the cathode (primary reactions) while, part of it is consumed by the secondary reactions that occur at the anode. To determine that, for each one of the deposition experiments in [Table 2.2](#), the cathode potential was measured via a multimeter against a SCE reference electrode, enabling the calculation of the energy that is actually consumed for the reactions on the working electrode. [Figure 2.13](#) shows this potential “break-down” for medium-low and medium-high applied current densities. Since nickel deposition follows a multi-step reaction mechanism (refer to [Chapter 1](#)), it was expected that part of the total energy provided to the system (E_{cell}) will be consumed at the cathode surface to drive the nickel deposition (E_C), another part will occur as ohmic drop due to the electrolyte’s resistance ($I\mathcal{R}$) while, the last part

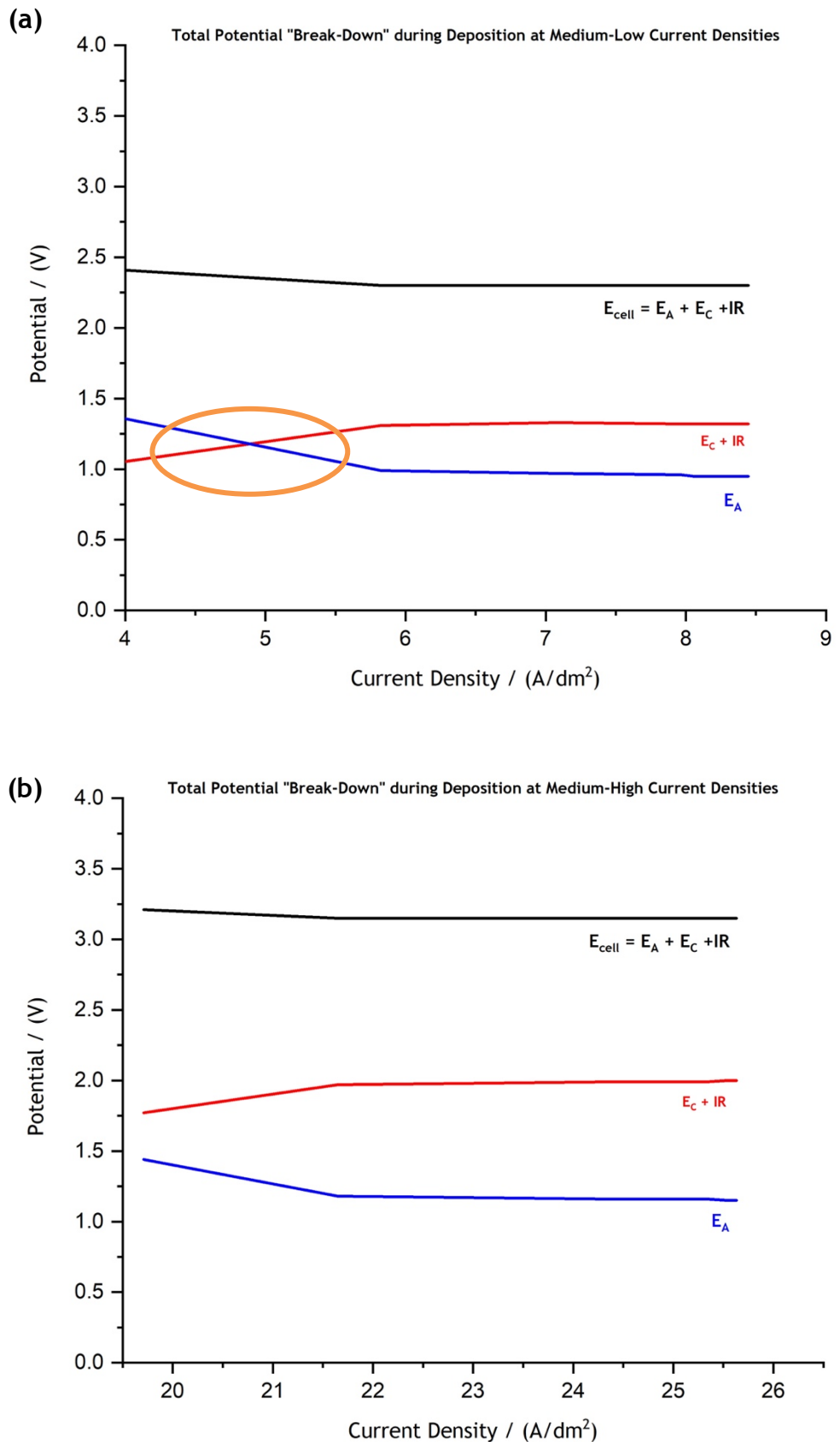


Figure 2. 13: Total system potential (black line) "break-down" for a (a) deposition experiment at 3.98 *ASD* and (b) deposition experiment at 19.71 *ASD*. Both depositions ran for 1800 *s*, at 1000 *rpm* and 50 °C. Cathode reactions potential (red line), anode reactions potential (blue line).

of it will drive secondary reactions mainly taking place at the anode surface (E_A). Using the configuration shown in [Figure 2.11](#), the multimeter indication will account for the sum of the first two ($E_C + IR$).

The findings of this investigation suggested that anodic reaction potential remains low regardless the experimental conditions and always lower than the cathode reaction one. For higher current densities ([Figure 2.13-b](#)), the *cathode reactions potential* / *anode reactions potential* ratio seems to stabilise and settle at a 50% – 50% proportion after a third of the deposition process is completed. Very interestingly, according to the results highlighted in circle in [Figure 2.13-a](#), during deposition at lower current densities most of the energy provided to the system is firstly consumed for the anodic reactions, before the cathodic reactions take over. This result agrees with the low current efficiency observed for deposition at 0.71 ASD before (refer to [Table 2.2](#)) and supports our assumptions that secondary reactions might be responsible for this effect. As it has already been mentioned, these investigations do not lie within this project's main interests and, therefore, were not pursued further. However, they provide a better insight on the system's electrochemical behaviour even at this preliminary stage.

2.4 Conclusions

The data gathered during the first phase of the project provided a complete and useful insight into the system behaviour and electrochemical characteristics.

pH and conductivity (σ) measurements returned results in agreement with literature. Both at room temperature and 50 °C the pH was determined at 4 while, conductivity varied between $\sigma = 55 - 61 \text{ mS/cm}$ at room temperature and $\sigma = 88 - 104.5 \text{ mS/cm}$ at 50 °C. A comparison between freshly prepared and aged electrolyte samples

revealed no significant variations in the value of either parameter. A summary of these properties is presented in page 7.

Linear sweep voltammetry measurements provided a first overview of the system's electrochemical behaviour. Cathodic polarisation curves were gathered in a systematic manner to determine efficient potential and current density deposition windows. Assuming Butler-Volmer type kinetics, the data were subsequently used for determining the corresponding Tafel plots. Based on the LSV results, the electrochemical parameters of the system were determined: $E_{eq,Ni} \equiv E_{rev} = -0.82 \text{ V}$, $\alpha_c = 0.194$, $\alpha_a = 1.806$, $i_0 = 0.42 \text{ A/dm}^2$, $i_{lim} = 2081.38 \text{ mA/cm}^2$. These values will be used as model input parameters in the modelling studies to follow.

Interesting results were observed during deposition experiments. Deposition by a DC power supply provided the ability to determine high current efficiencies for the process, record the total system potential during the process, as well as determine the part of the total potential consumed specifically by the cathodic reactions. The potential attributed to anodic reactions was always measured lower than the cathodic reactions potential while, higher current densities found to stabilise and settle the proportion between the cathodic and anodic reactions at 50% – 50%.

Following the electrochemical characterisation of the system, the development of a *COMSOL Multiphysics*[®] model of the RDE system was initiated.

References

- [1] “Data sheet on SAE 304 stainless steel,” [Online]. Available: <https://www.makeitfrom.com/material-properties/AISI-304-S30400-Stainless-Steel>. [Accessed 11 09 2019].
- [2] M. Toledo, “User Manual: SevenDirect SD23 pH/Cond Meters,” [Online]. Available: <https://www.mt.com/gb/en/home/library/user-manuals/lab-analytical-instruments/SevenDirect-SD23-User-Manual.html>. [Accessed 02 08 2022].
- [3] J. Ji, W. Cooper, D. Dreisinger and E. Peters, “Surface pH measurements during nickel electrodeposition,” *Journal of Applied Electrochemistry*, vol. 25, p. 642, 1995.
- [4] Y. Tsuru, M. Nomura and F. Foulkes, “Effects of boric acid on hydrogen evolution and internal stress in films deposited from a nickel sulfamate bath,” *Journal of Applied Electrochemistry*, vol. 32, pp. 629-634, 2002.
- [5] Y. Tsuru, M. Nomura and F. Foulkes, “Effects of chloride, bromide and iodide ions on internal stress in films deposited during high speed nickel electroplating from a nickel sulfamate bath,” *Journal of Applied Electrochemistry*, vol. 30, pp. 231-238, 2000.
- [6] A. Bard and L. Faulkner, *Electrochemical Methods: Fundamentals & Applications*, New York, USA: John Wiley & Sons, Inc., 2001.
- [7] J. Newman and K. E. Thomas-Alyea, *Electrochemical Systems*, Hoboken, New Jersey: John Wiley & Sons, Inc., 2004.
- [8] M. Halmdienst, W. Hansal, W. Kautek and G. Kaltenhauser, “Pulse plating of nickel: influence of electrochemical parameters and composition of electrolyte,” *Transactions of the IMF*, vol. 85, no. 1, pp. 22-26, 2013.
- [9] M. & S. M. Paunovic, in *Fundamentals of electrochemical deposition*, Hoboken, New Jersey, John Wiley & Sons, Inc., 2006, p. 348.
- [10] C. Q. Cui and J. Y. Lee, “Nickel deposition from unbuffered neutral chloride solutions in the presence of oxygen,” *Electrochimica Acta*, vol. 40, no. 11, pp. 1653-1662, 1995.

Chapter 3: Model Foundation & Implementation

As it was mentioned in [Chapter 1](#) already, one of the three main objectives of this project has been the development of a well-informed modelling tool, based on systematically gathered experimental data, which could assist our industrial collaborators to achieve their goal of volume electroforming of large parts with extremely high precision.

To develop such a modelling tool, the *Electrodeposition* module in *COMSOL Multiphysics*[®] was used. The system was set to work under galvanostatic mode (as is done in industry), the current at the cathode was determined, and the deposit thickness was calculated at each time step. This thickness was used by the model to move the boundary of the formed electrode as it evolved with time, while the local currents are computed. The electrode reactions chosen were of Butler-Volmer type, with nickel and its ions being the only electroactive species. The physical dimensions of the cell in use were used to fix reactor geometry.

COMSOL Multiphysics[®] was chosen for this project due to it being easily accessible as a commercial software, providing our industry partners with a business-to-business service and support. At the same time, the user-friendly simulation environment and, relatively, straightforward result post-processing render the use of the software flexible in a fast-pace working environment while allowing for faster and efficient client-to-client communication throughout the manufacturing process. Last but not least, *COMSOL Multiphysics*[®] can be installed in super-computers (e.g., Archie-West in Scotland [1]) as easily as in an average PC therefore, it offers the possibility of studying scaled-up models of very large parts. The simulations presented as part of

this thesis are based on results obtained using *COMSOL Multiphysics*[®] on a professional desktop PC.

3.1 The Finite Element Method

Whether chemical, mechanical, aerospace, or physical, all phenomena observed in the world can be described by a mathematical model. Practically this means that there is always a system of differential and/or integral equations which characterises each phenomenon. These, usually complex, equation systems (or models) are employed on domains of complex geometries and are developed on the basis of assumptions and approximations concerning the process under investigation using the laws and axioms of physics. Following their development, the mathematical models are evaluated by a numerical simulation, through the use of a numerical method and a computer [2].

COMSOL Multiphysics[®] utilises the Finite Element Method (FEM) for such numerical simulations. As per the definition given by Pepper and Heinrich in their book *“The Finite Element Method: Basic Concepts and Applications”* [3], *“...the finite element method is a numerical technique that gives approximate solutions to differential equations that model problems arising in physics and engineering”*. As any other numerical analysis method, FEM can be an important tool in the hands of engineers during process design and manufacturing. Numerical methods are the only alternative to analytical solutions when complex geometries, extraordinary material compositions and nonlinearities, among other things, are the case.

In such cases, while it might not be very difficult to identify the governing equations of a problem, their approximation functions are usually challenging to be constructed. Approximation functions are arbitrary, simpler functions than the

governing ones, which satisfy continuity and overcome non-linearities allowing for efficient declaration of a problem's boundary conditions. While their arbitrariness offers the user the freedom to choose the approximation functions that best serve their needs each time, it is also this characteristic that renders their selection a challenging task. The modeller's choice of the approximation functions directly affects the quality of the problem's approximations themselves, with selection becoming even more challenging without a systematic way of approaching the issue, and especially when the simulation geometry is complex [2].

By requiring a problem to be defined in a domain subdivided into a finite number of smaller elements, creating a mesh (Figure 3.1), FEM provides such a systematic approach of laying out the required approximation functions. For each one of the finite elements, the unknown variables are approximated using known functions. As a result, a set of finite linear equations is obtained, and linear algebra is used for solving these equations [4].

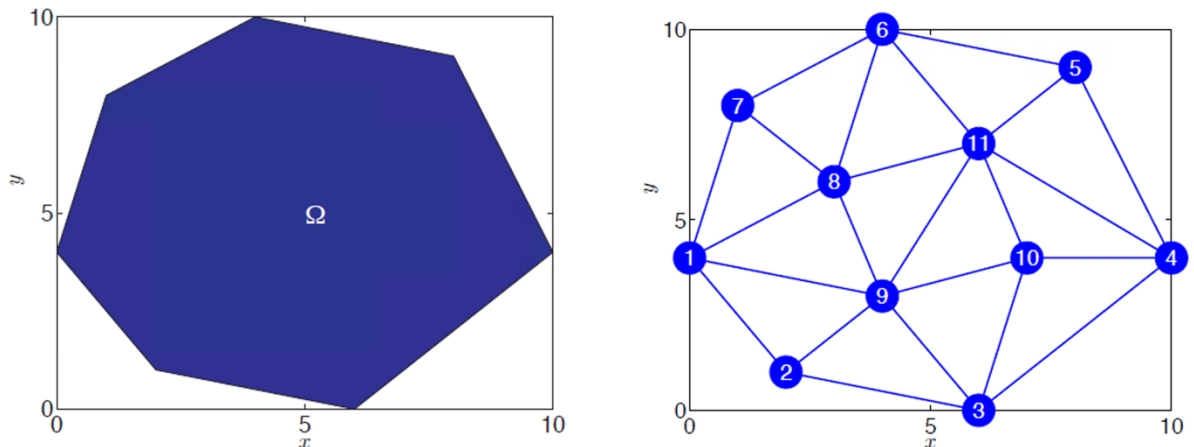


Figure 3. 1: Representative example of the mesh of a 2-D domain when the finite element method analysis is used. In this case, the domain spacing consists of 2-D triangular elements. [14]

The mesh's elements differ amongst one-, two- and multiple-dimension problems. Most commonly, in 1-D problems the elements appear as simple intervals, in 2-D

problems as squares or triangles, while in 3-D problems can be either cubes or tetrahedrons [4] (Figure 3.2). For this arrangement to be valid, the end points of each triangle (element) edge should be at a vertex of the mesh *i.e.*, no “hanging nodes” should appear (Figure 3.3). The density of any mesh can be adjusted according to the problem’s needs.

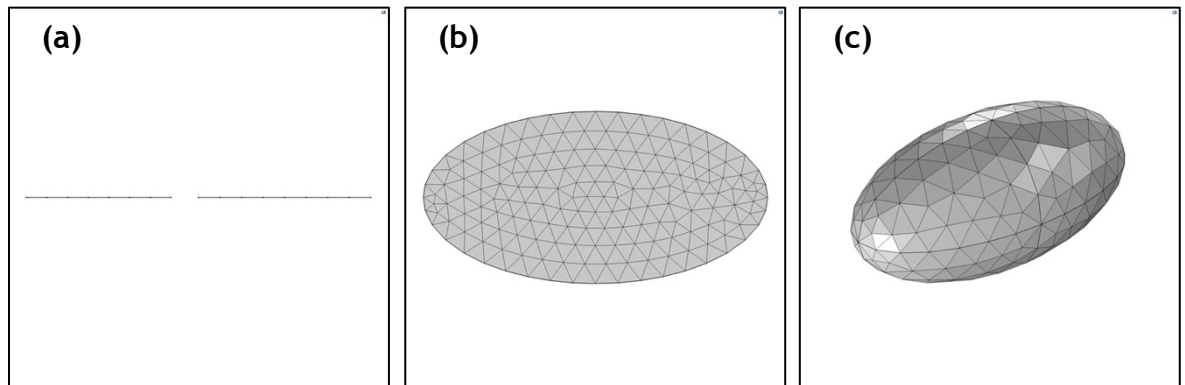


Figure 3. 2: Representative mesh spacing in COMSOL Multiphysics® of (a) a 1-D domain consisting of elements appearing as intervals, (b) a 2-D domain consisting of triangular elements and (c) a 3-D domain consisting of elements in the form of tetrahedrons.

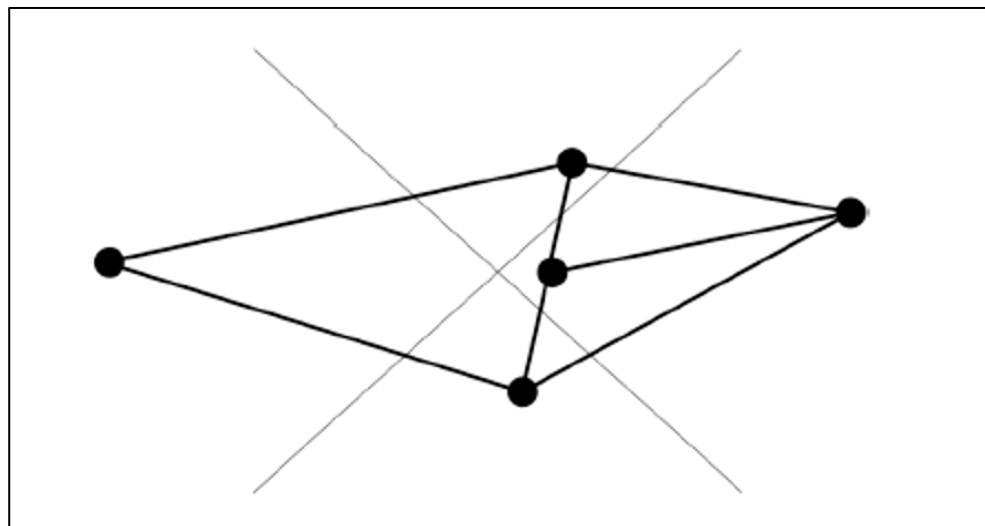


Figure 3. 3: Example of a “hanging node” [14].

When it comes to the finite difference approximation of a differential equation, the derivatives of this equation are replaced by difference quotients, *i.e.*, the function is expanded in a Taylor series, which takes into account the solutions at the different nodes in the domain. The resulting mathematical equation system is solved for each node according to the declared boundary conditions [2]. Since every differential equation describing the problem is solved for each one of the mesh nodes, as a general principle, the differential equations involved will be solved more times within a fine mesh including more elements, compared to a coarse one. Consequently, more solutions, on more domain points, are calculated providing a better solution to the problem. As a result, the simulation's final approximation will be closer to a "real" solution. At the same time, however, longer computation time is needed for the model to achieve convergence. Sensitivity studies of a model's meshing tolerance could save valuable time since meshes of high node densities are not always needed for a model to return a reasonably accurate solution. This is usually done by manually reducing the mesh size (usually a 50 % reduction in mesh size) and calculating the residual.

Once the residual size becomes independent of mesh spacing, very little would be gained from reducing the mesh size any further. A second method is using logarithmic mesh spacing, where the mesh is finest near the boundary or object of interest. However, the change in mesh spacing needs to be carefully handled due to computational issues and is often physics-controlled and calculated automatically by the software concerned.

As it is easily understood, subdividing the simulation domain into smaller elements, when employing the finite element method, provides the user with much more control over a problem's numerical simulation, if compared to other meshless approaches of numerical analysis. At the same time, it promotes an increased attention to detail by allowing the development of custom meshes varying in element size between local areas/boundaries of interest (smaller elements-finer mesh spacing) and the rest of the domain (bigger elements-coarser mesh spacing). In other words, through custom meshes, the finite element method allows for approximations

of better quality in the areas/boundaries of interest, making possible that way the numerical simulation of systems which include geometries of unique and complex shapes, the modelling of large-scale processes, as well as processes and phenomena which adapt their boundaries as they evolve with time.

As a process described by significant non-linearities and moving boundaries, nickel electrodeposition can be effectively modelled using the finite element method approach. In the following section, the development of a nickel electrodeposition model using *COMSOL Multiphysics*[®] is described in detail.

3.2 Developing the RDE Model

The first phase of this project's modelling studies included the development of a 2-D axisymmetric model of the rotating disk electrode geometry used for the laboratory experiments. Time-dependent studies, assuming secondary current distribution (SCD) were conducted, and the model was validated against deposition experiments in the laboratory in terms of the predicted thicknesses.

3.2.1 Geometry (2-D Axisymmetric)

For this first approach, the RDE setup was studied in its 2-D axisymmetric version. That way, compared to a 3-D model, fewer complex calculations are performed and, thus, the duration of those is significantly short. This approach is very helpful during the first steps of building a model as it allows the user to focus on the actual process of developing it, as well as to understand the way the software behaves and works.

As the experimental RDE setup is not symmetrical (refer to [Figure 2.2](#)), an axisymmetric representation of it could only be a simplified version of the actual geometry. The geometry is presented in [Figure 3.4](#). Respectively, [Figures 3.5-a](#) and [3.5-b](#) show

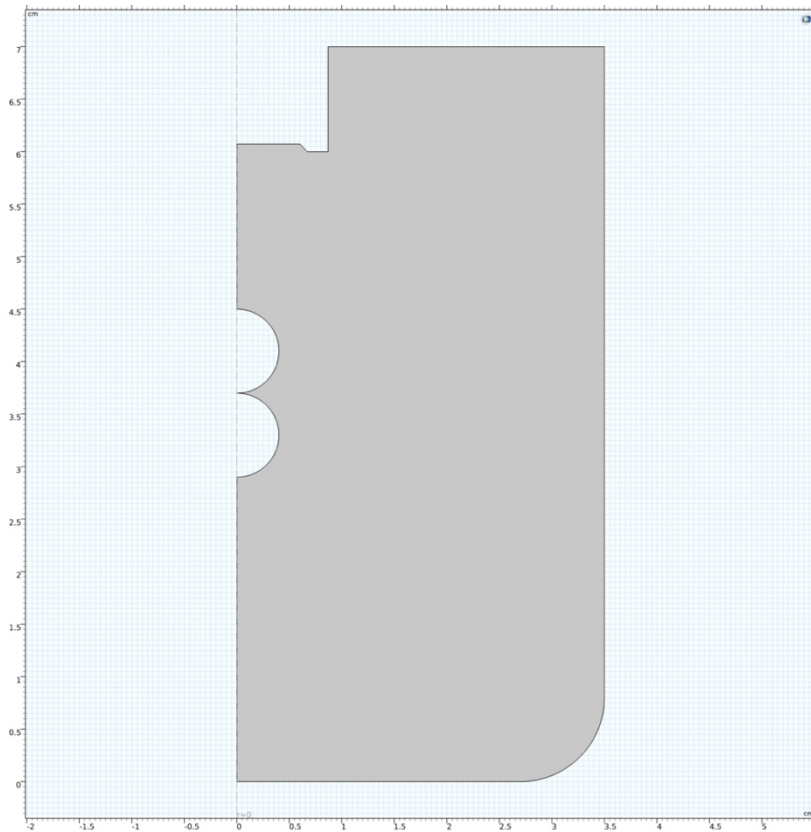


Figure 3. 4: Simplified 2-D Axisymmetric RDE Geometry used for modelling purposes.

magnifications of the cathode and anode surfaces, respectively. In [Figure 3.5-a](#), indicated by a circle, the recessed boundary of the RDE is also shown. This is an important transition point which should be precisely drawn to avoid convergence issues related to poor mesh spacing around it. This will also be discussed in the following sub-section.

3.2.2 Mesh

In our simulations we maintained a user-controlled mesh spacing, finer near the electrode surface and determined by a parameter called the maximum element growth rate within the electrolyte domain. Specifically, this parameter was set at 1.3 for the domain, and 1.1 for the recess and cathode boundaries, with reference to the fi-

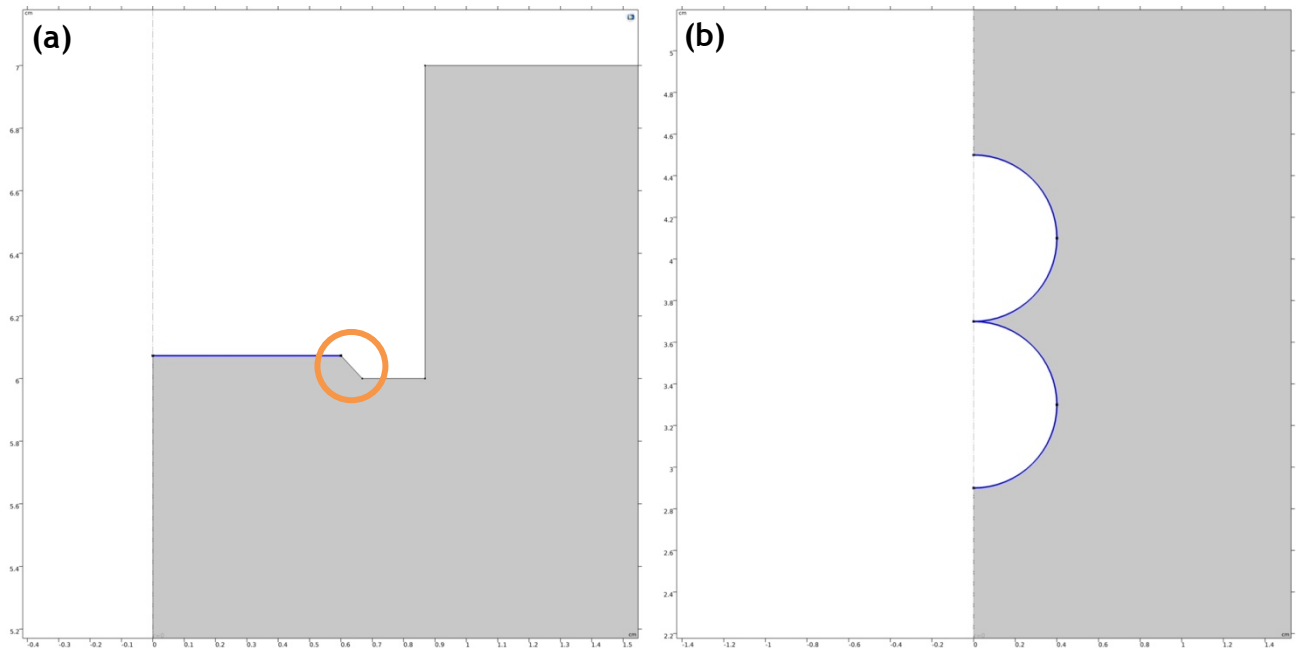


Figure 3. 5: (a) Cathode and (b) anode surface of the simplified 2-D Axisymmetric RDE model.

nest elements present. The maximum element growth rate limits the size difference of two adjacent mesh elements, *i.e.*, with a maximum element growth rate of 1.1, the most the element size can grow from one element to another is 10 %. As a last step, obeying to that user-declared limitation, the software creates the mesh applying a free triangular operation.

Another important aspect to monitor is the mesh quality. Within *COMSOL Multiphysics*[®], mesh quality is controlled by a series of mesh quality measures, including, but not limited to, elements' maximum angle, volume versus length ratio and growth rate. For this work, skewness was used as the element quality measure which is the default quality measure. Skewness is a “*measure of the equiangular skew which is defined as the minimum of the following quantity:*”

$$1 - \max\left(\frac{\theta - \theta_e}{180 - \theta_e}, \frac{\theta_e - \theta}{\theta_e}\right) \quad [3.1]$$

where θ is the angle over a vertex (2-D) or edge (3-D) in the element, θ_e is the angle of the corresponding edge or vertex in an ideal element, and the minimum is taken over all vertices (2-D) or edges (3-D) of the element” [5].

Element quality is a dimensionless parameter taking values between 0 and 1 and refers to the elements’ regularity; 0 corresponds to degenerated elements and 1 to perfectly regular ones. Any value below 0.1 describes poor quality elements. In fact, automated warnings will be generated by the software when elements of quality below 0.01 are generated since those must be fixed to avoid convergence issues.

The parameters characterising the mesh built for the 2-D axisymmetric are presented in [Table 3.1](#). To allow for better understanding of all the parameter given in this table, it is useful to clarify that the curvature factor limits how big a mesh element can be along a curved boundary while, the resolution of narrow regions controls the number of layers of mesh elements in narrow regions.

Table 3. 1: General and boundary, user-defined, element size parapa-
rameters for the 2-D axisymmetric RDE model

Element Size Pa- rameters	2-D Axisymmetric RDE Model			
	General	Cathode	Anode	Recess
Maximum Element Size (mm)	0.4	0.01	0.5	0.001
Minimum Element Size (mm)	0.001	–	–	–
Maximum Element Growth Rate	1.3	1.1	–	1.1

[Figure 3.6](#) shows the free triangular mesh spacing used in the 2-D axisymmetric RDE model and highlights the points of interest mentioned above. Since the main interest

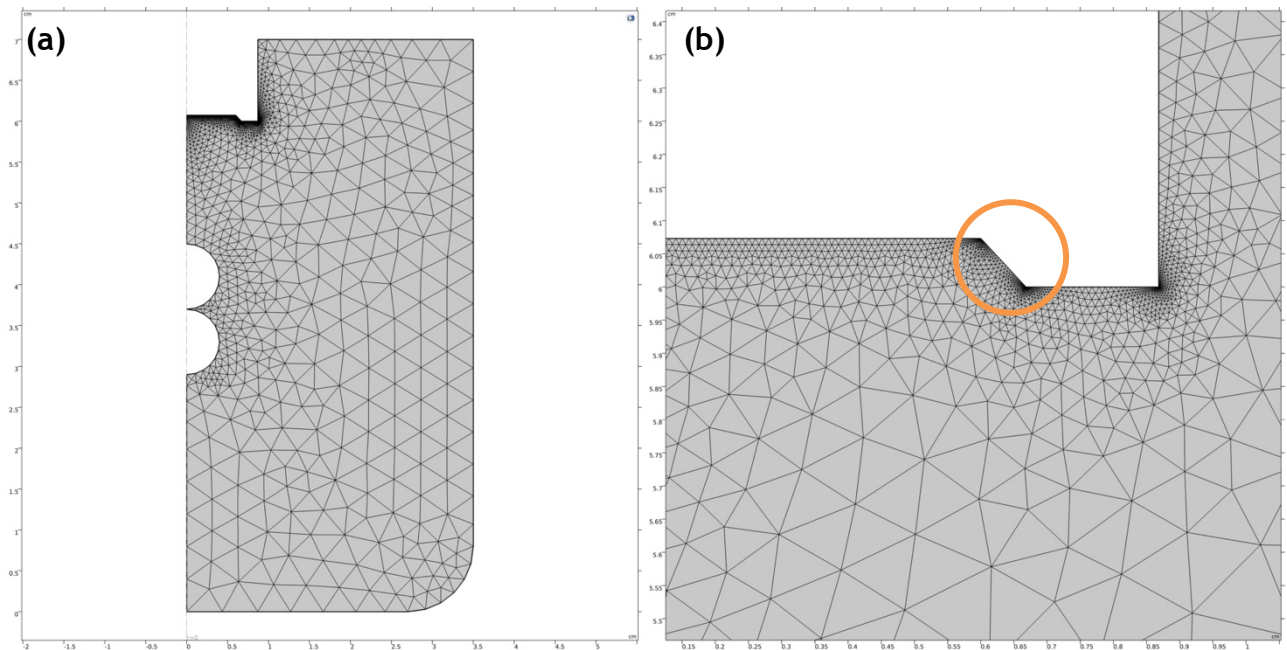


Figure 3. 6: (a) Mesh spacing of the 2-D axisymmetric RDE model domain. (b) Close view of the mesh around the cathode boundary and recess point (in circle), showing the transition from the domain mesh sizing to a much finer mesh around these areas.

is focused on the deposits formed on the cathode's surface, the mesh on the cathode boundary was set to being sufficiently fine. Special attention was given on the recess region at the border between the cathode and insulation surface at the RDE tip (indicated by the circle in [Figure 3.6-b](#)). Since this border is considered as a transition edge, the mesh there was generated to be really fine, even finer than that on the cathode surface in order to avoid any mesh deformation phenomena which could prevent the model from converging. The mesh developed for the 2-D axisymmetric RDE model included 3811 elements with a minimum element quality of 0.2605. This is translated into an average element quality of 0.8461.

It is important to mention here that, for all modelling studies discussed throughout this work, the final meshes were built through a trial-and-error approach. As long as the minimum element quality remained above 0.1, the mesh with the lowest number of elements to give reasonably fast solutions, while maintaining the average element

quality close to 1, was chosen. To confirm that the chosen mesh is actually the optimal one, finer and coarser, by 25 %, meshes were employed and the thickness profile graphs were observed; if the quality of these graphs was remaining the same and no additional information was provided, the mesh choice was confirmed. Systematic mesh sensitivity studies will be presented in detail in [Chapter 4](#).

3.2.3 Boundary and Initial Conditions Declaration - Mathematical Foundation

As it can be understood, boundary conditions are derived from the physics of the problem. Most commonly, electrochemical systems generate non-linear, complex problems which are not easily formulated. To minimise the complexity of the problems, phenomena like migration and ion diffusion were ignored and secondary current distribution was assumed to describe the system's kinetics.

Considering such simplifications being common, it is always more useful to focus on studying the behaviour of electrochemical systems and the functions that are used to describe the behaviour rather than the properties of the equations that might be chosen to define those functions. Consequently, potential theory, *i.e.*, the assumption that cell potential is solely governed by Laplace's equation (3.2), has always been an attractive approach to model an electrochemical problem:

$$\nabla^2 \varphi = 0 \quad [3.2]$$

where, $\nabla = i \frac{d}{dx} + j \frac{d}{dy} + k \frac{d}{dz}$ and φ is the local potential.

In that case, potential and current distributions are considered under the assumption that concentration is uniform throughout the domain (electrolyte volume). As long as the electrolyte's composition remains uniform, that approach can be applied both for the cases when electrode kinetics are taken into consideration as is done in secondary current distribution (SCD), as well as for the case of primary current distribution (PCD) when no kinetics are considered [6].

Taking it a step further from PCD when only the geometric characteristics of the electrochemical problem affect the calculations, SCD represents the results of more complex calculations taking place when slow electrode kinetics are taken into consideration and charge transfer is no longer neglected. In this case, the electrode's surface is polarised to accommodate the overpotential to drive the current. Since an additional hindrance to the reaction, which, in effect is the kinetic resistance at the electrode-electrolyte interface, the Laplace's equation solution is still possible but must include linear or logarithmic relations which are usually chosen to describe the relation between the surface overpotential and the potential derivative at the electrode.

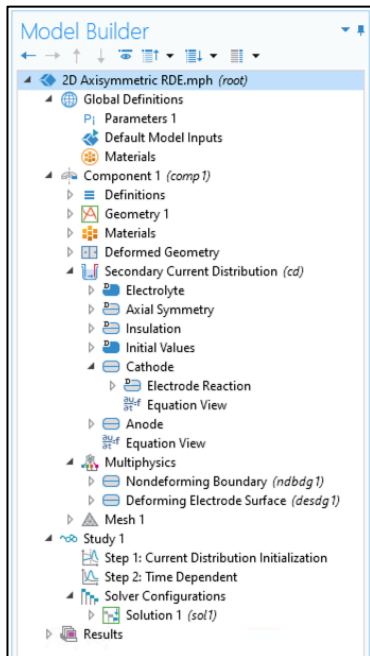


Figure 3. 7: Model Builder in COMSOL Multiphysics®

Following the mesh spacing of the domain, FEM is vitally dependent on the proper declaration of the problem's initial and boundary conditions. All boundary and initial conditions are declared within the software's *Model Builder* (Figure 3.7).

First the domains of interest are chosen. For the models discussed throughout this work, the electrolyte was the only studied domain (Figure 3.8-a). Within the SCD interface the electrolyte domain is solely characterised by the electrolyte conductivity which, for the nickel sulphamate electrolyte used in the RDE setup, was experimentally determined at an average value of $\sigma = 9.165 \text{ S/m}$, at $50 \text{ }^\circ\text{C}$.

Conductivity defines the dependence of the current on the potential gradient:

$$\nabla \cdot \mathbf{i}_l = Q_l, \mathbf{i}_l = -\sigma \nabla \varphi_l \quad [3.3]$$

where, \mathbf{i}_l is the current density vector in the electrolyte, Q_l the current source

(A/m^3) , φ_l the potential in the electrolyte (ionic) phase, and $\nabla = \mathbf{i} \frac{d}{dx} + \mathbf{j} \frac{d}{dy} + \mathbf{k} \frac{d}{dz}$.

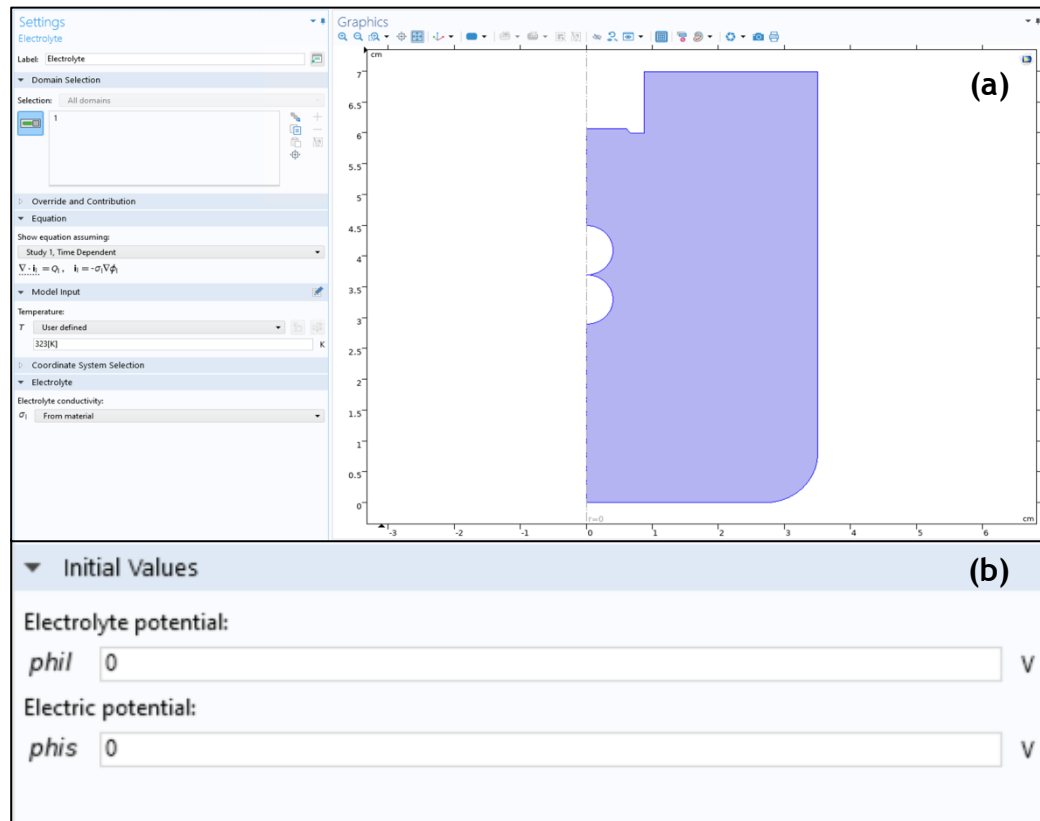


Figure 3. 8: (a) “Electrolyte” and (b) “Initial Values” nodes within the COMSOL Multiphysics® Model Builder. The domain equations are shown.

In the “Initial Values” node of the Model Builder (Figure 3.8-b), the user can define the starting values of the electrolyte potential (**phil**, *i.e.*, φ_l), as named in COMSOL Multiphysics®) and the electric (electrode) potential (**phis**, *i.e.*, φ_s), as named in COMSOL Multiphysics®). These values are simply starting guesses applied to the electrolyte domain, and they are mainly useful for stationary studies, providing a starting point for the solver. For time dependent studies, it is advisable to use a “Current Distribution Initialization” study step prior to the main “Time Dependent” study step. The “Current Distribution Initialization” step defines new values for the initial

values based on the primary assumption (fast kinetics). This sets the solver at a starting point closer to the solution, so that non-linearity in the kinetics do not cause convergence issues. For the purposes of this work **phil** and **phis** were set at the default 0 value and the “*Current Distribution Initialization*” study step was used to “guess” the initial values and provide the solver with an efficient starting point as working towards, easily achieved, convergence.

Moving forward, the “*Nondeforming Boundary*” and “*Deforming Boundary*” nodes are determined.

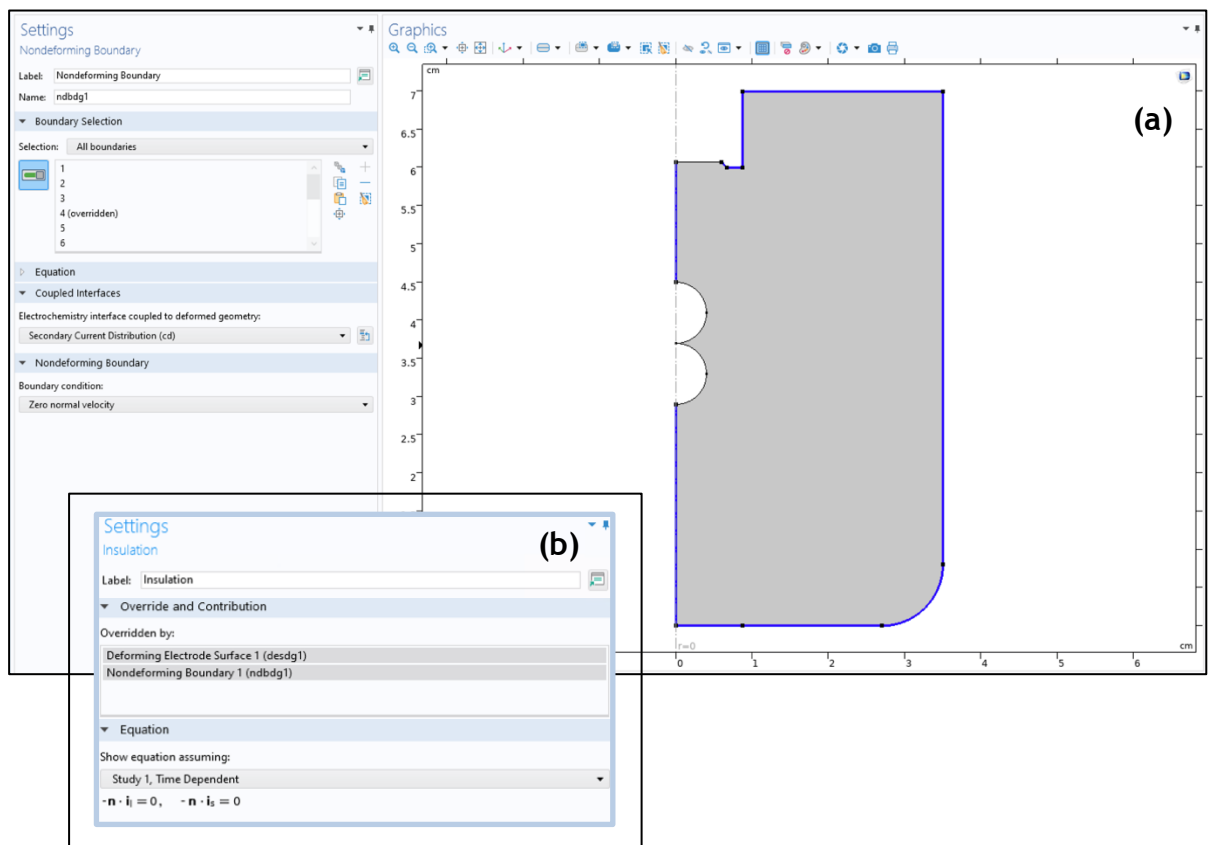


Figure 3. 9: (a) “*Nondeforming Boundary*” and (b) “*Insulation*” nodes within the COMSOL Multiphysics® *Model Builder*. The boundary equations are shown.

Non-deforming boundaries (Figure 3.9-a) include any non-conductive surface immersed in the electrolyte, cell/reactor walls, as well as auxiliary non-conductive tools (e.g., “masks”). Consequently, the “*Nondeforming Boundary*” node overrides the “*Insulation*” one which is governed by the principle that no current passes through these boundaries (Figure 3.9-b):

$$-\mathbf{n} \cdot \mathbf{i}_l = 0, -\mathbf{n} \cdot \mathbf{i}_s = 0 \quad [3.4]$$

where, \mathbf{i}_s is the current density vector at the electrode.

The “*Insulation*” node replaces the “*Nondeforming Boundary*” during stationary studies when geometry deformation is not studied since no boundary changes with time.

In time dependent studies like the one described here, the “*Deforming Boundary*”

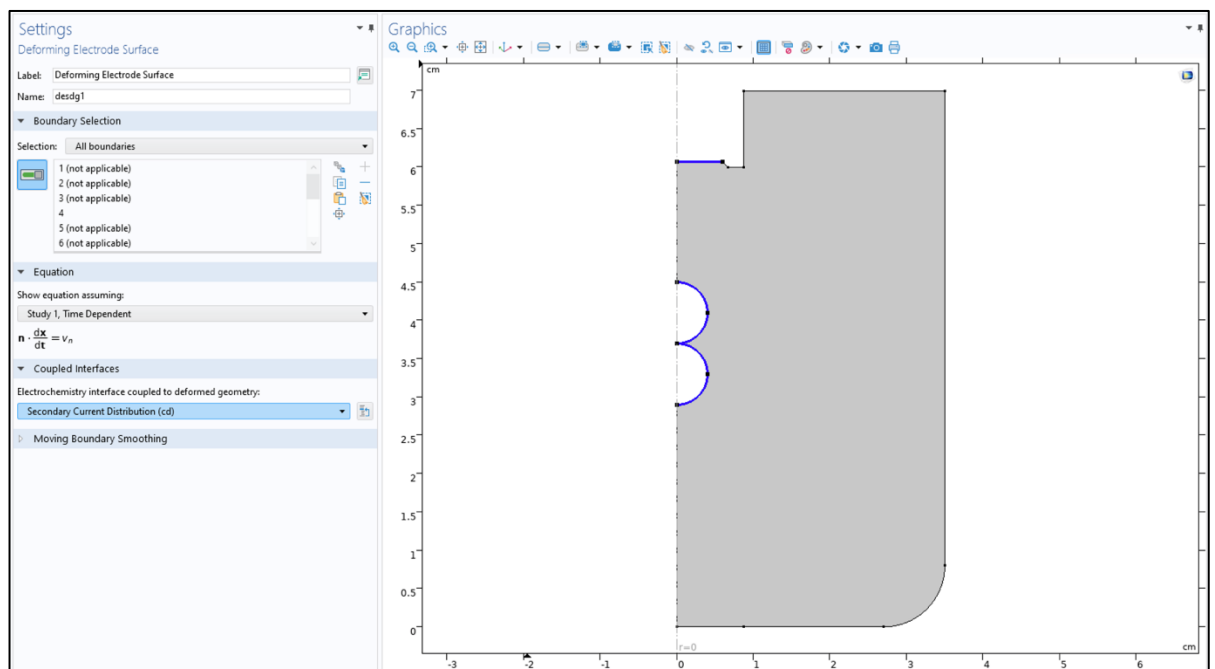


Figure 3. 10: “*Deforming Boundary*” node within the COMSOL Multiphysics® Model Builder. The boundary equations are shown.

node (Figure 3.10) reasonably includes the anode and cathode surfaces which are the boundaries that deform through time, as the deposition process progresses, and new layers of nickel are deposited on the mandrel.

The conditions at the electrode boundaries are declared in detail within the “Cathode” and “Anode” nodes (Figures 3.11-a & 3.11-b). The density and molar mass of the dissolving-depositing species (j) are the first that need to be set under these nodes. For nickel, which provides the dissolving-depositing species in the studied system, the density was set at $\rho_j = 8908 \text{ kg/m}^3$ and the molar mass at $Mr_j = 0.05869 \text{ kg/mol}$. For a specific reaction m , both these parameters assist in the determination of the resulting deposited layer thickness (s) and the electrode growth velocity (v_n), also taking into account any concentration ($C_{d,j}$) gradients that might appear:

$$\Delta s = \sum_j \frac{C_{d,j} - C_{d,j0}}{\rho_j / M_j} \quad [3.5]$$

and,

$$v_n = \sum_j \sum_m \frac{R_{d,j,m} M_j}{\rho_j} \quad [3.6]$$

where,

$$\frac{\partial C_{d,j}}{\partial t} = \sum_m R_{d,j,m} \quad [3.7]$$

with $R_{d,j,m}$ being the surface resistance ($\Omega \cdot m^2$) calculated automatically via the set conductivity (σ). The total current at the electrodes is calculated as the summation of all local currents ($i_{loc,m}$):

$$i_{total} = \sum_m i_{loc,m} + i_{dl} \quad [3.8]$$

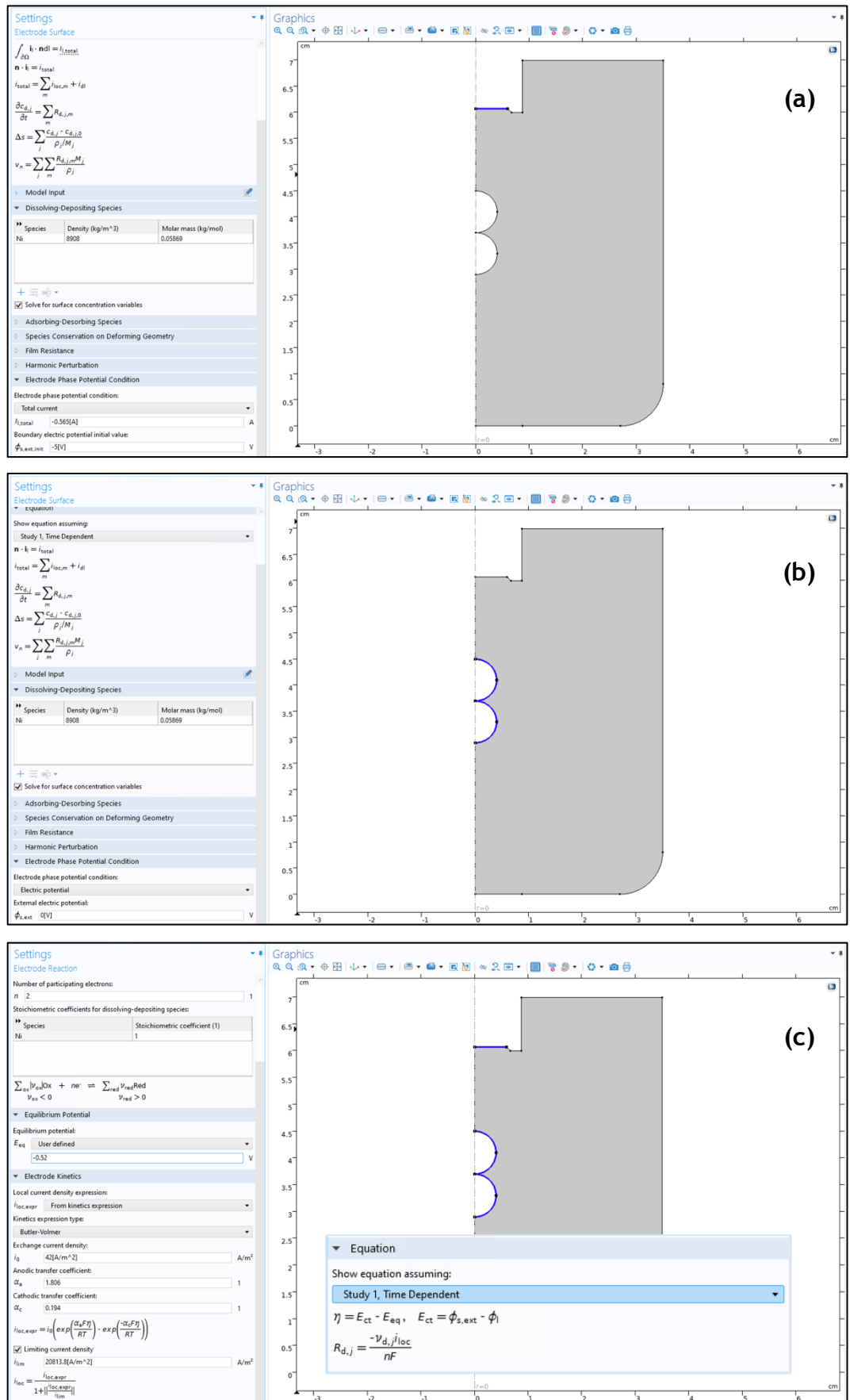


Figure 3. 11: (a) "Cathode" and (b) "Anode" nodes within the COMSOL Multiphysics® Model Builder. The boundary equations are shown. (c) The "Electrode Reaction" subnode appearing as part of both the "Cathode" and "Anode" nodes and including exactly the same information for both.

where, l is the electrode arc length and $i_{total} = n \cdot i_l$, $\int_{\partial\Omega} i_l \cdot n dl = I_{l,total}$ over the boundary Ω .

In this work, the Butler-Volmer equation (3.9) was used to mathematically describe the physics of the model(s) investigated.

$$i_{loc,m} = i_{0,m} \left(e^{\frac{\alpha_{a,m} F \eta_m}{RT}} - e^{\frac{-\alpha_{c,m} F \eta_m}{RT}} \right) \quad [3.9]$$

where, for a given reaction m , $i_{0,m}$ is the exchange current density, $\alpha_{a,m}$ and $\alpha_{c,m}$ are the anodic and cathodic charge transfer coefficients and, η_m is the activation overpotential. $F = 96485.3 \text{ C/mol}$ is the Faraday's constant, R is the universal gas constant and T the temperature under which the problem is studied. The term $e^{\frac{\alpha_{a,m} F \eta_m}{RT}}$ is the anodic component of the B-V equation, and $e^{\frac{-\alpha_{c,m} F \eta_m}{RT}}$ is the cathodic component.

This mathematical model, amongst others, relates the surface overpotential to the reaction rate, which is the first fundamental information someone should know about any reaction(s) taking place on the electrode(s) surfaces. Since the reaction rate is affected by the current density, the nature and quality of the electrode surface, the electrolyte, and the electrode potential, it is obvious that the correct determination of the model's initial values and boundary conditions are of the utmost importance for the credibility of calculated values.

In SCD the concept of the activation overpotential (η) is introduced. As soon as electrode kinetics are introduced in the models, the potential of the electrode in question differs from the equilibrium value due to resistance attributed to the rate of the electrolysis reaction. This difference between the actual potential and that at equilibrium is the activation overpotential (η), which, in reality, drives the electrode reaction. Within *COMSOL Multiphysics*® the inclusion of activation overpotential is handled in the following fashion. The current is related to the potential at the electrode surface, φ_s , by

$$i_s = -\sigma_s \nabla \varphi_s \quad [3.10]$$

and the current is related to the potential in the electrolyte, φ_l , by

$$i_l = -\sigma_l \nabla \varphi_l \quad [3.11]$$

Based on the overpotential, the electrolyte-electrode interface will be described by equation (3.12):

$$\eta_m = \varphi_s - \varphi_l - E_{eq,m} \quad [3.12]$$

where, $E_{eq,m}$ is the equilibrium potential for the reaction m .

The SCD interface uses relations between current density and overpotential at each location to solve any given problem. As it was mentioned before, the Butler-Volmer equation (3.9) is one of these equations and is included as an option in *COMSOL Multiphysics*[®].

In essence, Equation 3.9 provides a summation of cathodic and anodic components of the dynamic electrode interface and provides an overpotential value which corresponds to an overall anodic or cathodic reaction. In this regard, for nickel deposition or dissolution at the cathode and anode boundaries, respectively, using the B-V expression shown in Equation 3.9, one would compute positive (anodic) or negative (cathodic) values based on the overpotential experienced by it. Therefore, the B-V equation is applied to both the anode and cathode boundaries.

Actually, the exponential terms in the bracket in Equation 3.9 represent anodic and cathodic parts of a single reaction at an electrode for a “fast” electrode reaction, whose limitations are discussed later. A multi-step reaction, such as nickel deposition [7], is more difficult to fit into a simple expression such as Equation 3.9. In addition, the term outside the bracket on the right-hand side is dependent on concentration of the reactant. Parameters such as $\alpha_{c,m}$ and $\alpha_{a,m}$, again, are more difficult to ascertain if there are adsorbents, passivation or other parallel reactions occurring at the surface. However, for simplicity and validation, one can use an expression such as Equation 3.9, and explore how well it can describe the process.

Before the model development is discussed in detail in the following section, it is worth commenting on the fact that, for this work, the mass transport phenomena developing during a metal deposition process were not taken into account. Instead, secondary current distribution was assumed to describe the problem. Although in many cases tertiary current distribution analysis can be employed, by choosing a *Ni* electroforming system, where applied current is approximately 10 % of that dictated by mass transfer limitations, one is able to scrutinise and assess a system which should be under kinetic control. Also, the use of high-concentration electrolytes and the vigorous mixing of the electrolytic solutions are two more reasons for one to follow such an approach.

This approach is also compatible with the *COMSOL Multiphysics*[®] proposed use of each one of the three current distribution interfaces available in the software [8], providing additional confidence regarding the adequacy of the SCD interface to describe this problem's physics. In any case, it is important to stress out that these studies are expected to help towards the process's optimisation by, hopefully, providing an insight into complex phenomena controlled by reactor geometry and reaction kinetics. Since TCD may not provide additional information during reactor scaling-up and geometry optimisation studies, which are the main point of focus of the work presented here, the models to follow are SCD cases. Preliminary TCD studies will be discussed in [Chapter 6](#) for consistency and comparison reasons.

A Note on Convergence

As a general description, in *COMSOL Multiphysics*[®] a time-dependent solver computes a solution to a nonlinear system of equations at each timestep applying a set of iterative techniques based on Newton's method. Such solving techniques assess a function and its derivative at all timesteps. This derivative is known as the *Jacobian*, and it requires high computational power to be determined. To overcome this issue the software always tries to minimise re-assessing the *Jacobian* each time. In

case convergence cannot be reached, it reduces the user-defined timestep size and tries to compute the solution again. This is an efficient approach for the cases when solution fields change rapidly with time.

When *COMSOL Multiphysics*[®] default “Constant (Newton)” nonlinear method is applied, non-convergence issues can be addressed by updating the *Jacobian* on every iteration that the nonlinear solver takes as it tries to compute the solution at each timestep. If this is not enough, in case the problem is so strongly nonlinear that the “Constant (Newton)” method cannot still converge, there are other settings a user can modify; increase the “Maximum number of iterations” from the default value of 4 to 25 or higher, or even adjust the “Tolerance factor” to a more relaxed one. If the model is still not converging, the “Constant (Newton)” method can be changed to “Automatic (Newton)” which updates the *Jacobian* and uses a dynamic damping term. This method will require more computational power. As a last resort, the “Automatic highly nonlinear (Newton)” method can also be applied. This approach will be slower but more likely to converge since it starts with higher damping. For the purposes of this work the “Automatic (Newton)” nonlinear method was applied, with a maximum number of iterations at 4 and tolerance factor at 1.

3.2.4 Implementation & Assessment

The conditions used for both the RDE, and electroforming reactor models were chosen based on the practical experiments conducted in the laboratory using the RDE (0.2 L) setup presented in [Chapter 2](#). Linear sweep voltammetry experiments allowed the determination of the system’s electrochemical parameters which are needed as input parameters under the “*Electrode Reaction*” sub-nodes in the software ([Table 3.2](#)).

However, one model parameter remained to be determined before any results were obtained, the equilibrium potential ($E_{eq,Ni}$) (refer to [Figure 3.11-c](#)), needed for the calculation of overpotential according to [Equation 3.12](#). The theoretical value for nickel is $E_{eq,Ni} = -0.26 V$. However, our laboratory data shown in [Figure 2.8](#), suggest

slow nickel reduction kinetics, with a large overvoltage ($E_{eq,Ni} \equiv E_{rev} = -0.82 V$) before any current is observed.

Since it has been proposed that the *Ni* reduction reaction occurs through a multiple-step mechanism (Table 1.2), of which the rate determining step (RDS) is Equation 1.2 [7], it is difficult to incorporate electrode kinetics which depend on the number of surface sites, when there are three electrode reactions, or the surface sites change with electrode polarisation. Therefore, for model simplification and convenience, one has to only consider the overall reaction shown in Table 3.2.

Table 3. 2: Model physical and (electro)chemical input parameters.

	Parameter	Model	Comments
Electrolyte	Temperature	323 K	User defined (50°C)
	Electrolyte conductivity	0.9165 S/dm	From Experimental Data
Electrodes	Dissolving-depositing species	$M_{r_{Ni}} = 0.05869 \text{ kg/mol}$ $\rho = 8.908 \text{ kg/l}$	From literature
	Number of participating electrons	$n = 2$	$Ni \rightarrow Ni^{2+} + 2e^{-}$
	Stoichiometric coefficients for dissolving-depositing species	1	$Ni \rightarrow Ni^{2+} + 2e^{-}$
	Equilibrium potential	$E_{eq} = -0.52 V$	Reversible Potential from Experimental Data
	Exchange current density	$i_{0,m} = 0.42 \text{ A/dm}^2$	From Experimental Data
	Anodic transfer coefficient	$\alpha_{a,m} = 1.806$	From Experimental Data
	Cathodic transfer coefficient	$\alpha_{c,m} = 0.194$	From Experimental Data
Limiting Current Density	$i_{lim,m} = 208.138 \text{ A/dm}^2$	From Experimental Data	

Experimentation has shown that Tafel slopes range between 0.090 V/dec and 0.200 V/dec [9], which lends some support to the above proposition. However, including such complex kinetics in standard *COMSOL Multiphysics*[®] is non-trivial because the system allows for simple Butler-Volmer type of kinetics. To describe the actual multi-step mechanism as closely as possible, an appropriate $E_{eq,Ni}$ value should be determined.

To do so, the theoretical current density-potential (B-V) curve using the parameters extracted from the experimental polarisation curve in Figure 2.8, and which are presented in Table 3.2, was constructed. Figure 3.12 shows the overlap of the theoretical and experimental B-V curves.

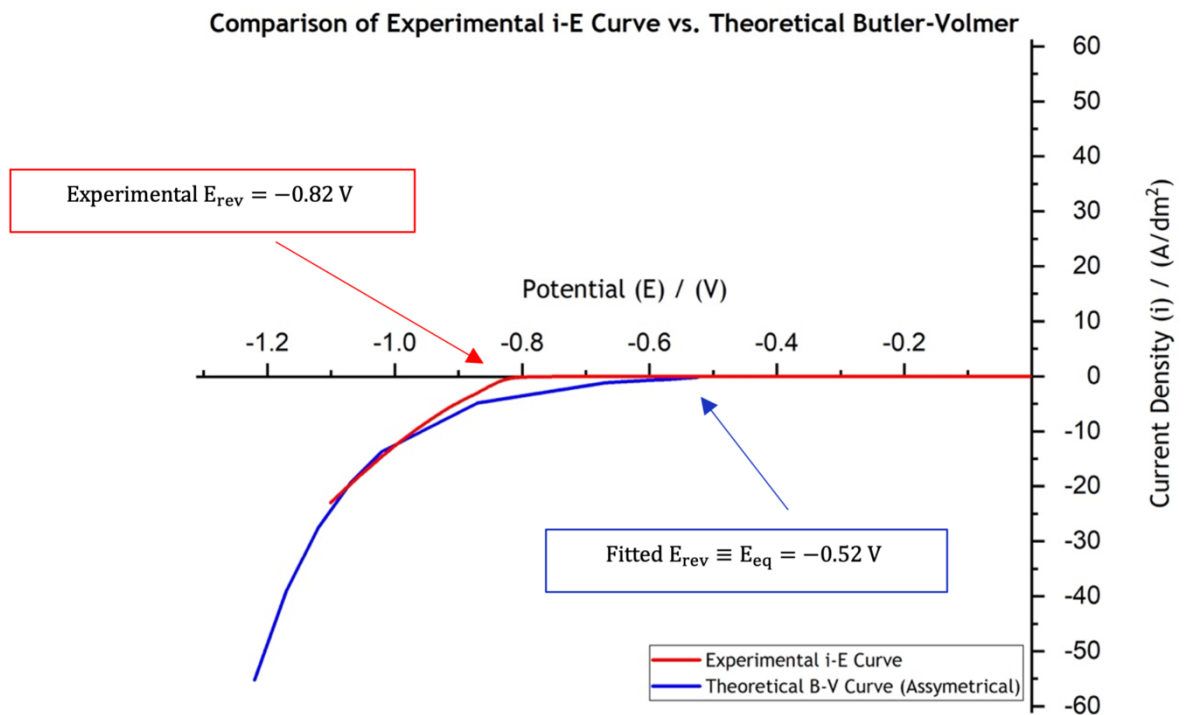


Figure 3. 12: Comparison of the experimental current density - potential curve, constructed based on data collected in the laboratory using linear sweep voltammetry (red curve), against the theoretical B-V curve for use in nickel electroforming models, “shifted” B-V curve (blue line). The corresponding linear sweep voltammetry was conducted with a scan rate of 0.005 V/s , at 50 °C and under agitation at 1500 rpm . The kinetic parameters used to plot the theoretical B-V curve were the ones presented in Table 3.2.

One finds that the experimental data fit in the region 20 mA/cm^2 to 50 mA/cm^2 ($2 - 5 \text{ ASD}$), which is the current region where nickel electroforming is performed in industry.

One important difference between the experimental data (red curve) and the fitted curve (blue one) is the large inactive region extending between 0 and -0.82 V for the experimental curve and between 0 and -0.52 V for the fitted theoretical B-V curve. In effect, a reversible potential used to fit the current potential data is -0.52 V . This value, which was subsequently used in the model, is different from the nickel theoretical thermodynamic value of $E_{\text{eq,Ni}} = -0.26 \text{ V}$. Although this difference may not incorporate an error in computation of current values, it will leave an uncompensated potential drop of 0.3 V , which will appear in lower values of cell potential in the computations to follow.

A second difference between the experimental data is observed at current densities lower or higher than the region where the data was used to fit the current. However, since most electroforming experiments are carried out at current densities in the region of interest where theoretical and experimental data match, the computed values should provide reasonable values for $i_{\text{eq,Ni}}$ distribution across the electrode surface.

It is important to mention here that some models on nickel plating [10] [11] include the hydrogen evolution reaction to compensate for such deviations between experimental and theoretical data. However, this is not a requirement for electroforming models because hydrogen evolution constitutes less than 1 % of the applied current. This means that even if the hydrogen reduction reaction was included in the model, experimental B-V parameters could not be collected, and hence, the validity of hydrogen evolution could never be tested.

Having established all boundary and initial conditions, the first results were obtained for the 2-D axisymmetric RDE model. The simulation was designed to represent prac-

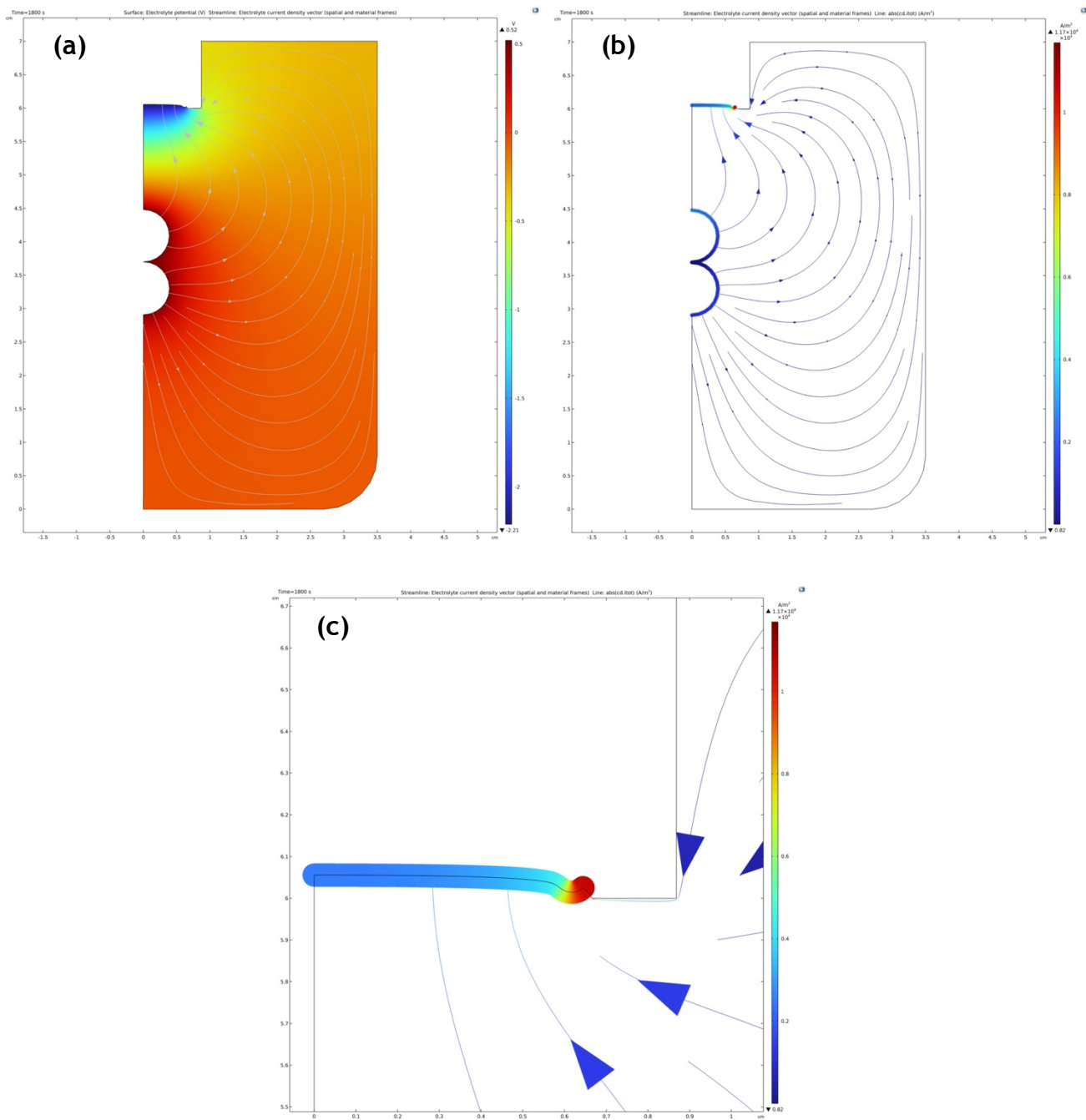


Figure 3. 13: 2-D representation of (a) the potential distribution, (b) the current distribution in the electrolytic volume and (c) the current distribution on the cathode surface. The results simulate potential and current distributions after 1800 s at 50 °C. The current streamlines are also shown in figure (b) emanating from the anode (at higher potential) and being collected at the cathode (at lower potential). The vertical distance between the electrodes' geometrical centres is also noted in figure (a) alongside the local average cathode surface potential and current after the final converged step.

-tical deposition experiments, at 50 °C, for 1800 s, under a cell voltage of 5 V ($\varphi_{s,ext,cathode} = -5\text{ V}$, $\varphi_{s,ext,anode} = 0\text{ V}$) and a current density of 50 A/dm² ($I_{l,total} = -0.565\text{ A}$). Deposition at that high current density using the RDE setup allowed for a thick enough deposit to be produced, sectioned, mounted in resin, and measured under the microscope without deforming (refer to [Figure 2.12](#)).

[Figure 3.13](#) shows the current and potential distribution results for models after the simulation had converged. The visualisation in [Figures 3.13-a & 3.13-b](#) allows one to check the potential distribution in the domain and near the electrode surface, as well as the current lines travelling to the electrode surface. The potential range within the electrolyte was simulated at $-2.21\text{ V} \leftrightarrow 0.52\text{ V}$. The current lines can be seen to bend away from the insulating cell walls since no current can pass through them, thereby they move towards the cathode surface, through the different lengths that they have to travel as they move through the electrolyte.

As this is a time-dependent model (due to the surface evolution of the formed electrode, the cathode surface changes with time as new layers of nickel are deposited), it was set to record a solution every 600 s therefore, four time-steps were set. The model was solved to provide convergent solutions varying between $t = 0$ (for a non-evolved surface) and the last for $t = 1800\text{ s}$ (for an evolved surface where a deposit was formed), reflecting deposition for 1800 s, similar to the process carried out in the laboratory.

In this regard, after the final converged time step, the local average cathode surface potential was determined at $\varphi_{s,cath\ aver} = -3.2810\text{ V}$. The calculated total current density values in the domain range from 0.82 A/m^2 to $1.17 \times 10^8\text{ A/m}^2$ as shown in [Figure 3.13-c](#). The local average cathode surface current density was determined at $i_{s,cath\ aver} = -4218.1\text{ A/m}^2$ ($i_{s,cath\ aver} = -42.181\text{ ASD}$). Interestingly, for $t_1 = 0\text{ s}$ the local average cathode surface current density is calculated at $i_{s,cath\ aver}^1 = -4995.7\text{ A/m}^2$ ($i_{s,cath\ aver}^1 = -49.957\text{ ASD}$), alongside a local average cathode surface potential at $\varphi_{s,cath\ aver}^1 = -3.6172\text{ V}$. As the simulation progresses in time, both

these values increase (become less negative) as shown in Table 3.3. These values changing is to be expected since, with time, the system itself changes. Even though the process starts with nickel depositing on stainless-steel, as the new nickel layers start depositing on the mandrel, the cathode surface changes (or “deforms”, as defined by *COMSOL Multiphysics*[®]), with the process evolving into deposition of nickel on nickel.

Moving forward, Figure 3.14-a presents the total electrode thickness change (reflecting the current distribution) simulated by the model. Figure 3.14-b presents the total electrode thickness change at all four converged time steps ($t_1 = 0\text{ s}$, $t_2 = 600\text{ s}$, $t_3 = 1200\text{ s}$, $t_4 = 1800\text{ s}$). In general, the current is predicted to be higher at the edges than at the centre of the disk as would be expected [12]. Consequently, a thicker thickness profile was predicted at the edges.

Table 3. 3: Local average cathode surface potential and current density at every converging step

Time Step	Local Average Cathode Surface Potential ($\varphi_{s,cath\ aver}$)	Local Average Cathode Surface Current Density ($i_{s,cath\ aver}$)
$t = 0\text{ s}$	-3.6172 V	-4995.4 A/m ²
$t = 600\text{ s}$	-3.5055 V	-4722.8 A/m ²
$t = 1200\text{ s}$	-3.3932 V	-4461.4 A/m ²
$t = 1800\text{ s}$	-3.2810 V	-4218.1 A/m ²

The model shows that the overall thickness distribution (reflecting the current distribution) follows the usual non-uniform current distribution as expected for an RDE; however, the low current at the insulator-RDE edge is caused by the recess due to the shadowing effect that the latter imposes [13].

For validation purposes, the experimentally achieved deposit thickness was measured by sectioning the sample and then mounting it in resin. The RDE deposit was

only sectioned along its diameter due to its very small size. The final specimen, which is shown in [Figure 3.15](#), was placed under a *Yenway* optical microscope, and studied at a $\times 20$ magnification.

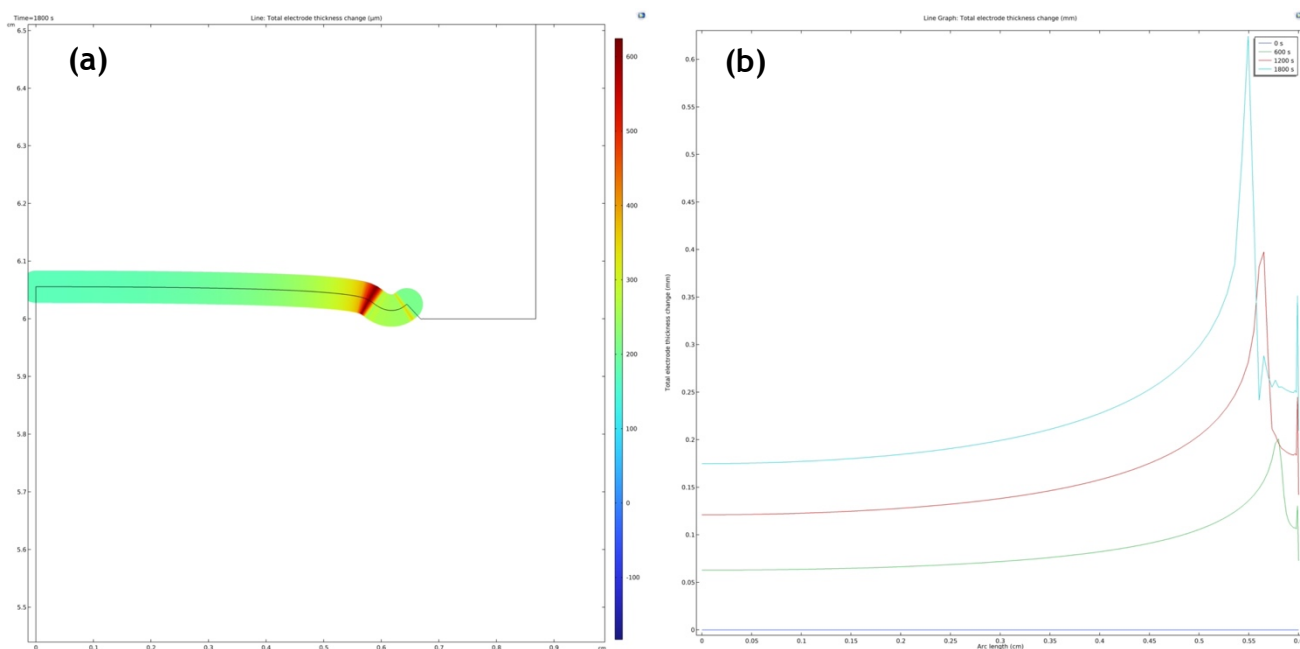


Figure 3. 14: (a) 2-D representation of the thickness distribution on the cathode surface. The results simulate the current distribution after 1800 s at 50 °C. (b) Total cathode thickness change with time. The thickness profiles at the four converged simulation steps are shown.

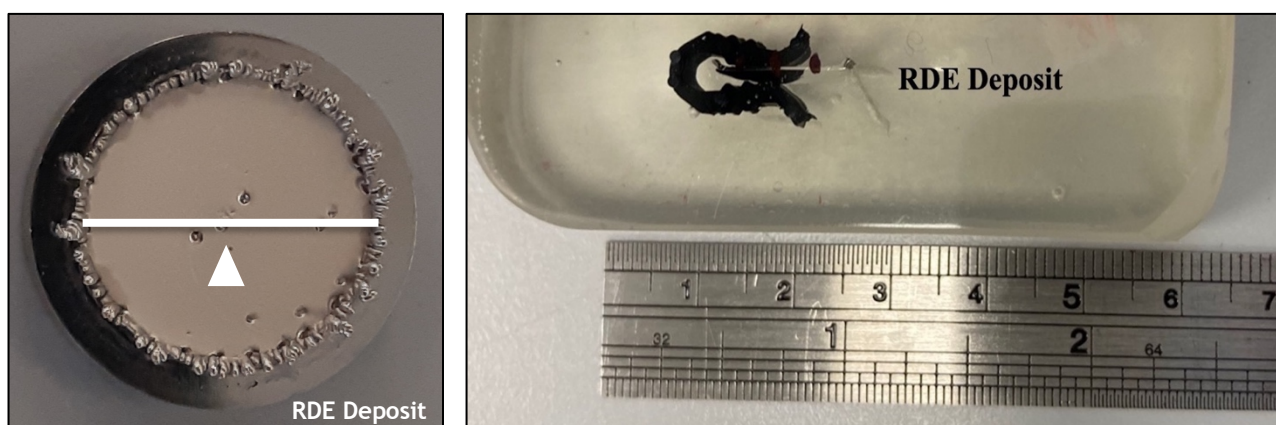


Figure 3. 15: Sectioning of the RDE nickel disk deposit for thickness measurements. The white arrows indicate the side face of the section measured under the microscope, following this being mounted in a resin specimen.

Figure 3.16 presents a comparison between the experimentally achieved and simulated thickness profile. Validation experiments reveal that the 2-D axisymmetric model slightly under-predicts thickness values compared to the experimentally achieved ones. The average predicted thickness was calculated at $\sim 0.22 \text{ mm}$ while the average experimental thickness was measured at $\sim 0.24 \text{ mm}$. These values refer to thicknesses of the 83 % of the arc length (from the centre, 0, up to 0.5 cm), excluding the leading edges where dendrites are formed. This exclusion of the leading edge, where dendrites are formed, during the experimental measurements is the reason why the experimental points do not vary while the modelling results do. The model cannot distinguish between the leading edge and the rest of the

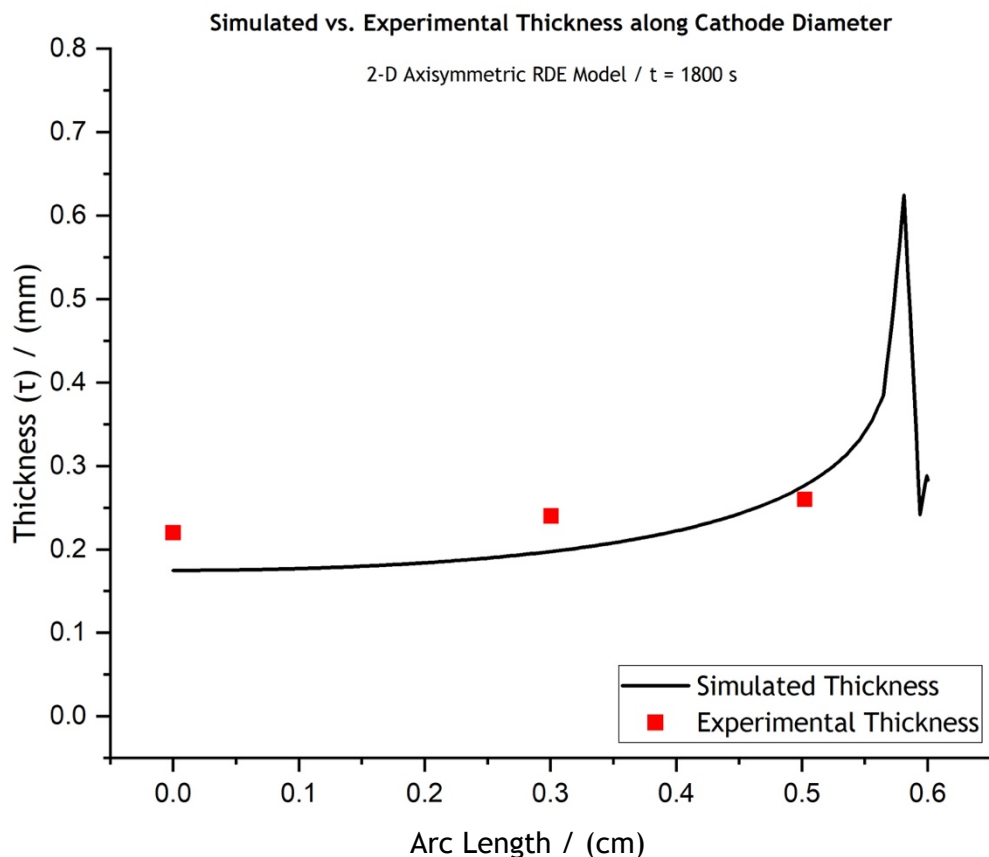


Figure 3. 16: Comparative graph of the experimentally achieved and the simulated thickness profiles for the RDE setup. The RDE deposit was produced at -5 V and -0.565 A , for 1800 s . These conditions allowed for a thick enough deposit to be sectioned, mounted in resin, and measured under the microscope without deforming. The arc length depicted corresponds to the RDE disk radius.

cathode surface therefore the modelling results always simulate the high current values accumulated at the circumference and, consequently, the higher thicknesses observed there due to dendrites being formed.

As a general comment, the experimental measurements seemed to validate the 2-D axisymmetric RDE model. However, as mentioned before, the RDE setup used for the practical experiments is not symmetrical therefore, even though it provided a good first insight into the modelling of the nickel electroforming process, the 2-D axisymmetric model would not be the most complete approach.

2-D models better describe the cases when problem physics only change in one direction. For the cases when physics changes occur in more than one direction, as happens in the investigated electrodeposition problem, 3-D models are expected to simulate the process more accurately. Consequently, the development of a 3-D RDE model followed.

A Note on the Simulation of Agitation Conditions

As it will be evident in the sections and chapters to follow, all modelling studies simulated the electroforming process under stagnant conditions. Neither the rotation speed of the RDE nor the electrolyte agitation in the prototype electroforming tank were taken into account for the simulations of this work. This was solely a limitation of the *COMSOL Multiphysics*[®] license provided for this project.

To simulate the rotation of the RDE, or the electrolyte agitation provided in the prototype tank by eductors, interfaces and features within the *Computational Fluid Dynamics* (CFD) module of *COMSOL Multiphysics*[®] were required. However, the *COMSOL Multiphysics*[®] license provided included only the *Electrodeposition* module while the cost for acquiring the *Computational Fluid Dynamics* one was prohibitive in the context of this project. For the sake of argument, a combination of alternative interfaces included in the available license, such as the *Laminar Flow* and *Transport*

of *Diluted Species* ones, might have provided an approximation of the results that the CFD module could return. However, it was decided that such alternatives would not be explored since just an approximation of actual fluid flow studies would not offer additional information useful in the context of this project, while the time needed to successfully develop such models would have required other, main tasks of the work to be neglected or abandoned.

In practice, agitation is mainly applied for the electrolyte concentration to remain as uniform as possible throughout the process and predominantly affects the potential and current distributions far from the cathode surface. Therefore, and since, for both the secondary current distribution (SCD) and the primary current distribution (PCD) cases, the software assumes that concentration is uniform throughout the electrolyte volume (refer to [Section 3.2.3](#)), it was decided that it is not of importance to simulate the agitation conditions for the purposes of this project. For the few tertiary current distribution (TCD) examples presented in some chapters, the tertiary behaviour of the ionic species involved is predominantly governed by the species' diffusion coefficients, allowing for agitation conditions to be neglected once more.

3.3 The 3-D RDE Model

A time-dependent 3-D model of the recessed rotating disk electrode (RDE), laboratory-scale (0.2 L), system was developed within the *Electrodeposition* module of *COMSOL Multiphysics*[®]. The discretised 3-D geometry is shown in [Figure 3.17](#), including 17255 elements with minimum element quality of 0.2149 and an average element quality of 0.652. The parameters characterising the mesh built for the 2-D axisymmetric are presented in [Table 3.4](#).

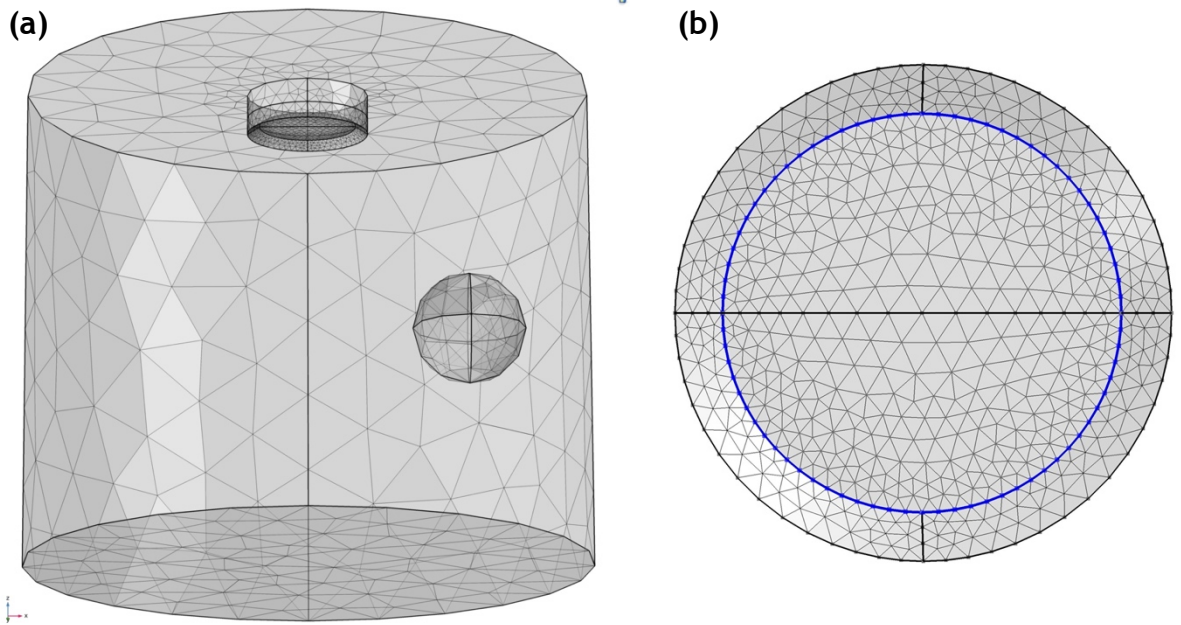


Figure 3. 17: (a) Mesh spacing of the 3-D RDE geometry domain. (b) The blue line highlights the “recess”, transition edge of the stainless-steel disk electrode in the RDE model.

Table 3. 4: General and boundary, user-defined, element size parameters for the 2-D axisymmetric RDE model

Element Size Parameters	3-D RDE Model			
	General	Cathode	Anode	Recess
Maximum Element Size (mm)	10	3	10	0.5
Minimum Element Size (mm)	0.5	–	–	–
Maximum Element Growth Rate	1.5	1.1	–	–

The boundary and initial conditions are declared through the exact same [Equations 3.3-3.12](#) presented in [Section 3.2](#). The only difference lies in the fact that the total

current at the electrodes, $I_{l,total} = \int_{\partial\Omega} \mathbf{i}_l \cdot \mathbf{n} dS$ is now reasonably calculated over the surface (dS) of the boundary Ω , instead over its length (l) which was the case in the 2-D axisymmetric model (refer to [Figure 3.11-a](#)). The 3-D model was also validated against practical experiments. The results are presented as part of the scaling-up studies in [Chapter 4](#).

The limitations experienced for the 2-D model do not suggest that it is worse than a 3-D one. 2-D models can provide sufficiently accurate results in a fraction of the time that their 3-D version would. Therefore, they play a very important role during preliminary studies of any first modelling attempt. At the same time, they might be chosen as the most time-effective modelling solutions in the fast-pace industrial environment. However, since the 3-D models would provide a more reasonable approach for problems when physics evolve over time throughout a volume, e.g., any electrodeposition problem, only 3-D modelling studies will be presented in the following chapters of this thesis.

3.4 Conclusions

COMSOL Multiphysics[®] was used to develop a 2-D axisymmetric model of the laboratory rotating disk electrode electrodeposition system. The model was built to simulate a galvanostatically controlled process, the current at the cathode was determined, and the deposit thickness was calculated at each converged time step. For simplification, secondary current distribution was assumed to describe the system's kinetics and the electrode reactions were chosen to be of Butler-Volmer type.

The simulation was designed to represent practical deposition experiments, at 50 °C, for 1800 s, under a cell voltage of 5 V ($\varphi_{s,ext,cathode} = -5 V$, $\varphi_{s,ext,anode} = 0 V$) and a current density of 50 A/dm² ($I_{l,total} = -0.565 A$). The potential range in the electrolytic domain was simulated at $-2.21 V \leftrightarrow 0.52 V$, while the calculated total current density values vary between 0.82 A/m² and $1.17 \times 10^8 A/m^2$ throughout the electrolyte. At the final converged time step, the local average cathode surface potential was determined at $\varphi_{s,cath\ aver} = -3.2810 V$ and the local average cathode surface current density at $i_{s,cath\ aver} = -4218.1 A/m^2$ ($i_{s,cath\ aver} = -42.181 ASD$). It was observed that these values change as the electrodeposition system evolves with time. The model confirmed that the overall thickness distribution follows the non-uniform current distribution. When validated against practical experiments, it was found that the 2-D axisymmetric model slightly under-predicts the deposit thickness value which was calculated at $\sim 0.22 mm$, while the average experimental one was determined at $\sim 0.24 mm$. Nevertheless, it was confirmed that 2-D models can provide sufficiently accurate results while being time-effective modelling solutions.

Following the 2-D model's validation, and in order to provide a more complete approach to the nickel deposition problem under investigation, a 3-D model was developed using the exact same input parameters and boundary conditions. The 3-D model's validation studies will be presented in the next chapter.

References

- [1] "Research Computing for the West of Scotland," (Managed by) University of Strathclyde, [Online]. Available: <https://www.archie-west.ac.uk/>. [Accessed 02 August 2021].
- [2] J. N. Reddy, *An introduction to the Finite Element Method*, Boston: McGraw-Hill Education, 2005.
- [3] D. Pepper and J. Heinrich, *The finite element method: basic concepts and applications*, Boca Raton: Taylor & Francis, 2005.
- [4] M. Berggren, *A Brief Introduction to the Finite Element Method*, Umeå: Department of Computing Science, Umeå University, 2012.
- [5] "Mesh Element Quality and Size," [Online]. Available: https://doc.comsol.com/5.5/doc/com.comsol.help.comsol/comsol_ref_mesh.15.18.html. [Accessed 11 01 2022].
- [6] J. Newman and K. E. Thomas-Alyea, *Electrochemical Systems*, vol. 3rd ed., Hoboken, NJ: John Wiley & Sons Inc., 2004, pp. 419-458.
- [7] S. Roy and E. Andreou, "Electroforming in the Industry 4.0 Era," *Current Opinion in Electrochemistry*, vol. 20, p. 108-115, 2020.
- [8] M. Pfaffe, "COMSOL Blog: Which Current Distribution Interface Do I Use?," COMSOL Multiphysics, 10 February 2014. [Online]. Available: <https://www.comsol.com/blogs/current-distribution-interface-use/>. [Accessed 19 May 2021].
- [9] Y. Tsuru, M. Nomura and F. R. Foulkes, "Effects of boric acid on hydrogen evolution and internal stress in films deposited from a nickel sulfamate bath," *Journal of Applied Electrochemistry*, vol. 32, pp. 629-634, 2002.
- [10] R. Y. Ying, P. K. Ng, Z. Mao and R. E. White, "Electrodeposition of copper-nickel alloys from citrate solutions on a rotating disk electrode: II . Mathematical modeling," *Journal of the Electrochemical Society*, vol. 135, p. 2964, 1988.
- [11] S. Hessami and C. W. Tobias, "A mathematical model for anomalous codeposition of nickel-iron on a rotating disk electrode," *Journal of the Electrochemical Society*, vol. 136, p. 3611, 1989.
- [12] E. Andreou and S. Roy, "Modelling the electroforming process: significance and challenges," *Transactions of the IMF*, 2021.

- [13] T. Dinan, "Experimental Investigation of the Current Distribution on a Recessed Rotating Disk Electrode," *Journal of the Electrochemical Society*, vol. 138, p. 2947, 1991.

Chapter 4: Results on Modelling the Scaling-Up of the Nickel Electroforming Process

4.1 Introduction

Most of the studies discussed in [Chapter 1](#), as well as the models presented in [Chapter 3](#), refer to investigations that were conducted in the laboratory-scale. However, as it has already been mentioned, the main focus of this project has been the optimisation and simulation of the nickel electroforming for aerospace applications. Therefore, it is important to highlight the need for cautious adaptation of previous findings to the inherent characteristics of large-scale additive manufacturing. To provide just a couple of examples, in these cases, it should be kept in mind that geometry sensitivity studies cannot be focused on simulating current distribution and/or mass transport phenomena for close electrode positions, as it is usually the case in laboratory-scale studies. Aerospace industry protocols determine the closest position that two electrodes could be placed at therefore, any effort to simulate real close electrode positions would not be of any use to industry.

However, it would be very useful, for example, to determine whether the anode position with reference to the cathode is “irrelevant” to the model. On another, rather dividing aspect, the need, or not, of modelling hydrogen evolution and tertiary current distribution should be considered cautiously. For one, even though specific processes (*e.g.*, copper deposition) might easily result being affected by hydrogen evolution, this may not be the case for electroforming. In industry, nickel electroforming at currents between 5 – 20 ASD, using 100 L tanks under agitation, may be adequately described by SCD. In simulating such a process, therefore, the inherent characteristics of the system need to be considered to allow for comprehensive

and informed modelling.

Approaching the issue from such a perspective and utilising the power of numerical analysis and the increasingly available computational resources, modelling the scale-up of an electroforming process could be used for making well-educated decisions on the limitations of an industrial-scale electroforming process. This would enable one to visualise the process conditions needed to obtain a particular electroform. A second consideration for such modelling is the availability of commercial software which can be implemented for an industrial process, and the limitations of such modelling tools.

When it comes to scale-up modelling of processes with industrial interest, modellers should be able to comprehensively determine the way in which a model's input parameters, geometric characteristics, and assumed physics, might be affected as the scale of a simulation increases. The inclusion of too many fitting parameters confounds engineering information, such as if size and shape of reactors (in the simplest case these are plating tanks) should be changed, current density should be increased or decreased or whether pulsating currents should be chosen [1], or how electrolyte - which influences electrode kinetics - should be chosen. In other words, the geometric and analytical limits of all models should be thoroughly researched and based on experimentally determined parameters, as far as possible, before any scaling up process is attempted. Nevertheless, such a research approach is missing nowadays, leaving important, scale-related, questions unanswered.

In an effort to shed light onto such a modelling methodology, which examines and elucidates the approach to resolving some of those uncertainties, this chapter discusses the comparison of a 3-D, laboratory-scale, RDE model and its industrial, scaled-up, version. Geometry optimisation and model sensitivity studies of both models are included. While an RDE-type system is seldom used in industry, the simplicity of the geometry allows one to explore issues arising due to scale up. In addition, for both the RDE, as well as the industrial-scale system, experiments related to parameter determination and validation are reported here.

For geometry optimisation studies, the relative position of the anode, with reference to the cathode position, and the anode size were varied for both the laboratory-scale and industrial-scale models. Subsequently, the model sensitivity studies were focused on how the input parameters, process physics, mesh spacing, and computation times might be affected by the setup's sizing-up.

COMSOL Multiphysics[®] was once more used for the studies presented here.

4.2 The Industrial-Scale Reactor

One of the objectives of this industrial PhD project has been set out to be the optimisation of the industrial collaborators' reactor and reactor parts to enable electroforming of complex shapes and sizes. This can be achieved through design of mandrels and reactor parts or tools through modelling, to control the deposit growth rate. To cross-validate model predictions against practical experiments of a similar industrial-scale setup, a 18 L electroforming tank was designed and manufactured for the purposes of the project. Studying electroforming experiments in that scale allows for a better understanding of the process and system's behaviour, helps towards educated choices during the scaling up of related process models and enables testing of the process for volume manufacturing. As a result, informed tools and mandrel designs could be developed, the number of manufacturing trials could be minimised, and conforming parts could be produced in volume manufacturing.

[Figure 4.1](#) shows the complete, prototype electroforming tank setup at the UoS industrial workshop. The CAD design and interior tank schematics are provided in [Figure 4.2](#).

The 18 L tank reactor, manufactured by *PolyPlas Engineering Ltd.*, is made of polypropylene (PP) due to the material's good mechanical properties at temperatures up to 80 °C and chemical resistance to dilute acids [2]. The system uses a *SIEBEC MC15*

pump and filter system to achieve sufficient electrolyte circulation. The *M15* magnetic drive pump allowed for a maximum flowrate of $1.5 \text{ m}^3/\text{h}$, while particles of even $0.5 \mu\text{m}$ were filtered using an on-line filter. A *SIEBEC* polypropylene $1/4''$ educator nozzle was used to circulate the electrolyte within the tank. The electrolyte was heated by a 0.5 kW *BRAUDE Polaris* cylindrical non-corrodible heater. A *BRAUDE Tankmaster MP* temperature and level controller was used for continuous monitoring and controlling of the solution.

The worktops were supplied by *Mark Finn Laboratory Equipment* and the whole setup was put together at the industrial workshop of the Chemical & Process Engineering department by the workshop's technician, Mr. Michael Watt.

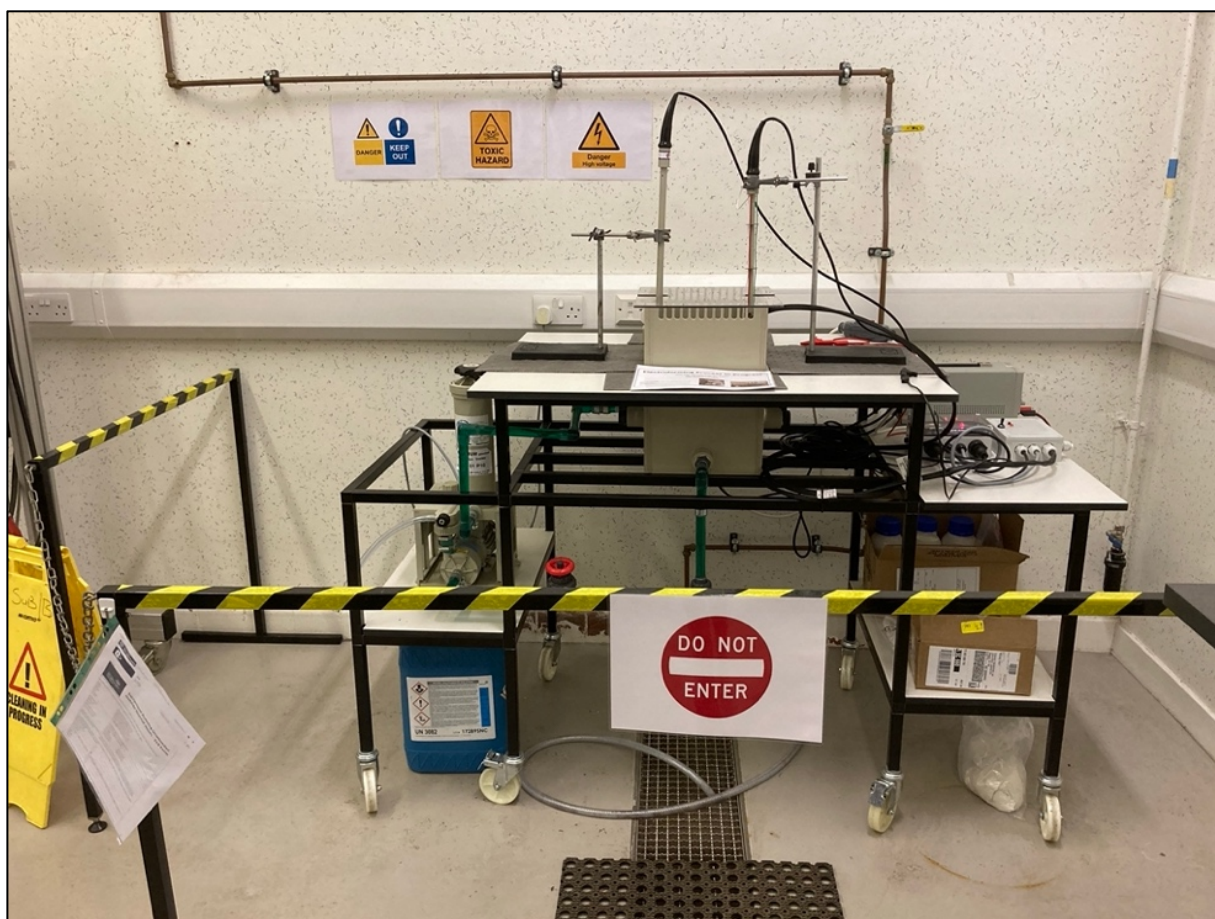


Figure 4. 1: The industrial scale (18L), prototype electroforming reactor setup used for the practical experiments against which the validity of the results, of both models presented in this chapter, were validated.

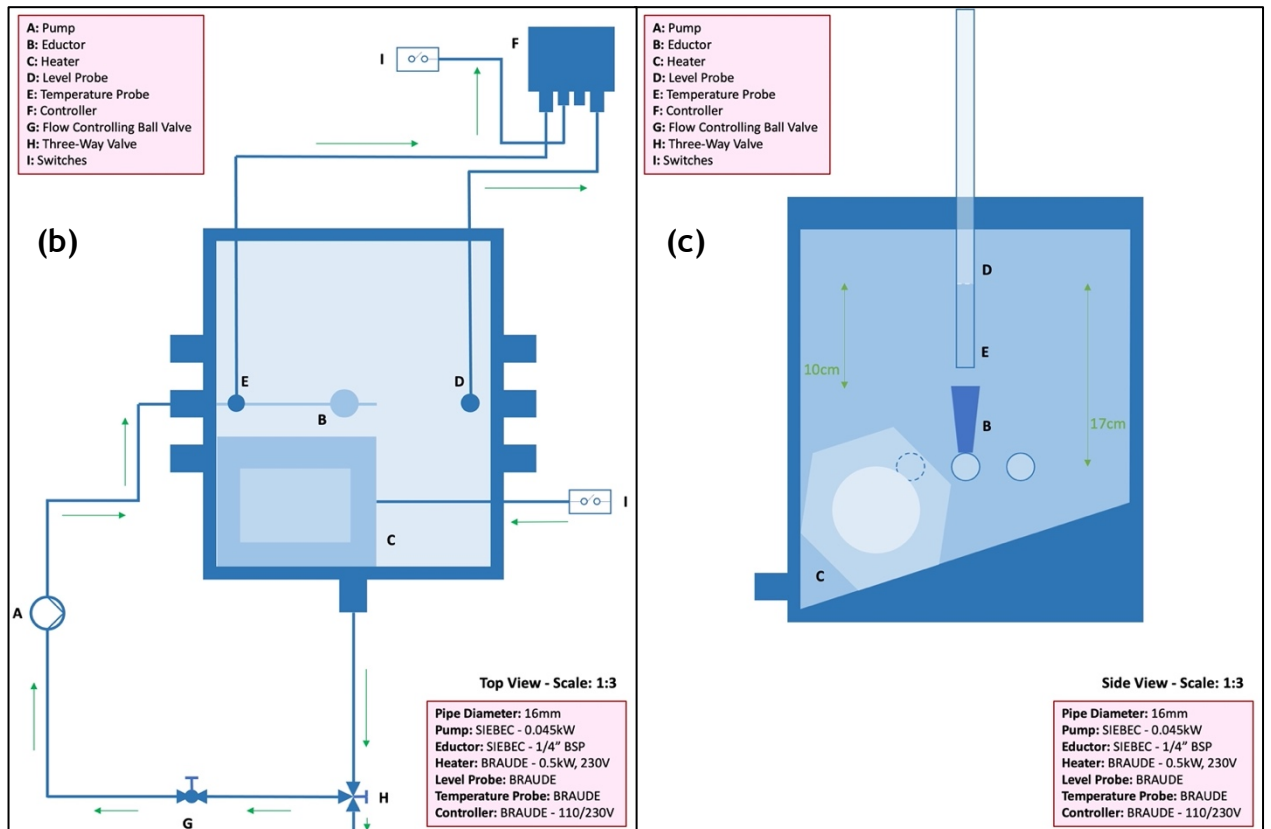
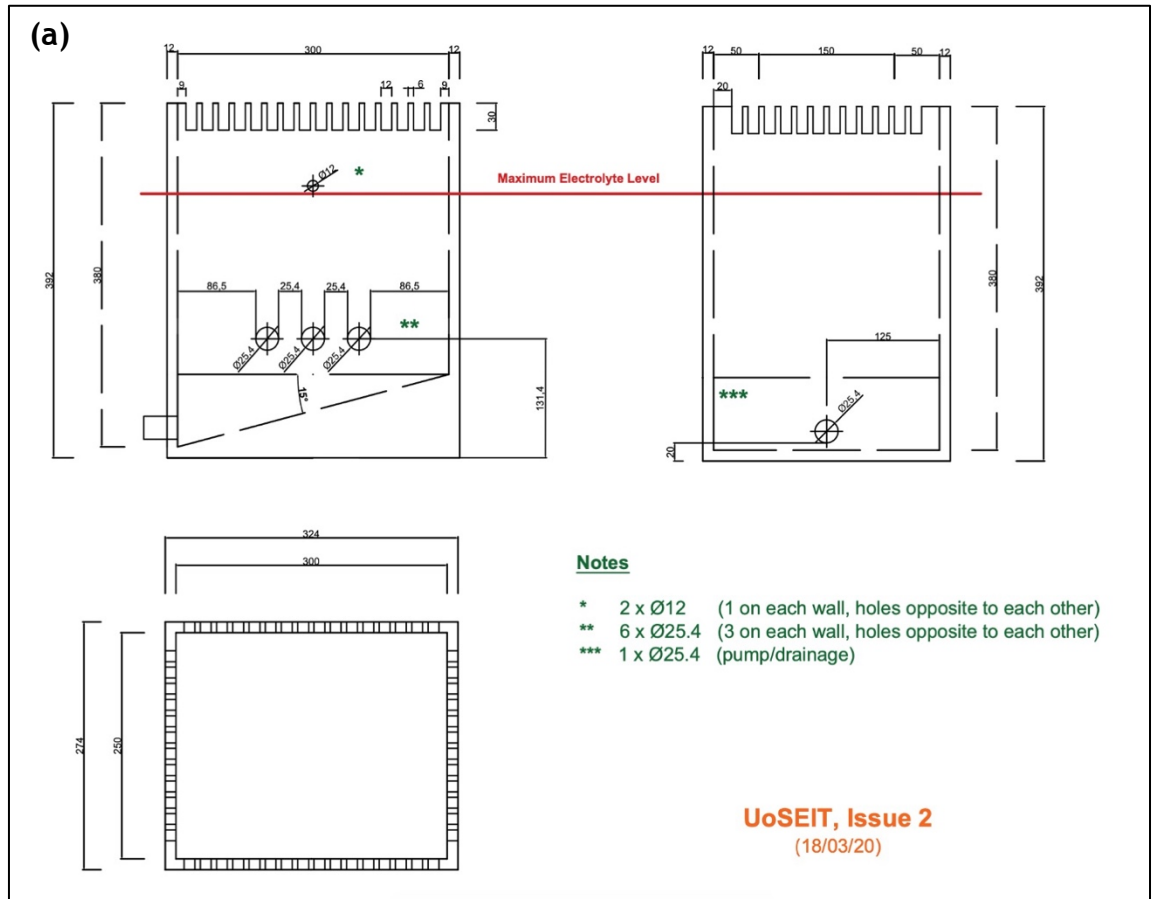


Figure 4. 2: (a) CAD design of the prototype electroforming tank developed for the purposes of the project, (b) in scale (1:3) top view schematic of the tank's interior including equipment, (c) in scale (1:3) side view schematic of the tank's interior including equipment.

The electricals of the system were set up by the university's electrical technician, Mr. John Redgate. The titanium anode basket used was provided by *Radius Aerospace* and was modified ($L = 20\text{ cm}$, $W = 5.3\text{ cm}$, $H = 13.5\text{ cm}$), to fit the prototype tank, by the workshop's technician, Mr. Michael Watt (Figure 4.3-a). The industrial grade nickel pellets used to fill the anode basket were also provided by *Radius Aerospace*. The scaled-up disk mandrel ($D = 0.63\text{ dm}$) was manufactured by Mr. Michael Watt and was made of 304 stainless steel (Figure 4.3-b).

The anode basket and mandrels used in the process were immersed in the electrolyte by mounting them on 12 mm copper busbars of > 99 % purity (Figure 4.4). Current was applied by a 20 A, 18 V RS PRO Switching DC Power Supply using 30 A, steel, BU-65-0 Farnell crocodile clips. For the scaled-up experiments, the same electrolyte as in the RDE experiments was used and deposits of 70 μm (nominal) were deposited for verification of model calculations.

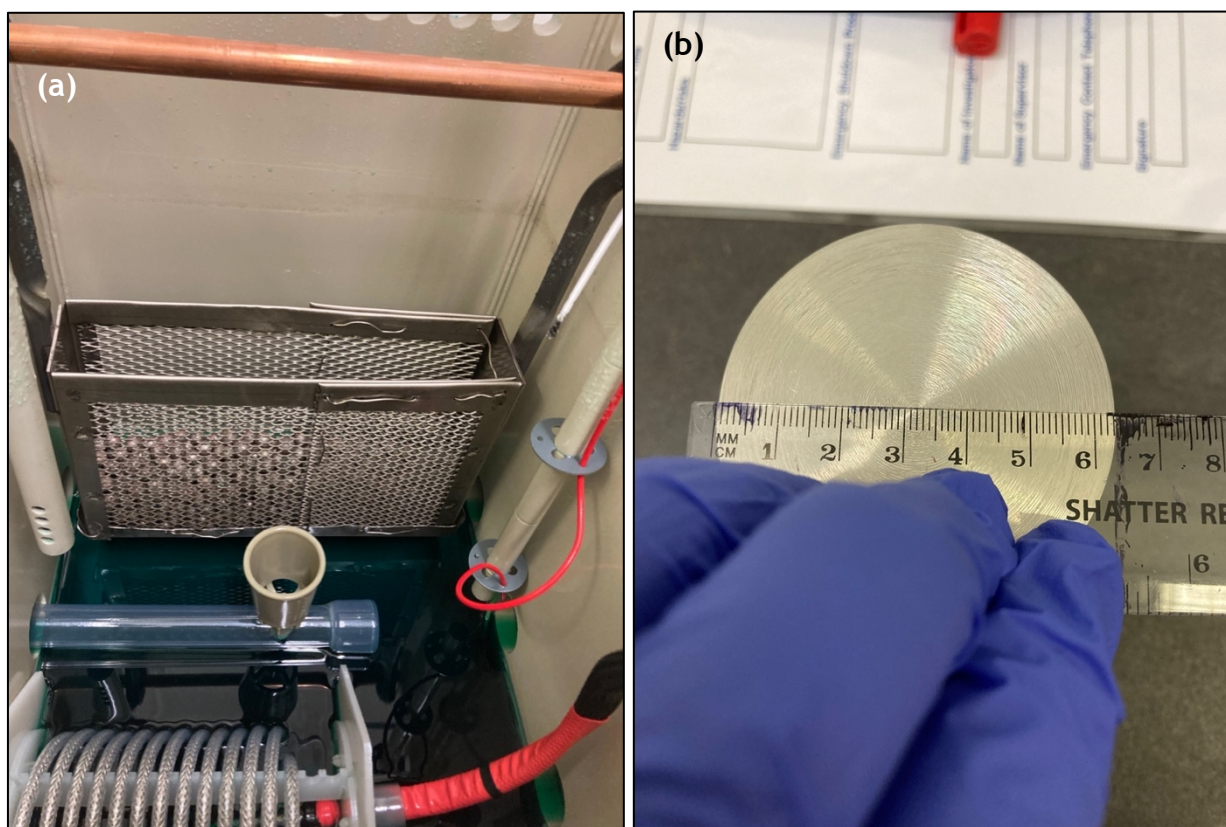


Figure 4. 3: (a) The anode basket filled with nickel pellets and fitted in the prototype electroforming tank, (b) The 304 stainless-steel, scaled-up, disk mandrel.

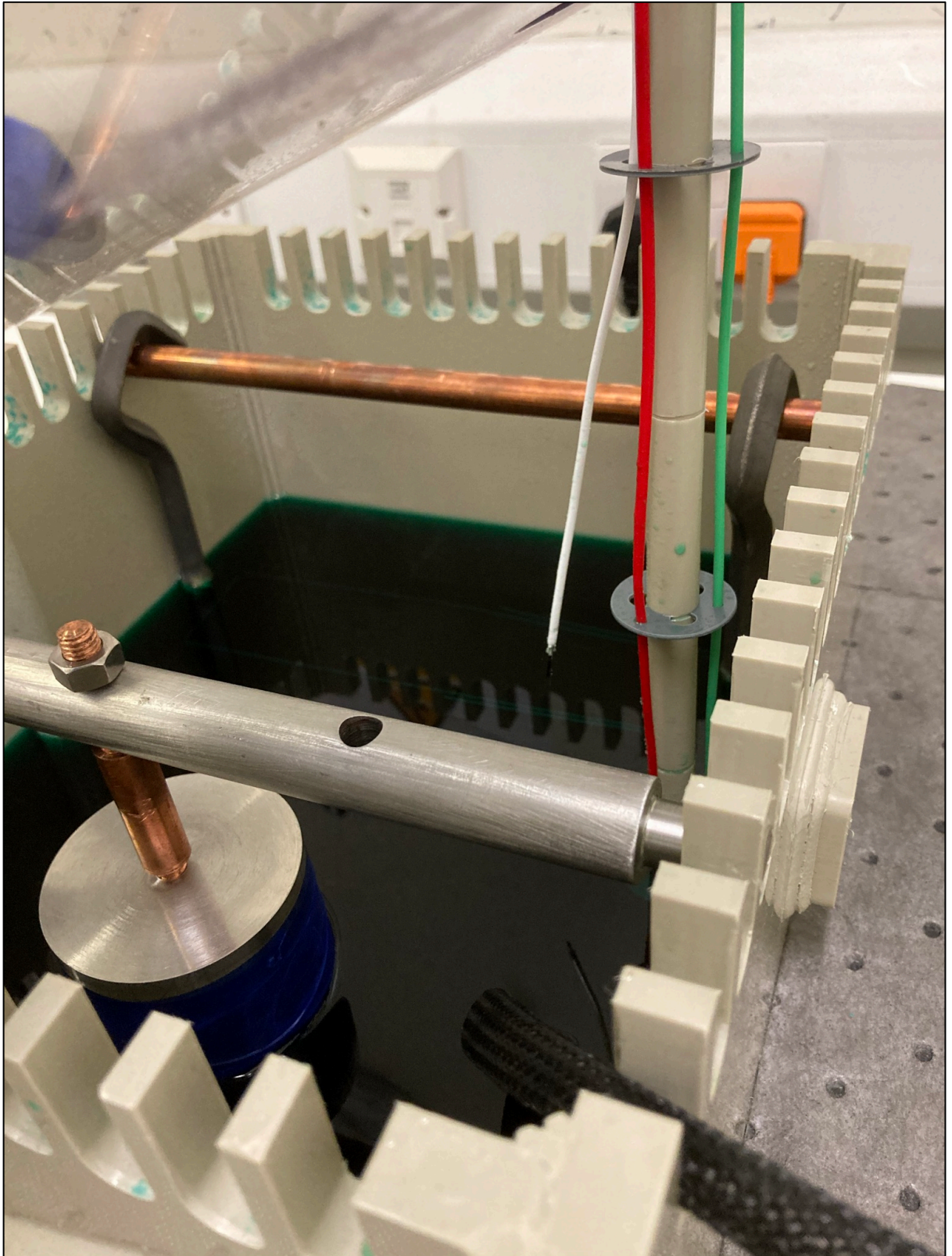


Figure 4. 4: Complete scaled up electroforming setup; titanium anode basket filled with Ni pellets and stainless-steel disk mandrel immersed in nickel sulphamate electrolyte.

One needs to clarify here that the shapes and sizes of the laboratory-scale (presented in [Chapter 3](#)) and tank reactors are dissimilar. This is intentional, because RDE are usually employed in laboratories, whereas a tank system is the “work horse” in industry. In the laboratory, glassware availability dictates the reactor shape, which is mostly cylindrical, whereas in industry plastic sheets are used to form more rectangular reactor structures.

4.3 Control simulations

A time-dependent 3-D model of the recessed rotating disk electrode system was developed within the *Electrodeposition* module of *COMSOL Multiphysics*[®] as already presented in [Chapter 3](#). A second time-dependent model was, subsequently, developed to represent the scaled-up, 18 L, electroforming reactor. The 3-D discretised geometries for the laboratory-scale RDE and the scaled-up electroforming reactor are shown in [Figures 4.5-a & 4.5-b](#). Both electroforming systems consist of a cathode and an anode immersed in the electrolytic volume. It is reminded that a stainless-steel disk $\sim 0.12 \text{ dm}$ in diameter ($A_{RDE} = \sim 0.0113 \text{ dm}^2$) was used as the deposition substrate (cathode) for the RDE experiments discussed throughout this work ([Figure 4.5-c](#)). In the scaled-up system, a stainless-steel disk $\sim 0.63 \text{ dm}$ in diameter ($A_{mandrel} = 0.31 \text{ dm}^2$) playing the role of the mandrel (cathode) ([Figure 4.5-d](#)) was used. In both cases the $\frac{(cathode\ area)}{(anode\ area)}$ ratio was being kept greater than $1/2$ as is practised in industry. When compared, the two systems present $1/90$ electrolyte volume ratio and a $1/28$ deposition (cathode) area ratio. The difference in areal and volumetric ratios is expected as per dimension analysis due to the fact that they scale as $(length)^2$ or $(length)^3$.

As it has been described before, the first part of developing a model in *COMSOL Multiphysics*[®] is an efficient mesh generation for the model’s domain and electrode

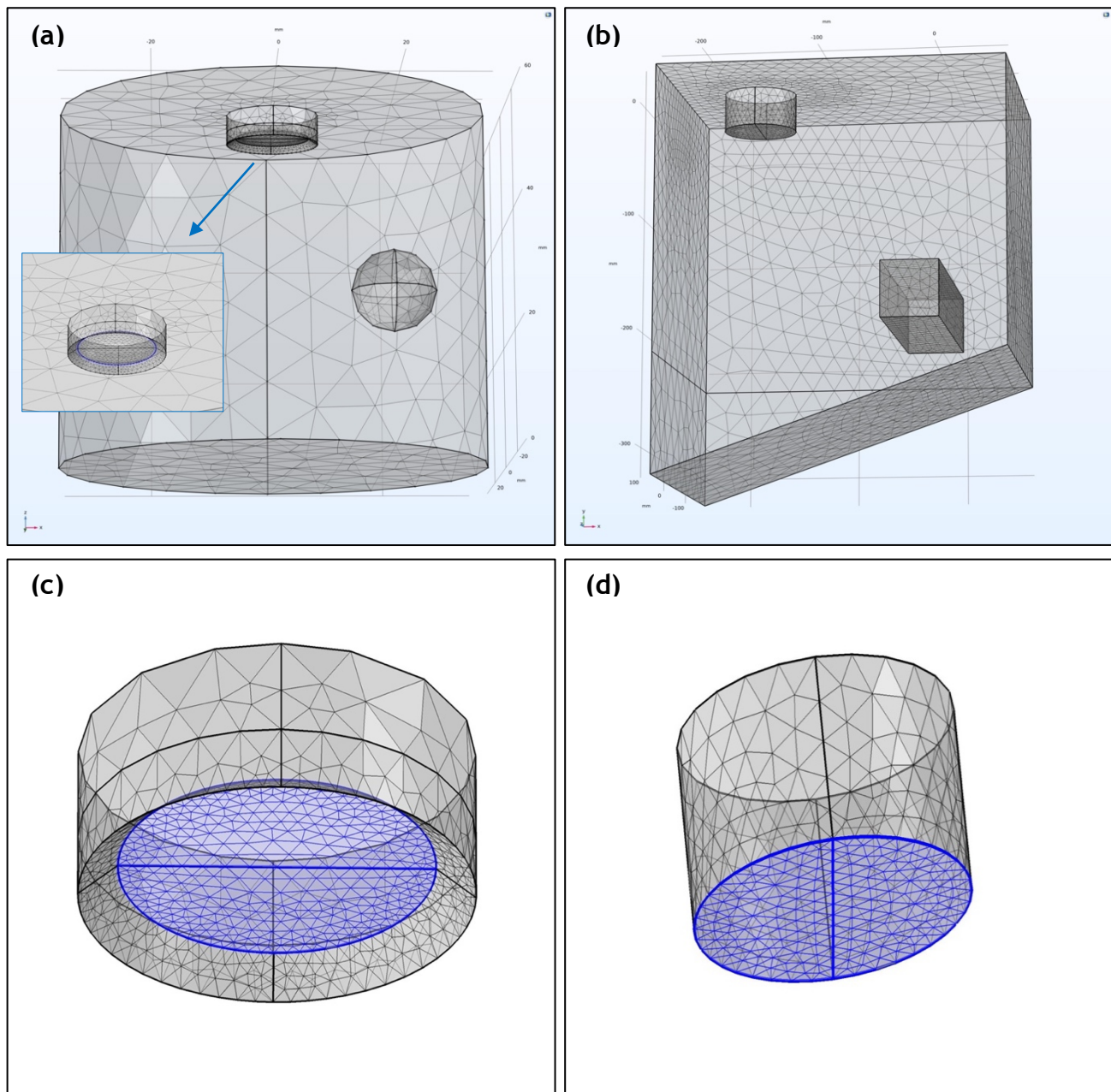


Figure 4. 5: (a) Mesh spacing of the 3-D, laboratory-scale (0.2 dm^3), RDE geometry domain and (b) mesh spacing of the 3D, industrial-scale (18 dm^3), prototype electroforming reactor domain. The blue line in the zoom-in capture of figure (a) highlights the “recess”, transition edge of the stainless-steel disk electrode in the RDE model. Highlighted in blue, the deposition (cathode) areas of (c) the laboratory-scale setup and (d) the scaled-up setup are also shown. The RDE and scaled-up deposition areas present a ratio of 1:28.

surfaces. A user-defined mesh spacing was chosen for both models. [Figures 4.5-a & 4.5-b](#) show the mesh spacing of both models and highlights the points of interest. Since the main interest is focused on the deposits formed on the cathode’s surface,

the mesh on the cathode boundary was the finest in both models.

For the RDE, the mesh spacing presented in [Section 3.3](#) was applied. This included 17,255 elements with minimum element quality of 0.2149 ([Figure 4.5-a](#)). On the other hand, the scaled-up model included 132,291 elements with minimum element quality of 0.2045 to accommodate the larger domain ([Figure 4.5-b](#)). Therefore, the meshes were developed to present similar average element qualities; 0.652 for the RDE model and 0.6603 for the scaled-up one.

As a next step, secondary current distribution (SCD) was once more chosen to describe the problem physics. The electrochemical input parameters needed to describe the electrochemical system were determined experimentally in the laboratory and are provided in [Table 3.2](#). All simulation experiments presented in this chapter were designed to represent practical deposition experiments, at 50 °C, for 3 h, when the cell voltage lies at 2.5 V. Since electrolyte nickel concentration is high, no concentration gradients need to be taken into consideration therefore, to simplify the calculations, no mass transfer limitations were considered.

For the “control” simulation experiments, in the RDE model the cathode phase condition was described by a total applied current $I_{l,total} = -0.0372 \text{ A}$ and an applied boundary electric potential $\varphi_{s,ext,init} = -2.5 \text{ V}$. Similarly, for the industrial-scale model the boundary condition at the cathode was described by a total current $I_{l,total} = -1 \text{ A}$ and an electric (or electrode) potential initial value at $\varphi_{s,ext,init} = -2.5 \text{ V}$. Anode boundary conditions were set at 0 V for both models to achieve 2.5 V cell voltage in both cases. In terms of current density, the above stated values correspond to deposition at 3.2 A/dm^2 in both scales, a value representative of those used for nickel deposition in industry [3].

[Figure 4.6](#) shows the current and potential distribution results for the two models after the simulation had converged. The visualisation in [Figures 4.6-a & 4.6-b](#) allows one to check the potential distribution in the domain and near the electrode surface

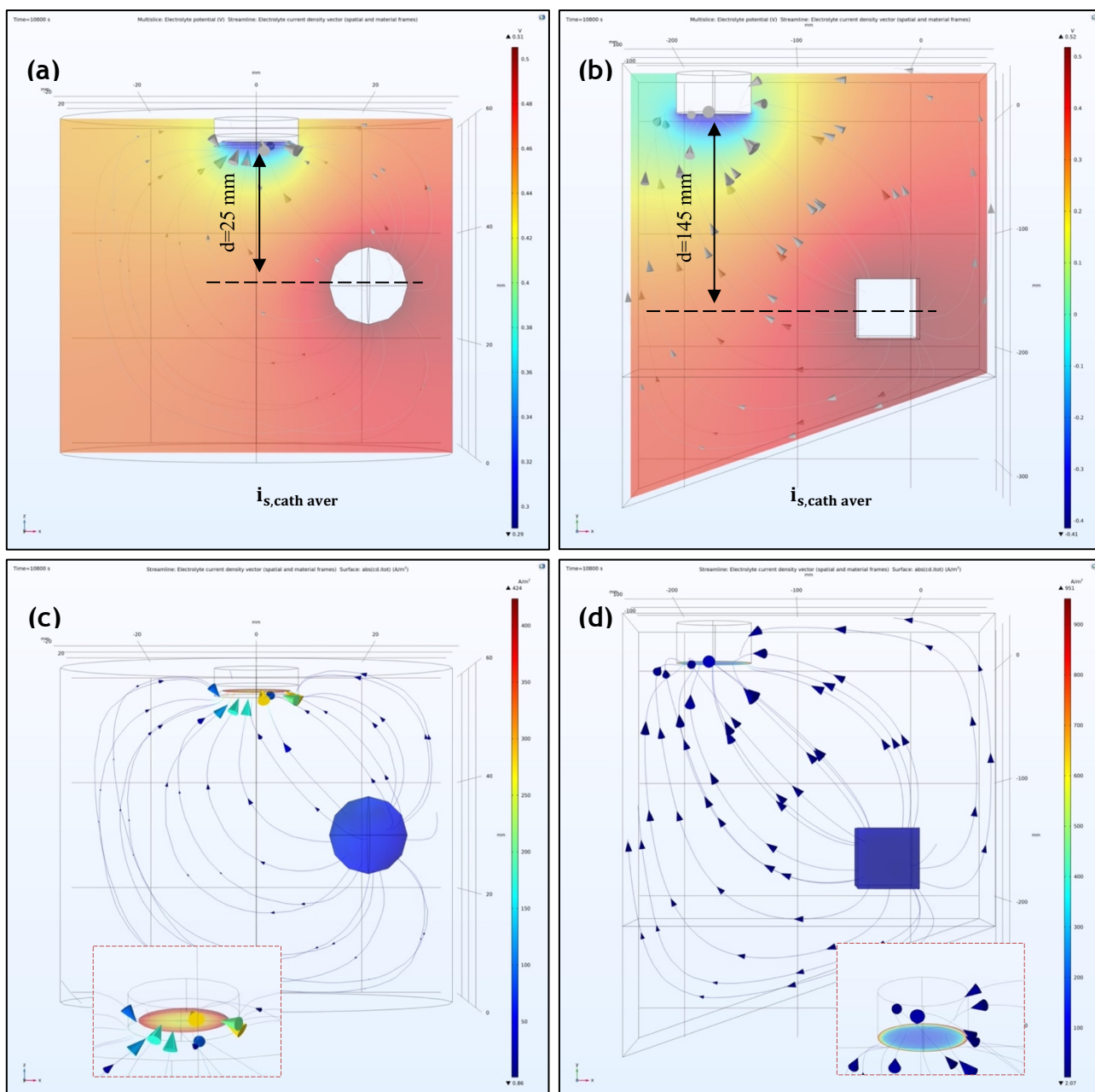


Figure 4. 6: 3-D representation of potential distribution in the electrolyte volume of (a) the RDE and (b) the electroforming reactor. 3-D representation of current distribution on the cathode surface for (c) the RDE and (d) the electroforming reactor. The results simulate potential and current distributions after 3h at 50 °C. The current streamlines in both electrolytic volumes are also shown in figures (c) and (d) emanating from the anode (at higher potential) and being collected at the cathode (at lower potential). The vertical distance between the electrodes' geometrical centres is also noted in figures (a) and (b). Current distribution on the cathodes' surface is shown in the cathode surface close ups provided in figures (c) and (d).

as well as the current lines travelling to the electrode surface. Control simulations showed that the potential drop within the electrolyte is different for the two models: $0.29\text{ V} \leftrightarrow 0.51\text{ V}$ for the RDE system and $-0.41\text{ V} \leftrightarrow 0.52\text{ V}$ for the tank apparatus. The maximum potential value immediately next to the anodes is the same (*i.e.*, $\sim 0.52\text{ V}$ as would be expected for dissolution to proceed), the potential near the cathode surface is different for the two systems. This difference is induced by the reactor boundaries; not only do the current lines bend away from the insulator walls since no current can pass through them, thereby leading them towards the cathode surface, but also through the different lengths that the current lines have to travel as they move through the electrolyte. Indeed, the surface potential at the cathode for the RDE and electroforming reactor differ due to the larger ohmic drop for the latter system.

To verify the predicted system behaviour the value of the local potential at the cathode surface was followed. Both models were set to record a solution every 30 min (1800 s) therefore, seven time-steps were set. The model was solved to provide convergent solutions varying between $t = 0$ (for a non-evolved surface) and the last for $t = 10800\text{ s}$ (for an evolved surface where a deposit was formed), reflecting deposition for 3 h , similar to what would be used in industry. In this regard, after the final converged time step, the local average cathode surface potential was determined at $\varphi_{s,\text{cath aver}} = -0.30845\text{ V}$ for the RDE and $\varphi_{s,\text{cath aver}} = -0.98490\text{ V}$ for the scaled-up system. Although there is a slight change in the electrode surface potential due to the evolution of the deposit (*i.e.*, that the cathode boundary had changed), but the essential difference between the two systems, *i.e.*, the difference in scale leading to very different ohmic drops, and hence cathode potentials, is retained.

By comparing these local potential values within the electrolyte immediately next to the cathode, *i.e.*, $\varphi_{l,\text{local}}$, one can ascertain the energy needs due to ohmic drop for this process. Here, as indicated in [Figures 4.6-a & 4.6-b](#), the distance between the cathode's surface and the (centre of) anode lies at 25 mm for the RDE model and 145 mm for the scaled-up one. At the same time, the cathode surface local potential

in the tank system model is calculated to be three times higher than the one at the RDE cathode surface, *i.e.*, the longer distance between the electrodes results in higher energy requirement for the process to be driven. The calculated current density values range from 0.86 A/m^2 to 424 A/m^2 at the cathode surface for the RDE while, they range between 2.07 A/m^2 and 951 A/m^2 for the electroforming reactor conditions in [Figures 4.6-c & 4.6-d](#).

Moving forward, [Figure 4.7](#) presents the deposit thickness profiles (reflecting the current distribution) predicted for the two different reactors. In general, the current is predicted to be higher at the edges than at the centre of the disk as would be expected [4]. Consequently, increase in thickness profiles was predicted at the edges. In [Figure 4.7-a](#), the model shows that the overall thickness distribution (reflecting the current distribution) follows the usual non-uniform current distribution as expected for an RDE; however, the low current at the insulator-RDE edge is caused due to the recess due to the shadowing effect of the recess [5]. The current distribution for the cathode (mandrel) within the electroforming reactor ([Figure 4.7-b](#)), on the other hand, shows typical non-uniform thickness distribution, with high current at the edges and lower current at the centre.

Experimental Validation

For validation purposes nickel deposits were produced for both the RDE and the electroforming reactor systems. The experimental conditions in the 18 L electroforming reactor process were the same as the ones presented for the control simulations above (-2.5 V and -1 A , for 10800 s). For practical issues, the RDE deposit used for the 2-D axisymmetric RDE model validation in [Chapter 3](#) was also used for the validation of the 3-D RDE model (-5 V and -0.565 A , for 1800 s). This deposit was subsequently compared against a 3-D RDE model also set to simulate the process at -5 V and -0.565 A for 1800 s.

While the RDE deposit was only sectioned along its diameter due to its very small

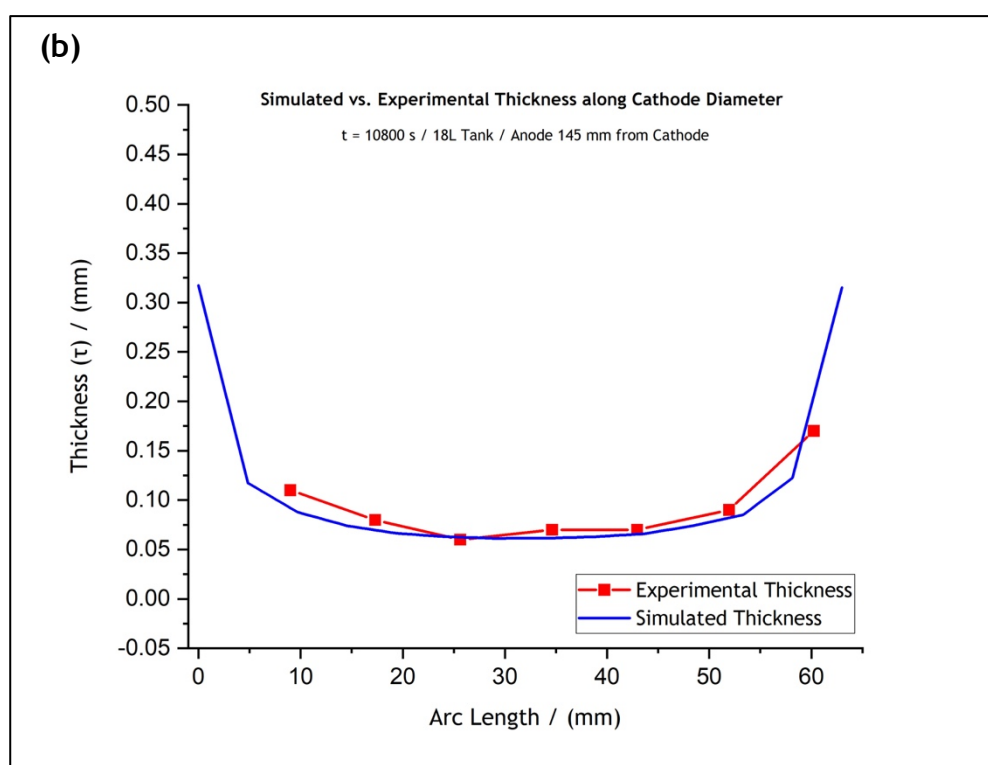
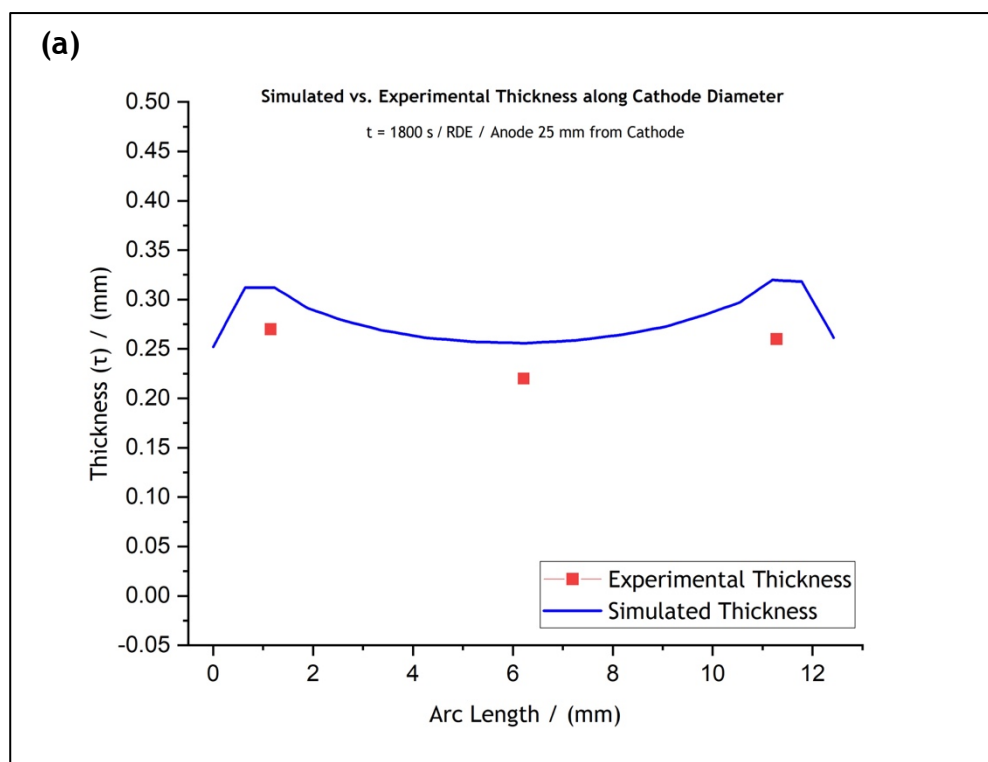


Figure 4. 7: Comparative graphs of the experimentally achieved and the simulated thickness profiles for (a) the laboratory-scale RDE setup and (b) the prototype electroforming reactor setup. The RDE deposit was produced at -5 V and -0.565 A , for 1800s , while the reactor deposit was formed at -2.5 V and -1 A , for 10800s . These conditions allowed, in both cases, for thick enough deposits to be sectioned, mounted in resin, and measured under the microscope without deforming.

size, the deposit obtained in the tank system, since it was significantly larger, was cut into three strips; one strip was retrieved along the diameter and two more on the left and right side of this middle section. The final specimen that was placed under the *Yenway* optical microscope and studied at a $\times 20$ magnification is shown in [Figure 4.8](#).

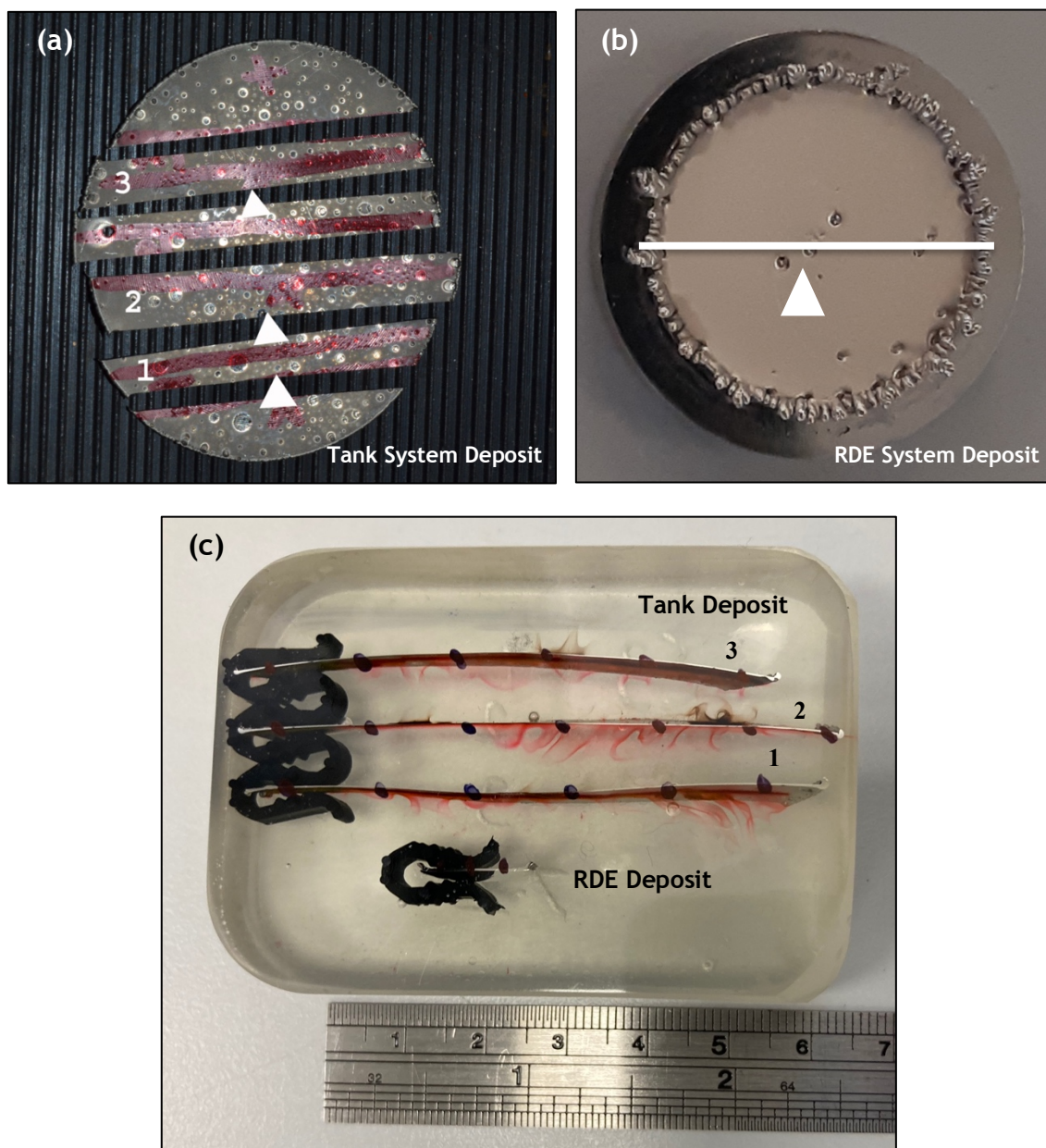


Figure 4. 8: Sectioning of nickel disk deposits formed (a) in the tank system and (b) in the RDE system for thickness measurements. The white arrows indicate the side face of its section measured under the microscope, following these being mounted in a (c) resin specimen.

Figures 4.7-a & 4.7-b present a comparison between the experimentally achieved and simulated thickness profiles. Validation experiments revealed that the RDE model slightly over-predicts thickness values compared to the experimentally achieved ones, while the scaled-up model's prediction is in reasonable agreement with the experimental thickness profiles (Figures 4.7-a & 4.7-b). For the RDE setup, the average predicted thickness was calculated at $\sim 0.27 \text{ mm}$ while the average experimental thickness was measured at $\sim 0.24 \text{ mm}$. For the industrial-scale model, the computed thickness was calculated at $\sim 0.075 \text{ mm}$, while the average experimental thickness was measured at $\sim 0.07 \text{ mm}$.

The larger difference between the model and experiments for the RDE is attributed to the formation of large dendrites for the RDE (refer to Figure 2.11), and smaller ones for the tank deposits (Figure 4.9). For a recessed RDE, one would expect the current to be lower at the edges, as is shown in Figure 4.7-a, but our experiments show that the plating system provides large dendrites (refer to Figure 2.11).



Figure 4. 9: Real-life nickel electroform produced in the prototype electroforming reactor at -2.5 V and -1 A , for 10800 s , at $50 \text{ }^\circ\text{C}$, under agitation.

A simple dimensional approach can be used to assess the influence of dendrite formation on electrodes of differing sizes. The two deposits have a surface area of πr^2

and a perimeter of $2\pi r$. Since the dendrites appear at the perimeter, and the remaining current with the surface area, one can assume that the current “stolen” by the edges scale as $2\pi r / \pi r^2$ or $2/r$. Therefore, dimensional analysis suggests that dendritic growth at the edges should be limited for the scaled-up mandrel, which presents a larger deposition surface vs perimeter, compared to its scaled down, RDE, replica. A corollary of this observation is that edge effects seem to influence critically the prediction of SCD models. Therefore, for model validation, the effect of scaling can be an important consideration; whereas the RDE data [Figure 4.7-a](#) could be inferred (incorrectly) as the model deviating from experiments, the same calculations at a large scale, *i.e.*, [Figure 4.7-b](#) validate the model.

4.4 Mesh Sensitivity Studies

Once the validity of the models was checked, separate sets of calculations involving mesh sensitivity studies were carried out for both models shown in [Figures 4.5-a & 4.5-b](#). The aim of these studies was the systematic investigation of how mesh density affects the quality of the modelling results. As mentioned before, the mesh developed for the RDE model includes 17,255 elements with minimum element quality of 0.2149 and an average element quality of 0.652 ([Figure 4.5-a](#)). The scaled-up model includes 132,291 elements with minimum element quality of 0.2045 and an average element quality of 0.6603 ([Figure 4.5-b](#)). In other words, to develop meshes with a similar high element quality (~ 0.65 in average), eight times more elements were needed for spacing the industrial-scale model domain compared to the number of elements used for the RDE model.

Specifically, for the RDE model, the general element size parameters for the original, user-defined mesh were 10 mm for the maximum element size, 0.5 mm for the minimum element size, 1.5 for the maximum element growth rate, a curvature factor of 0.6 and a resolution of narrow regions at 0.5. For the scaled-up model, the general

element size parameters for the original user-defined mesh were 30 mm for the maximum element size, 0.5 mm for the minimum element size, 1.1 for the maximum element growth rate, a curvature factor of 0.6 and a resolution of narrow regions at 0.5. The values provided for the last three parameters are always kept constant since they prevent the formation of inverted mesh elements for even the coarsest meshes studied here. That way, mesh-related issues, which could prevent the model from converging, are minimised.

These general element size parameters are affected by the element size parameters at each one of the individual boundaries. For the cases presented here, the original element size parameters for each boundary of both models studied are given in [Table 4.1](#). These initial element size parameters were changed by -50% and -75% (*i.e.*, finer by 50% and 75%) for the RDE model.

It is important to note here that the mesh spacing of the anode boundary for both models, as well as the RDE recess boundary, is controlled by setting an upper limit for the maximum element size. The minimum element size and maximum element growth rate for these boundaries (“–” entries in [Table 4.1](#)) are controlled by the “General” mesh characteristics.

Table 4. 1: User-defined, general and boundary, user-defined, element size parameters for both the RDE and scaled-up models.

Element Size Parameters	RDE Model				Scaled-Up Model		
	General	Cathode	Anode	Recess	General	Cathode	Anode
Maximum Element Size (mm)	10	3	10	0.5	30	5	10
Minimum Element Size (mm)	0.5	–	–	–	0.5	–	–
Maximum Element Growth Rate	1.5	1.1	–	–	1.1	1.1	–

However, for the cathode boundary, where the deposition takes place, all three mesh parameters are user-defined to allow for the maximum control over the spacing of this electrode surface.

A change only by -50% was investigated for the scaled-up model due to limitations related to the computational power of the PC hardware we use; meshes finer than 50% than the control mesh exceeded the computational capacity of the hardware. The local thickness profiles at the cathode boundary retrieved for -50% and -75% change in the RDE model mesh spacing and -50% change in the scaled-up model are shown in [Figures 4.10 & 4.11](#), respectively. As is expected, a finer mesh would result in smoother thickness curves since calculations are conducted at more nodes, providing solutions at more “points” throughout the electrolytic volume. However, no significant changes in the simulated thickness are observed for the RDE or the electroforming reactor, except at the outside edges where either the effect of recess or insulator is felt. On the other hand, the computation time increased significantly; from 25 s ([Figure 4.10-a](#)), to 2 min ([Figure 4.10-b](#)), to 36 min ([Figure 4.10-c](#)) for the RDE, and from $\sim 5\text{ min}$ ([Figure 4.11-a](#)) to $\sim 36\text{ min}$ ([Figure 4.11-b](#)) for the scaled-up system. In practice, therefore, it may be useful to optimise mesh size against computation times, especially when complicated mandrel shapes and sizes are studied.

Further still, the initial element size parameters were also changed by $\pm 5\%$, $\pm 10\%$, $\pm 12\%$, $\pm 15\%$ and $\pm 25\%$. Negative changes of these initial values mean that the mesh was made finer while positive changes led to coarser meshes. The observations were made based on the effect that all the above changes had on the thickness profiles, are summarised in [Table 4.2](#). The thickness profile graphs for the $\pm 5\%$, $\pm 10\%$, $\pm 12\%$, $\pm 15\%$ and $\pm 25\%$ are provided in the Supplementary Materials section of this publication ([Figures 4.12 & 4.13](#)). All changes are discussed in this section.

Regarding the RDE model ([Figure 4.12](#)), as [Table 4.2](#) reveals, an increase of element size parameters by 12% is the threshold after which a minor deterioration of the thickness profiles’ smoothness was observed while, major negative effect was obser-

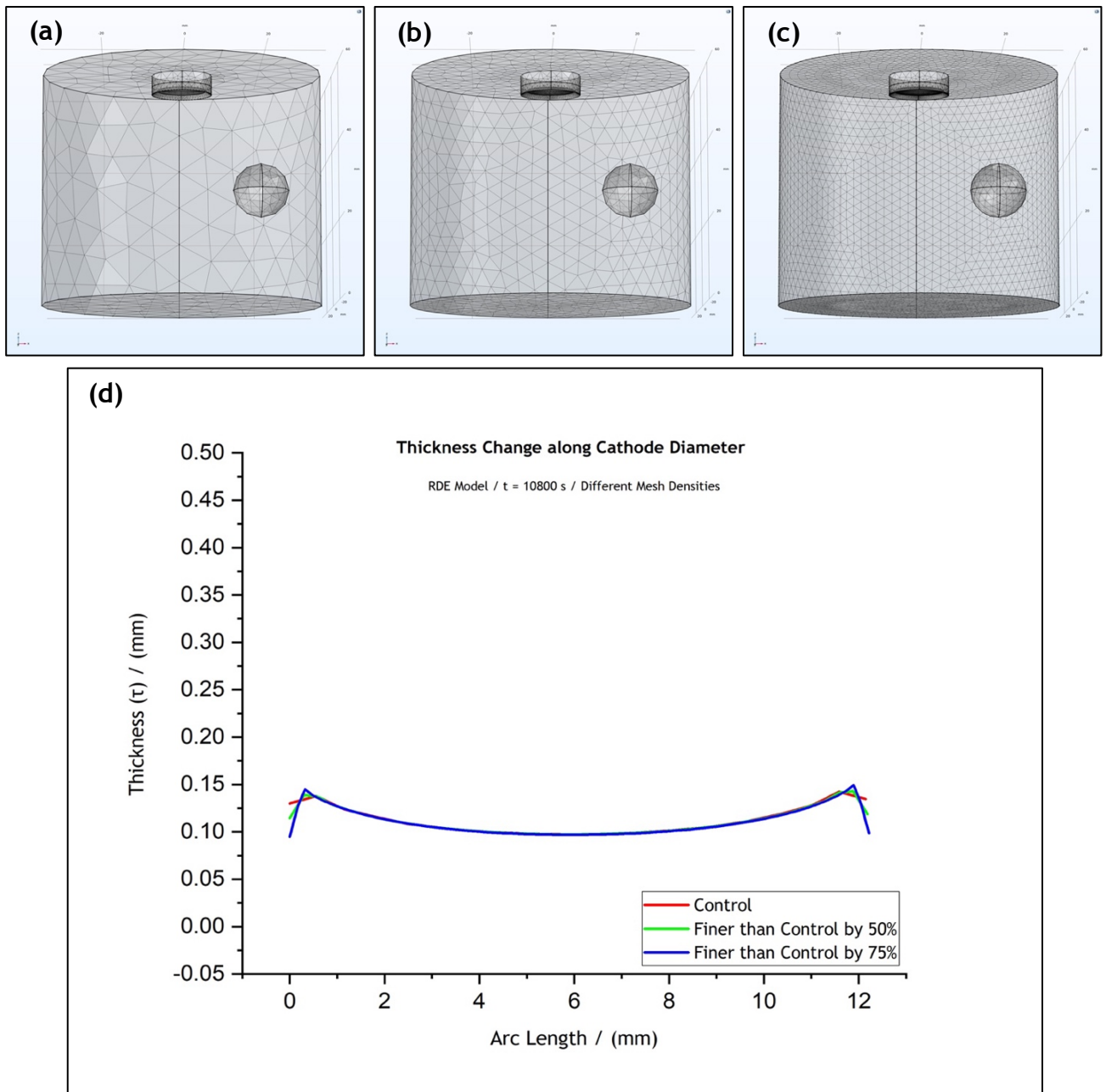


Figure 4. 10: (a) Control mesh density (red), (b) mesh spacing finer than the control by 50% (green), (c) mesh spacing finer than the control by 75% (blue). Figure (d) shows an overlap of the thickness profiles predicted by the RDE model for the different mesh densities. The results simulate a 3 h process at 50 °C.

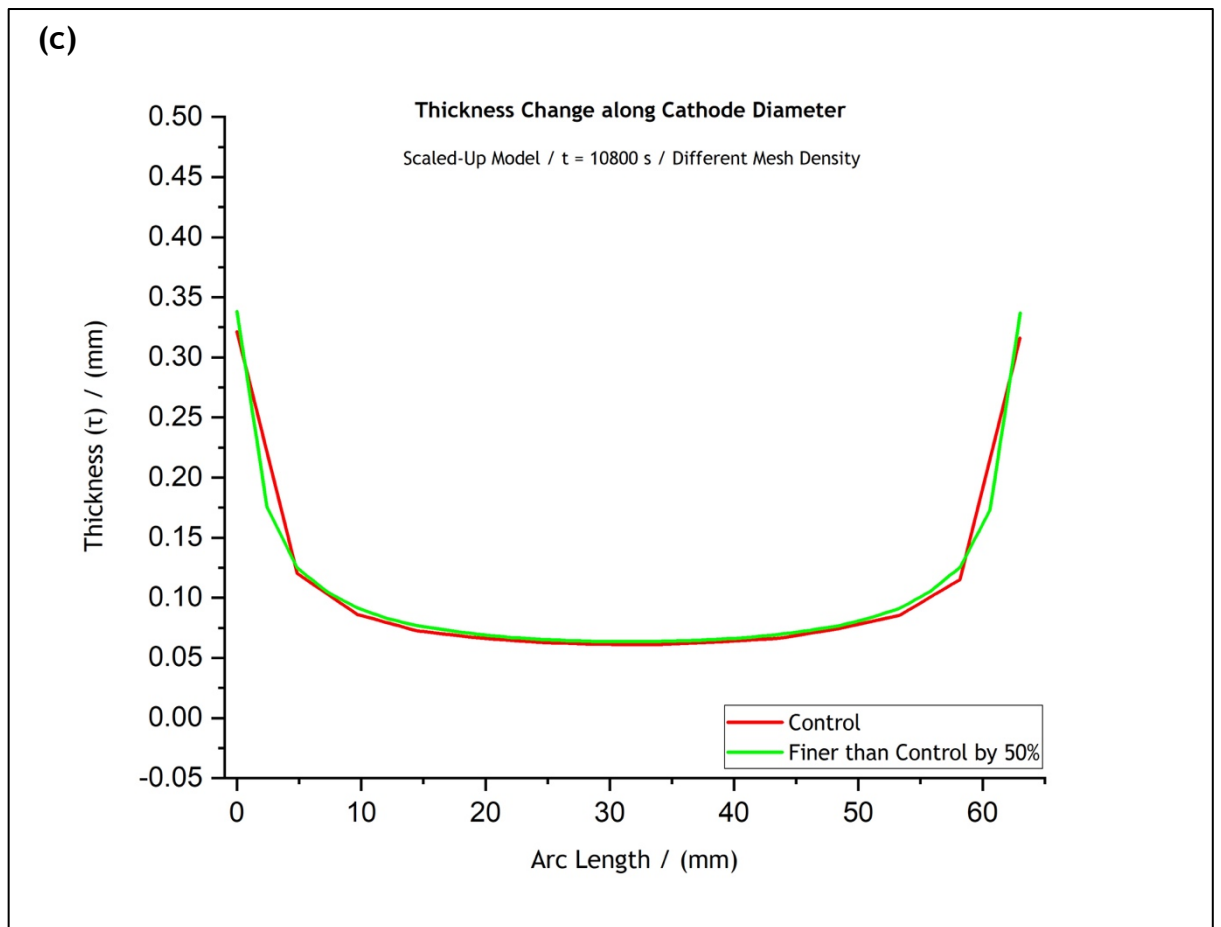
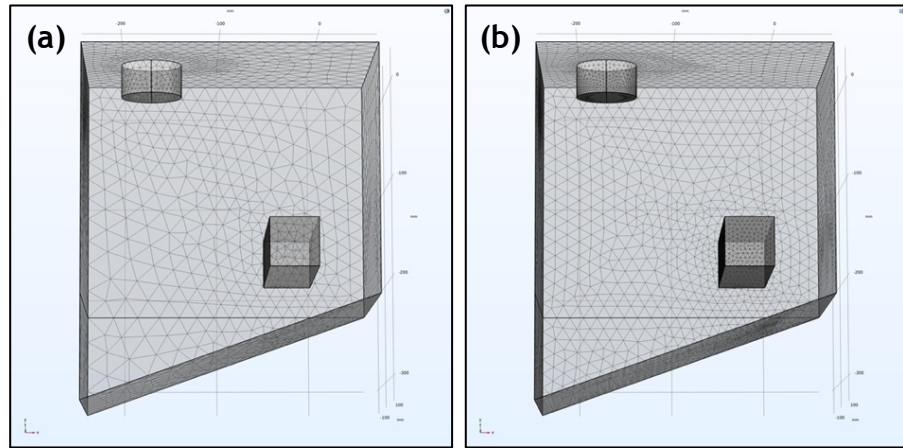


Figure 4. 11: (a) Control mesh density (red), (b) mesh spacing finer than the control by 50% (green). Figure (c) shows an overlap of the thickness profiles predicted by the scaled-up model for the different mesh densities. The results simulate a 3 h process at 50 °C.

Table 4. 2: Comprehensive presentation of the effect of various changes in mesh’s density on the thickness profiles modelled for both the RDE and industrial-scale models.

Mesh Density Change (%)	Effect on Results’ Quality					
	No Effect		Minor Effect		Major Effect	
	RDE	Scaled-Up	RDE	Scaled-Up	RDE	Scaled-Up
+5%	✓	✓				
-5%	✓	✓				
+10%	✓	✓				
-10%	✓	✓				
+12%		✓	✓			
-12%	✓	✓				
+15%			✓	✓		
-15%	✓	✓				
+25%				✓	✓	
-25%		✓	✓			
+50%				✓	✓	
-50%					✓	✓
-75%					✓	

-ved following an increase by 25% or more. On the other hand, any decrease of element size parameters by up to 15% did not affect the thickness profiles. Indeed, a decrease of 25% was determined to be the threshold where a minor effect on the thickness profiles is observed while a decrease of 50% or greater affected the profiles by showing a change in outputs where edge effects dominate.

The corresponding studies for the tank system (Figure 4.13), revealed a slightly different mesh tolerance. Only a decrease by 50% had a major effect on the predicted thickness profile affected the results near the edges of the electrode, while an increase of the element size by 15% and 25% led to only a minor deterioration of the thickness profiles' smoothness towards the edges. Overall, the effect on the quality of the thickness profiles retrieved and presented in Figures 4.12 & 4.13 was mainly observed at the edges. As shown in the zoomed in areas on the graphs, the thickness profiles at the middle of the deposits (arc length between 2 – 8 mm for the RDE system, and 12 – 48 mm for the tank system) are relatively undisturbed by changes in mesh spacing. Since this middle part of the deposit is used in practice, the fact that both models do not present significant mesh spacing sensitivity along that arc length is important. In industry, the area closer the edges, where the changes were observed, corresponds to the deposit part which would be discarded during post-processing to remove dendrites. Therefore, mesh-related model sensitivity may be of lower importance for electroformed products.

4.5 Geometry Sensitivity Studies

Once the models were validated, one progressed on to reactor optimisation. Geometry sensitivity studies were conducted for both the RDE, and the tank system models, investigating the effect that the anode position and cell boundaries have on the current and potential distribution. Following that, the observations at the two different scales were compared.

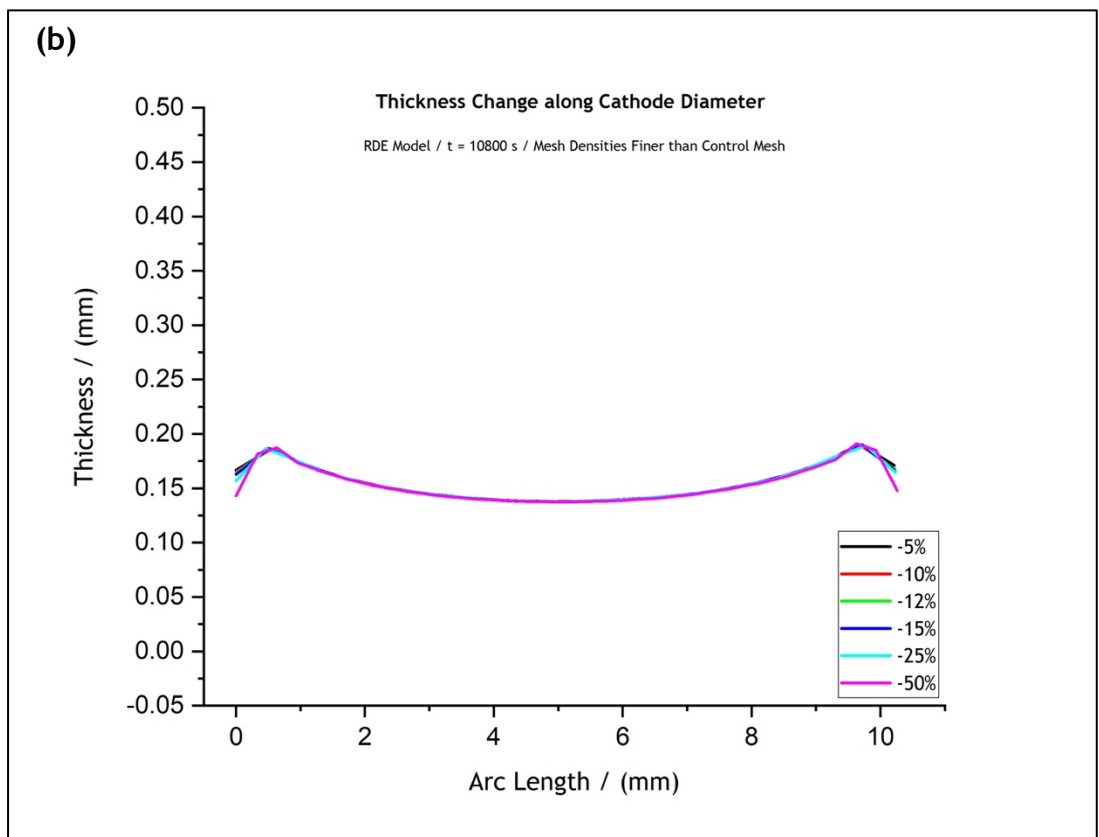
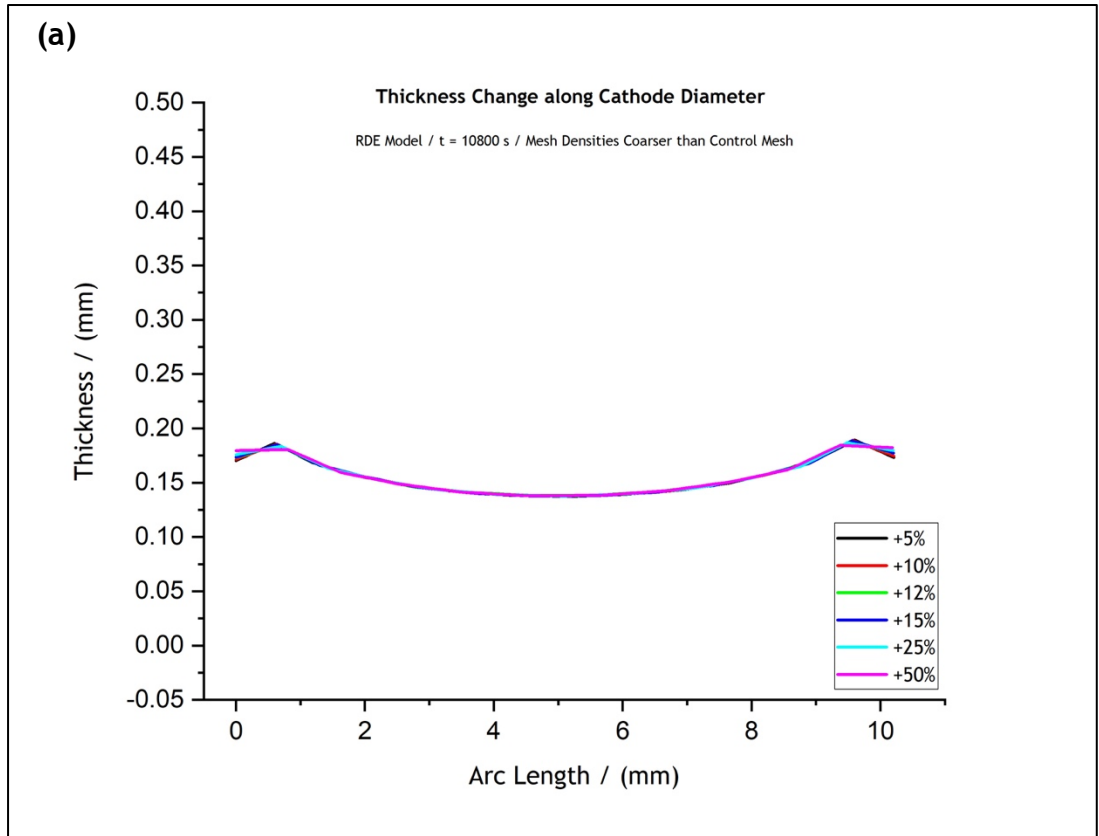


Figure 4. 12: Overlap of thickness profiles predicted by the RDE model following (a) an increase of the element size parameters by various percentages and (b) a decrease of the element size parameters by various percentages. Figure (a) shows the change in the results' quality for meshes coarser than the control mesh while, figure (b) shows the change in the results' quality for meshes finer than the control mesh. The results simulate a $3 h$ process at 50 °C.

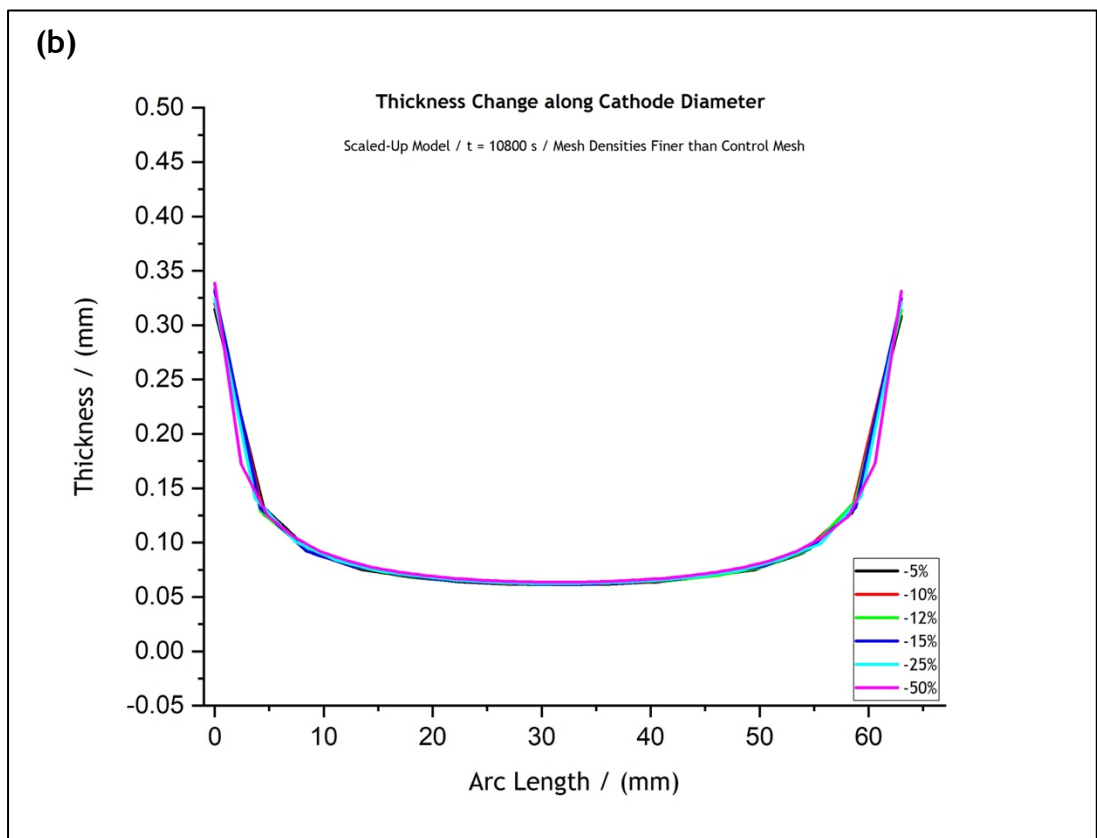
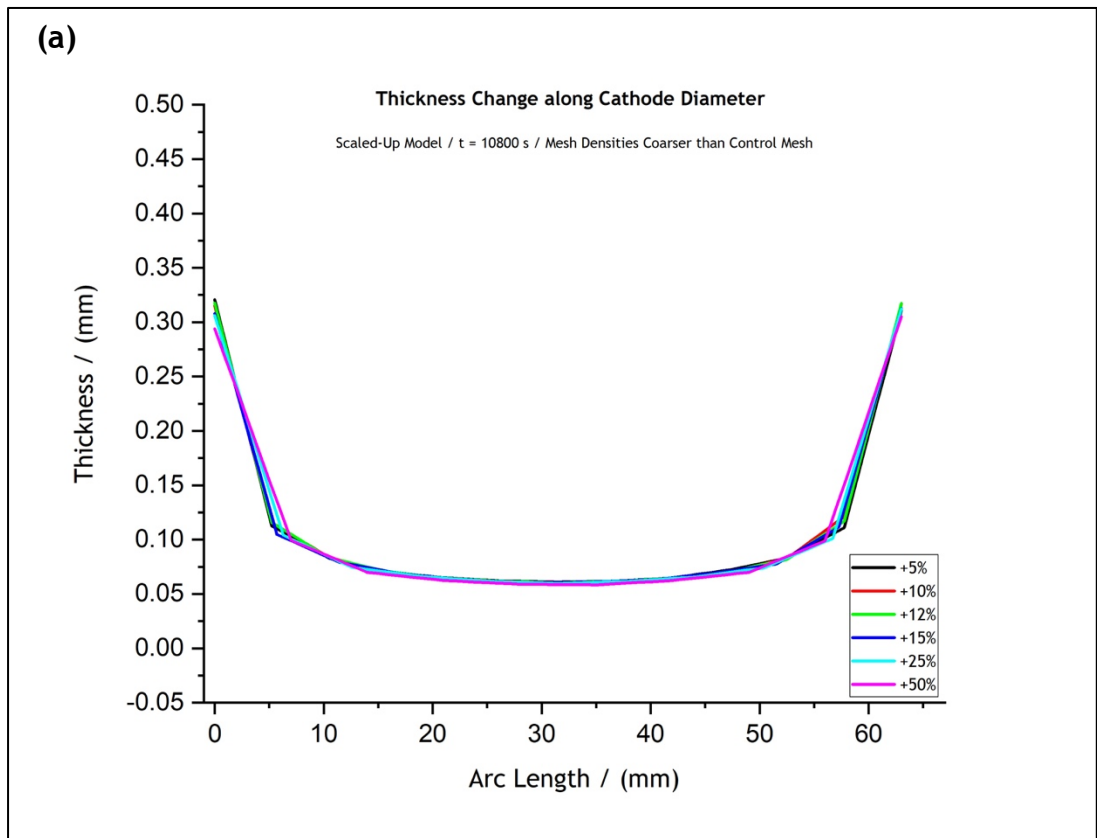


Figure 4. 13: Overlap of thickness profiles predicted by the scaled-up model following (a) an increase of the element size parameters by various percentages and (b) a decrease of the element size parameters by various percentages. Figure (a) shows the change in the results' quality for meshes coarser than the control mesh while, figure (b) shows the change in the results' quality for meshes finer than the control mesh. The results simulate a $3 h$ process at $50 \text{ }^\circ\text{C}$.

4.5.1 RDE System Model

4.5.1.1 Anode position

Geometry optimisation studies were first focused on how the distance between the electrodes affects the predicted thickness profiles of the deposits. In layman's terms this process examines when the anode placement is "felt" by the cathode (or mandrel), and at what distance this is effectively immaterial. In industry one needs to accommodate ergonomics and variation in cathode shapes, and if an arrangement were obtained when anode placement does not affect the current distribution at the cathode, then that arrangement can be used for a variety of systems.

At first, the anode position was changed only along the z-axis, with no change along the x-axis as vs. control simulations, (Figure 4.5-a). The anode remained off-centre at 10 mm from cathode same as that for the control case, whilst it was moved to 10 mm, 25 mm and 40 mm along the x-axis, such as shown in Figure 4.14. The computed results suggest that thickness profile along the RDE's diameter (Figure 4.14-d) does not experience any significant change. The different anode positions and their effect on the deposit thickness profile, as well as the cathode local current and potential values, are shown in Figures 4.14-a, 4.14-b & 4.14-c. The alteration of the anode position affects the surface potential of the cathode, mainly due to the changing ohmic drop within the electrolyte; the value of φ_s decreases as the anode is placed further and further away.

As a next step the anode was positioned in the centre of the cell and was varied along the x-axis, with reference to the cathode position. The position of the anode is shown in Figures 4.14-a, 4.15-b & 4.15-c. The thickness profile (Figure 4.15-d) again seemed to be unaffected by the movement of the anode. However, the local current density presents a notable change only when the anode is placed closest to the cathode surface, *i.e.*, 10 cm from the cathode, when the thickness profile observed to be flatter (Figure 4.15-d / red line) compared to the other ones corresponding to the other two anode positions.

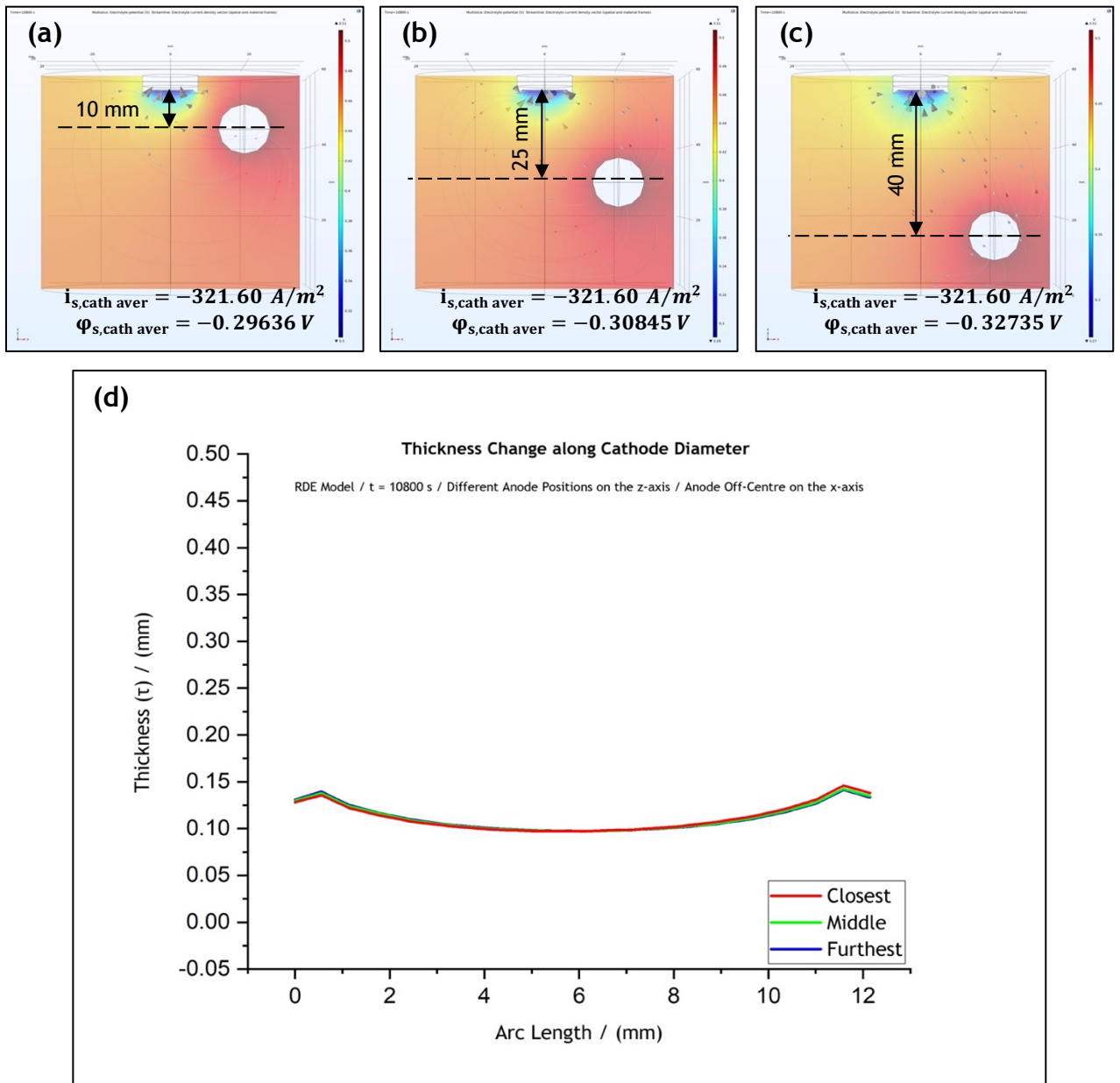


Figure 4. 14: (a)-(c) Variations of anode position along the z-axis, with a fixed x-axis position. (d) Effect of anode position on the predicted thickness profile for anode position at 10 mm (red); 25 mm (green); and 40 mm (blue).

In this regard further investigation was carried out where the anode was placed in two extreme positions: in the centre of the cell along the x-axis and at 7 mm, the closest possible, from the cathode surface (Figures 4.16-a & 4.16-c), and off-centre at 43 mm from the cathode surface (Figures 4.16-b & 4.16-d). The thickness profile

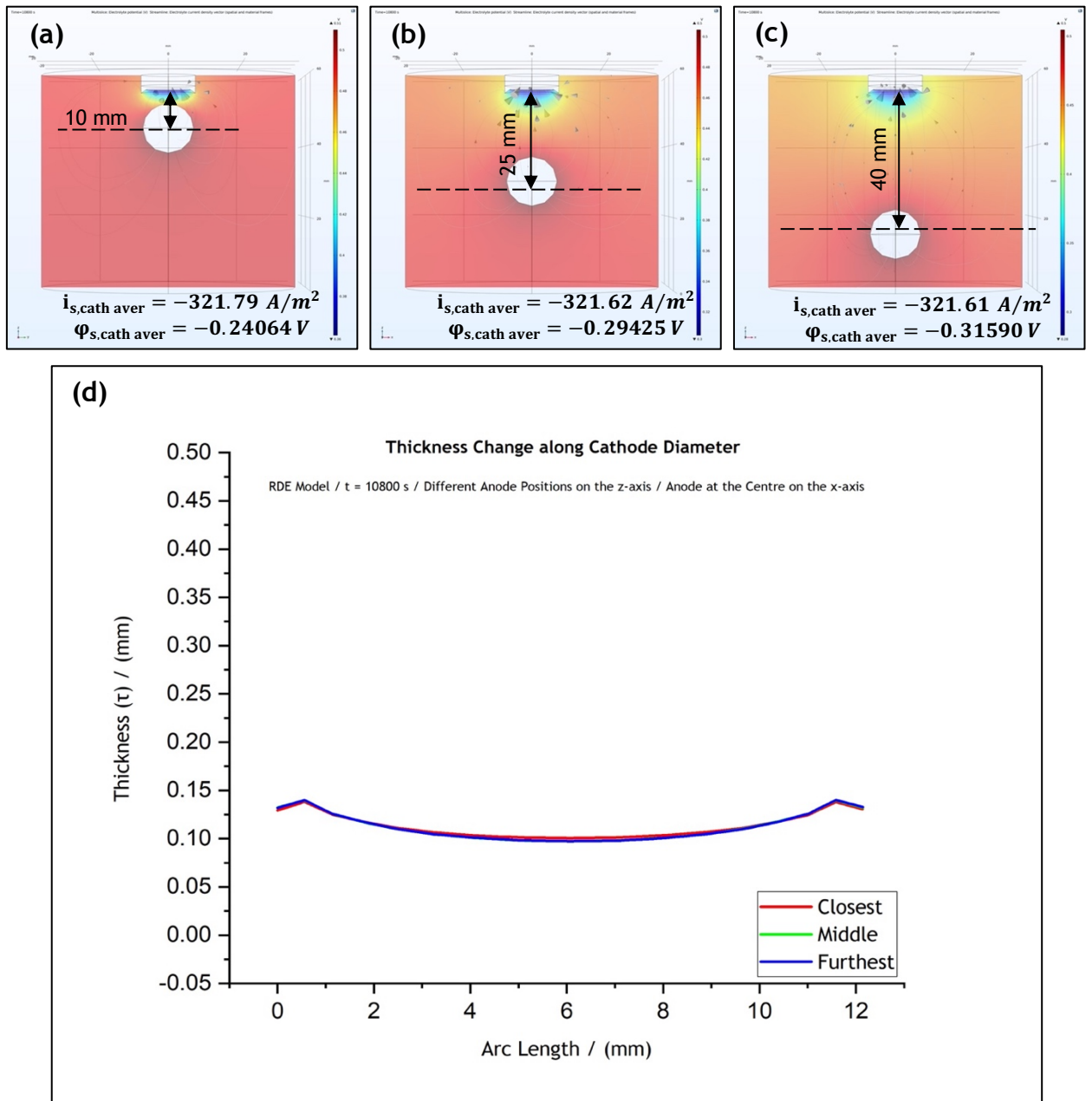


Figure 4. 15: (a)-(c) Variations of anode position along z-axis, with a fixed x-axis position at the centre of the cell. (d) Effect of anode position on the predicted thickness profile for anode position at 10 mm (red); 25 mm (green); and 40 mm (blue).

(Figure 4.16-e) is differentiated from the control profile only for the anode position closest to cathode. For the position furthest from cathode, the thickness profiles overlap with the control thickness profile (and hence cannot be seen in the figure). This indicates that local current density presents a notable change when the anode

is placed closest to cathode (Figure 4.16-a). The local potential at the cathode surface differs due to the difference in ohmic drop with its value being ~33.9% higher when the anode is positioned at 7 mm from the cathode surface (refer to Figures 4.16-a & 4.16-b).

Our results suggest that the anode affects significantly the cathodic local potential and current density values only when it is placed closer than 10 mm from the cathode surface. For any greater distance between the two electrodes the anode position does not significantly affect the cathode current density value or thickness profile. In practice, it is rare for the anode vs cathode distance to be significantly less than 10 mm. Indeed, our results indicate that it may be prudent to place it at some distance where the current distribution is less sensitive to their placement.

4.5.1.2 Cell boundaries

The next set of optimisations was focused towards determining the effect of reactor boundaries. In industry, often very large-scale systems are used, and the size of anode and cathode are changed depending on clients' needs without any changes to tank or reactor size. It is important, therefore, to elucidate what is likely to happen to current distribution (or deposit thickness) when such arbitrary changes are made, and if engineering judgement can be applied to mitigate these changes.

For this set of studies, the electrode boundaries were kept the same as in the control simulation (25 cm from the cathode surface) (Figure 4.6-a) while the cell dimensions were doubled and potential distribution and current density at the cathode were simulated. The results of these computations are shown in Figures 4.17-a & 4.17-c. Following that, another study was carried out with the anode positioned at the bottom (48 cm from the cathode surface) (Figures 4.17-b & 4.17-d). The thickness profiles predicted for both cases are presented in Figure 4.17-e.

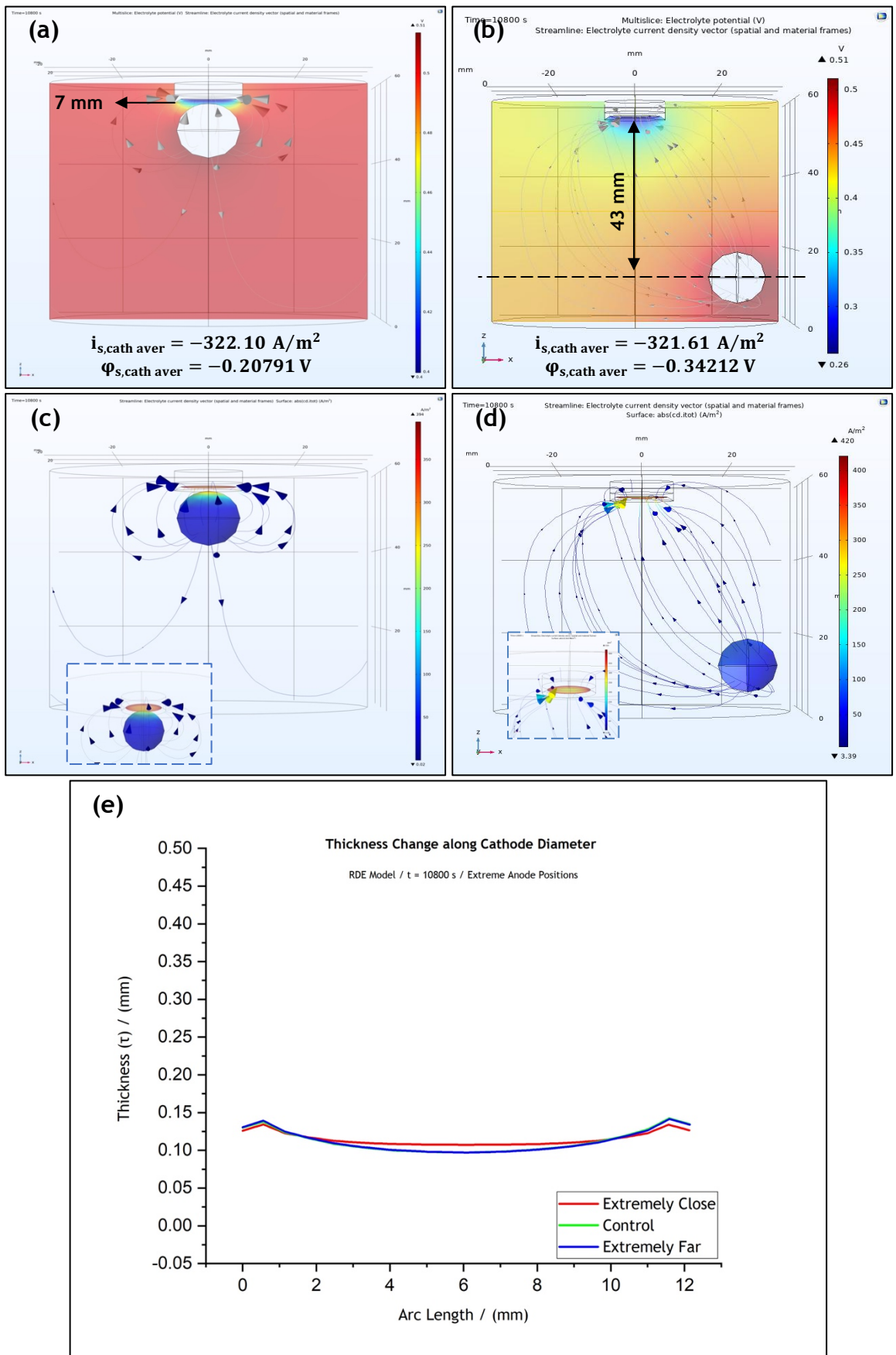


Figure 4. 16: 3-D representation of the potential distribution in the electrolyte volume of the RDE model when the anode is placed at (a) 7 mm and (b) 43 mm from the cathode surface. 3-D representation of the current streamlines on the cathode surface of the RDE when the anode is placed at (c) 7 mm and (d) 43 mm from the cathode surface. (e) Thickness profiles predicted for the geometries shown in figures (a) and (b). The results simulate potential and current distributions after 3 h at 50 °C. Anode distances are provided with reference to its geometric centre.

For both cases, the predicted thickness profile and local current density at the cathode remained unaffected. As it can be seen in [Figures 4.17-c & 4.17-d](#), the cathodic local current density was calculated at -321.60 A/m^2 for both cases. Indeed, for both cases studied as part of that set of simulations, thickness profile was found to be identical as the one observed for anode distances greater than 10 mm from the cathode surface ([Figure 4.17-e](#)). These results suggest that the size of the cell would not affect thickness distribution.

Based on our results, one can confidently suggest that, unless the distance between the electrodes is closer than 10 mm and the anode faces the cathode surface frontally, the anode position does not significantly affect the current distribution. This is important in an industrial situation, because often the placement of anode and cathode is dependent on electrode shape and size and ease of handling. Our computations show that slight changes in the position of the anode do not influence the thickness of the electroformed part, which is important in practice.

If a frontal placement of the anode, is required, additional geometry aids, like masks and thieves, might be needed to achieve the desired thickness uniformity. It is important to highlight here that exploring the effect of the anode is not of interest in this case because electroforming systems use anodes with surface areas at least double in size compared to cathode surface to avoid anode passivation [3]. As a result, real-life production setups render the size of the anode surface to be, somehow, irrelevant to the model design for electroforming.

4.5.2 Electroforming Reactor

The next reasonable step of this study was to investigate whether the conclusions drawn following the RDE simulations are also confirmed for the electroforming reactor. In this case too, the effect of three different anode positions in the industrial scale system's behaviour was investigated. These positions are shown in [Figures 4.18-a, 4.18-b & 4.18-c](#). Specifically, the system was studied with the anode placed at

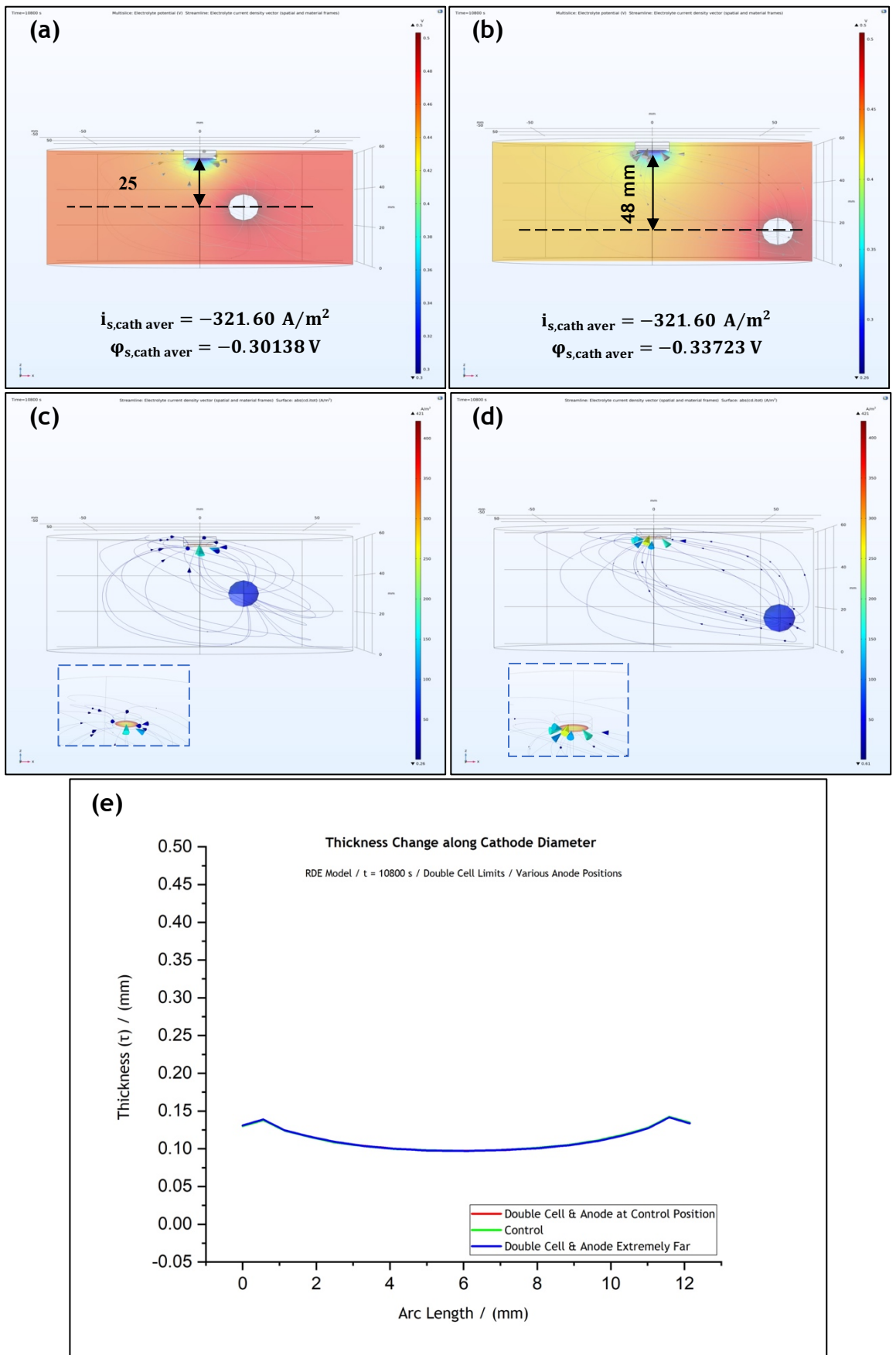


Figure 4. 17: 3-D representation of the potential distribution in the electrolyte volume of the RDE model when the cell boundaries are double than the control simulations and the anode is placed off-centre, at (a) 25 mm and (b) 48 mm from the cathode surface. 3-D representation of the current distribution on the cathode surface for the two cases when the anode is placed at (c) 25 mm and (d) 48 mm from the cathode surface. (e) Thickness profiles predicted for all anode positions. The results simulate potential and current distributions after 3 h at 50 °C. Distances are provided with reference to the anode's geometric centre.

the control position, 160 mm from cathode (Figure 4.18-a), at 5 mm below the cathode but off-centre (Figure 4.18-b), and at 10 mm from cathode facing its surface frontally (Figure 4.18-c). The off-centre and frontal positions are determined with reference to the anode's geometric centre.

The effect of each one of the anode positions on the thickness profile, as well as the cathodic local current and potential values for each case, are shown in Figure 4.18. The computed results suggest that thickness profile along the mandrel's diameter (Figure 4.18-d) is the same for the two cases when the cathode is off-centre; a more uniform thickness (hence current density) for the central part of the cathode is observed only for part (c). The alteration of the anode position has an effect on the local potential due to changes in ohmic drop within the electrolyte. These results are very similar to the findings for the RDE simulations discussed earlier.

The alteration of the anode position has an effect on the local potential, but the local current density on the cathode surface remained unaffected. Local current density was calculated at around -322 A/m^2 for all anode positions. These results are in total agreement with the ones expected following the RDE simulations discussed earlier.

Studies on the effect of anode position where the dimensions of the cell were doubled (36 L) were also conducted (Figure 4.19). Three different anode positions were examined; these varied between the frontal anode position at 10 mm from cathode and two other anode positions shown in Figures 4.19-a, 4.19-b & 4.19-c. For all three cases the predicted thickness profile is presented in Figure 4.19-d. Once more, the current distribution at the mandrel is identical for the cases when the anode is placed further away and becomes more uniform over the central part of the mandrel when the anode is placed frontally at 10 mm from the cathode surface.

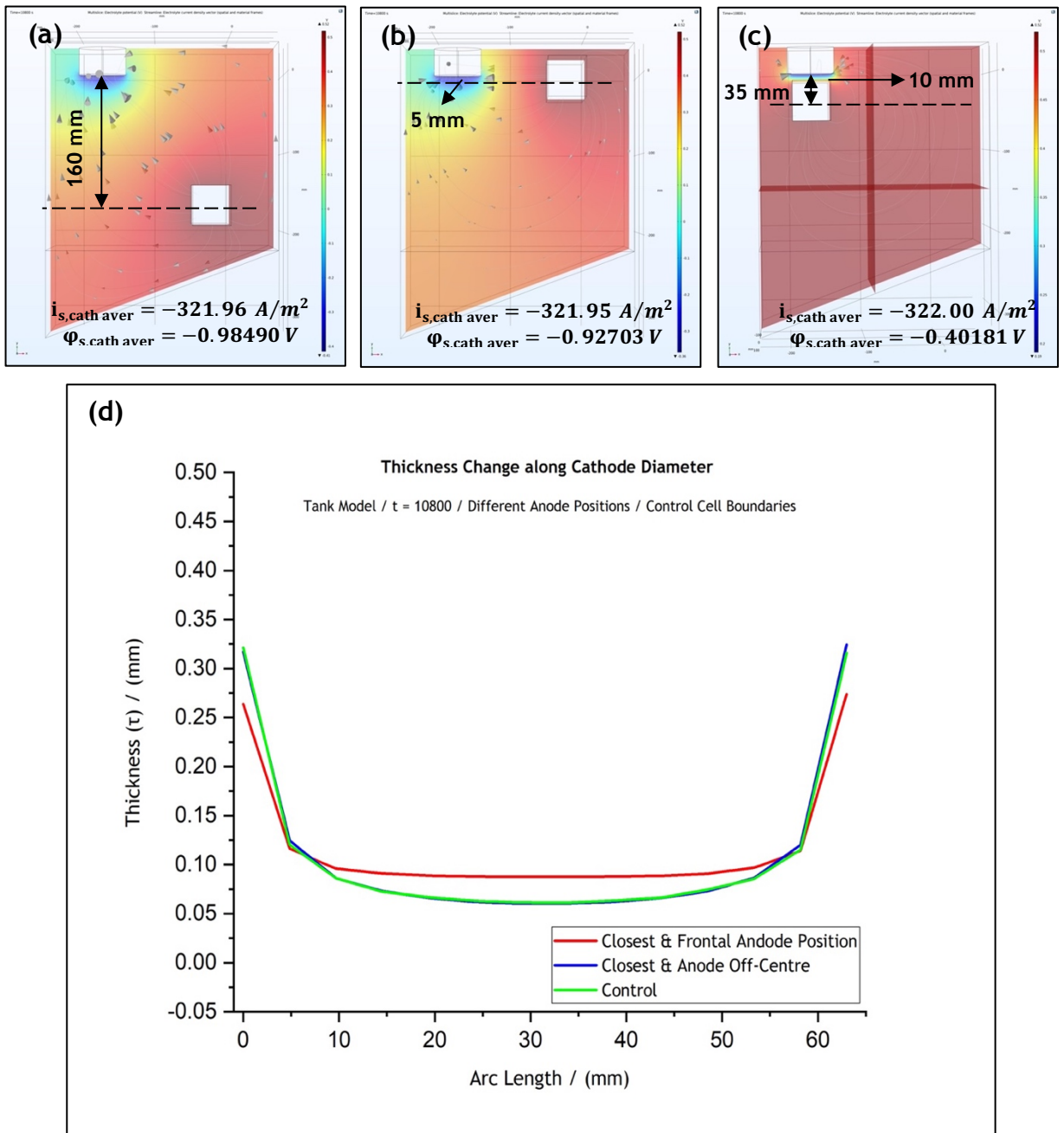


Figure 4. 18: (a)-(c) 3-D representation of the potential distribution in the electrolyte volume of the tank system model for anode positions at different distances from the cathode surface. Current streamlines in the electrolyte are also shown. (d) Effect of anode position on the predicted thickness profile. The local cathodic potential and current density values are provided for each case. The results simulate potential and current distributions after 3 h at 50 °C. Distances are provided with reference to the anode's geometric centre.

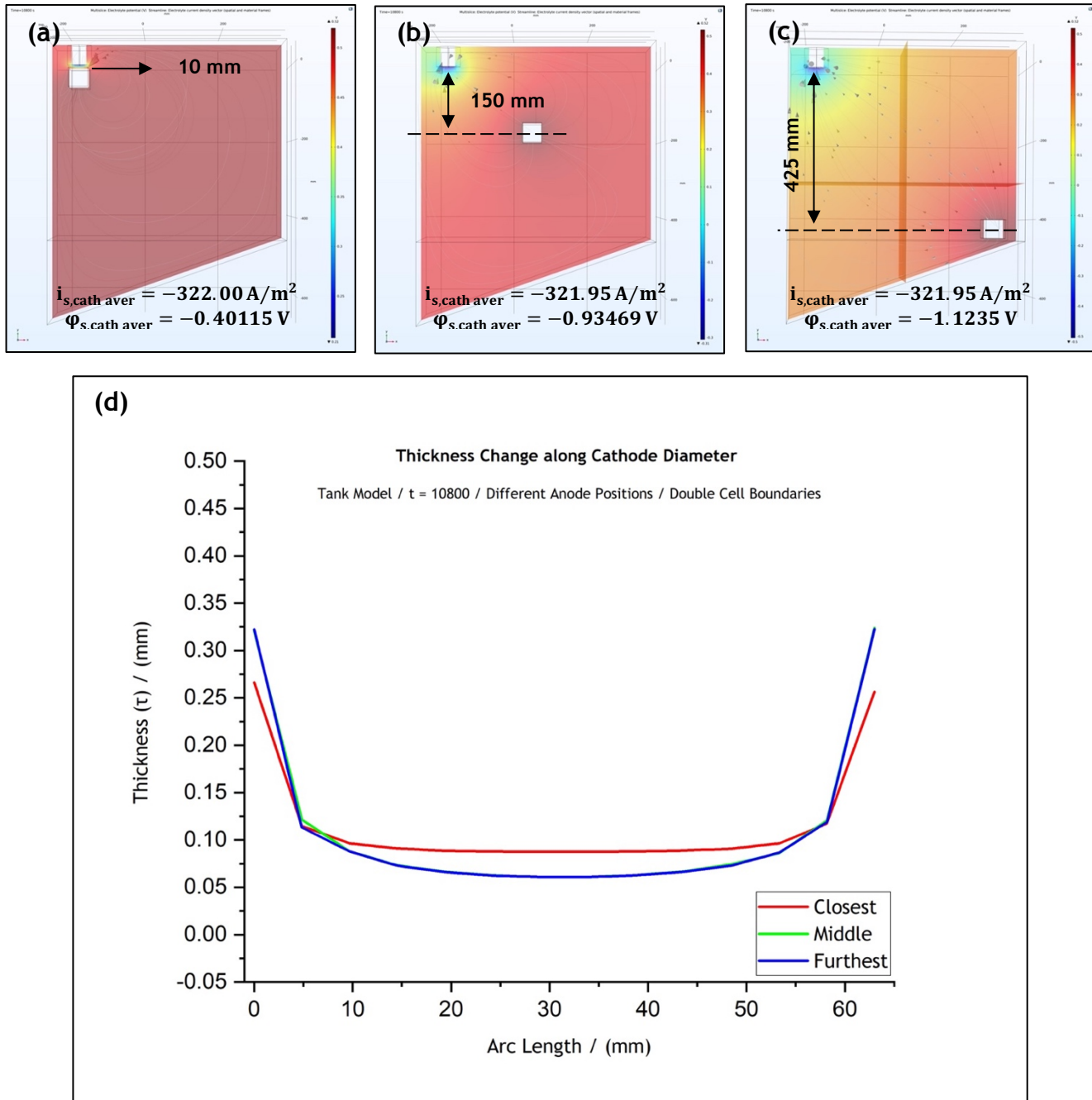


Figure 4. 19: (a)-(c) 3-D representation of the potential distribution in the electrolyte volume of the tank system model for anode positions at different distances from the cathode surface when cell boundaries are doubled. Current streamlines in the electrolyte are also shown. (d) Effect of anode position on the predicted thickness profile. The local cathodic potential and current density values are provided for each case. The results simulate potential and current distributions after 3 h at 50 °C. Distances are provided with reference to the anode’s geometric centre.

4.6 Conclusions

Nickel electroforming, time-dependent, models of two different scales were developed using a commercial software and were successfully validated against experimental data. The models were based on the assumptions of secondary current distribution (SCD) using Butler-Volmer kinetics. One model was developed to simulate the nickel electroforming process in a laboratory using a rotating disk electrode (RDE) while the second one represented an industrial, 18L, electroforming reactor configuration.

Electrochemical experimental data, collected via polarisation studies (refer to [Chapter 2](#)), were used as input for both models. The reaction at the cathode and anode were based on the overall nickel reduction and dissolution reactions, respectively. Current-potential data was used to fit exchange current density and forward and backward charge transfer coefficients. The model could be used to predict current-potential data even though a detailed reaction mechanism was not used.

At first a set of control simulations, modelling deposition processes in both scales at current values similar with those applied by the industry, were carried out to determine the potential and current at the electrode surface. The simulated results suggested that the total current and anode potential remain fixed, while the cathode surface local potential is adjusted by the model to calculate the local current density, which is then summed up to obtain the total current density and compared against the value set for the simulation.

The results obtained were validated by cross-checking the thickness of an electroformed disk using the RDE as well as the electroforming reactor. It was found that the formed material on the RDE was thinner than the predicted value. The thickness of the disk formed within the electroforming reactor, on the other hand, agreed reasonably with the values computed by the model. The difference in the agreement between the calculated and experimental value for the RDE was attributed to the growth of dendrites along the circumferential edge of the disk.

Mesh sensitivity studies were conducted to determine both models' inherent mesh spacing tolerance, as well as any differences observed between the two scales. Developed meshes for both models presented with a similar high element quality at ~ 0.65 . The control meshes of both models were modified by $\pm 5\%$, $\pm 10\%$, $\pm 12\%$, $\pm 15\%$, $\pm 25\%$, $\pm 50\%$ and -75% . Regarding the RDE model, an increase of mesh element size by 12% and a decrease of 25% were found to be the thresholds after which a minor deterioration of the thickness profiles' smoothness was observed. For the electroforming reactor model, the corresponding results revealed that an increase of the element size by 15% and a decrease by 50% had a major effect on the predicted thickness profiles' smoothness. However, no significant changes in the simulated thickness were observed for either model while the computation time increased significantly for the finest meshes in both scales. Therefore, in practice, it is suggested mesh spacing should be optimised against computation times.

Studies on the effect of anode location, which dictated the anode-cathode distance, on current uniformity within the RDE or reactor were performed using the models. It was found that anode positioning did not play a major role on the uniformity of the deposit. Secondly, the geometry of the reactor was changed to determine the effect of reactor boundaries on current uniformity.

For both scales, placing the anode frontally to the cathode, and within 10 mm of the deposition surface, resulted in increased thickness uniformity all over the electroform's "useful" area. Outside the 10 mm proximity zone, the models suggested that changes in anode position increases the ohmic potential drop but stops affecting current distribution. These results are relevant to industrial situations because one would like to minimise changes to the electroforming process due to anode positioning or reactor geometry.

References

- [1] S. R. Wolfgang E. G. Hansal, *Pulse Plating*, Bad Saulgau: Leuze Verlag, 2012.
- [2] C. Hindle, "Polypropylene (PP)," British Plastics Federation, [Online]. Available: <https://www.bpf.co.uk/plastipedia/polymers/pp.aspx#physicalproperties>. [Accessed 30 09 2021].
- [3] S. Roy and E. Andreou, "Electroforming in the Industry 4.0 Era," *Current Opinion in Electrochemistry*, vol. 20, p. 108-115, 2020.
- [4] E. Andreou and S. Roy, "Modelling the electroforming process: significance and challenges," *Transactions of the IMF*, 2021.
- [5] T. Dinan, "Experimental Investigation of the Current Distribution on a Recessed Rotating Disk Electrode," *Journal of the Electrochemical Society*, vol. 138, p. 2947, 1991.

Chapter 5: The Case of the Mechanical Vane

Following the scaling up studies presented in [Chapter 4](#), and having established the model's efficiency, the next stage included experimental and modelling studies of a part of industrial interest. Even though the model developed was validated in two different scales, the mandrel geometries under investigation have been simple ones. Therefore, a more complex geometry, with a more challenging profile, had to be studied for consistency and further validation purposes. To do that, the industry partner provided us with a mechanical vane mandrel with application in gas turbines to be used for part development following the approach laid out in [Chapter 2](#).

5.1 Mechanical Vanes in Gas Turbine Engines

A gas turbine engine is technically a heat engine which utilises air (working fluid) to provide thrust. The working cycle of the engine involves four stages: intake, compression, combustion, and exhaust. The main parts of a gas turbine are shown in [Figure 5.1](#) [1]. The goal of the engine is essentially to draw in air (intake), bring it to as a high pressure as possible (compression), mixing it with fuel to expand and accelerate it (combustion) before the energy produced is recovered in the turbine to power both the fan and the compressor. The air is finally travelling with its remaining kinetic energy through the nozzle (exhaust) where it undergoes further acceleration and is sent out the back of the engine to produce thrust [2].

Vaness play an important role as parts of a gas turbine engine, and they can be found both in the compressor and turbine. The function of a compressor is to cause a substantial rise in pressure to a flowing gas [3].

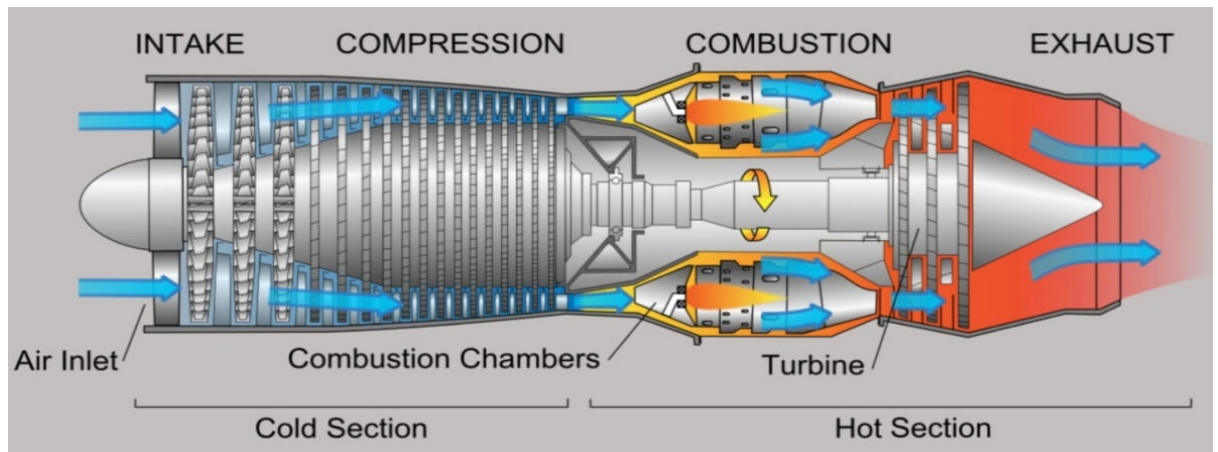


Figure 5. 1: Gas turbine components and principle. (Figure produced by engineeringlearn.com [1])

Centrifugal flow compressors [4] employ an impeller (Figure 5.2-a) to accelerate the air and a diffuser (Figure 5.2-b) to increase pressure at the required level while, axial flow compressors [5], employ rows of rotating blades and stationary vanes, alternately, to accelerate and diffuse the air until the required pressure rise is achieved. Regardless their type, vanes are static parts which guide the air among the different stages of rotating blades along the compressor (e.g., impeller vanes, diffuser vanes) ensuring that it always enters the next stage at an efficient angle to eliminate swirls and prevent turbulent flow, or even absorb vibrations which could impose an additional load to other vanes, like stator vanes (Figure 5.2-c) do [2].

On another part of the engine, the turbine (Figure 5.3-a) provides the power to drive the compressor and accessories as well as provide the required shaft power to a propeller or rotor (in case a jet is not the only way to generate propulsion). The turbine utilises the energy produced at the combustion system to lower the pressure and temperature of the gases produced during that stage. Using the same concept of alternating rows of stationary nozzle guide vanes and moving blades as the compressor, the turbine is able to produce the driving torque [2]. The design of the nozzle guide vane (Figure 5.3-b) and turbine blade passages is governed by aerodynamic considerations, which lead to a basic aerofoil shape for optimum efficiency and compatibility with the compressor and combustion design.

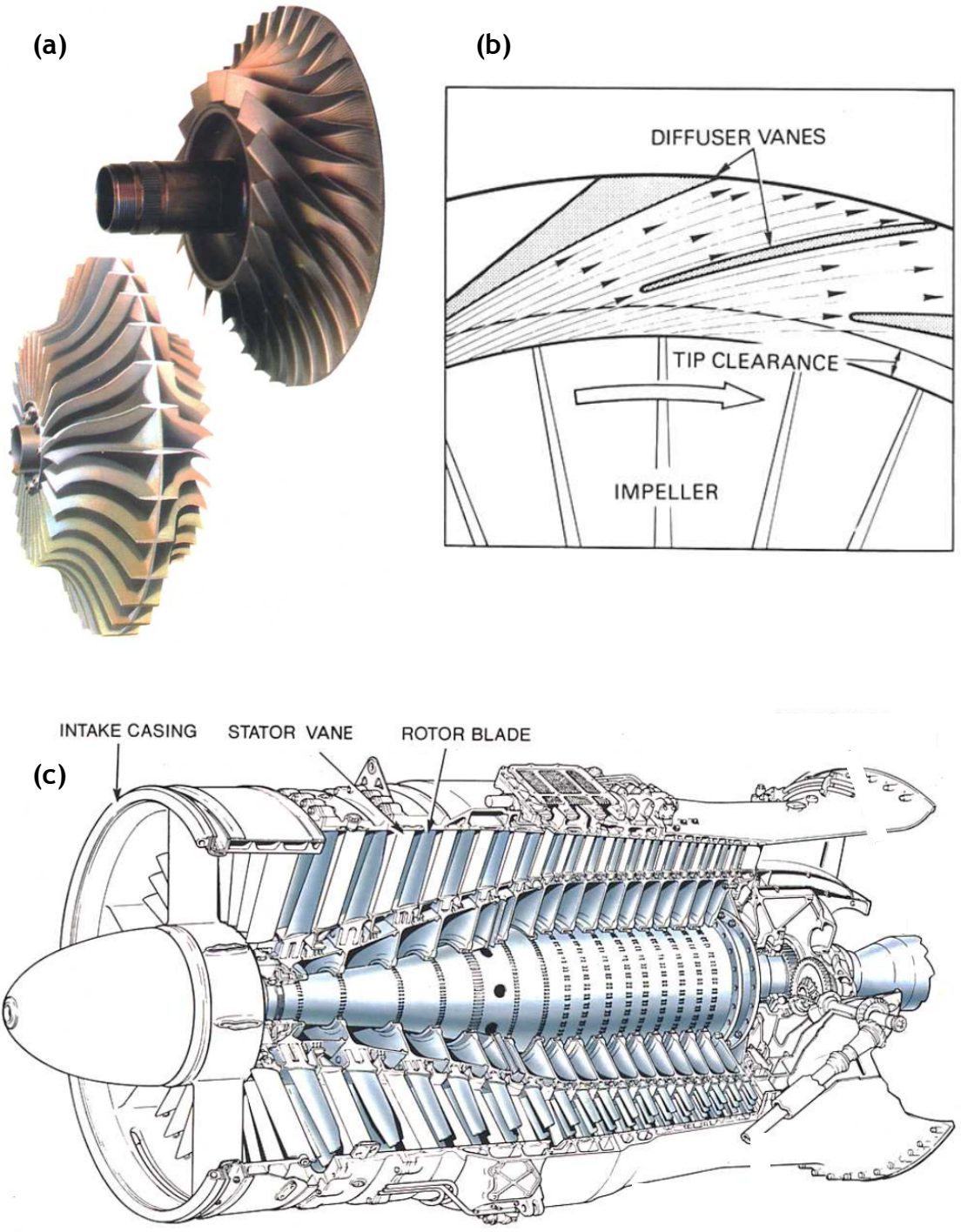


Figure 5. 2: (a) Impellers for centrifugal compressors, (b) air entry to the diffuser and diffuser vanes guiding the flow, (c) stator vanes in an axial flow compressor [2]

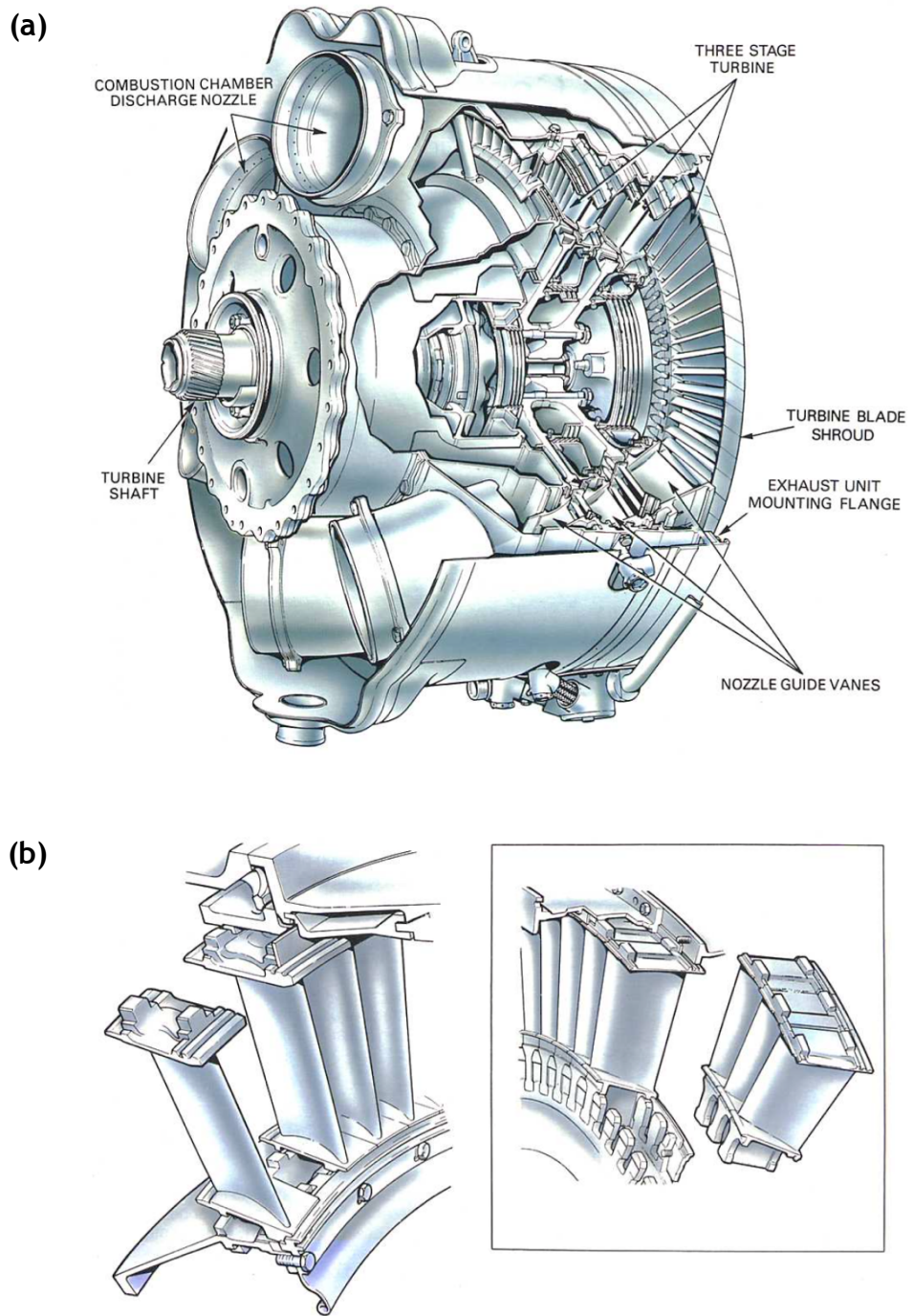


Figure 5.3: (a) Representative turbine schematic showing the position of nozzle guide vanes, (b) nozzle guide vanes detailed schematic [2]

Nozzle guide vanes help increasing gas velocity in an impulse turbine whilst reducing the pressure, guiding the gas towards the blades which experience an impulse force as a result. In a reaction turbine, on the other hand, the nozzle guide vanes control the direction of the gas flow without changing the pressure, which is felt as a reaction force by the converging blade passages due to the expanding and accelerating gas. Usually, gas turbine engines use an impulse-reaction combination. In all cases, the aerofoil shape of nozzle guide vanes forms a convergent duct between adjacent vanes to allow for minimising turbulent flow effects [2].

The nozzle guide vanes are usually hollow parts and can be cooled by passing air through them to reduce high thermal stresses and gas loads effects. Due to their static function, nozzle guide vanes do not endure rotational stresses therefore, heat resistance is the most required property for these parts. Consequently, nickel and nickel alloys are good candidate materials for vane applications [6] [7] [8] [9], however cooling might be required to prevent melting. Ceramic coatings can be employed to enhance heat resistance and, thus improve engine efficiency [10] [11] [12].

In general, mechanical vanes play an integral role in gas turbine engine design. Since their main function is to guide and optimise the air flow as the fluid moves through the engine, their design must abide by strict profile and thickness requirements, followed by low tolerances during manufacturing [13] [14] [15]. As near net shape parts, vanes are a very interesting challenge for the electroforming process therefore, in the following sections the experimental and modelling studies of an attempt to electroform such a vane geometry are presented.

5.2 The Vane Geometry

As it has already been mentioned, the industry partner provided a 304 stainless steel mandrel of a vane (Figure 5.4) for experimental and simulation studies. The geometry of this vane mandrel presented a challenging profile, with precision curves which would be very difficult (if possible at all) to be developed by any other traditional metal manufacturing process (e.g., forging or casting).

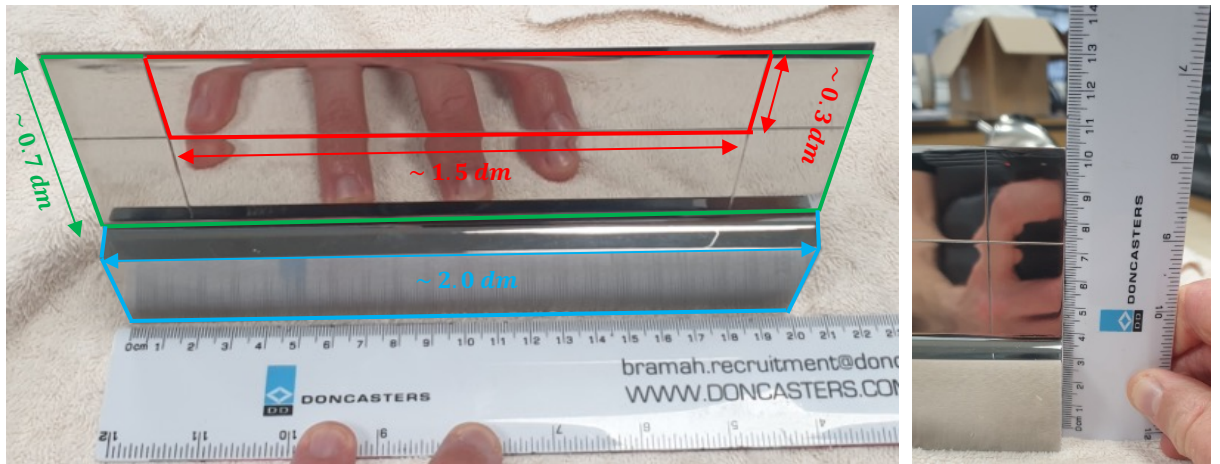


Figure 5. 4: Vane mandrel made of 304 stainless steel provided by Radius Aerospace for research and development of a real-life product. The area in red is always electroformed, the area in green may be masked or electroformed, the area in blue is always masked.

With reference to [Figure 5.4](#), the area in red (inside of the scribed lines) is always required to be electroformed while the area in green may be masked or electroformed and the area in blue should always be masked. Keeping in mind that there are two faces on the mandrel, and assuming that the curvature area at the “tip” is negligible, the total electroforming area is $A_{vane} = \sim 0.9 \text{ dm}^2$ (both sides), allowing for a trim allowance area of $\sim 1.9 \text{ dm}^2$, out of the total mandrel area of $\sim 2.8 \text{ dm}^2$.

The challenging profile of this mandrel is evident by the schematics shown in [Figure 5.5](#). The design requirements suggest that the part should present a changing profile in terms of thickness, starting from a thicker deposit of 1.2192 mm nominal at the tip, or “nose” (section AT), and transitioning to a thinner deposition of 0.127 mm nominal close to the geometry end boundary (section AY). For the part sections in between, section AU, section AV and section AW, the nominal target thicknesses are identified at 0.254 mm , 0.1524 mm and 0.127 mm , respectively. The detailed thickness profile transition requirements, as well as the acceptable tolerance, are presented in [Table 5.1](#). The colour code used to identify the part sections of different thicknesses in [Figure 5.5](#) is also used in [Table 5.1](#) for easy identification of the corresponding thickness targets.

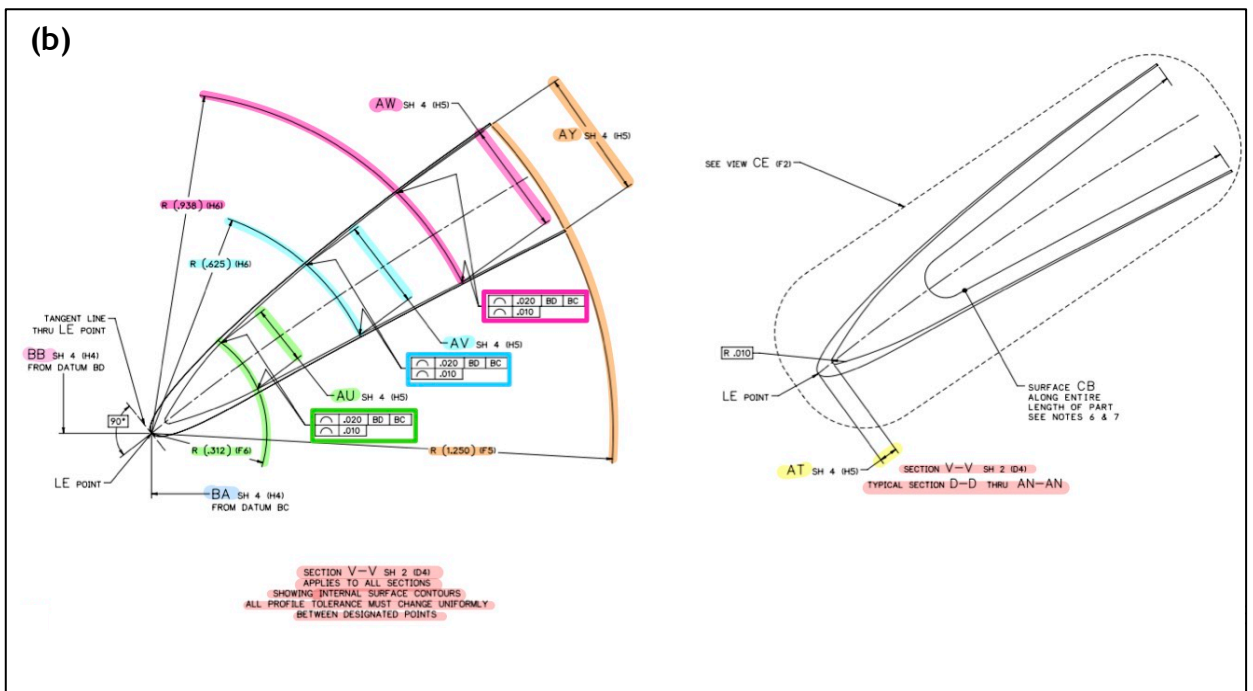
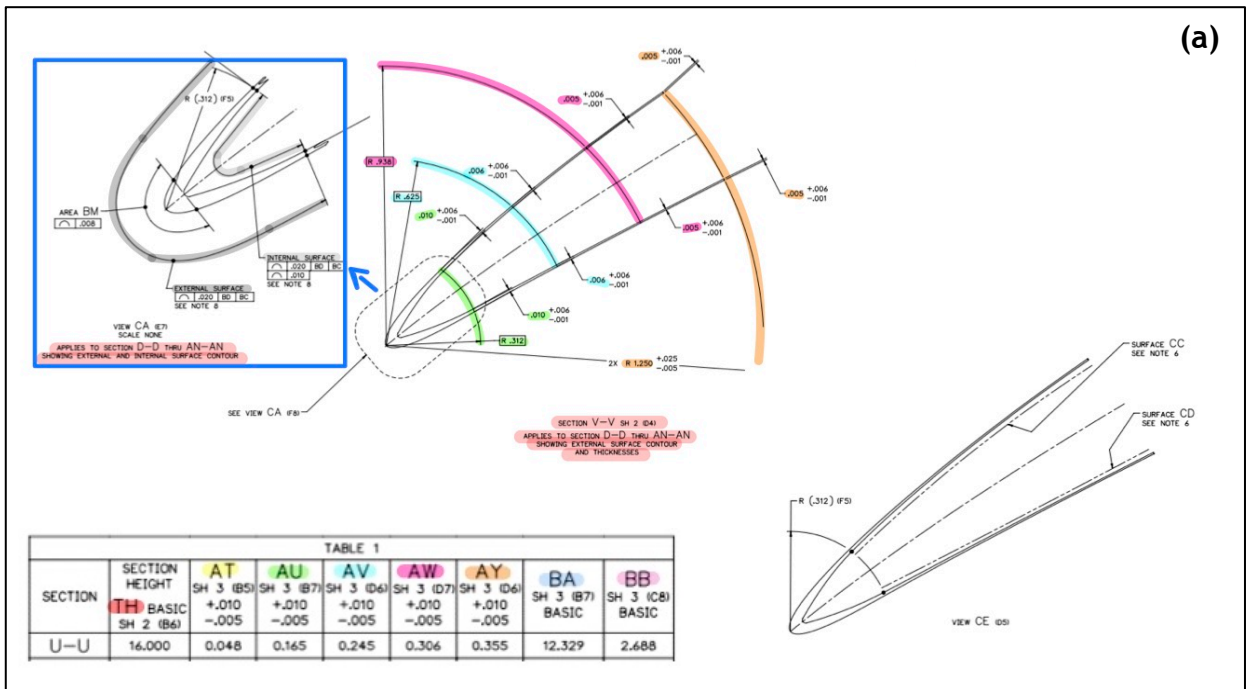


Figure 5. 5: Schematic of the vane mandrel geometry profile showing (a) the thickness target and (b) the tolerance for all five sections of the part.

Table 5. 1: Thickness target for the different sections of the vane mandrel. Nominal thickness targets and tolerances are provided.

Thickness Target (mm)					
Part Section	AT ("nose")	AU	AV	AW	AY (end boundary)
Nominal	1.2192	0.254	0.1524	0.127	0.127
Tolerance	0.254	0.1524	0.1524	0.1524	0.1524
	-1.27	-0.0254	-0.0254	-0.0254	-0.0254
Minimum	1.0922	0.2286	0.127	0.1016	0.1016
Maximum	1.4732	0.4064	0.3048	0.2794	0.2794

Figure 5.6 shows a plot of the thickness profiles corresponding to the minimum, nominal (target) and maximum thicknesses acceptable for each part section.

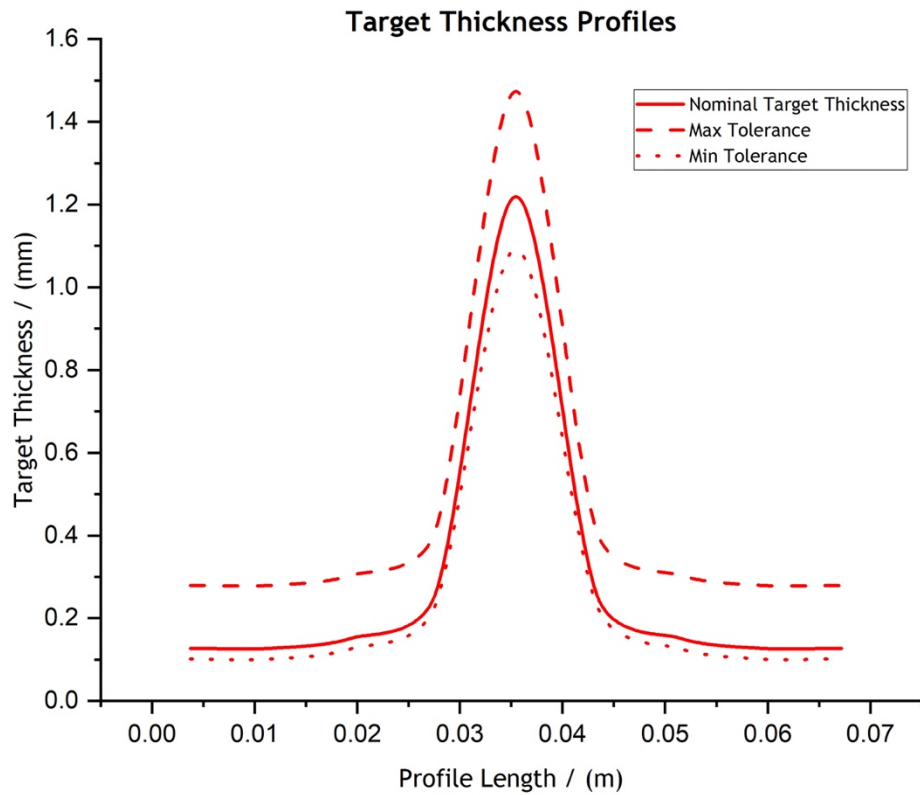


Figure 5. 6: Thickness profiles of the minimum (dotted line), nominal-target (straight line) and maximum (dashed line) acceptable thicknesses for each section.

5.3 Experimental Results

Nickel deposits were formed under various experimental conditions to assess both the predictability and consistency of the process. Table 5.2 summarises the details of the experiments conducted in the electroforming tank reactor using the mechanical vane mandrel. The equivalent mass of the deposited nickel presented here include the dendritic growth area around the leading edges, since the dendrites contribute towards current consumption.

Table 5. 2: Process parameters of the deposition experiments conducted in the electroforming tank reactor using the mechanical vane mandrel.

Deposit	Applied Current (A)	Current Density (A/dm ²)	Duration (h)	Deposit Mass (g)
R1	1	1.11	5	5.4
R2	2.2	2.44	5	10.39
R3	4.4	4.89	5	19.79
R4	4.4	4.89	2.5	12
R5	6.5	7.22	3.5	19.5
R6	6.5	7.22	5	30.856
R7	6.5	7.22	6	41.363

As it can be concluded based on the information shown in Table 5.2, the process results are predictable. Doubling the applied current density and keeping the deposition time the same leads to an almost double deposited nickel mass (compare electroforms R1 & R2, R2 & R3). The same behaviour is observed if deposition duration is doubled while the applied current density remains the same (compare electroforms R5 & R7). At the same time, if both the applied current density and deposition duration are halved the deposited nickel mass will remain approximately the same (compare electroforms R2 & R4).

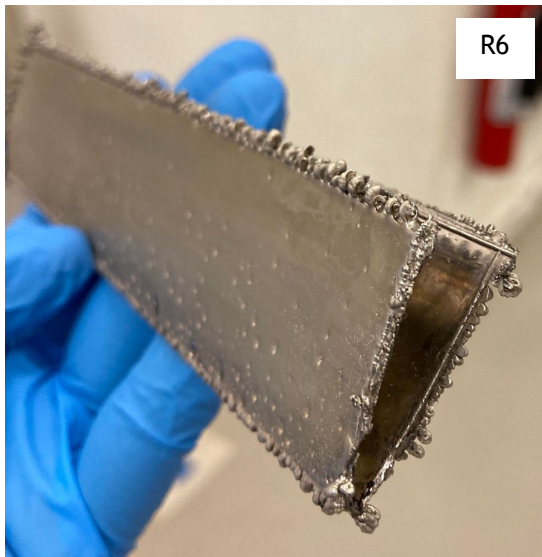


Figure 5. 7: Nickel mechanical vane electroforms R5, R6 and R7. The difference in the dendrites size is highlighted, with R5 presenting the thinnest dendrites around its leading edges and R7 the thicker ones. Electroforms R5, R6 and R7 were produced at $7.22 A/dm^2$ after deposition for 3.5 h, 5 h and 6 h, respectively, at 50 °C.

Through a closer inspection of electroforms R5, R6 and R7, which are shown in [Figure 5.7](#), someone can determine the growth rate of the process in terms of depositing nickel mass. By keeping the current density at $7.22 A/dm^2$, deposition for 3.5 h leads

to a growth rate of $\sim 5.57 \text{ g/h}$ (R5), deposition for 5 h leads to a growth rate of $\sim 6.2 \text{ g/h}$ (R6) while, deposition for 6 h leads to a growth rate of $\sim 6.9 \text{ g/h}$ (R7).

These results suggest an average process growth rate of $\sim 6.2 \text{ g/h}$. Since all deposits were weighted as a whole, including the dendritic growth around their leading edges, the small differences in the deposited nickel mass among the three deposits is attributed to the different dendrite sizes observed. The dendrites observed around electroform R5 are considerably thinner than the ones observed around electroforms R6 and R7, in order of increasing dendrite size, as it is shown in [Figure 5.7](#).

On another front, the systematic experimental approach revealed a correlation between the applied current density and the electroforms' surface finishing. As it can be seen in [Figure 5.8](#), electroforms R1 and R2 which were produced by deposition at 1.11 A/dm^2 and 2.44 A/dm^2 , respectively, for 5 h, presented a shiny surface finishing while, electroform R4 which was produced by deposition at 4.89 A/dm^2 for 2.5 h, presented a matte surface finishing. Interestingly enough, electroform R3, produced by deposition at 4.89 A/dm^2 for 5 h, presented a matte surface finishing at the sides and a shiny one in the middle.

A surface with little or no roughness allows only a small range of incident directions for which light can be reflected toward a point of observation, resulting in these surfaces being identified as shiny ones by an observer [16]. Since shiny surfaces are observed either at lower current densities, or after deposition at higher current densities for shorter periods, these observations suggest that the first layers are deposited on the cathode creating a smooth which appears shiny. As more layers are being deposited, either because of faster deposition at higher current densities, or because of longer deposition periods even at lower current densities, the surface roughness increases hence the surface appears with a matte finishing.

As a general comment, the qualitative analysis of the surface appearance of electroforms discussed here indicates that deposition progresses from the sides of the cathode towards the middle of it. The faster deposition rate at the sides of the mandrel

is also confirmed by the thickness distribution studies carried out for the vane electroforms and which are discussed in detail in the following section.

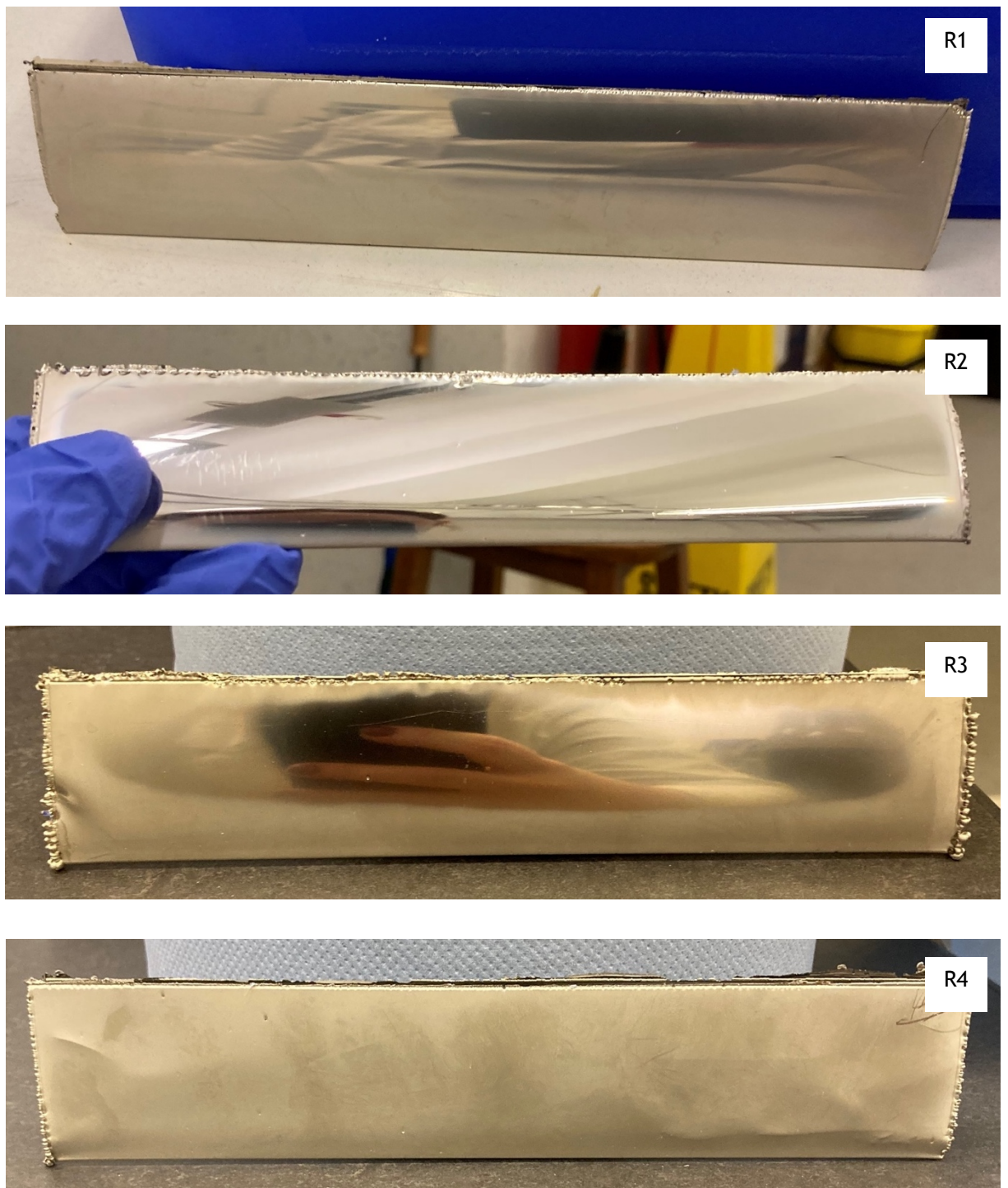


Figure 5. 8: Nickel mechanical vane electroforms R1, R2, R3 and R4. The gradual change in surface finishing is highlighted. Electroforms R1, R2 and R3 were produced at $1.11 A/dm^2$, $2.44 A/dm^2$ and $4.89 A/dm^2$, respectively, after deposition for $5 h$ at $50\text{ }^\circ\text{C}$. Electroform R4 was produced at $4.89 A/dm^2$ after deposition for $2.5 h$ at $50\text{ }^\circ\text{C}$.

5.4 Model & Validation

A time-dependent 3-D model of the mechanical vane system was developed within the *Electrodeposition* module of *COMSOL Multiphysics*[®] following the same approach that was used for the two 3-D models already discussed in [Chapter 4](#). Both the experimental and modelling studies of the mechanical vane geometry were conducted considering the deposition area to be the one indicated in red in [Figure 5.4](#), while the rest of the mandrel area was kept masked. [Figure 5.9](#) below shows the mandrel geometry as introduced in the modelling software. Here, the front ([Figure 5.9-a](#)) and back ([Figure 5.9-b](#)) view of the mandrel are provided, with the deposition area indicated in blue. Throughout this chapter, “front” indicates the mandrel face closer to the anode. In the circle, the tip of the mandrel, also referred to as the “nose”, is highlighted.

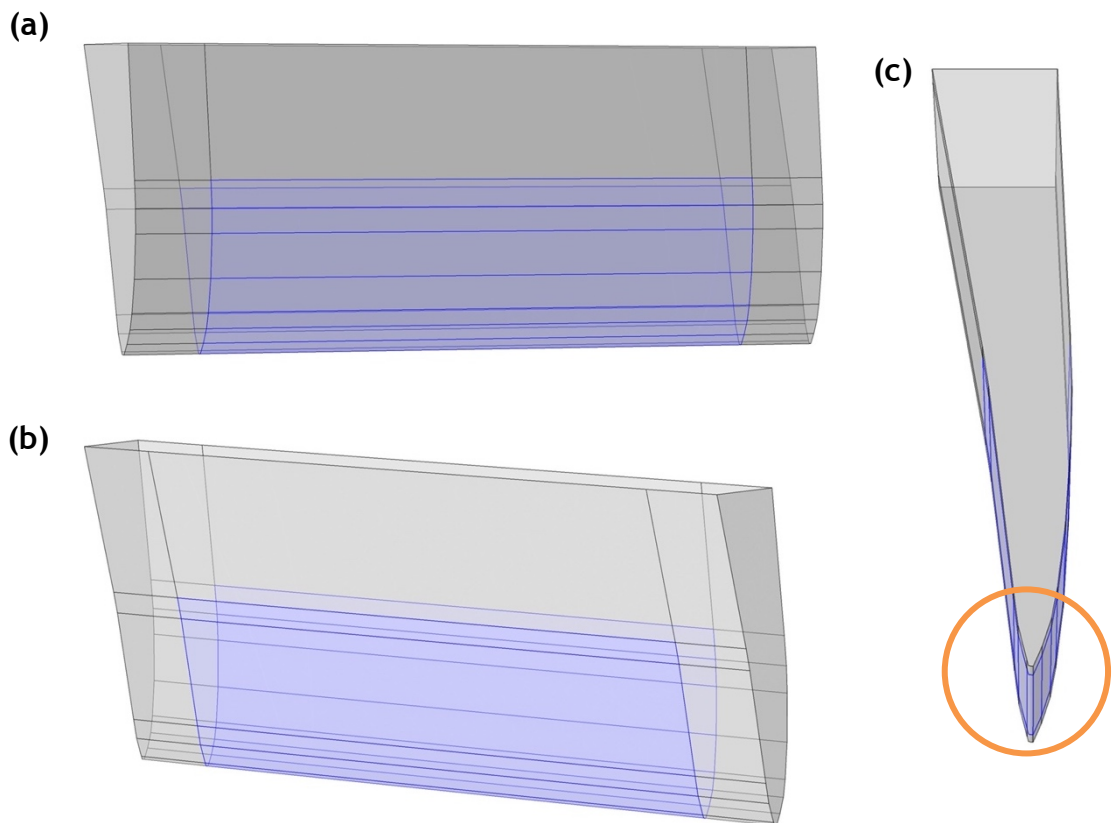


Figure 5. 9: 3-D geometry of the mechanical vane mandrel used in *COMSOL Multiphysics*[®]. (a) Front and (b) back views of the deposition area. (c) Side view of the mandrel revealing the challenging profile of the tool. The “nose” of the mandrel indicated in the circle.

Figure 5.9-c shows the side view of the mandrel which reveals the challenging curved profile of the tool.

A user-defined mesh spacing was chosen for the vane model (Figure 5.10-a). This included 164,759 elements with minimum element quality of 0.2108 and an average element quality of 0.6564. Once more, the mesh on the cathode boundary was the finest (Figure 5.10-b). The meshing parameters are provided in Table 5.3. The area below the orange line in Figure 5.10-b indicates what was considered to be the “nose” area. Because of the significantly intense curvature of the mandrel’s tip, the mesh spacing there had to be extremely fine to avoid convergence issues due to inverted mesh elements. The rest of the mandrel area was spaced using a smooth increase in mesh element size while the remaining geometry, including the anode boundary, was spaced based on the general parameters provided in Table 5.3. The mesh was mainly made up of tetrahedrals, with some triangular elements also used to optimise mesh spacing close to challenging edges, like the ones enclosing the deposition area and highlighted in orange in Figure 5.10-b.

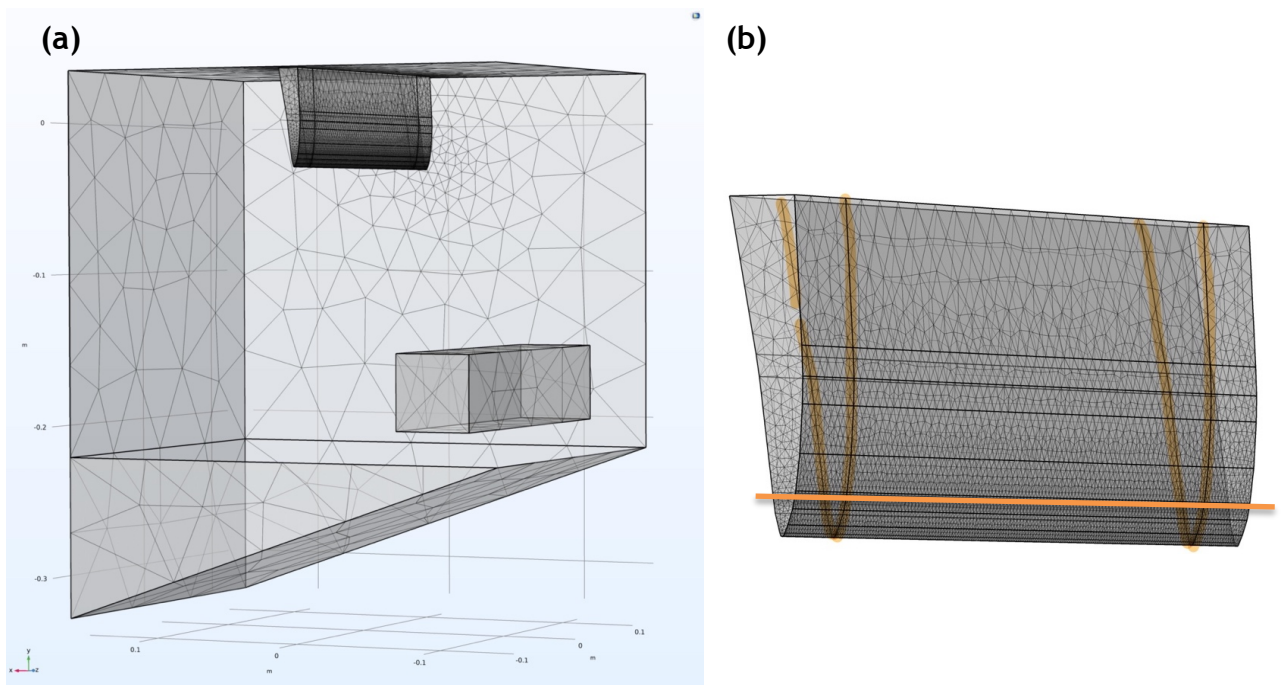


Figure 5. 10: Mesh spacing of (a) the whole 3-D mechanical vane model domain and (b) the whole mandrel area.

Table 5. 3: User-defined, general and boundary, user-defined, element size parameters for both the RDE and scaled-up models.

Element Size Parameters	General	“Nose”	Rest of Cathode
Maximum Element Size (mm)	100	1.5	5
Minimum Element Size (mm)	1	–	–
Maximum Element Growth Rate	1.3	1.1	1.1

Secondary current distribution (SCD) was once more chosen to describe the problem physics. The electrochemical input parameters provided in Table 3.2 were used for the development of the mechanical vane model too. The simulations discussed in this chapter were designed to represent practical deposition experiments, at 50 °C, for 5 h, when the cell voltage lies at 5.4 V and deposition is conducted at a current density of $\sim 4.8 \text{ A/dm}^2$. To achieve that, the cathode phase condition was described by a total applied current $I_{l,total} = -4.4 \text{ A}$ and an applied boundary electric potential $\varphi_{s,ext,init} = -5.4 \text{ V}$, while the anode boundary was described by an applied boundary electric potential $\varphi_{s,ext} = 0 \text{ V}$ to represent a cell voltage at 5.4 V.

Figure 5.11 shows the current and potential distribution results after the simulation had converged. The simulations suggested a potential range within the electrolyte of -1.64 V to 0.51 V (Figure 5.11-a) and a current density range between 3.32 A/dm^2 and $2.28 \times 10^4 \text{ A/dm}^2$ (Figure 5.11-b). It is worth mentioning here that this maximum value of the local current density, much higher than the limiting current density of 208 A/dm^2 , is calculated for random spots around the anode area and therefore does not indicate any irregularities close to the working electrode. The current lines are shown here to, once more, bend away from the insulator walls since no current can pass through them, travelling towards the cathode surface and

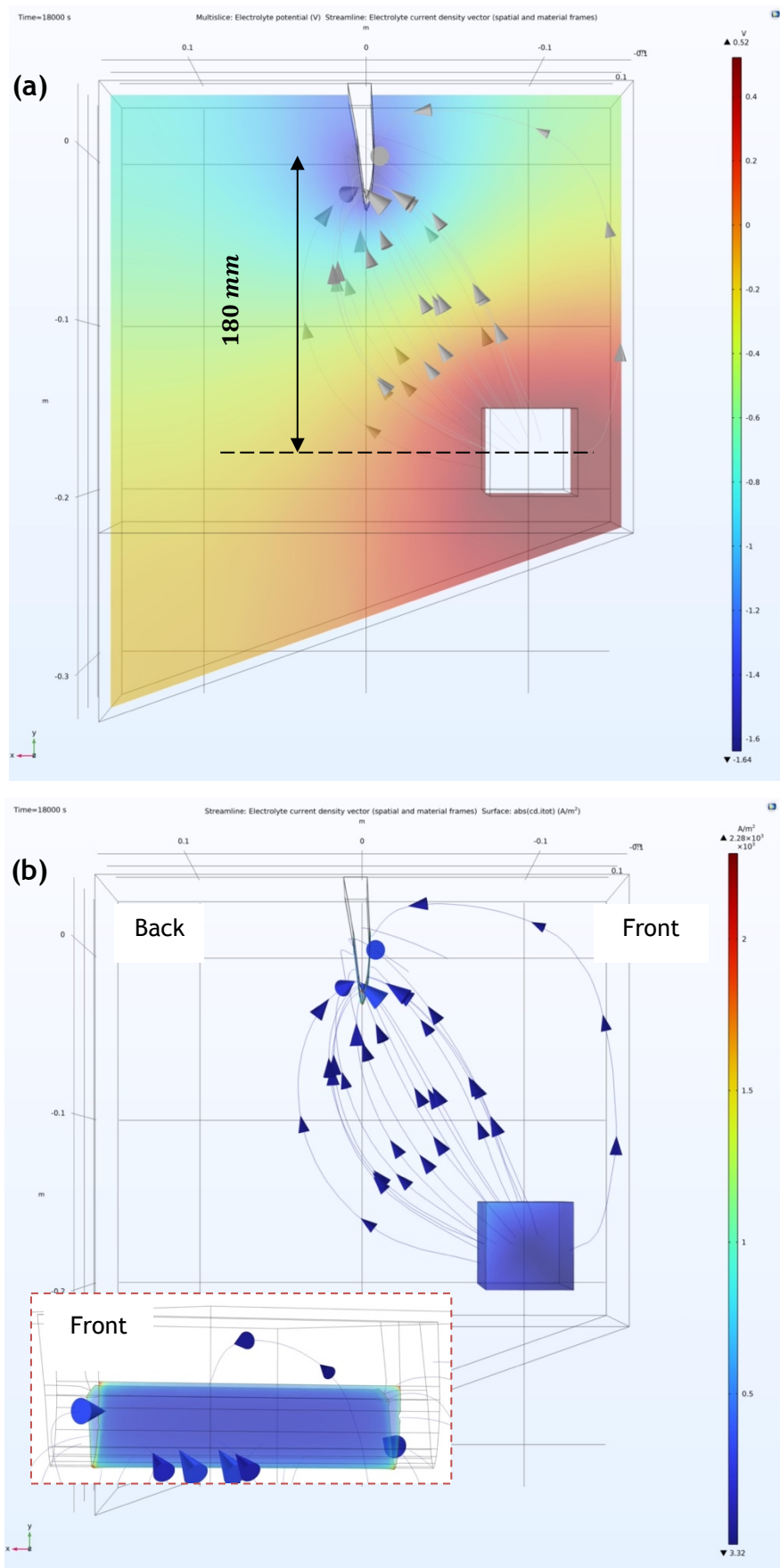


Figure 5.11: 3-D representation of (a) the potential and (b) the current distribution in the electrolyte volume of the mechanical vane model. The results simulate potential and current distributions after 5h at 50 °C. The vertical distance between the electrodes's geometrical centres is noted in figure (a). Current distribution on the cathode surface is shown in the cathode surface close up provided in figure (b).

concentrating specifically around the “nose”. These results agree with what is observed in practice; the vane deposits always present higher thicknesses at the “nose” compared to the remaining deposition surface.

Subsequently, [Figure 5.12](#) presents the simulated deposit thickness distribution. Since the current is predicted to be higher at the edges and the “nose”, a higher thickness was predicted at these areas. The range of the predicted thickness lies at an average of 0.2 – 0.45 mm, with the values reaching 0.45 mm closer to the leading edges and the “nose”. In [Figure 5.12](#) only the front face of the mandrel is shown just for visualisation purposes. Detailed numerical graphs follow as part of the model validation below.

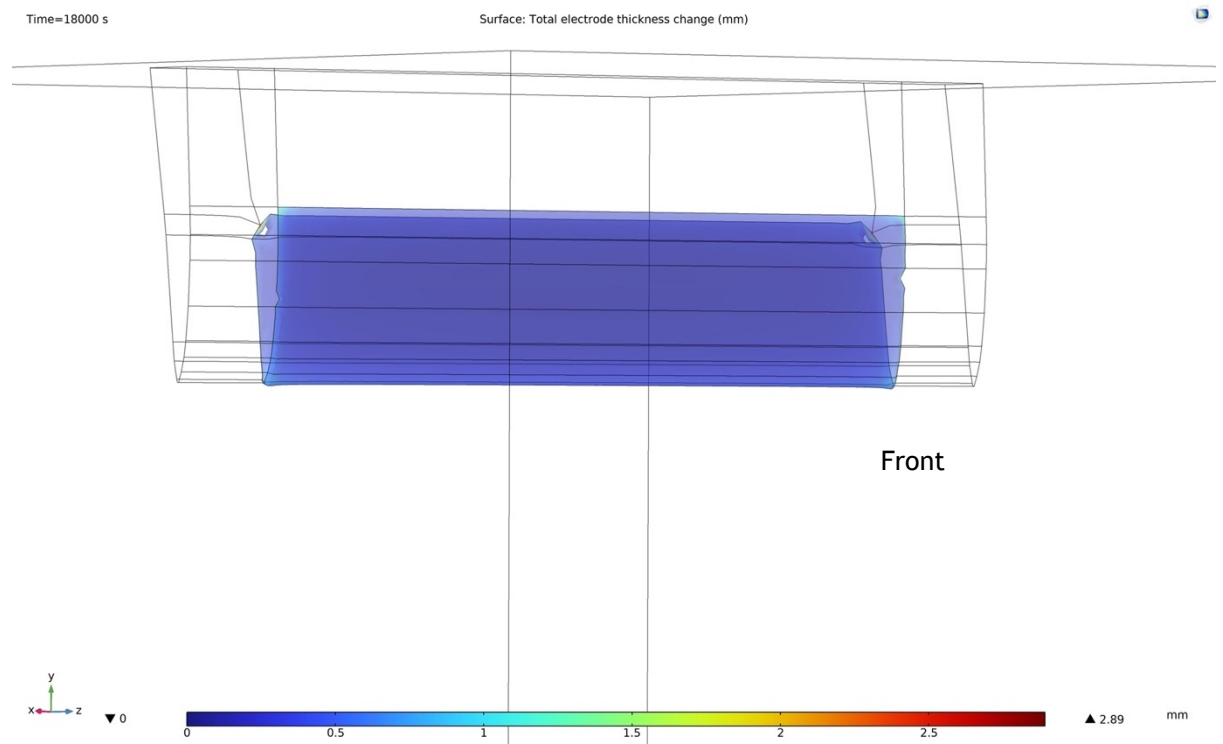


Figure 5.12: Simulated deposit thickness distribution on the mechanical vane deposition area. Only the “front” face is shown. The simulated non-uniform thickness distribution follows the previously simulated non-uniform current distribution, with higher currents at the edges and lower at the centre.

To validate the modelling results deposit R3 (Figure 5.13) was used. The experimental conditions applied to form this deposit were the same as the ones chosen for the simulations above ($-5.4 V$ and $-4.4 A$, for $18000 s$).

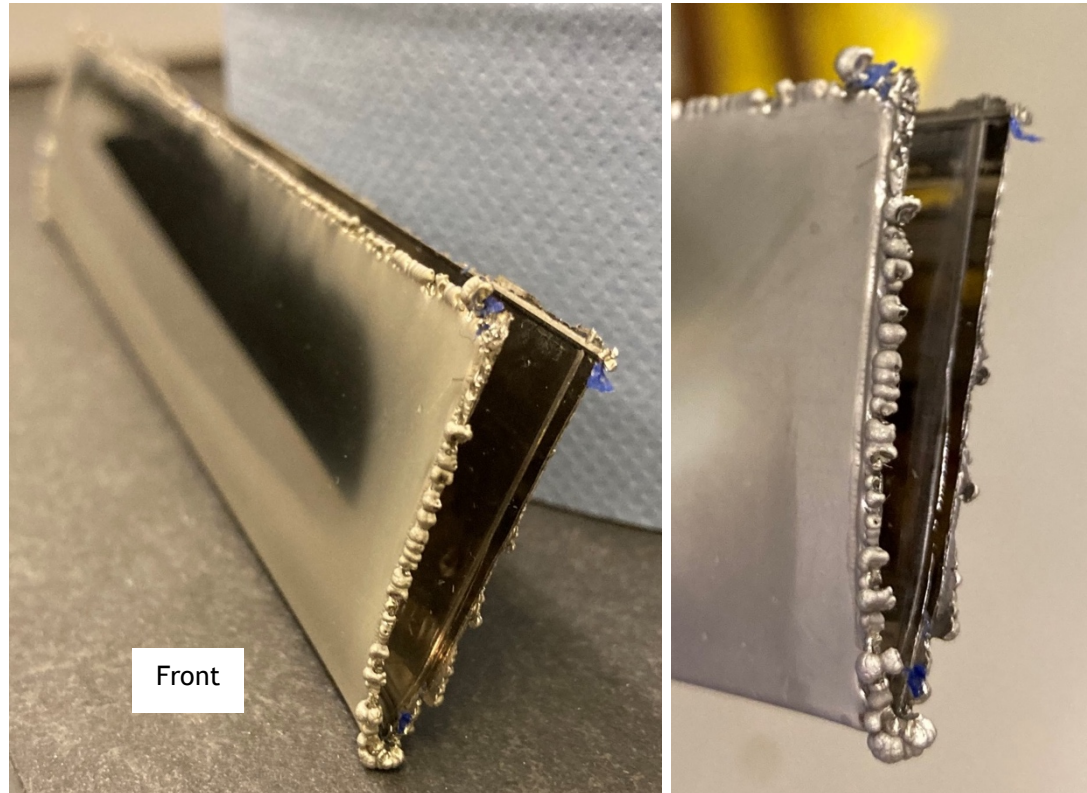


Figure 5. 13: Mechanical vane deposit R3. The deposit was formed of pure nickel and deposition was conducted at $-5.4 V$ and $-4.4 A$, for $18000 s$, at $50 ^\circ C$. “Front” indicates the mandrel side closer to the anode. The dendrites formed at the leading edges are also shown here.

Deposit R3 was sectioned across its width in three strips, as shown in Figure 5.14-a. One strip was retrieved from the middle of the part and two more on the left and right side of this middle section. The three strips were subsequently mounted in resin (Figure 5.14-b). The final specimen was placed under the optical microscope and studied at a $\times 20$ magnification in terms of the sections’ thickness. Measurements

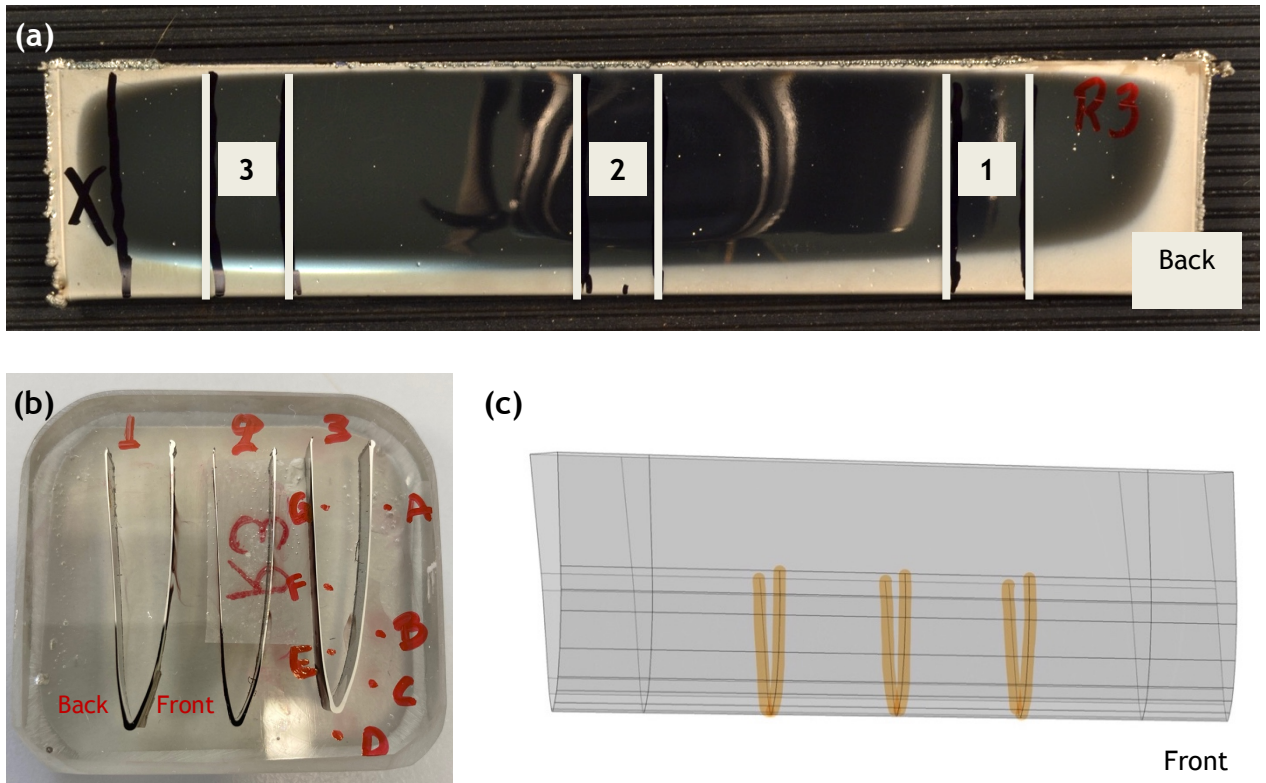


Figure 5.14: (a) The three strips deposit R3 was sectioned in as seen from the “back” face of the mandrel. (b) Mandrel sections mounted in resin specimen. (c) Corresponding boundaries along which simulated thickness results were retrieved. Section length is measured from point I to points II and III shown in figure (c).

Table 5. 4: Deposit R3 thickness measurements collected under the optical microscope.

Deposit Strip	Deposit R3 Thickness (<i>mm</i>)						
	4.4 A (CC) – 5 A/dm ² – 5 h – 50°C						
1	A	B	C	D*	E	F	G
	0.21	0.23	0.31	0.65	0.17	0.12	0.12
2	A	B	C	D*	E	F	G
	0.2	0.2	0.27	0.59	0.19	0.11	0.1
3	A	B	C	D*	E	F	G
	0.21	0.23	0.3	0.66	0.19	0.13	0.12

* Average of three measurements at the “nose”.

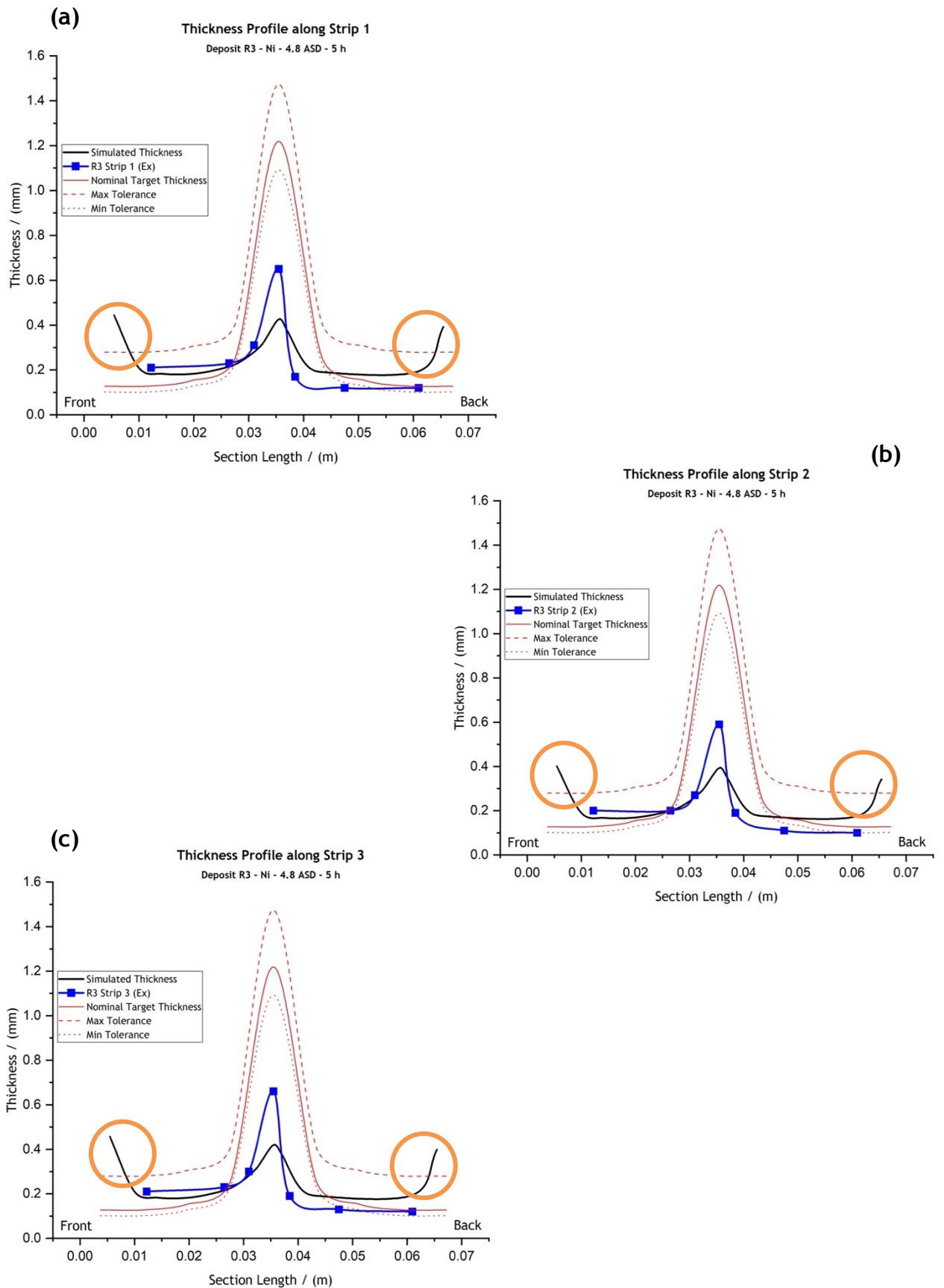


Figure 5. 15: Comparative graphs of the experimental and simulated thickness profiles for (a) strip 1, (b) strip 2 and (c) strip 3 of the mechanical vane deposit R3. Deposition of R3 was conducted at -5.4 V and -4.4 A , for 18000 s , at $50\text{ }^\circ\text{C}$. “Front” indicates the mandrel side closer to the anode. Circles highlight thicknesses that correspond to dendritic growth.

were taken at seven points (A-G) along each strip profile as indicated in [Figure 5.14-b](#). The highest thickness was measured at the “nose” at an average of 0.63 mm. [Table 5.4](#) summarises all the thickness measurements obtained for the specimen shown in [Figure 5.14-b](#). Figures of all optical microscope thickness measurements are provided in [Appendix I](#) at the end of this chapter. The corresponding predicted thicknesses were retrieved from the modelling results along the three edges highlighted in orange in [Figure 5.14-c](#).

Comparative plots of the experimental and simulated thickness profiles for each strip are provided in [Figures 5.15-a to 5.15-c](#). [Figures 5.16-a & 5.16-b](#) provide, respectively, overlaps of the experimental and simulated thickness profiles of all three strips deposit R3 was sectioned in. Point A corresponds to a length section of 0.012 m while points D and G to 0.036 m and 0.061 m respectively. No thickness measurements were taken at the leading edges where dendrites formed. However, the higher thicknesses at the leading edges were simulated by the model as highlighted by the orange circles in [Figure 5.15](#).

As it can also be seen in [Figure 5.15](#), the model follows the experimentally observed thickness distribution with higher thicknesses simulated at the “nose” and lower ones at the front and side faces of the mandrel. Nevertheless, the model underpredicts the thickness at the “nose” area by almost 30 %, while it is in reasonably good agreement with experimental thicknesses at the front and back faces of the tool.

Another interesting observation was that both experimental and modelling results in [Figure 5.16](#) suggest that the sides of the mandrel grow faster than its middle. Blue and red lines, corresponding to strips 1 and 3 retrieved from the sides of deposit R3, are perfectly overlapping across the section length, while the orange line, corresponding to strip 2 retrieved from the middle of the deposit, lies consistently lower. This result is consistent with the qualitative observation that deposition is higher at the sides of the vane, as presented in the last paragraph on page 11.

The agreement between the experimental and modelling results is not good, how-

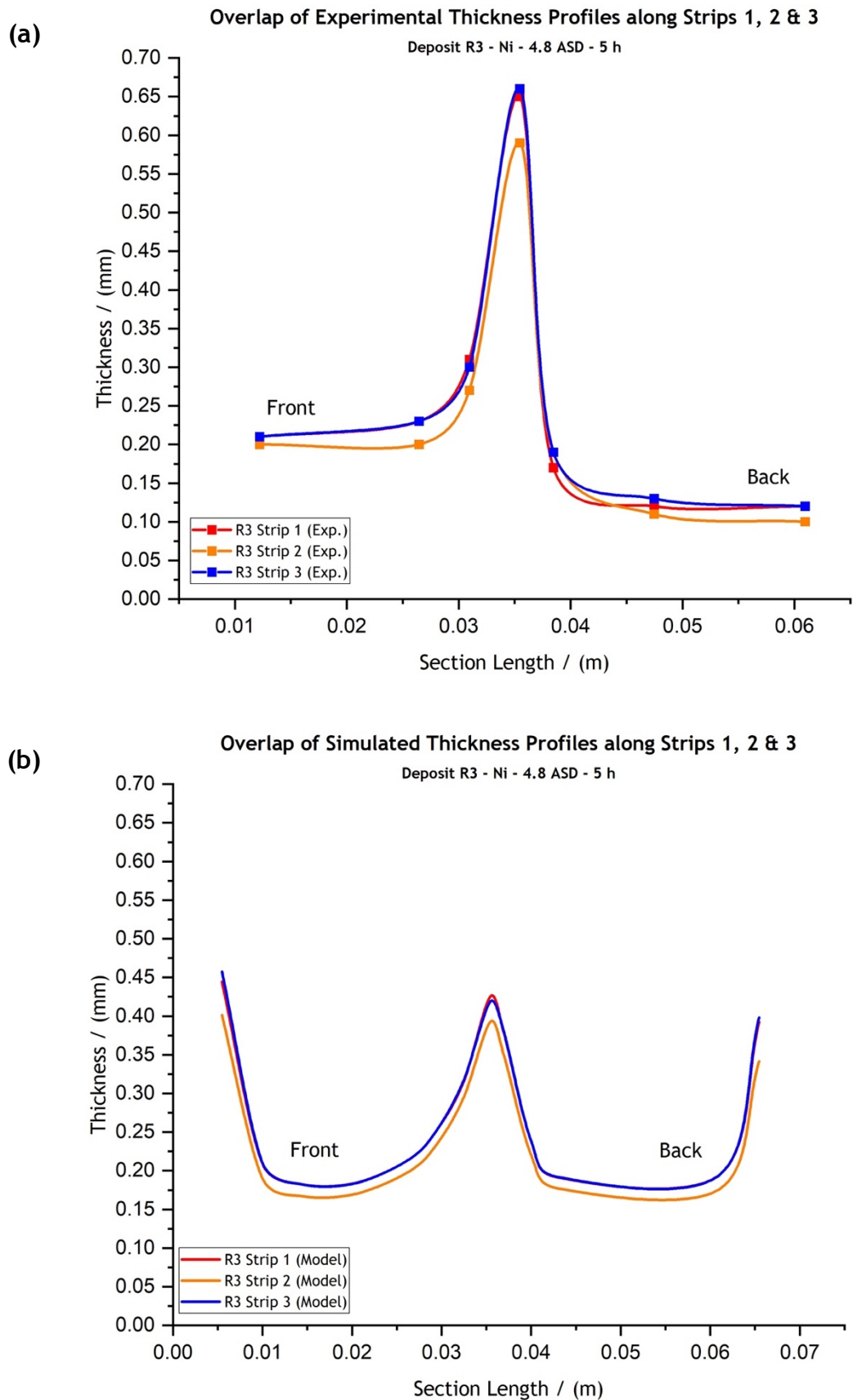


Figure 5. 16: Overlaps of (a) the experimental and (b) the simulated thickness profiles for strips 1, 2 and 3 of the mechanical vane deposit R3. Deposition of R3 was conducted at $-5.4 V$ and $-4.4 A$, for $18000 s$, at $50 ^\circ C$. “Front” indicates the mandrel side closer to the anode.

ever, when it comes to the thicknesses of the front and back faces of the deposit. Reasonably, experimental results suggest that the front face, the one closer to the anode, grows faster than the back face, resulting to higher thicknesses on the front face (Figure 5.16-a). This difference is not depicted in the modelling results which suggest no difference in the thickness, and consequently in the deposition rate, between the two faces (Figure 5.16-b). On another note, target thicknesses (red lines) are provided in Figure 5.15 for reference only; to achieve these thicknesses, someone should simply apply higher currents for the same deposition duration, or just run the process for longer. Longer deposition hours were not possible within the working hours of a university-based laboratory. Higher currents were applied, though, resulting in thicker deposits, like electroform R6 shown in Figure 5.7. For clarity, Figure 5.17 shows the experimental and simulated thickness profiles for the corresponding strips 1, 2 and 3 of electroform R6. As it can be seen here, deposition at $7.22 A/dm^2$ for 5 h results in thicknesses within the target values towards the tool's sides, while even at the middle of the mandrel, where deposition progresses slower, thicknesses touch the minimum target thickness values. Nevertheless, Figure 5.17 also demonstrates that the model underpredicts the thickness values. In that instance, the model underpredicts both the thicknesses at the “nose” area (by almost 40 %) as well as those at the front and back faces of the mandrel (by almost 20 %). Subsequently, the conclusion is drawn that the deviation between the experimental and simulation results increases with the increase of the applied current density value.

Even though the mechanical vane model might be necessary to undergo further optimisation studies in order to improve the agreement with the experiments, in terms of the numerical results, it is proposed here that it can confidently be used for qualitative studies as is. Although the mechanical vane model underpredicts the thicknesses to be achieved at higher current densities, it, at least, confirms that vane electroforms can be successfully produced. For deposition at current densities up to $\sim 5 A/dm^2$ simulated thicknesses can even be quantitatively, and not only qualitatively, validated by experiments. Since our industrial partners produce the mechanical vane electroforms at $\sim 2 A/dm^2$, the model is proposed to fit the purposes of this specific process.

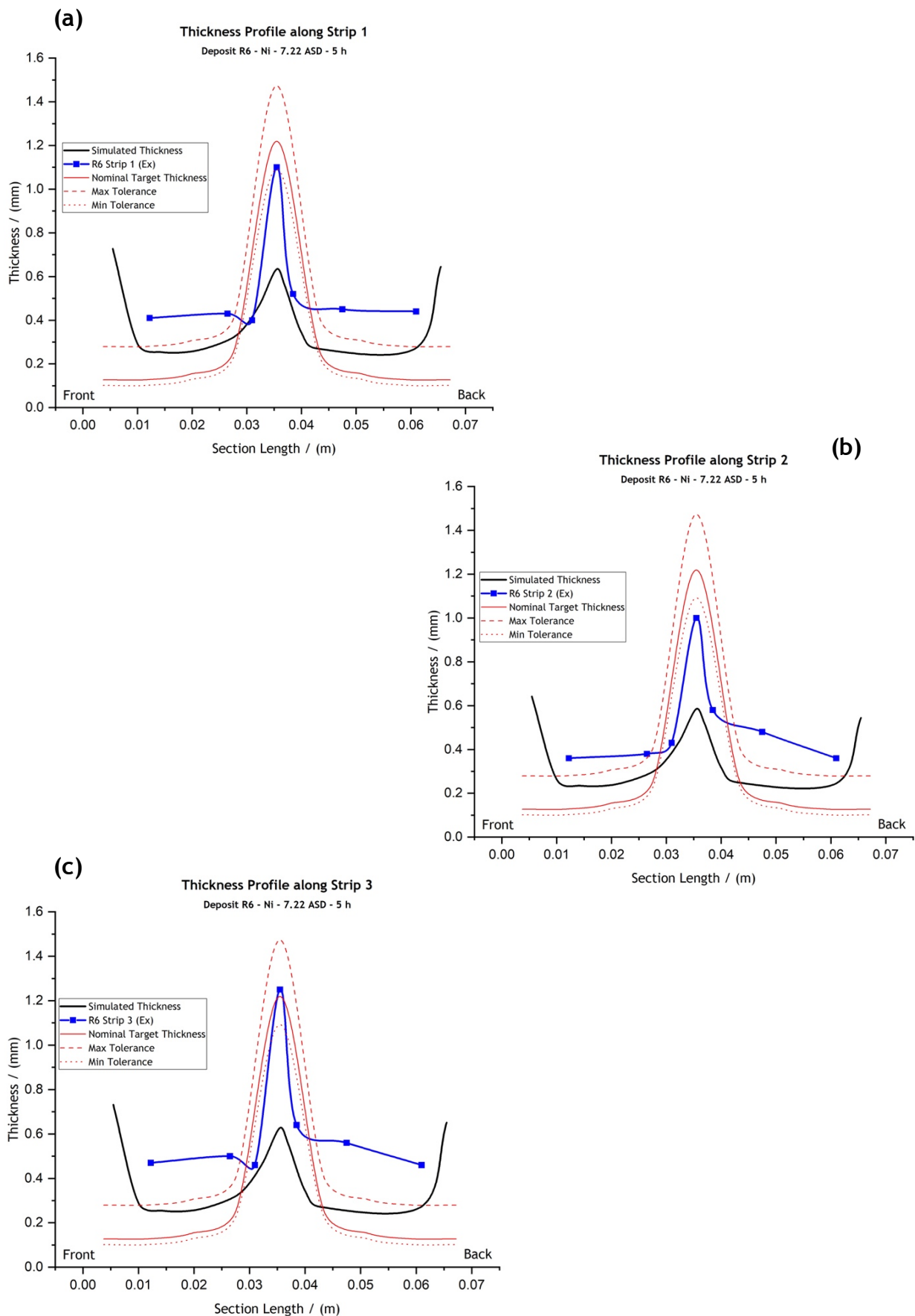


Figure 5. 17: Comparative graphs of the experimental and simulated thickness profiles for (a) strip 1, (b) strip 2 and (c) strip 3 of the mechanical vane deposit R6. Deposition of R6 was conducted at -6.5 V and -6.5 A , for 18000 s , at $50\text{ }^\circ\text{C}$. “Front” indicates the mandrel side closer to the anode.

5.5 Deposit Structural Characterisation

Even though structural characterisation of the electroforms was not one of the direct objectives of this project, it was believed that an analysis of that kind, at a preliminary level, would allow for a complete qualitative validation of the experimental studies, allowing to confirm the material growth mechanism, grain size and composition of the electroforms. Scanning electron microscopy (SEM) was used for this purpose [17].

Scanning electron microscopes are tools used for materials characterisation, providing information about defects in, the surface structure and composition of the studied samples. Surfaces up to submicron and nano-level can be analysed that way. The microscope uses a beam of high-energy electrons to scan a sample's surface under high vacuum. While scanning the surface, the electron beam excites the surface atoms which emit secondary electrons. Secondary electrons present very low energies ($\sim 50 \text{ eV}$) limiting their available paths through solid matter. As a result, secondary electrons can only escape through the sample surface providing high-resolution images. Another advantage is the fact that the secondary electrons' signal is highly localised at the electron beam's point of impact, allowing for images with a resolution of below 1 nm to be collected [18].

Scanning electron microscopy can also be applied for compositional analysis of the samples under investigation using a beam of using back-scattered electrons (BSE). Back-scattered electrons present much higher energies than the secondary electrons since they emerge from deeper than the sample surface. Consequently, they can only provide images of poor resolution, significantly lower than the resolutions of images secondary electrons can obtain. However, back-scattered electrons can be used alongside X-ray spectra for elemental analysis since their signal intensity is directly related to the atomic number of the sample elements. Every time the electron beam excites an inner shell electron of the sample, this is removed, and a higher-energy electron fills its position releasing energy. As a result, characteristic X-rays are emitted. These X-rays are subsequently gathered by an X-ray detector and energy



Figure 5. 18: The *Hitachi S3700-N Scanning Electron Microscope* used for the purposes of this project. The equipment is located at the *Advanced Materials Research Laboratory (AMRL)* at the University of Strathclyde.

dispersive spectroscopy (EDS) is used to identify the elements present in the sample, map their distribution, as well as measure their abundance [19].

For the SEM measurements presented here, a *Hitachi S3700-N Scanning Electron Microscope* was used (Figure 5.18), located at the *Advanced Materials Research Laboratory (AMRL)* at the University of Strathclyde. The microscope is equipped with both secondary electrons and back-scattered electrons detectors. Emission of secondary electrons was used for surface analysis while back-scattered ones were used for compositional analysis of the samples, alongside energy dispersive spectroscopy (EDS) for detailed elemental analysis. Analysis was run under a 10 kV emission field.

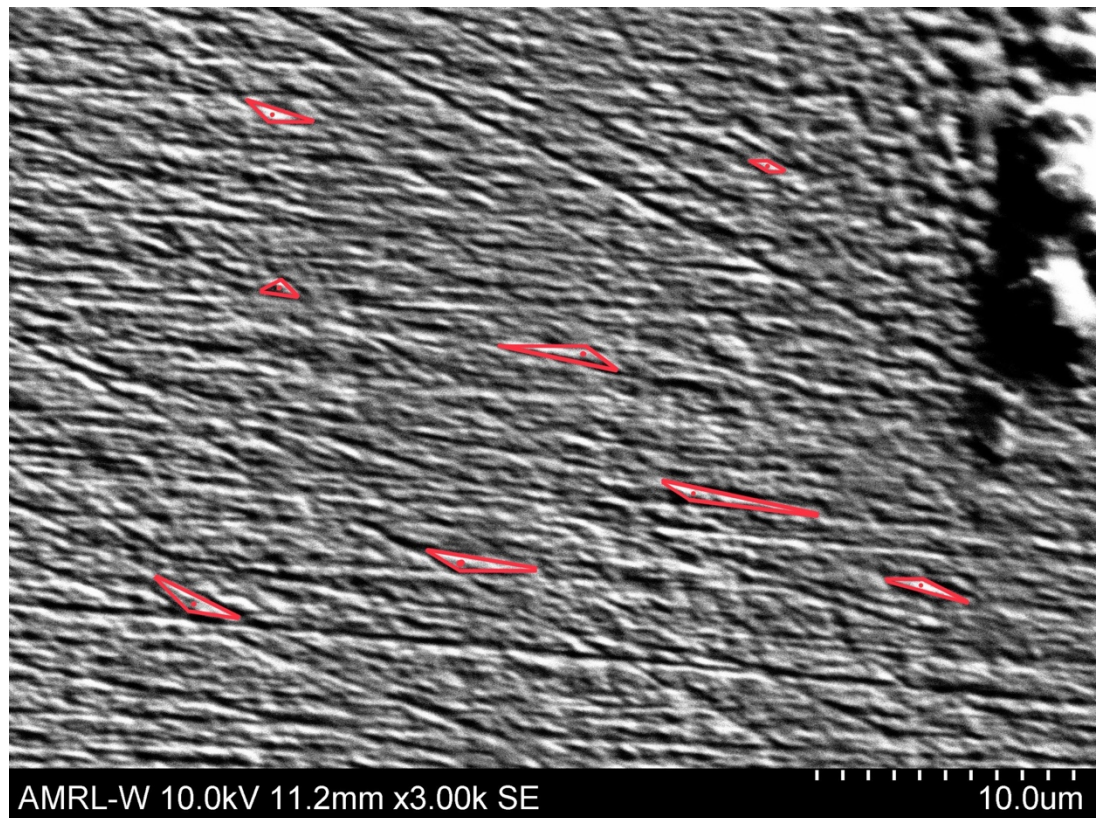


Figure 5. 19: Scanning electron microscopy imaging of the strip 2 section surface of the etched R3 electroform at magnification $\times 3,000$. The red triangles indicate the boundaries of what believed to be pyramid-shaped nickel grains evolving during deposition. The red dots within the red triangles indicate the “tip” point of the pyramid-shaped grains indicating growth on the z -direction (outwards from the page level).

[Figure 5.19](#) was produced by SEM imaging of the strip 2 section surface of the etched R3 electroform using the secondary electrons beam. The resin specimen, including the three electroform strips, as shown in [Figure 5.14-b](#), was gold-coated before introduced in the SEM chamber for analysis and fixed on the SEM holder by copper tape. This allowed for the resin specimen to be conductive and allow for the electrons to interact with the metallic samples, *i.e.*, the three electroform strips. The specimen was etched by being immersed in a solution of 50% nitric and 50% acetic acid for 5 s. Even though various etching solutions and immersion times were used, all etched specimens obtained did not exhibit sufficient microstructural detail for analysis. The most reasonable explanation for that was that the excessive, in

comparison with the metallic samples size, amount of resin, needed to mount the three strips, was interfering with the etching solution. However, for the purposes of this work, the quality of etching shown in [Figure 5.19](#) was considered to be sufficient.

Analysis of [Figure 5.19](#) suggested that pyramid-shaped nickel particles are developing and growing layer by layer in a lamellar fashion. The red triangles indicate the boundaries of what believed to be pyramid-shaped nickel grains evolving during deposition. The red dots within the red triangles indicate the “tip” point of the pyramid-shaped grains indicating growth on the z -direction, *i.e.*, outwards from the page level. This particle evolution mechanism has also been reported in other works [20] [21]. In an effort to provide an explanation for lamellar growth of various metal electrodeposits, Winand [22] [23] suggested that lamellar growth is one of the several types of deposit growth mechanisms which occur due to the competition among crystals that grow vertically and crystals that grow laterally.

This competition takes place since lateral crystal growth will at some point be stopped either due to a decrease of the local current density or simply because a neighbouring crystal will get on the way. Specifically for nickel, Delplancke *et al.* [24] reported lamellar growth in $Ni - P$ foils while, Tian *et al.* [25] successfully developed a lamellar $Ni - W - Graphene Oxide$ coating. The latter suggested that lamellar growth is driven by an increase in current (up to $12 A/dm^2$) which enhances nucleation and inhibits grain growth by graphene oxide sheets. Additionally, they also suggested that lamellar growth is a result of the alternating growth of lateral and vertical crystals. Importantly, it is this lamellar growth that is proposed to enhance the deposits' corrosion resistance due to the high corrosion potential and low corrosion current [25] [26].

While further in-depth structural analysis of these samples - not possible in the timeframe of this project - is suggested for the future, SEM imaging led to another interesting structure-related observation. As it can be seen in [Figure 5.20](#), at magnification $\times 50$ under the electronic microscope of the etched R3 electroform, the growth mechanism presents a periodicity which leads to “necklace”-like zones of

$\sim 100 \mu\text{m}$ in thickness at the “nose”. This observation is an important one since, to the author’s best knowledge, it has not been reported before. Even though this seems to be a material behaviour worth investigating further in the future, the working theory in the context of this project is that these periodic layers coincide with a periodic re-nucleation of the active NiOH_{ads} intermediate, formed during the rate determining step of the nickel deposition mechanism proposed in [Chapter 1](#) (refer to [Table 1.2](#)).

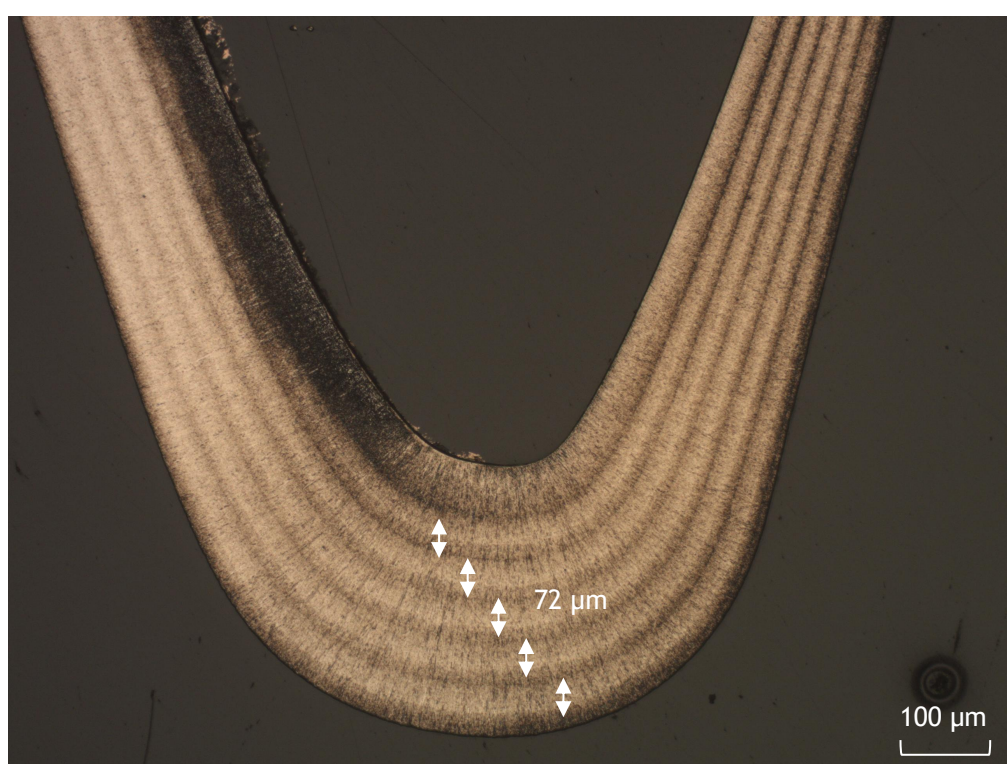


Figure 5. 20: Electronic microscope imaging of the strip 2 “nose” section surface of the etched R3 electroform at magnification $\times 50$. The growth mechanism presents a periodicity which leads to “necklace”-like zones of $\sim 72 \mu\text{m}$ in thickness.

In the author’s opinion, further investigations of this behaviour are of essence to determine whether this periodic layer formation coincides with a periodic transition between different crystallographic phases, or re-nucleation, possibly also affecting

the internal stresses developing in the final products, either in a positive or a negative way.

Following the analysis presented so far, the backscattered-electron beam was used for compositional analysis of the sample, alongside energy dispersive spectroscopy (EDS) for detailed elemental analysis. The spots of analysis are shown in [Figure 5.21](#) and the elemental analysis is provided in [Table 5.5](#).

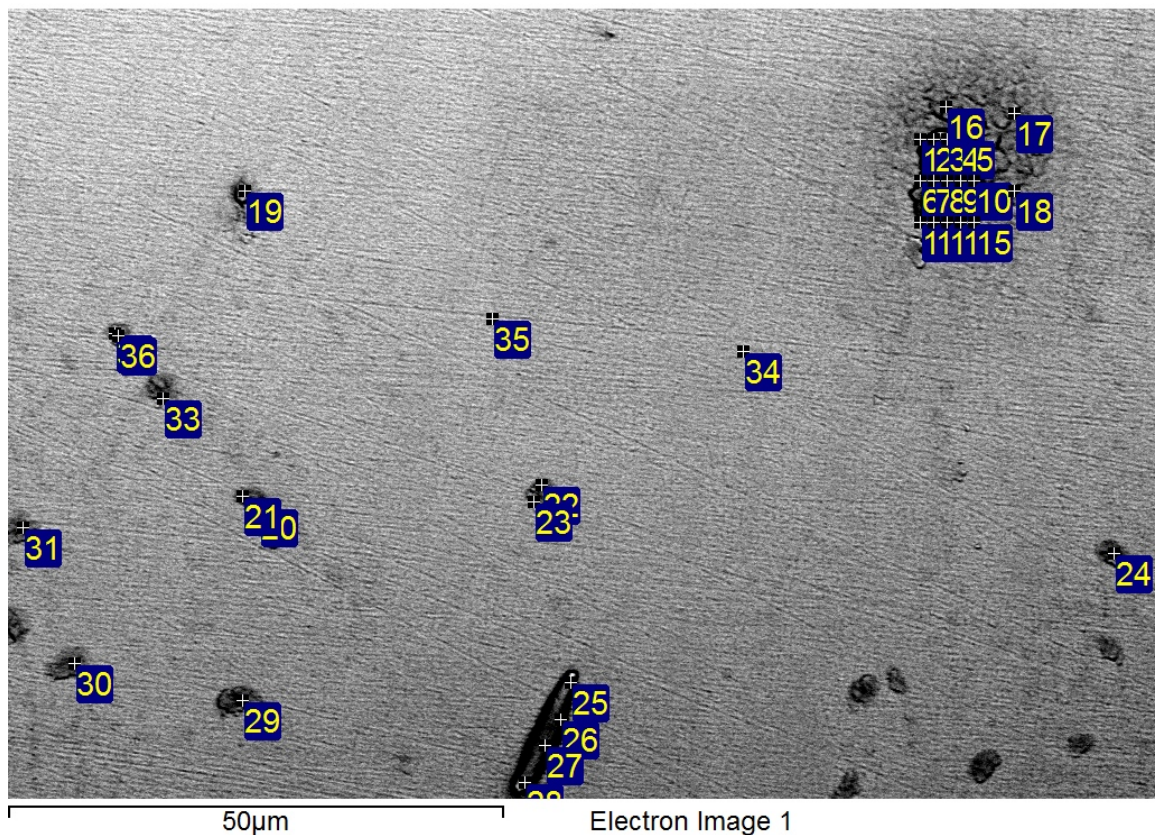


Figure 5. 21: Spots of elemental analysis under the scanning electron microscope using the backscattered-electron beam alongside energy dispersive spectroscopy.

As it is evident, elemental analysis suggests that the electroform consists, predominantly, of pure nickel. The only other element consistently present in the sample

Table 5. 5: EDS elemental analysis of the etched R3 electroform.

Spectrum	Ni	O	N	Si	Cl	Ca	Total
1	83.04	12.58		1.30		3.08	100.00
2	87.37	12.63					100.00
3	94.37	5.63					100.00
4	94.34	5.66					100.00
5	91.88	8.12					100.00
6	92.77	7.23					100.00
7	89.54	10.46					100.00
8	90.29	9.71					100.00
9	94.32	5.68					100.00
10	78.63	18.84	2.53				100.00
11	93.72	6.28					100.00
12	92.84	7.16					100.00
13	94.16	5.84					100.00
14	62.11	26.32		3.24		8.33	100.00
15	64.19	34.49			1.33		100.00
16	97.11	2.89					100.00
17	95.63	4.37					100.00
18	73.99	22.80	3.21				100.00
19	98.76	1.24					100.00
20	99.01	0.99					100.00
21	100.00						100.00
22	99.11	0.89					100.00
23	99.17	0.83					100.00
24	98.95	1.05					100.00
25	99.14	0.86					100.00
26	99.09	0.91					100.00
27	98.96	1.04					100.00
28	99.15	0.85					100.00
29	98.92	1.08					100.00
30	98.99	1.01					100.00
31	98.99	1.01					100.00
32	98.95	1.05					100.00
33	99.16	0.84					100.00
34	98.80	1.20					100.00
35	100.00						100.00
36	98.91	1.09					100.00

was found to be oxygen at low levels throughout the deposit, mostly at 1% or less. This might be an additional indication supporting the working theory that the active $NiOH_{ads}$ intermediate, which is periodically re-nucleating throughout the process, is also the source of the oxygen measured in the sample. The other elements (N, Si, Cl, Ca) occasionally measured as part of the sample's composition are included in the resin composition and, as such, could be considered random occurrences in which case should be ignored. However, one notices that the corresponding oxygen content at these locations is also high. It is possible that there the surfactant may have been "included" in the deposit, which would explain the presence of other elements and oxygen.

5.6 Conclusions

Nickel deposits were formed to validate a 3-D, time-dependent, secondary distribution model of a mechanical vane geometry. The mandrel presents industrial interest as the final parts are used for demanding aerospace applications.

Qualitative analysis of the experimental results suggested that deposition progresses from the sides of the cathode towards its centre, with a faster deposition rate at the sides of the mandrel compared to that in the middle. The process was also confirmed to be completely predictable, with the deposited nickel mass presenting an analogous relationship with both the applied current density and deposition time; between any two experiments, keeping the applied current density the same and doubling the deposition duration leads to electroforms almost double in terms of the deposited nickel mass. The same behaviour is observed if deposition duration is kept the same while the applied current density is doubled. This allows for determination of the average growth rate of a process. Additionally, deposition experiments revealed a correlation between the applied current density and the electroforms' surface finishing, with higher current densities leading to final parts with a matte surface

finishing. The same surface finishing is also observed after deposition at lower current densities for longer periods.

Regarding the modelling studies of the mechanical vane geometry, simulations of a process at 4.89 A/dm^2 for 5 h predicted the experimentally observed thickness distribution, with higher thicknesses simulated at the “nose” and lower ones at the front and side faces of the mandrel. However, thickness at the “nose” area was under-predicted by almost 30 %, while was found to be in reasonably good agreement with experimental thicknesses at the front and back faces of the part. On the other hand, simulations of a process at 7.22 A/dm^2 for 5 h underpredicted both the thicknesses at the “nose” area (by almost 40 %) and those at the front and back faces of the part (by almost 20 %). The conclusion was drawn that deviation between experimental and simulation results increases with an increase of the applied current density value.

Even though the mechanical vane model was consistently underpredicts the thicknesses to be achieved at higher current densities, it confirms that vane parts can be successfully electroformed. It is proposed here that the model presented in this chapter can confidently be used for qualitative studies of the mechanical vane geometry as is. For electroforming at current densities up to $\sim 5 \text{ A/dm}^2$ simulated thicknesses can even be quantitatively, and not only qualitatively, validated by experiments. Since the part is industrially formed at $\sim 2 \text{ A/dm}^2$, the model is proposed to fit the purpose of simulating this specific process. However, it is suggested that further optimisation studies are of essence in order to quantitatively improve the agreement between experimental and modelling results.

Lastly, scanning electron microscopy was used to structurally characterise the electroforms at a preliminary level, allowing for a complete qualitative validation of the experimental studies. Imaging suggested that pyramid-shaped nickel particles evolve during deposition. Another interesting observation revealed, for the first time ever to the author’s best knowledge, a periodicity in the growth mechanism which leads to “necklace”-like zones of $\sim 100 \mu\text{m}$ in thickness at the “nose” area. In the context

of this project, it is proposed that these periodic zones might coincide with a periodic re-nucleation of the active $NiOH_{ads}$ intermediate, formed during the rate determining step of the nickel deposition mechanism. Elemental analysis also supports this theory since the only other element, except for the prevalent nickel, consistently present in the sample was oxygen. Further structural investigations are believed to be of great importance to determine whether this periodic layer formation also coincides with a periodic transition between different crystallographic phases, possibly affecting the internal stresses developing in the final products.

References

- [1] "Engineering Learn," Engineering Learn, [Online]. Available: <https://engineeringlearn.com/gas-turbine-components-and-principle/>. [Accessed 05 09 2022].
- [2] Rolls-Royce, *The Jet Engine*, vol. 5th edition, Derby: Rolls-Royce, 1986.
- [3] S. L. Dixon and C. A. Hall, *Fluid Mechanics and Thermodynamics of Turbomachinery*, Oxford: Butterworth-Heinemann, 2014.
- [4] P. M. Came and C. J. Robinson, "Centrifugal compressor design," *Proceedings of the Institution of Mechanical Engineers, Part C*, vol. 213, pp. 139-155, 1999.
- [5] S. J. Gallimore, "Axial flow compressor design," *Proceedings of the Institution of Mechanical Engineers, Part C*, vol. 213, pp. 437-449, 1999.
- [6] R. J. Smith, G. J. Lewi and D. H. Yates, "Development and application of nickel alloys in aerospace engineering," *Aircraft Engineering and Aerospace Technology*, vol. 73, no. 2, pp. 138-147, 2001.
- [7] S. J. Patel, "A century of discoveries, inventors, and new nickel alloys," *The Journal of The Minerals, Metals & Materials Society*, vol. 58, pp. 18-20, 2006.
- [8] D. C. Wright and D. J. Smith, "Forging of blades for gas turbines," *Materials Science and Technology*, vol. 2, no. 7, pp. 742-747, 1986.
- [9] A. W. Gebisa and H. G. Lemu, "Additive manufacturing for the manufacture of gas turbine engine components: literature review and future perspectives," in *Turbo Expo: Power for Land, Sea, and Air*, Oslo, 2018.
- [10] S. Wu, Y. Zhao, W. Li, W. Liu, Y. Wu and F. Liu, "Research progresses on ceramic materials of thermal barrier coatings on gas turbine," *Coatings*, vol. 11, no. 1, p. 79, 2021.
- [11] M. Peters, C. Leyens, U. Schulz and W. A. Kaysser, "EB-PVD thermal barrier coatings for aeroengines and gas turbines," *Advanced Engineering Materials*, vol. 3, no. 4, pp. 193-204, 2001.
- [12] M. Arai and T. Suidzu, "Porous ceramic coating for transpiration cooling of gas turbine blade," *Journal of Thermal Spray Technology*, vol. 22, pp. 690-698, 2013.

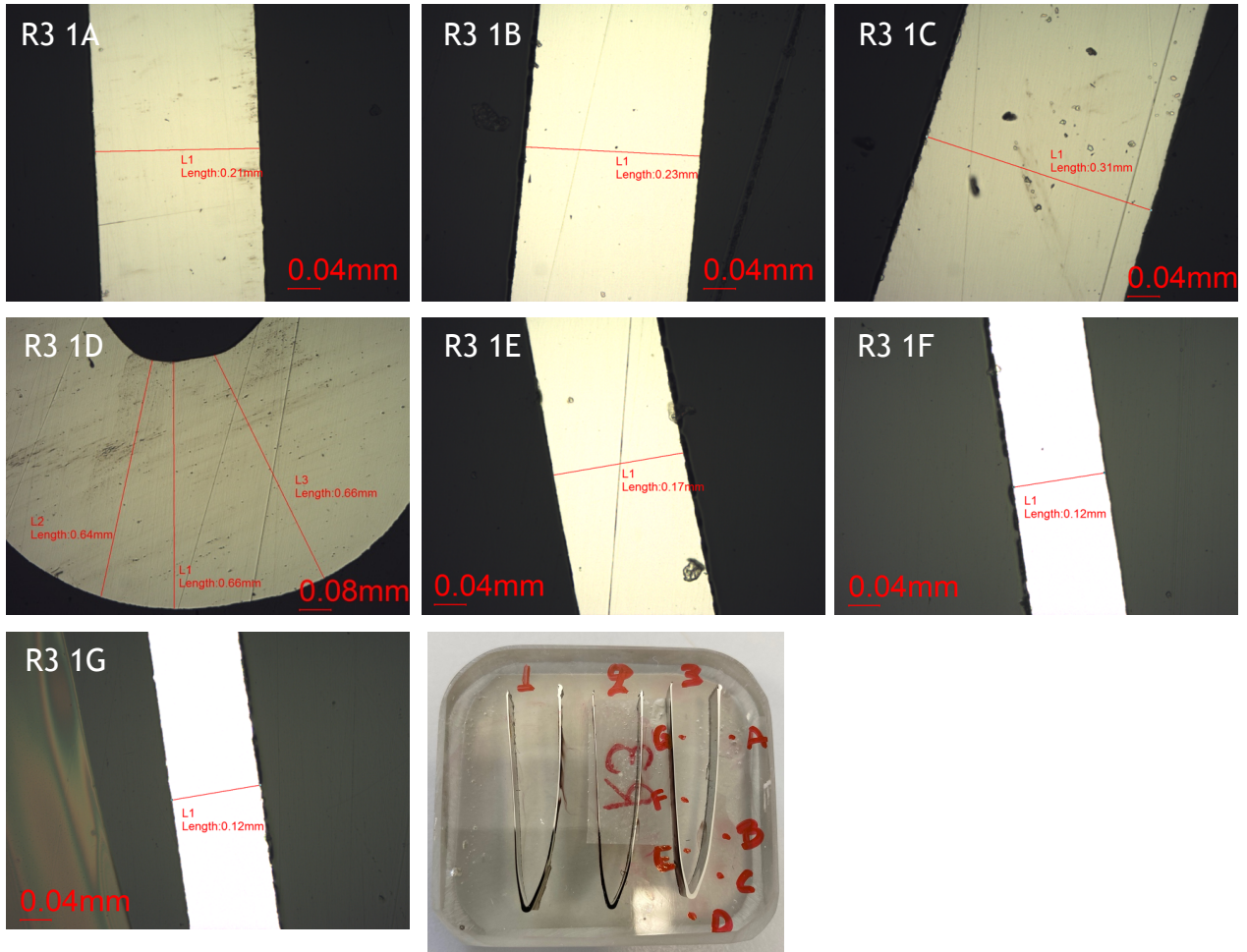
- [13] N. Madhwesh, K. V. Karanth and N. Y. Sharma, "Impeller treatment for a centrifugal fan using splitter vanes - A CFD approach," in *Proceedings of the World Congress on Engineering*, London, 2011.
- [14] T. Goel, D. J. Dorney, R. T. Haftka and W. Shyy, "Improving the hydrodynamic performance of diffuser vanes via shape optimization," *Computers & Fluids*, vol. 37, pp. 705-723, 2008.
- [15] L. Hogner, A. Nasuf, P. Voigt, M. Voigt, K. Vogeler, M. Meyer, C. Berridge and F. Goenaga, "Analysis of high pressure turbine nozzle guide vanes considering geometric variations," in *Proceedings of ASME Turbo Expo 2016: Turbomachinery Technical Conference and Exposition*, Seoul, 2016.
- [16] J. T. Todd and J. F. Norman, "The visual perception of metal," *Journal of Vision*, vol. 18, no. 3, pp. 1-17, 2018.
- [17] K. D. Vernon-Parry, "Scanning electron microscopy: an introduction," *III-Vs Review*, vol. 13, no. 4, pp. 40-44, 2000.
- [18] D. J. Stokes, *Principles and Practice of Variable Pressure Environmental Scanning Electron Microscopy (VP-ESEM)*, Chichester: John Wiley & Sons., 2008.
- [19] J. Goldstein, *Scanning Electron Microscopy and X-Ray Microanalysis*, US: Springer, 2003.
- [20] M. K. K. Jr. and M. K. Mahapatra, "Microstructure of Electrodeposited Nickel: Role of Additives," *Journal of Materials Engineering and Performance*, vol. 29, no. 11, pp. 7555-7566, 2020.
- [21] L. Wanga, Y. Gaoa, T. Xua and Q. Xuea, "A comparative study on the tribological behavior of nanocrystalline nickel and cobalt coatings correlated with grain size and phase structure," *Materials Chemistry and Physics*, vol. 99, pp. 96-103, 2006.
- [22] R. Winand, "Electrocrystallization: fundamental considerations and application to high current density continuous steel sheet plating," *Journal of Applied Electrochemistry*, vol. 21, pp. 377-385, 1991.
- [23] R. Winand, "Electrodeposition of metals and alloys - New results and perspectives," *Electrochimica Acta*, vol. 39, pp. 1091-1105, 1994.
- [24] "Influence of Low Phosphorus Concentration on the Electrocrystallization and the Properties of Ni-P Foils," *Journal of The Electrochemical Society*, vol. 140, p. 2800, 1993.

- [25] S. Tian, K. Gao, H. Zhang, H. Cui and G. Zhang, "Corrosion Resistance and Anti-wear Properties: Ni-W-GO Nanocomposite Coating with Lamellar Structure," *Transactions of the Indian Institute of Metals*, vol. 73, no. 3, pp. 713-724, 2020.
- [26] Z. Li, Y. Wu, Z. Xie, C. Kong and H. Yu, "Grain Growth Mechanism of Lamellar-Structure High-Purity Nickel via Cold Rolling and Cryorolling during Annealing," *Materials*, vol. 14, p. 4025, 2021.

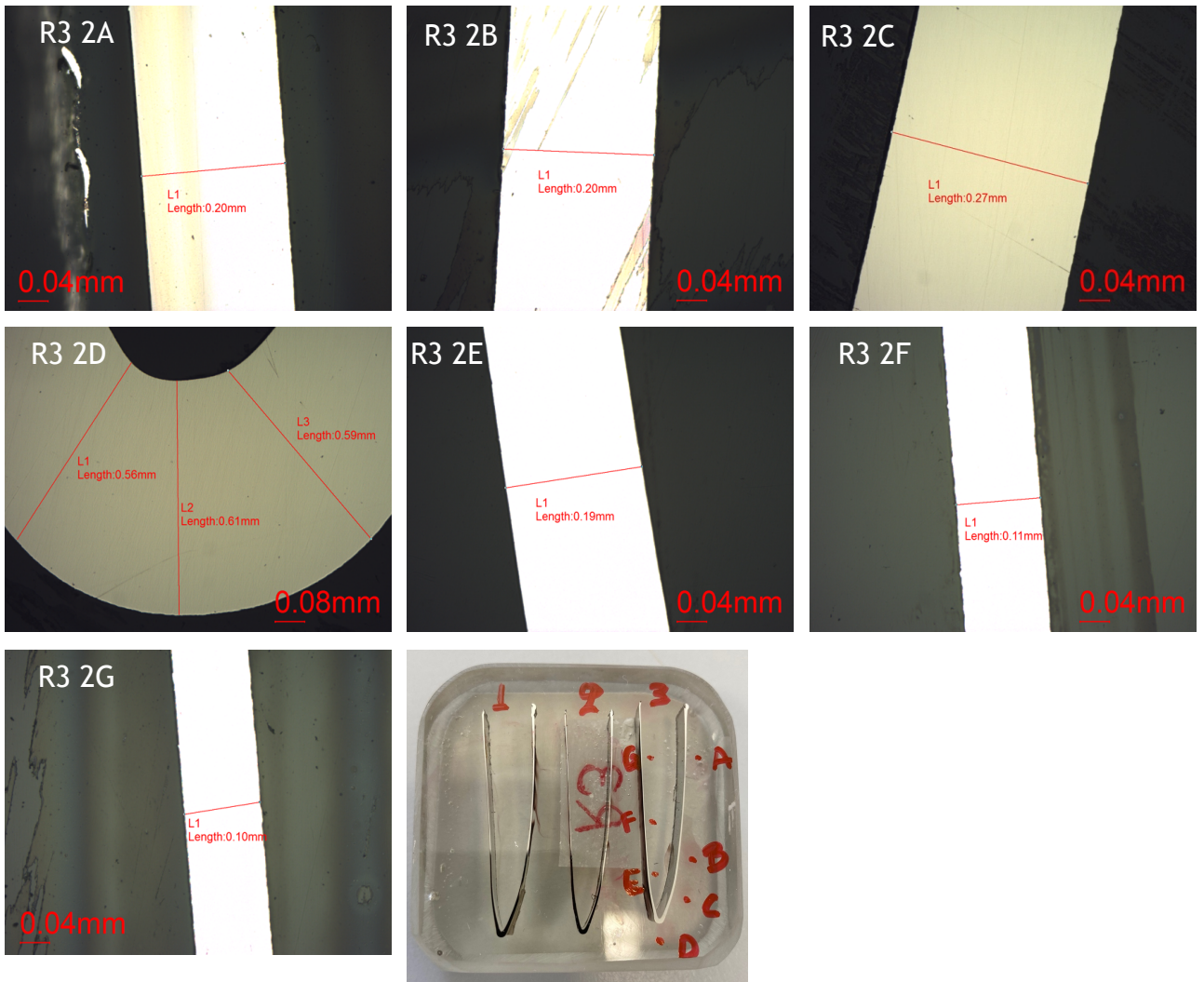
Appendix I

Optical Microscope Pictures Indicating the Thickness Measurements of the R3 Electroform

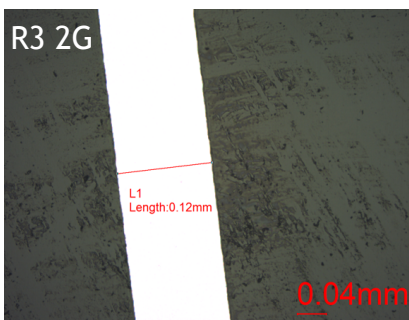
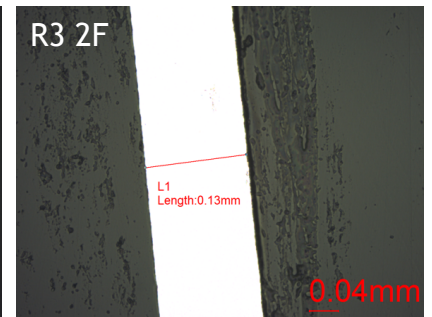
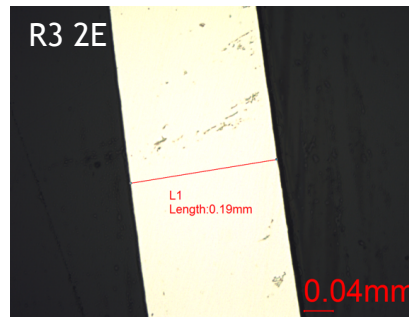
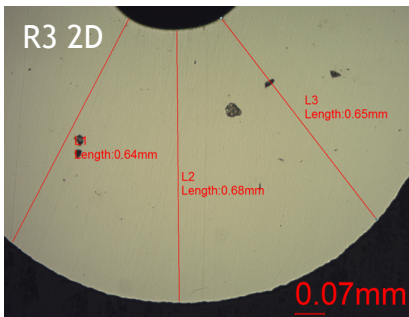
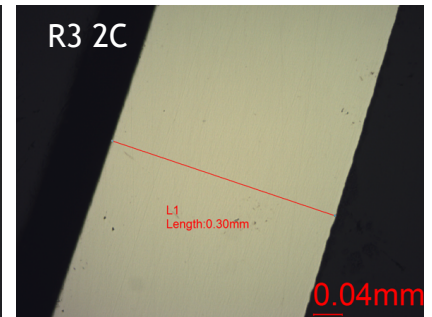
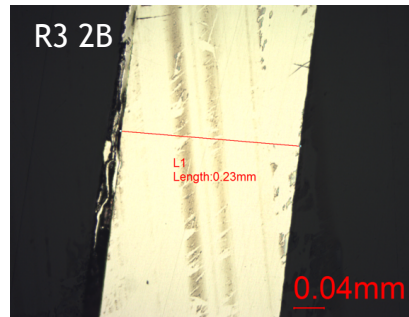
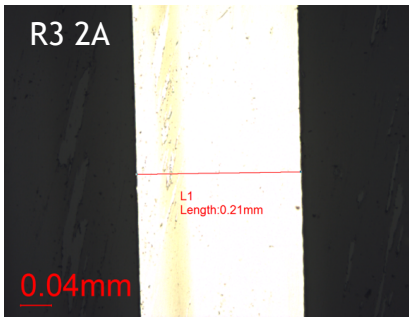
Strip 1



Strip 2



Strip 3



Chapter 6: Electroforming Process Model Assessment

The objective of this chapter is to further qualitatively assess the limitations and strengths of both the software and model ability to simulate the electroforming process. Two study cases are presented here.

In the first section of the chapter the usefulness of modelling studies in identifying “mask” and “thief” geometries that fit the purpose is discussed. “Masks” are non-conductive objects used to transform specific areas of a cathode to non-conductive ones. Literature suggests that the use of “masks” has been used widely to achieve the desired current distribution in microfabrication, predominantly applied for the fabrication of patterned electronic devices, *e.g.*, circuit boards, usually alongside a lithographic process [1] [2] [3] [4] [5]. “Masks” can also assist highly sensitive projects such as the study of mass transfer in the microscopic scale [6]. However, the usefulness of “masks” in the large scale is less dominant, even though there are reports about their role in modern additive manufacturing [7] [8].

“Thieves”, on the other hand, are conductive objects which are used to minimise current accumulation at mandrel areas where this is not acceptable. The majority of published studies report the use of “thief” electrodes to ensure uniformity in deposits, by sacrificing large quantities of material depositing on their surface where current is high [9]. Once more, most of these studies refer to thin film development [10] [11] [12], while there are others related to the rotating disk electrode setup in the laboratory scale [13]. In this chapter, an effort to develop a systematic approach of studying the use and assess the effectiveness of such auxiliary tools is made.

In the second section, a comparison between primary, secondary, and tertiary current distribution is attempted. The effect of the different physics in modelling results is studied for both the RDE and the scaled-up disk models. This is weighed against the extra computational effort (regarding the collection of data, information, setting up the problem, as well as computation time) needed for the different systems to converge, and the useful information about metal deposition derived.

6.1 “Masks” & “Thieves”

Even though the time frame of this project would not allow for extensive modelling studies of the use of auxiliary tooling in the electroforming process, in this section a study of the deployment of “masks” and “thieves”, as part of process optimisation, is presented. Since the duration of this project did not allow for these models to be validated through practical experiments, the purpose of the investigations presented below was to establish the way that “masks” and “thieves” could provide improvements as a part of the process, determine their level of effectiveness and recognise any possible limitations in their use.

For the modelling studies discussed in the following sections, the 2-D axisymmetric RDE model was used assuming secondary current distribution. As already presented in [Chapter 3](#), the simulation was designed to represent practical deposition experiments, at 50 °C, for 1800 s, under a cell voltage of 5 V ($\varphi_{s,ext,cathode} = -5 V$, $\varphi_{s,ext,anode} = 0 V$) and a current density of 50 A/dm² ($I_{l,total} = -0.565 A$). Deposition at that high current density using the RDE setup allowed for a thick enough deposit to be produced, sectioned, mounted in resin, and measured under the microscope without deforming (refer to [Figure 3.15](#)).

The SCD, 2-D axisymmetric, RDE model was chosen for the purposes of the following studies since it allows for short simulation times of a simplified geometry which, nevertheless, provides a clear insight into the effects of “masks” and “thieves” on the system behaviour. For consistency and due to our industrial partner expressing an interest in doing so, examples of the use of “masks” as part of the mechanical vane model, presented in [Chapter 5](#), are also discussed in this chapter.

6.1.1 “Masks”

“Masks” are non-conductive objects used either to transform specific areas of a cathode to non-conductive ones (*i.e.*, areas which should not be deposited), or to manipulate the current movement in the electrolytic volume by guiding the current through specific paths, in order to control the current distribution close to specific cathode areas of interest (*e.g.*, away from the leading edges). Two different “mask” shapes were studied using the RDE, 2-D axisymmetric, model; a “ring mask” and a “shell mask”.

6.1.1.1 The “Ring Mask”

The RDE geometry including the “ring mask” is shown in [Figure 6.1-a](#). The mask is essentially a flat ring ([Figure 6.1-b](#)), of width $w_{ring} = 1.5 \text{ cm}$ (outer radius $r_{outer} = 2 \text{ cm}$ and inner radius $r_{inner} = 0.5 \text{ cm}$), placed between the electrodes, at a fixed distance from the cell walls ($d_{wall} = 1.5 \text{ cm}$) and centred with reference to the RDE. This configuration means that the mask covers $\sim 17 \%$ of the cathode radius (0.1 cm out of the 0.6 cm of the cathode radius) as shown in [Figure 6.1-a](#), leaving exposed a cathode area of radius $r_{exp} = 0.5 \text{ cm} \equiv r_{inner}$. The effect of the mask’s distance from the cathode surface was the first parameter to be studied. In [Figure 6.2](#), position 1 corresponds to the mask’s closest possible position to the cathode surface (0.05 cm , *i.e.*, $500 \mu\text{m}$), position 2 the closest position that is allowed in industry (0.5 cm) and

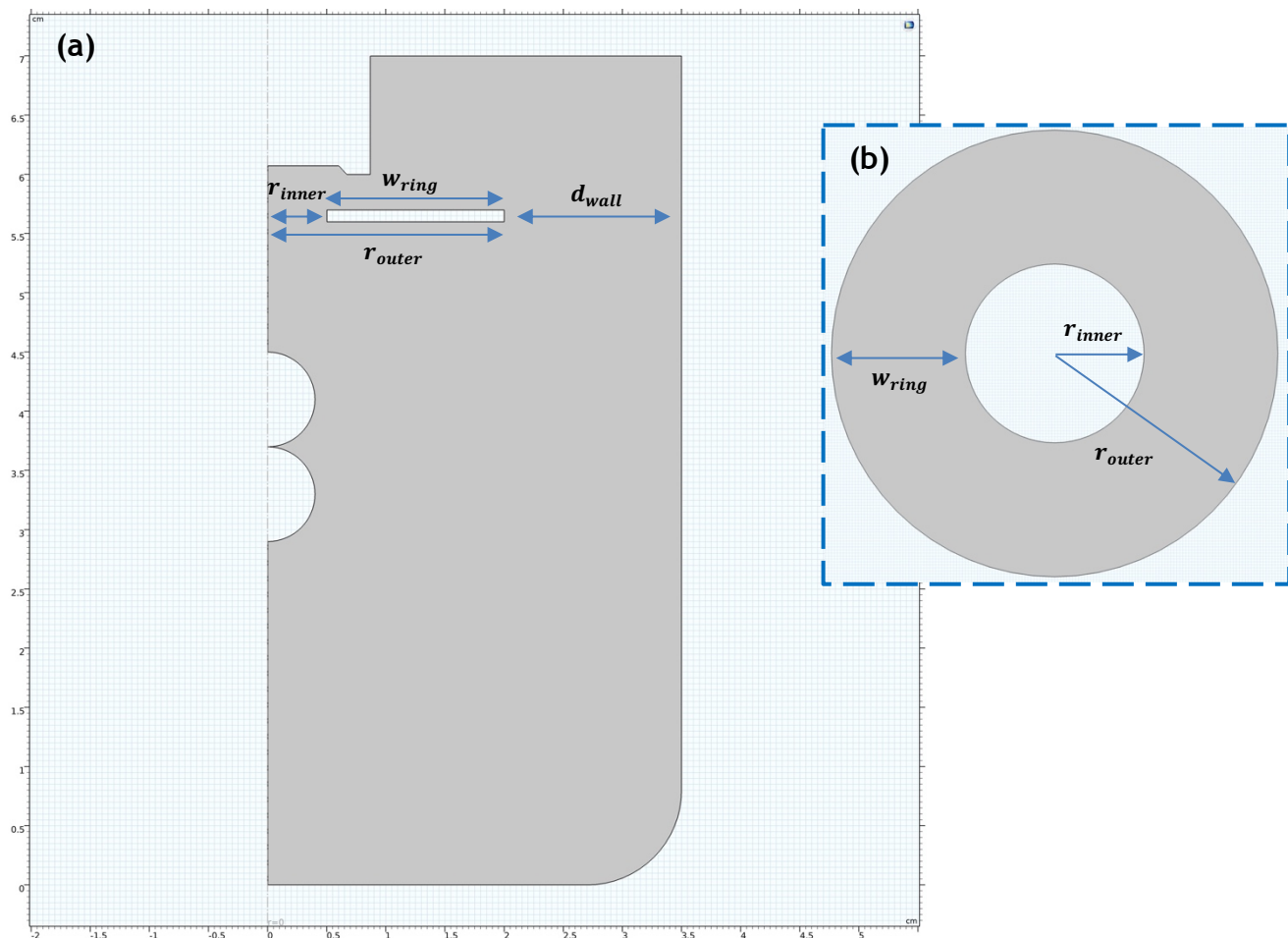


Figure 6. 1: (a) 2-D axisymmetric geometry of the RDE setup including a “ring mask” placed between the electrodes at $d_{wall} = 1.5 \text{ cm}$ from the cell walls. (b) Top view of the “ring mask”; $w_{ring} = 1.5 \text{ cm}$, $r_{outer} = 2 \text{ cm}$, $r_{inner} = 0.5 \text{ cm}$

position 3 a position “considerably far” from the cathode (1.4 cm).

Figure 6.3 reveals the potential and current distribution in the electrolyte domain for all three cases. In terms of potential distribution, it is evident that this is not significantly affected by the presence of the mask. A slight increase of potential values (*i.e.*, less negative values) near the cathode-electrolyte interface is observed as the mask is moved further away from the cathode surface. For position 1 potential values near the cathode-electrolyte interface are calculated around -3.13 V (Figure 6.3-a), around -2.58 V for position 2 (Figure 6.3-b) and around -2.48 V for position

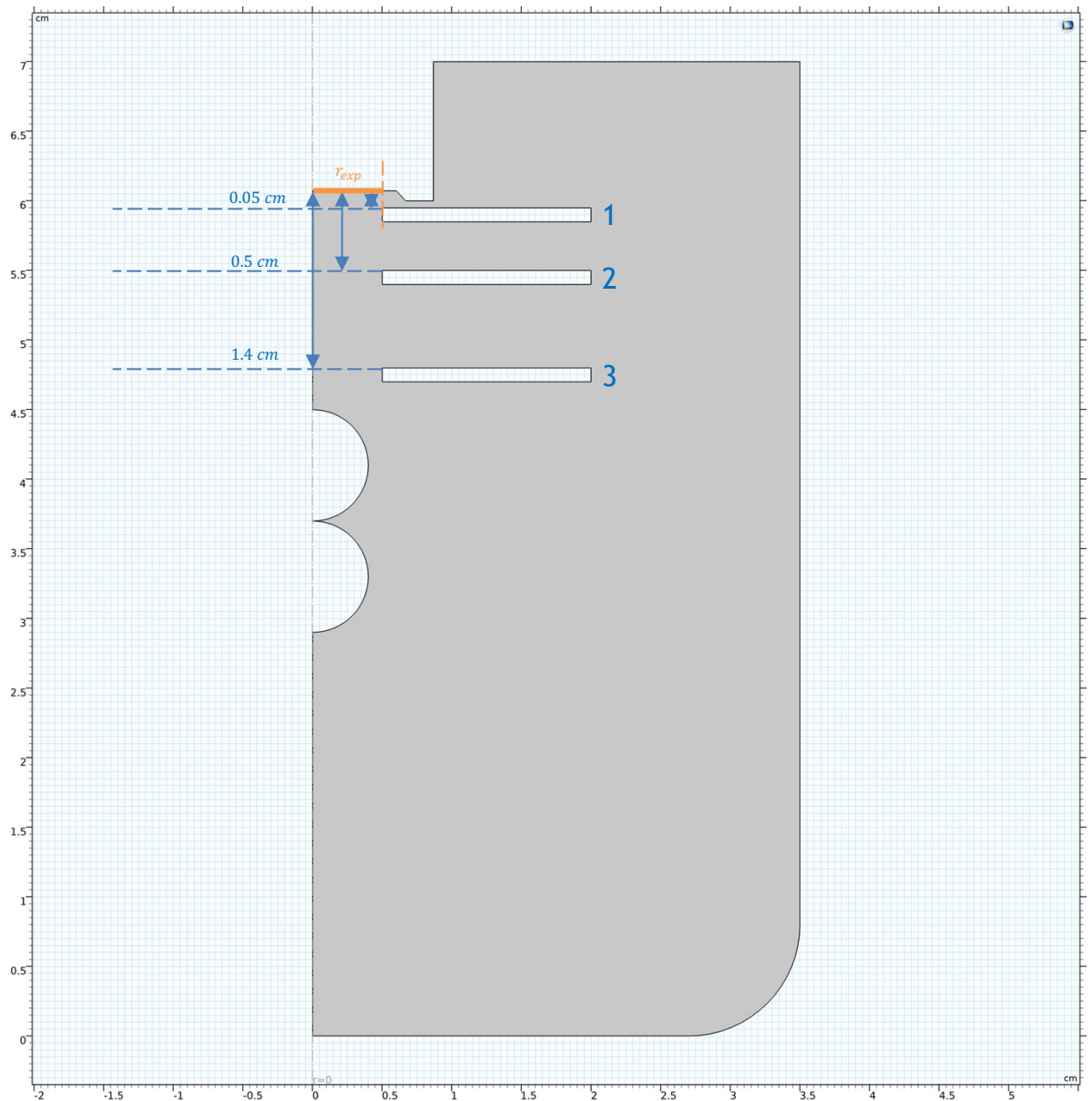


Figure 6. 2: Different “ring mask” distances from the cathode surface. Position 1 at 0.05 cm, position 2 at 0.5 cm and position 3 at 1.4 cm from the cathode surface. Radius of the “exposed” cathode area ($r_{exp} = 0.5\text{ cm} \equiv r_{inner}$) indicated in orange.

3 (Figure 6.3-c) Overall, this shows a lower potential drop in the electrolyte for the last case, possibly up to 0.5 V. In all three cases, the current streamlines “travel” around the mask edges and reach the cathode surface from all sides, and a closer look at current distribution is warranted.

In the case of position 1 (Figure 6.3-a) streamlines seem to be reaching the exposed cathode surface perpendicularly almost exclusively, indicating a more uniform current distribution across the exposed cathode surface.

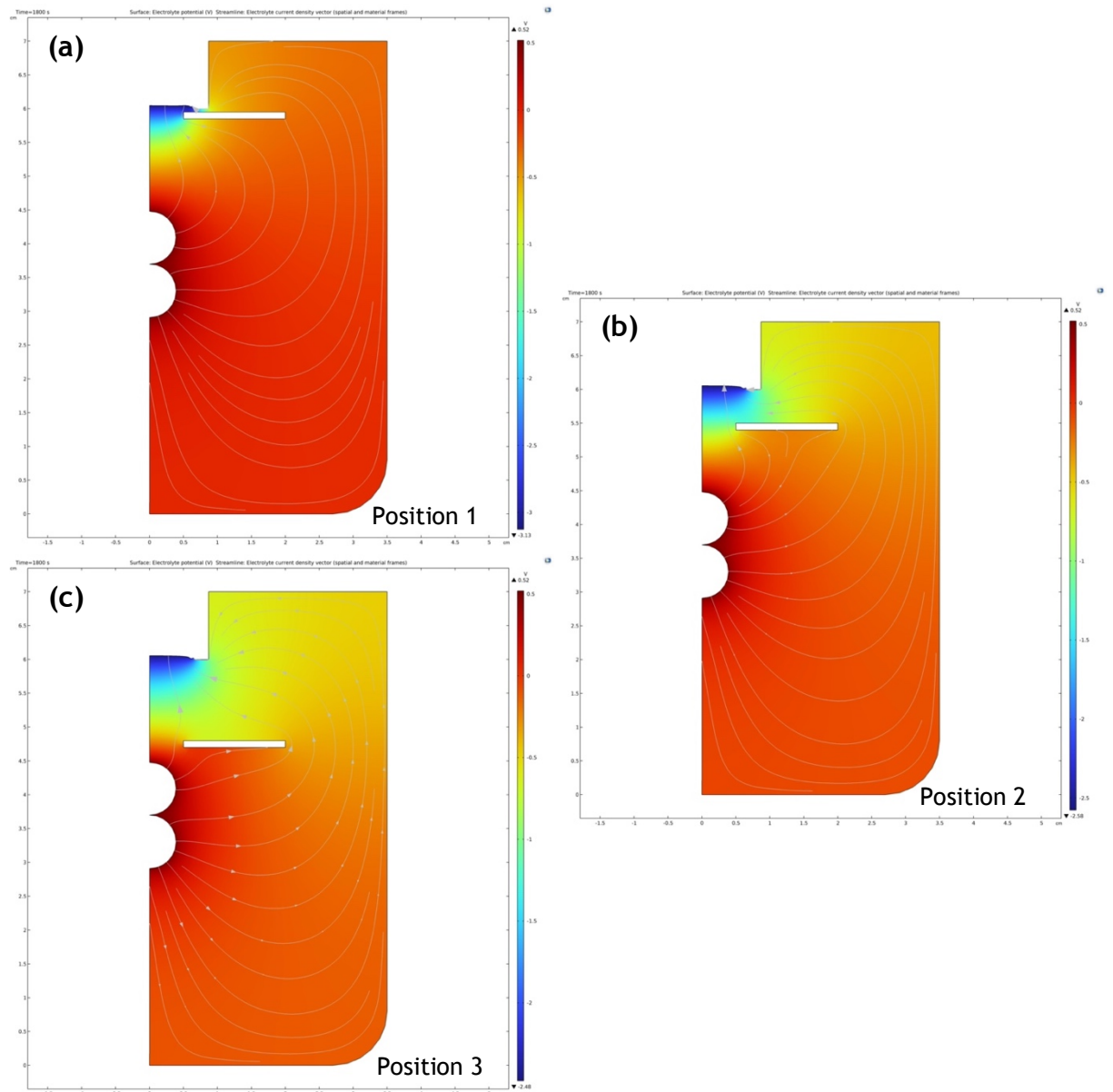


Figure 6. 3: 2-D representation of the potential and current distribution in the electrolytic volume for the case when the “ring mask” is placed at (a) 0.05 cm, (b) 0.5 cm and (c) 1.4 cm from the cathode surface.

This observation is also supported by the simulated thickness profiles for each case shown in Figure 6.4. Evidently, the thickness profile (blue line) for the case when the mask is positioned within 0.05 cm from the cathode surface presents an almost flat, linear area up to 0.4 cm from the cathode centre.

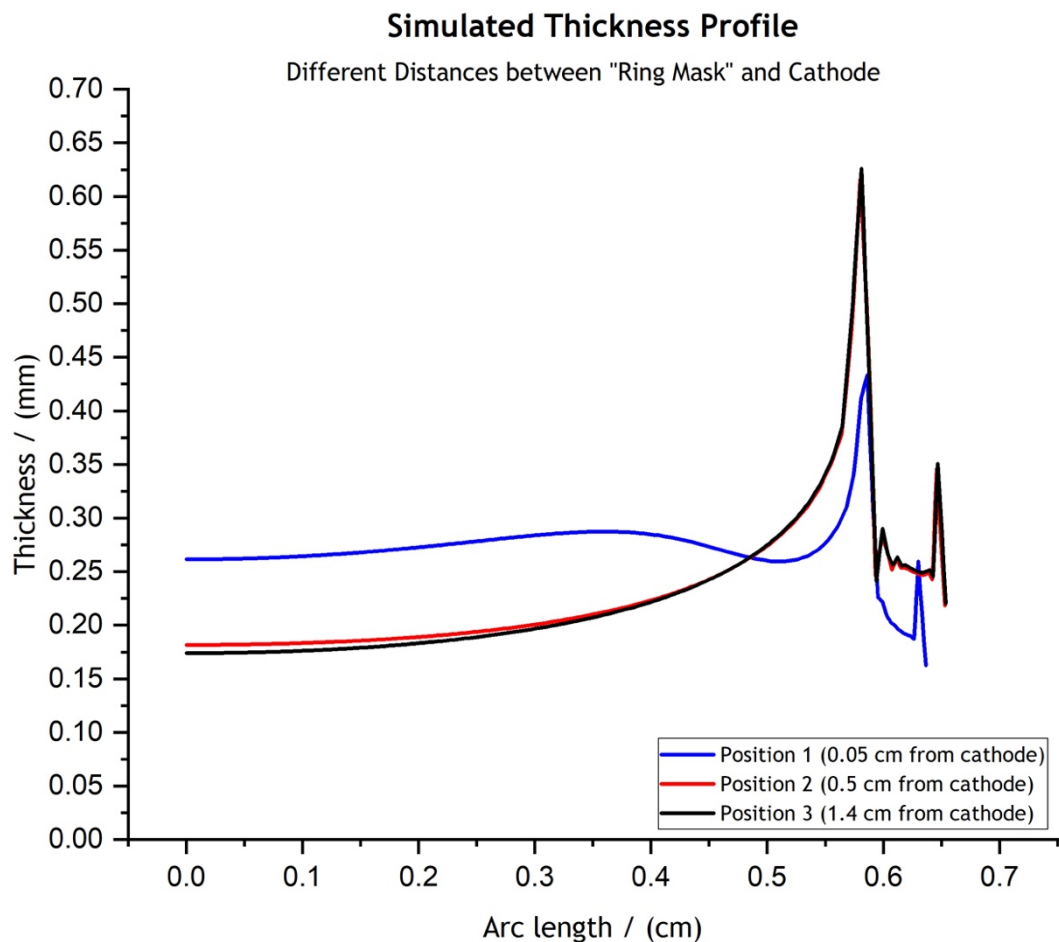


Figure 6. 4: Simulated thickness profiles for the different positions of the “ring mask”

However, no difference is observed in the simulated thickness profile between the cases when the mask lies at positions 2 and 3 (red and black lines). Additionally, thickness is calculated to be higher, at an average of 0.25 mm, for the case when

the mask lies at position 1. This value decreases at an average of 0.2 mm for the cases when the mask lies at positions 2 and 3. Even more importantly, the closer the mask is placed to the cathode (position 1), the lower the maximum thickness at the cathode's edge appears to be, indicating a potential minimisation of the dendritic growth around the leading edge. Nevertheless, for all three cases, thicknesses are calculated to be lower at the cathode centre and higher as we move towards the edge.

These results are also shown in terms of the thickness distribution on the cathode surface in [Figure 6.5](#). The 2-D representation of the thickness distribution allows for an additional observation. Interestingly, the closest mask position decreases the surface area where the thickness reaches its highest values (highlighted in circle in [Figure 6.5-a](#)), minimising the surface of high current accumulation between $0.58 - 0.6\text{ cm}$ in terms of radius. The corresponding surfaces for the cases of positions 2 and 3 (highlighted in circle in [Figures 6.5-b & 6.5-c](#)) lie between $0.55 - 0.6\text{ cm}$ in terms of radius.

The most important conclusion deriving from the above results is that the use of the “ring mask” can actually optimise thickness uniformity and potentially minimise dendritic growth only when it is placed very close to the cathode surface (within 0.05 cm). However, this seems to be much closer than the closest, safest, distance (0.5 cm) between a mandrel and a mask possible in an industrial setup. This is obtained at the expense of a higher potential drop between the anode and the cathode because the insulator “squeezes” the potential and current near the cathode. In effect, a higher “potential pressure” is required to achieve greater uniformity.

As a next step, and based on the observation that, if possible, the current would always make a detour around any obstacle as it “travels” towards the cathode surface, the idea was to investigate the effect of a “mask” shape which would provide more strict boundaries, hopefully also allowing for a more uniform deposition rate between the mandrel's centre and its edges.

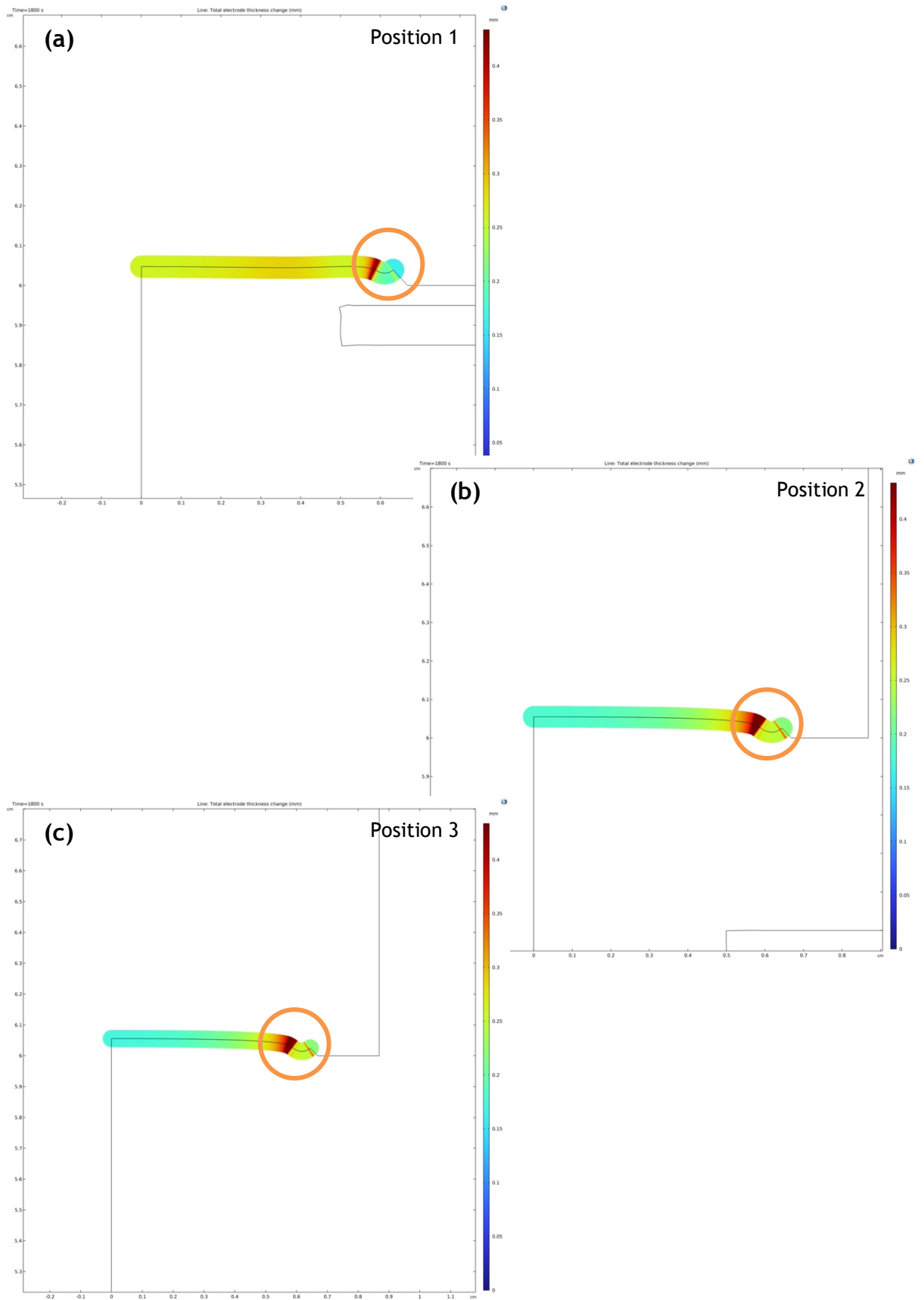


Figure 6. 5: 2-D representation of the thickness distribution on the cathode surface for the case when the “ring mask” is placed at (a) 0.05 cm, (b) 0.5 cm and (c) 1.4 cm from the cathode surface. For clarity, the colour code indicates lower thicknesses with blue (starting at 0 in the deep blue part of the scale) and higher thicknesses with red.

6.1.1.2 The “Shell Mask”

For this second set of modelling studies, a “mask” geometry which could enclose, like an outer shell, the RDE tip was studied.

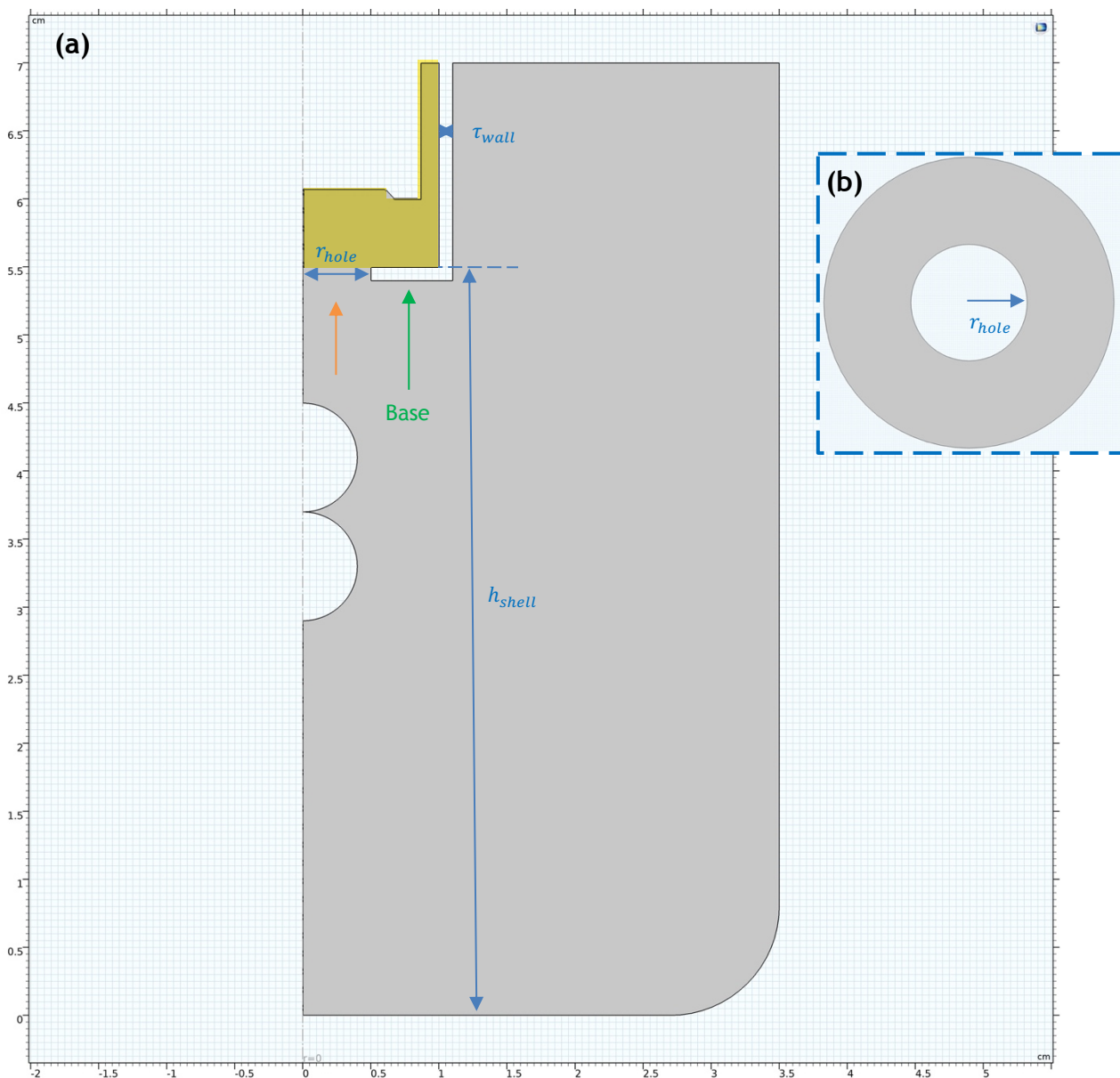


Figure 6. 6: (a) 2-D axisymmetric geometry of the RDE setup including a “shell mask” placed between the electrodes at $h_{shell} = 5.4$ cm from the bottom of the cell. (b) Top view of the mask’s base hole; $r_{hole} = 0.5$ cm. The mask is essentially a hollow cylinder with wall thickness $\tau_{cyl.wall} = 0.1$ cm and a hole at the base. The base of the mask is indicated by the green arrow.

The “shell mask” configuration, with the mask positioned between the two electrodes at $h_{shell} = 5.4 \text{ cm}$ and centred to the RDE, is provided in [Figure 6.6-a](#). The mask itself is essentially a hollow cylinder with wall thickness $\tau_{cyl.wall} = 0.1 \text{ cm}$ and a hole at the base (indicated by the green arrow). The hole at the cylindrical shell’s base ([Figure 6.6-b](#)) allows for the cathode surface to remain in contact with the electrolyte. That way the RDE is always “protected” from the sides and the current can only reach the cathode surface through the base hole indicated by the orange arrow. The height where the bottom part of the mask sits (h_{shell}), as well as the inner radius (r_{hole}) of the base hole ([Figure 6.6-b](#)) can be adjusted to increase or decrease the surface of the yellow area in [Figure 6.6-a](#).

Before this set of simulations is discussed, it is important to acknowledge the fact that the “shell mask” changes the RDE flow profile significantly. While the “ring mask” allows the development of a standard RDE flow profile (refer to [Figure 2.6](#)), including both laminar and centrifugal fluid motion, the introduction of the “shell mask” leads to turbulence “near” the cathode surface. Even though fluid flow was not simulated for the purposes of this project (refer to [Section 3.2.4, A Note on the Simulation of Agitation Conditions](#)), it is important to keep in mind that this change of the flow profile at the cathode-electrolyte interface could contribute towards the different potential and current distributions that are reported for the case of the “shell mask”.

Moving forwards, first, simulations were run with the mask base lying at three different heights representing three different positions as shown in [Figure 6.7](#). In order to make our simulations comparable to the “ring” mask, Position 1 corresponded to “shell mask” base at $h_{shell} = 5.85 \text{ cm}$, position 2 to “shell mask” base at $h_{shell} = 5.4 \text{ cm}$ and position 3 of the “ring mask” corresponded to “shell mask” base at $h_{shell} = 4.7 \text{ cm}$. The distance between the “mask’s” base and the cathode surface was 0.05 cm for position 1, 0.5 cm for position 2 and 1.4 cm for position 3.

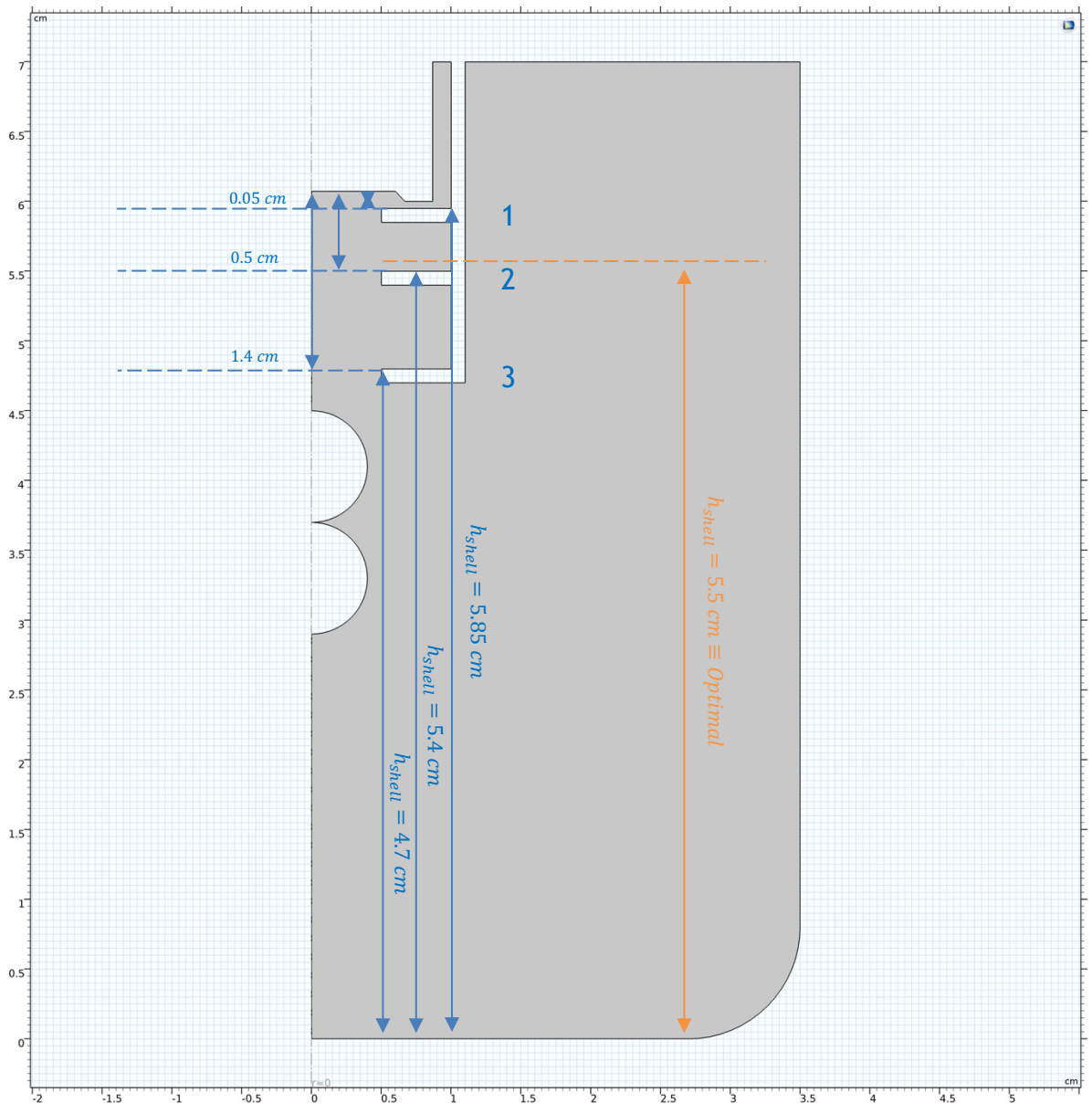


Figure 6. 7: Different “shell mask” base distances from the cathode surface. Position 1 at 0.05 cm, position 2 at 0.5 cm and position 3 at 1.4 cm from the cathode surface. Radius of the mask’s base hole at $r_{hole} = 0.5\text{ cm}$. The orange dash line indicates the optimal position of the mask base at $h_{shell} = 5.5\text{ cm}$ or 0.4 cm from the cathode.

Figure 6.8 shows the potential and current distribution in the electrolyte domain for all three cases. In terms of potential distribution in the electrolytic volume “far from” the area between the electrodes, it is evident that its order is not significantly affected by the presence of the “mask”, presenting a different behaviour than what

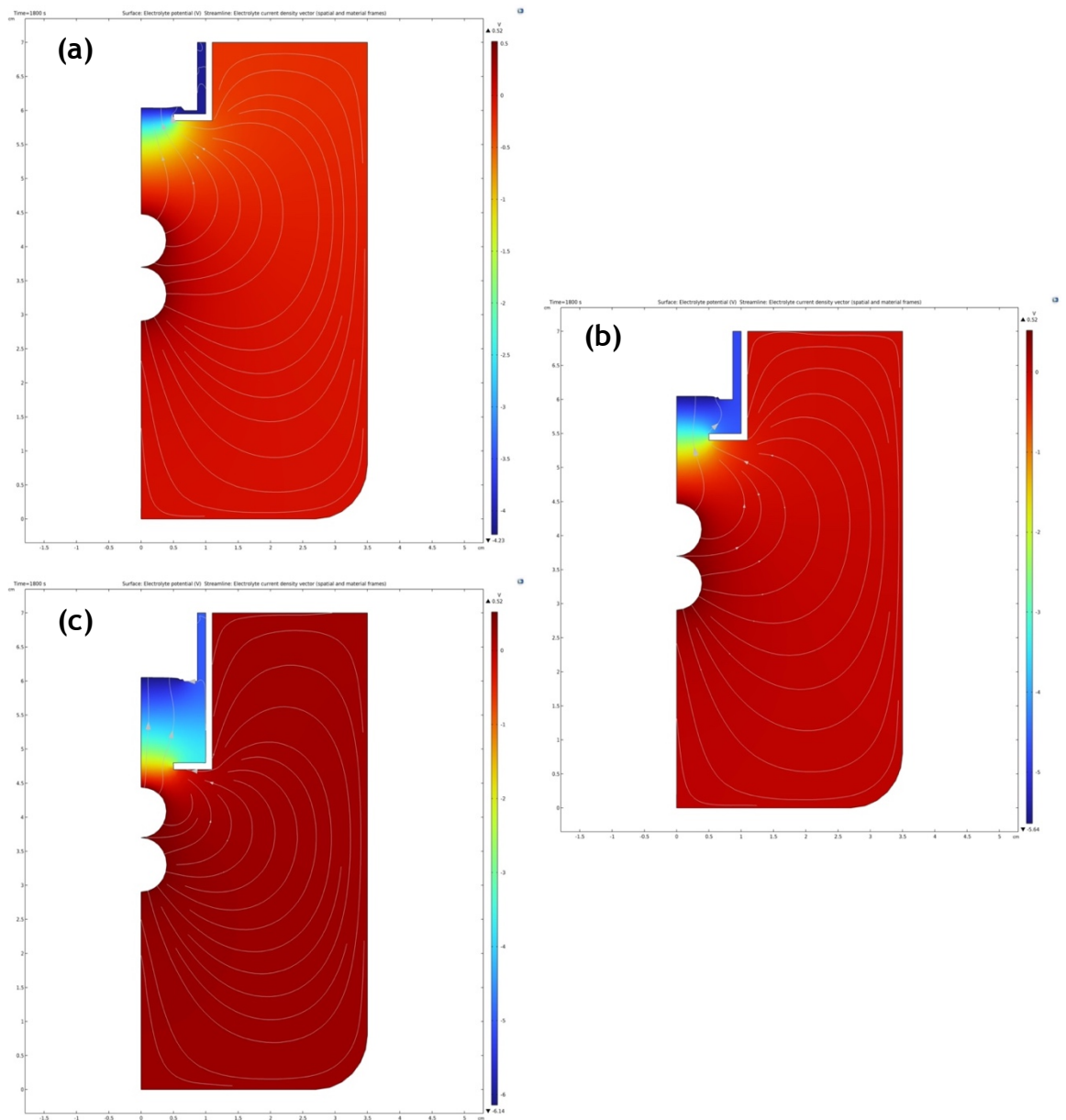


Figure 6. 8: 2-D representation of the potential and current distribution in the electrolytic volume for the case when the base of the “shell mask” is placed at **(a)** $h_{shell} = 5.85\text{ cm}$ or 0.05 cm from the cathode surface, **(b)** $h_{shell} = 5.4\text{ cm}$ or 0.5 cm from the cathode surface and **(c)** $h_{shell} = 4.7\text{ cm}$ or 1.4 cm from the cathode surface.

was observed for the “ring mask” system (Figure 6.3). However, near the cathode-electrolyte interface a reverse behaviour is observed in the case of the “shell mask” compared to that in the case of the “ring mask”; here, as the “shell mask” base “moves away from” the cathode surface a decrease of potential values (*i.e.*, more

negative values) is observed. This indicates that more energy is “trapped” between the cathode and the mask when there is more room between the two. For position 1 potential values near the cathode-electrolyte interface are calculated around -4.23 V (Figure 6.8-a), around -5.64 V for position 2 (Figure 6.8-b) and around -6.14 V for position 3 (Figure 6.8-c). In all three cases, the current streamlines are only able to “travel” through the hole at the base of the mask, always reaching the cathode surface frontally (*i.e.*, “from underneath”).

On another difference, streamlines seem to be reaching the exposed cathode surface perpendicularly in the case when the base of the “shell mask” lies at position 2 (Figure 6.8-b), indicating a more uniform current distribution across the exposed cathode surface. Interestingly, position 2 coincides with the closest “mask” placement possible in industry, indicating that the use of the “shell mask” overcomes the limitation imposed previously by the “ring mask” which had to be placed much closer than it would ever be possible in an industrial setup.

The simulated thickness profiles for the three “shell mask” positions also support the above observation. As it can be seen in Figure 6.9, the thickness profile for the case when the “mask” base is positioned within 0.5 cm from the cathode surface (red line) presents an almost flat area up to 0.42 cm from the cathode centre, suggesting a uniform thickness of an average 0.25 mm across the cathode diameter.

At the same time and contrasting the “ring mask” behaviour, placement of the “shell mask” base at the closest position 1 (blue line) from the mandrel surface returned the worst results, predicting a significantly non-uniform thickness distribution at the cathode, due to “over-squeezing” of the potential field.

Even though a significantly higher thickness was calculated for the case of position 1, at an average of 0.35 mm , the simulated thickness profile suggests that position 1 should also be considered as an alternative. Both the calculated thickness values

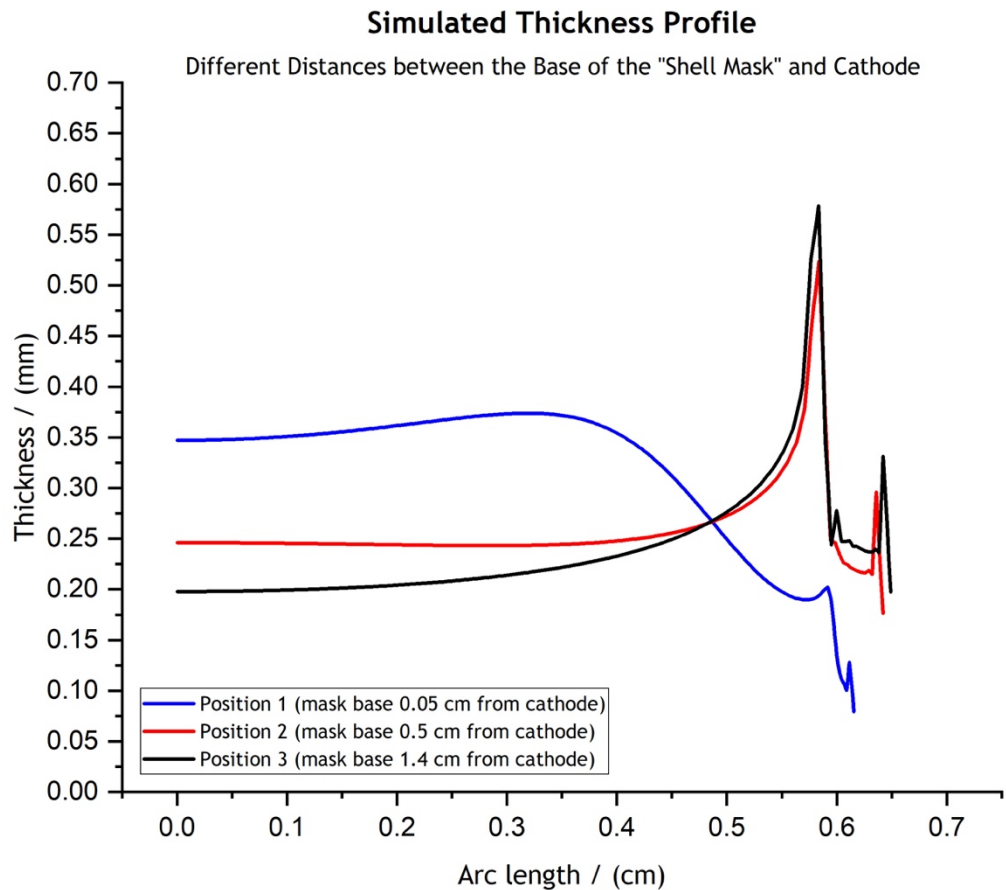


Figure 6. 9: Simulated thickness profiles for the different distances of the “shell mask” base from the cathode surface.

(average of 0.2 mm) and the predicted uniformity decrease significantly for the case when the “shell mask” base is placed at position 3.

The results are also shown in terms of the thickness distribution on the cathode surface in [Figure 6.10](#). The 2-D representation of the thickness distribution, provided here for consistency, also confirms that the placement of the “shell mask” base at the closest position 1 from the mandrel surface results in high non-uniformity at the cathode, due to “over-squeezing” of the potential field.

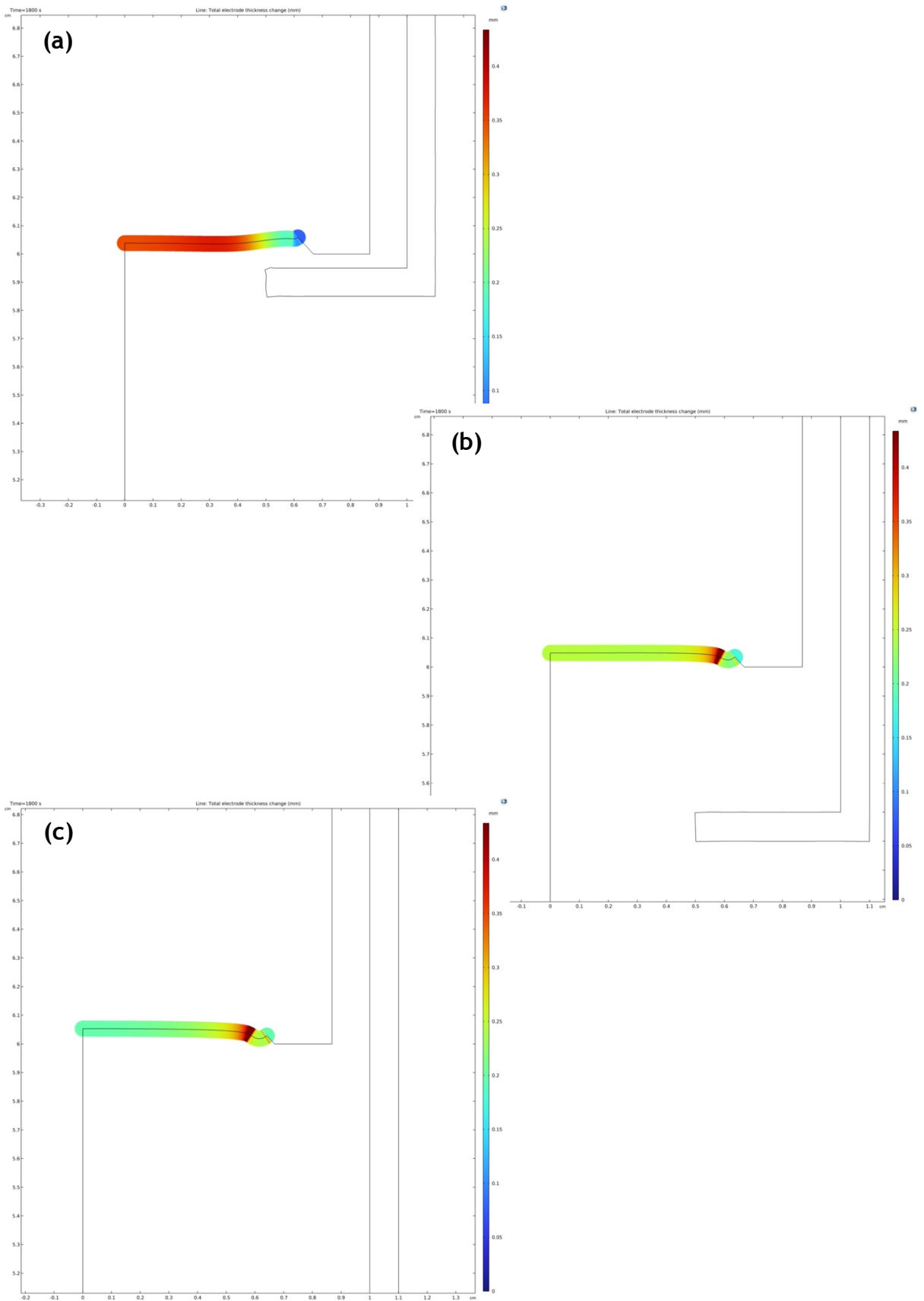


Figure 6. 10: 2-D representation of the thickness distribution on the cathode surface for the case when the base of the “shell mask” is placed at (a) $h_{shell} = 5.85 \text{ cm}$ or 0.05 cm from the cathode surface, (b) $h_{shell} = 5.4 \text{ cm}$ or 0.5 cm from the cathode surface and (c) $h_{shell} = 4.7 \text{ cm}$ or 1.4 cm from the cathode surface. For clarity, the colour code indicates lower thicknesses with blue (starting at 0 in the deep blue part of the scale) and higher thicknesses with red.

At an effort to flatten the simulated thickness profile further (*i.e.*, enhance thickness uniformity), various other positions within 0.15 cm from position 2 were investigated. These sensitivity studies of the “mask” position revealed that thickness uniformity could be enhanced if the base of the “shell mask” is placed at $h_{shell} = 5.55$ cm, or 0.4 cm from the cathode surface (refer to Figure 6.7). Even though the potential and current distribution in the electrolyte (Figure 6.11-a), as well as the thickness distribution at the cathode (Figure 6.11-b) are not affected by the different positioning of the “mask”, it is evident in Figure 6.11-c that this optimal position (green line) provides a significantly improved thickness uniformity compared to the second best achieved in position 2 (red line). At the same time, the optimal position at 0.4 cm from the cathode surface, also results in a slightly higher average thickness of 0.27 mm and a slightly decreased thickness closer to the leading edge. Nevertheless, even in that case, the problem of high current accumulation at the leading edge remains, highlighted by the circle in Figure 6.11-b.

As another step, the effect of making the base hole smaller was thought to be of some interest, maybe allowing for a deeper insight into the current’s distribution mechanism. Consequently, the “shell mask” was kept at its optimal position (0.4 cm from the cathode surface) while the radius of the hole at its base was decreased by 0.1 cm ($r'_{hole} = 0.4$ cm). As it can be seen in Figure 6.12, such a modification in the “mask” geometry does not provide an enhancement in thickness uniformity (Figure 6.12-c). Even worse, it predicts a lower average thickness and a higher value for the thickness closer to the leading edge.

Having established that thickness uniformity can be enhanced by identifying a suitable “mask” geometry and placing it at an optimal position (with reference to the cathode surface), investigating whether it is possible to also decrease the current accumulation at the leading edge was the only reasonable next step. For that purpose, a combination of a “mask” and a “thief” was deployed.

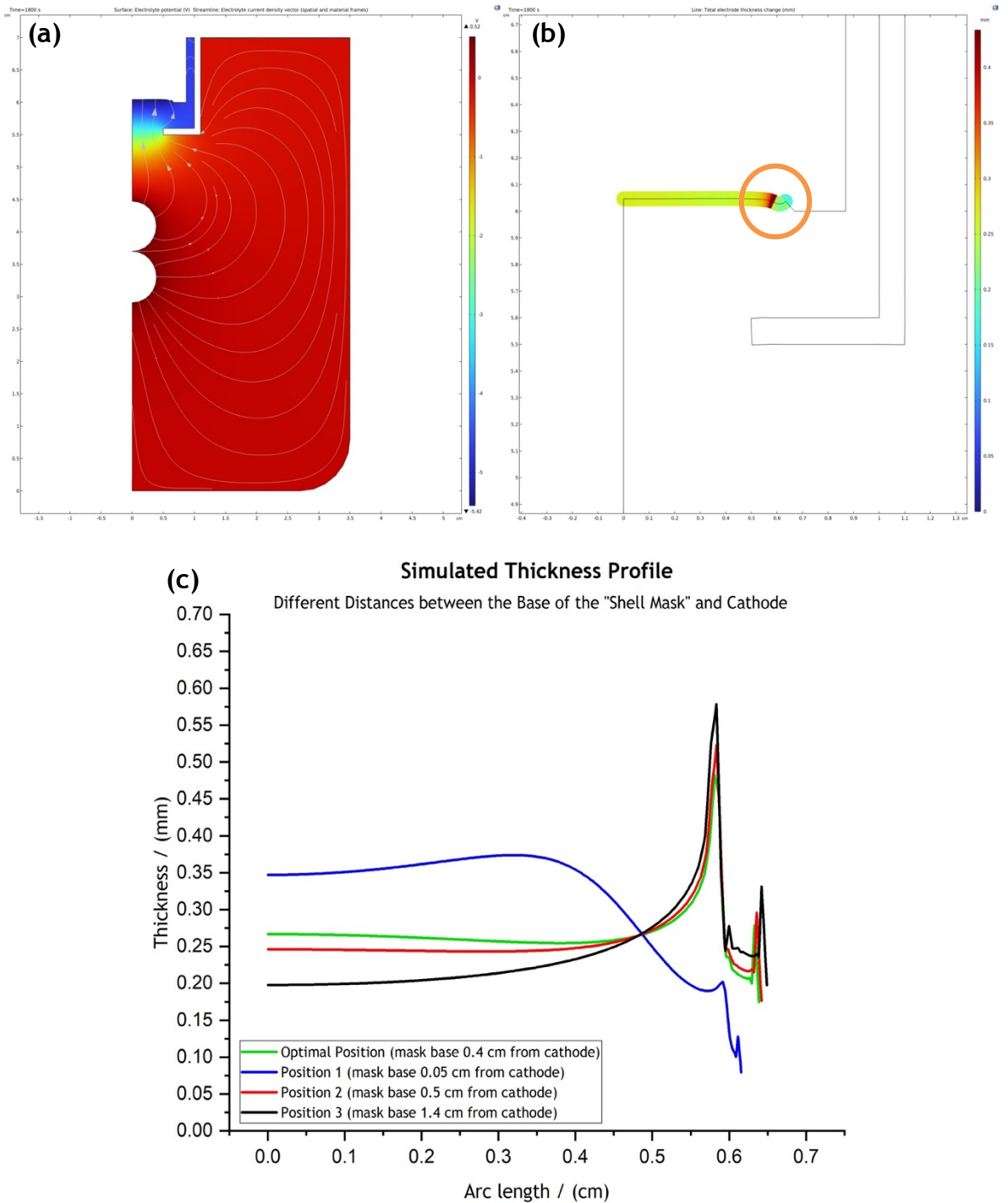


Figure 6. 11: 2-D representation of (a) the potential and current distribution in the electrolytic volume and (b) the thickness distribution on the cathode surface for the case when the base of the “shell mask” is placed at its optimal position ($h_{shell} = 5.5 \text{ cm}$, or 0.4 cm from the cathode surface). (c) Comparative graph of the simulated thickness profiles for the cases when the “shell mask” base is placed at its optimal position, position 1, position 2 and position 3. High current accumulation at the leading edge highlighted in circle in (b).

6.1.2 The “Shell Mask” - “Ring Thief” Configuration

Unlike “masks”, “thieves” are conductive objects which can “steal” any excess current accumulating at specific cathode areas, e.g., the mandrel leading edges, to help with minimising or eliminating phenomena like the growth of dendrites.

In the 2D-Axisymmetric RDE model, only “ring thieves” could be investigated. As an additional advantage, this “thief” geometry can easily be represented in real life by any metal wire, making potential experimental validation studies much easier.

In terms of physics, the model had to be slightly modified since “thieves” need to be declared as additional electrode surface boundaries; “thieves” essentially work as cathodes. However, this configuration should not be confused with the rotating ring-disk electrode (RRDE) setup. “Thieves” are not used as working electrodes, they are just additional negatively charged surfaces, other than the cathode surface, that “steal” some of the current “travelling” through the electrolyte away from the cathode. The model remained almost the same as the one that has been used so far for all 2-D axisymmetric in this work. The only addition was a third electrode boundary interface, representing the “thief” boundaries. The “thief” boundary was described by an external potential value of $\varphi_{s,thief} = -5 V$. All the other input parameters remained the same as those applied for every electrode boundary (refer to [Table 3.2](#)).

As mentioned earlier, “thieves” were studied in terms of their ability to minimise current accumulation at the leading edge of the RDE. The aspiration was that a “thief” placed close to the leading edge would function complimentary to the “shell mask” presented earlier by “stealing” the excess current accumulating at the edge.

After trying various configurations through a trial-and-error approach, the “shell mask” - “ring thief” configuration of [Figure 6.13](#) was chosen to be presented here. the “ring thief” was of an inner radius $r_{inner} = 0.5 \text{ cm}$ and an outer radius $r_{outer} = 0.8 \text{ cm}$ and width $w_{thief} = 0.3 \text{ cm}$. It was placed within 0.05 cm from the cathode

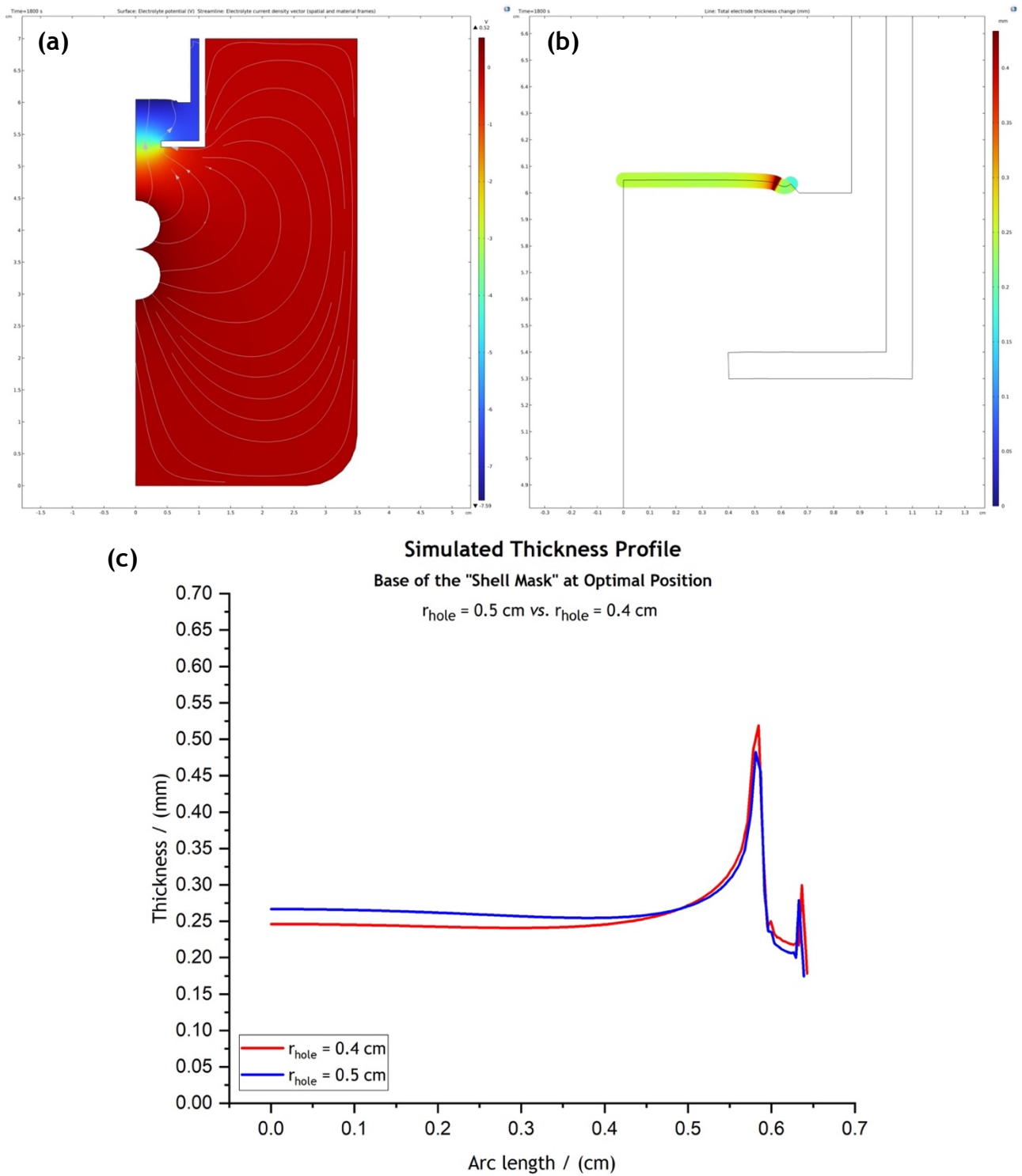


Figure 6. 12: 2-D representation of (a) the potential and current distribution in the electrolytic volume and (b) the thickness distribution on the cathode surface for the case when the base of the “shell mask” is placed at its optimal position ($h_{shell} = 5.5 \text{ cm}$, or 0.4 cm from the cathode surface) and the hole at its base is decreased by 0.1 cm ($r_{hole} = 0.4 \text{ cm}$). (c) Comparative graph of the simulated thickness profiles for two different sizes of the “shell mask” base hole; $r_{hole} = 0.5 \text{ cm}$ vs. $r_{hole} = 0.4 \text{ cm}$.

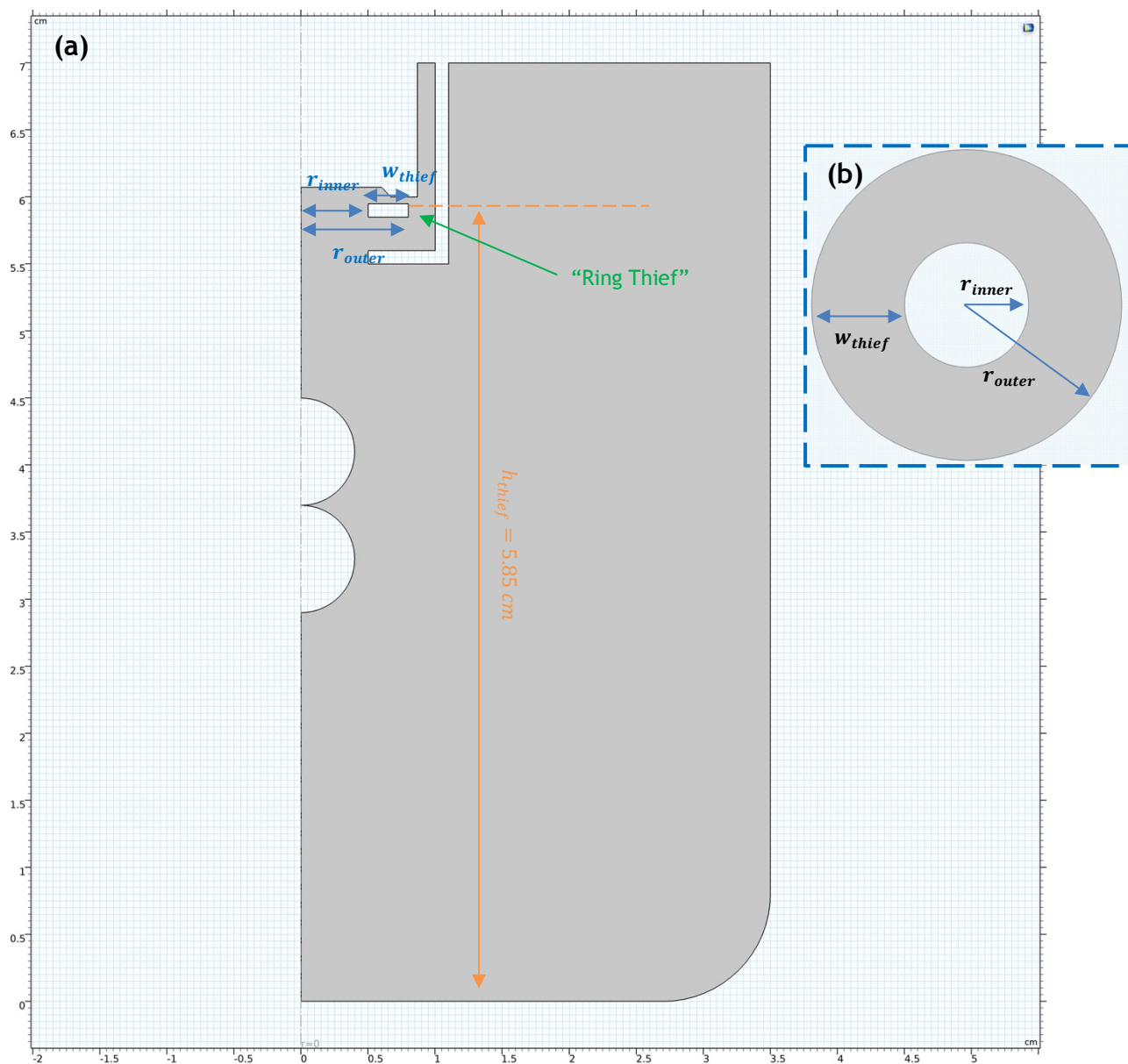


Figure 6. 13: (a) 2-D axisymmetric geometry of the RDE setup including the “shell mask” at its optimal position and a “ring thief” placed between the “mask” and the cathode at $h_{thief} = 5.85 \text{ cm}$, or 0.05 cm from the cathode surface. (b) Top view of the “ring thief”; $r_{inner} = 0.5 \text{ cm}$, $r_{outer} = 0.8 \text{ cm}$. The “thief” has a width $w_{thief} = 0.3 \text{ cm}$ and is indicated by the green arrow.

surface ($h_{thief} = 5.85 \text{ cm}$), centred to it, and closest to the leading edge. The simulation results are shown in Figure 6.14. As it can be seen in Figure 6.14-a, the presence of the “ring thief” slightly affects the potential close to the cathode-electrolyte interface. This value (-5.04 V) was slightly increased (*i.e.*, became less negative)

compared to the corresponding one (-5.64 V) for the case when only the “shell mask” was present and placed at its optimal position (refer to [Figure 6.8-b](#)). Most importantly, the thickness distribution on the cathode surface was improved compared to the one shown in [Figure 6.11-b](#) for the case of the “shell mask”. That effect can be seen more clearly in [Figure 6.14-c](#). The thickness profile simulated for the “shell mask” - “ring thief” configuration (red line) was found to be even more flat than the one predicted for the case when only the “shell mask” was used (blue line). This means that, if the area of high currents ($0.5\text{ cm} - 0.6\text{ cm}$) is treated as a “trim area”, to be cut off of the final electroform, significantly uniform parts can be produced. However, the main goal of these studies, the minimisation of current accumulation at the leading edge, was not achieved. Even though the thief “steals” part of the “excess” current, the area of interest is not at all relieved from high currents (area in circle in [Figure 6.14-b](#)). Since this increase in current appears very close to the boundary’s edge, this is a non-trivial task.

As a general comment, the RDE modelling studies suggest that the use of “thieves” would not lead to significant breakthroughs in terms of the dendritic growth at the edges. At the same time, such results do not justify the increased complexity in setting up the process that accompany their deployment in the industrial environment. It is clear that the points made so far, regarding the effectiveness of “masks” and “thieves”, refer to the non-complex geometry of the RDE and the laboratory scale.

In the next section, a few very basic examples of the use of “masks” in the industrial scale and alongside the more challenging geometry of the mechanical vane are discussed.

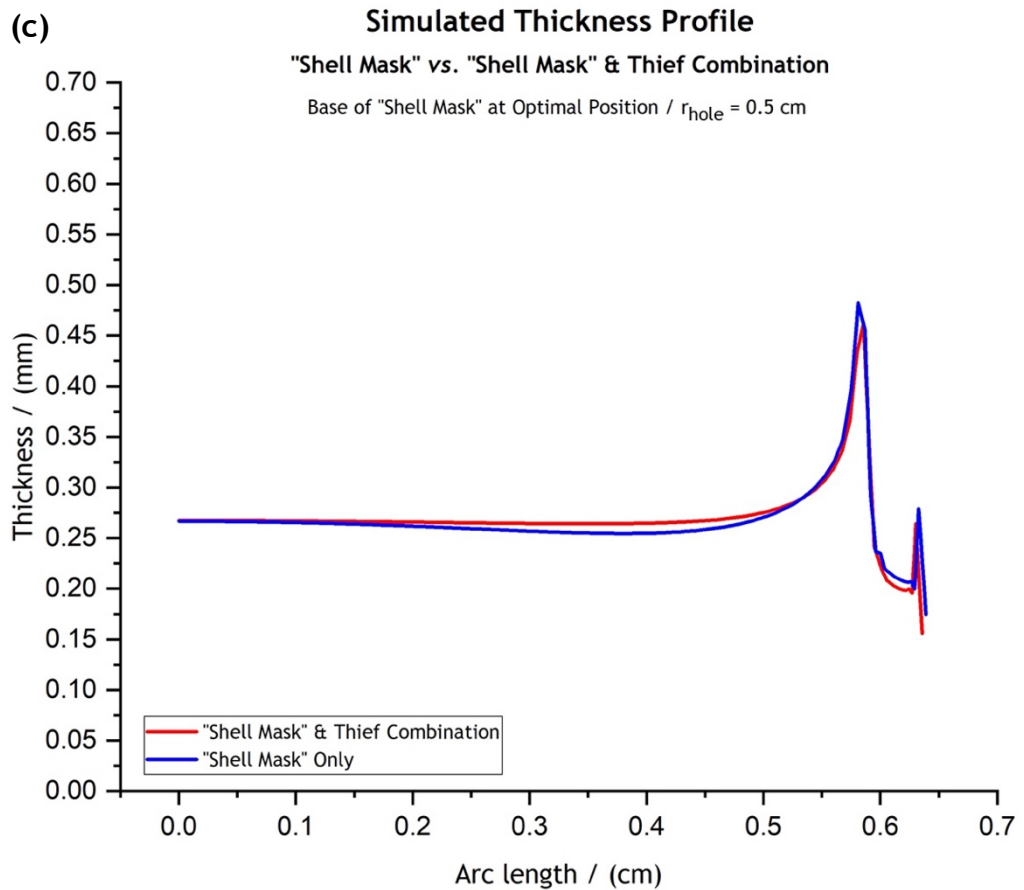
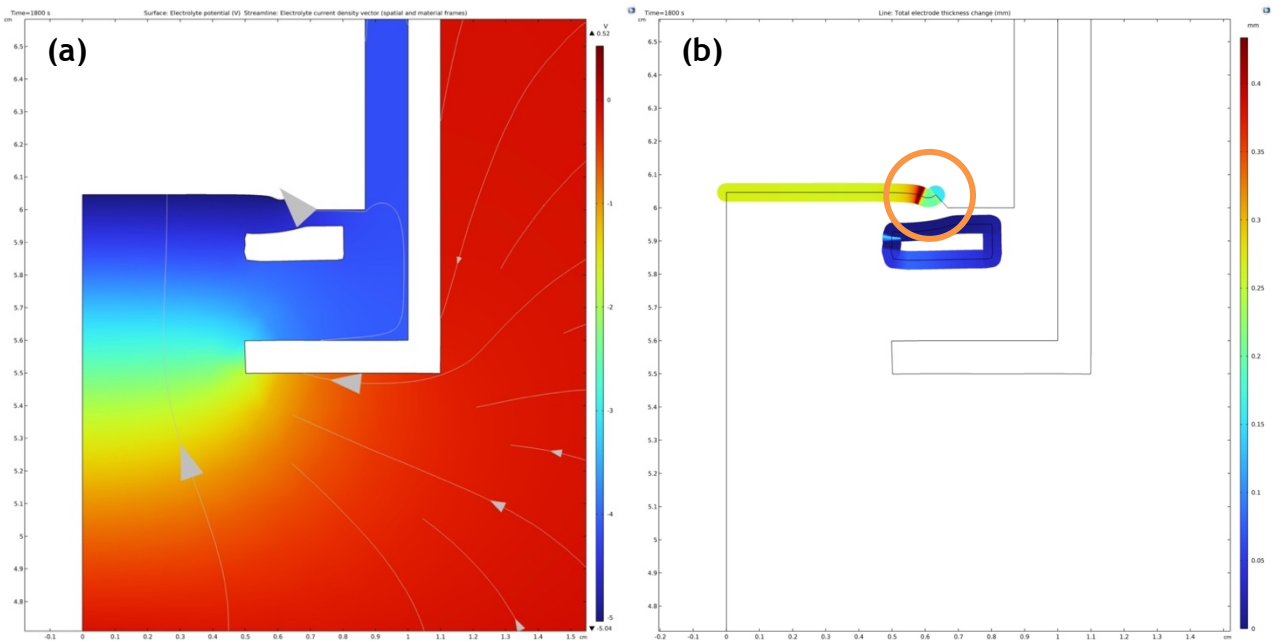


Figure 6. 14: 2-D representation of (a) the potential and current distribution in the electrolytic volume and (b) the thickness distribution on the cathode surface for the case when the “shell mask” - “ring thief” configuration is used. (c) Comparative graph of the simulated thickness profiles for the case when the “shell mask” - “ring thief” configuration is used vs. the case when only the “shell mask” is used placed at its optimal position.

6.1.3 “Masks” alongside the Mechanical Vane Mandrel

As it has already been presented in [Chapter 5](#), the thickness requirements for the mechanical vane geometry call for deposits thicker at the “nose” area and considerably thinner at the sides. Based on the experimental results presented in [Figure 5.17](#) for deposit R6, if the process parameters are set so that they accommodate higher thicknesses at the “nose” (e.g., higher applied currents, longer deposition times) then the sides will overgrow even the acceptable maximum thickness tolerance. This behaviour constitutes a really good example of a case when the use of “masks” should be considered in industry for process optimisation purposes.

Based on the very promising results previously obtained through the use of the “shell mask”, a similar “mask” geometry was also used alongside the vane mandrel. This is shown in [Figure 6.15](#).

The “shell”-type “mask” used here was essentially a box with a slit on its bottom side to allow for the “nose” area to get through it ([Figure 6.15-b](#)), and without a top side. The “mask” was positioned around the cathode at $h_{mask} = 23\text{ cm}$ from the flat bottom of the prototype tank ([Figure 6.15-a](#)). The masking box was of a length $l_{mask} = 21\text{ cm}$ ([Figure 6.15-a](#)), width $w_{mask} = 3.1\text{ cm}$ and depth $d_{mask} = 3.5\text{ cm}$ ([Figure 6.15-b](#)).

The idea was to “protect” most of the vane mandrel surface from all sides, allowing the current to reach it from the exposed area “from the top” of the “mask”, as indicated in [Figures 6.16-a & 6.16-b](#) by the orange arrows resulting in thinner deposits there compared to the “nose” area of the mandrel. The “nose” was the only mandrel area left exposed by the “mask”, with the current reaching it directly. This arrangement would result in higher current accumulation around the “nose” area ([Figure 6.16-b](#)) and, consequently, higher thicknesses there ([Figures 6.16-c](#)).

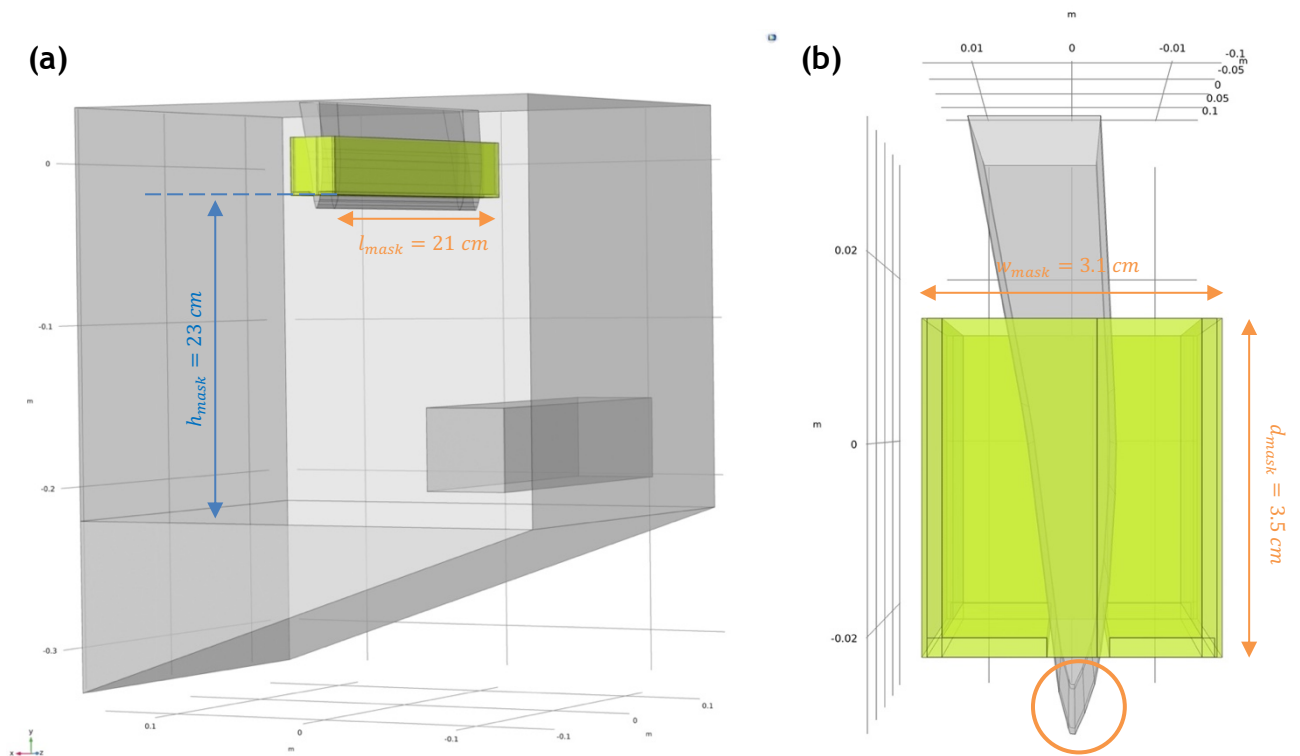


Figure 6. 15: (a) 3-D geometry of the mechanical vane setup including a “shell”-type “mask” at $h_{mask} = 23 \text{ cm}$ from the flat bottom of the prototype tank. (b) Side view of the “shell”-type “mask”. The dimensions of the “mask” are also shown. The circle indicates the “nose” area of the mandrel.

As Figure 6.17 indicates, the simulations suggested that the deployment of the “shell”-type “mask” alongside the mechanical vane mandrel would prevent over-growth at the sides of the mandrel and increase the thickness of the “nose”, bringing the overall thickness distribution across the mandrel’s surface closer to the target thickness profile. Specifically, the green profiles in Figure 6.17 indicate that the mandrel’s back and front sides will grow slower, while the “nose” will grow faster, compared to what is the case when no “mask” is deployed (indicated by the blue thickness profiles). This means that, in practice, the process could be run for slightly longer than 5 hours (resulting in deposit R6, black thickness profile), in order to eventually allow the “nose” to reach its target thickness while the front and back side thicknesses are also kept within the lower acceptable thickness targets.

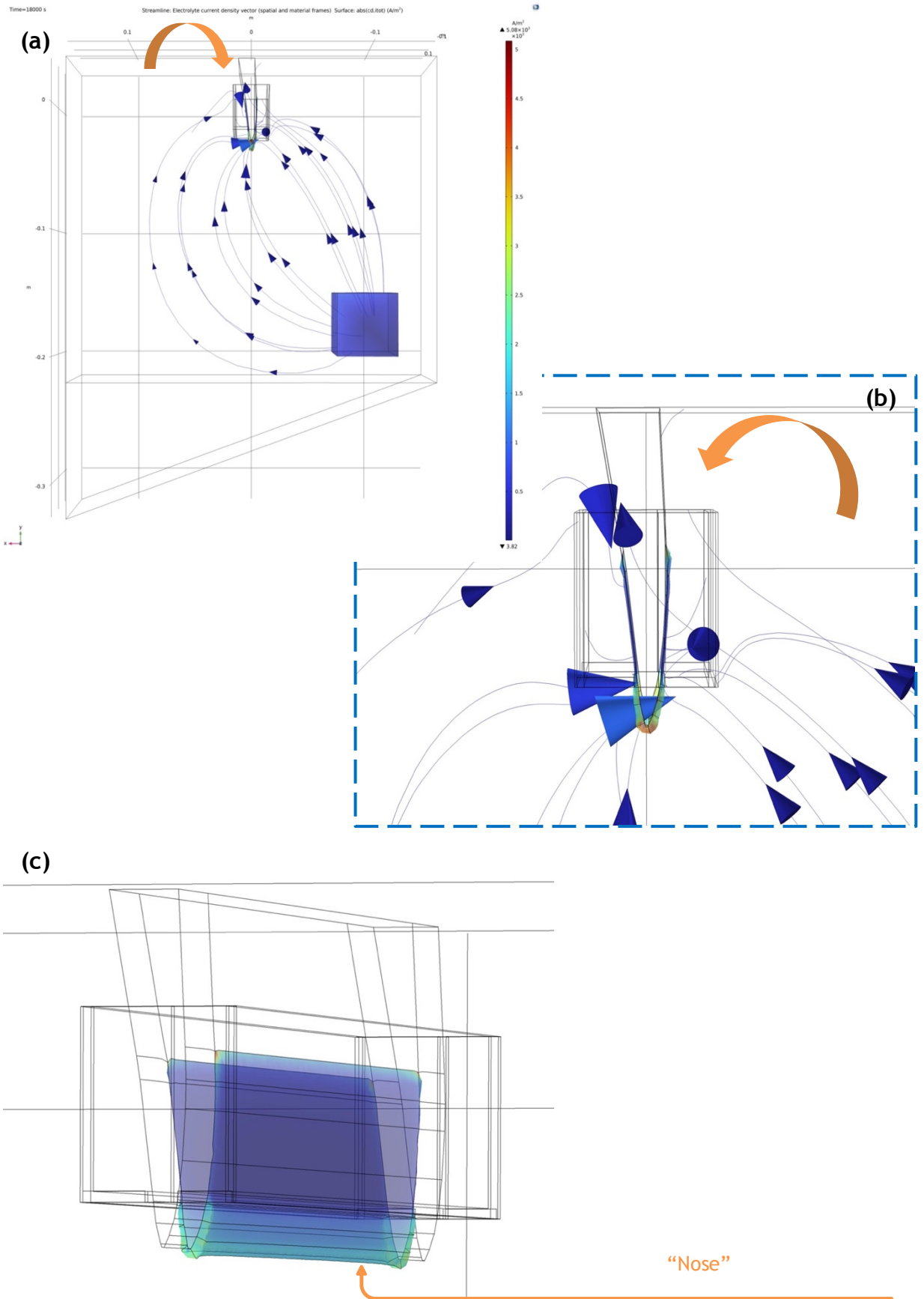


Figure 6. 16: (a) 3-D representation of the current distribution in the electrolytic volume, (b) current streamlines' behaviour close to the mandrel surface and (c) thickness distribution on the cathode surface for the case when the a "shell"-type "mask" is used alongside the mechanical vane mandrel. The arrows in (a) and (b) indicates the current reaching the mandrel sides indirectly "from the top" while, (c) indicates the exposed "nose" area of the mandrel which the current reaches directly.

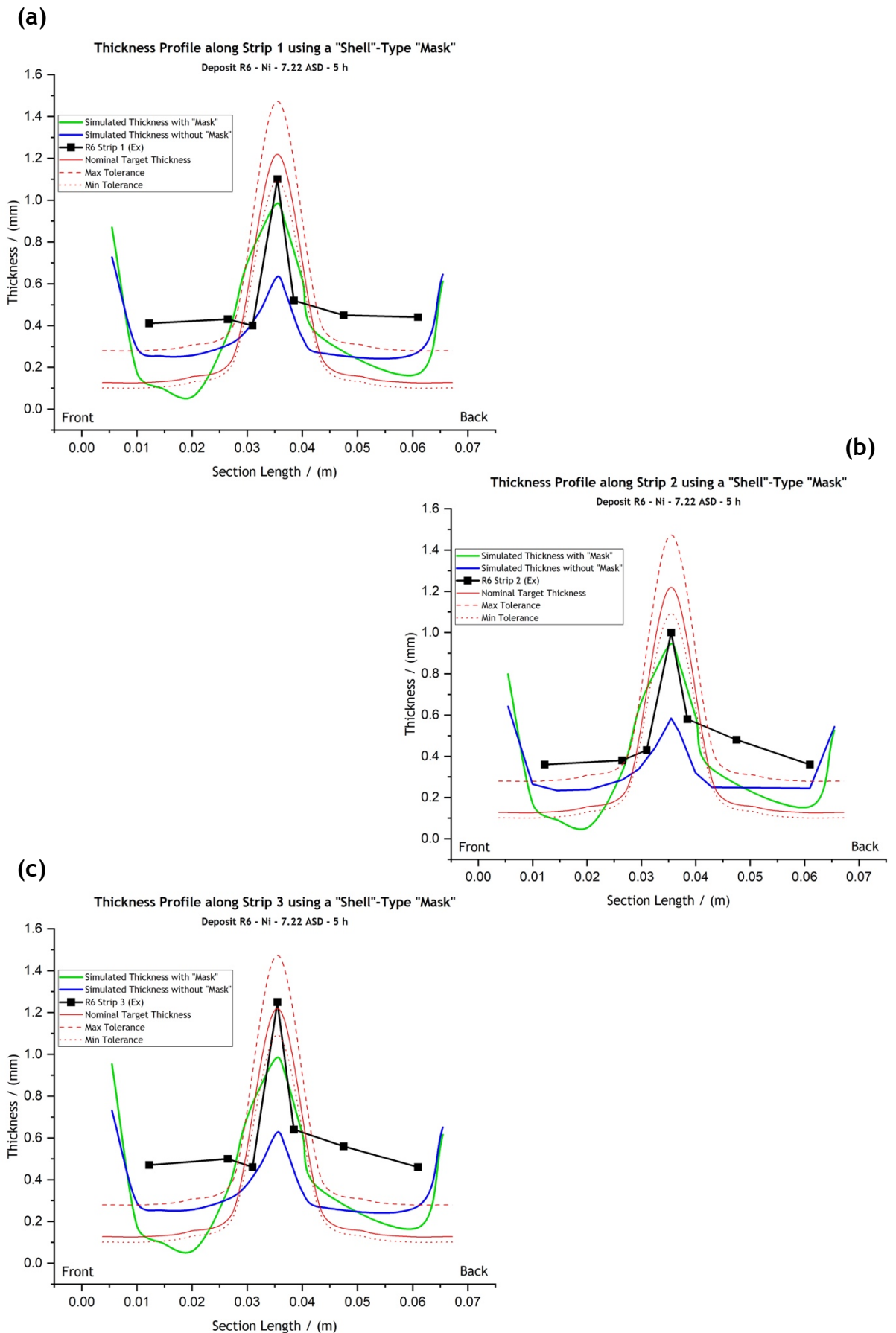


Figure 6. 17: Comparative graphs of the experimental and simulated thickness profiles for (a) strip 1, (b) strip 2 and (c) strip 3 of the mechanical vane deposit R6. Green line represents the simulated thickness for R6 alongside a “shell”-type “mask”, while the blue line represents the simulated thickness for R6 without the use of a “mask”. “Front” indicates the mandrel side closer to the anode.

Of course, one should keep in mind that these modelling results have not been confirmed by practical experiments therefore, they should be accepted cautiously. However, the fact that the modelling results confirm the working theory of what a “shell”-type “mask’s” function should be is of great importance. Carrying out such simulations shows the value of a well-informed modelling tool which allows manufacturers to virtually investigate potential optimisation paths before deciding to invest time, money, materials, and energy to the manufacturing process of a part.

6.2 Primary, Secondary & Tertiary Current Distribution

As it has already been discussed in [Chapter 3](#), all modelling studies presented so far have assumed secondary current distribution physics since such models fit the purpose of the work carried out as part of this project. Furthermore, one of the main goals of the project has been to investigate exactly this; whether simpler and faster SCD modelling studies can be efficiently deployed in industry to enhance process optimisation and identify new possibilities in product development.

Nevertheless, and since the adequacy of SCD models is often doubted against, what considered to be, more complete tertiary current distribution models, it was deemed appropriate to present here a rudimentary comparison between PCD, SCD, and TCD electroforming models.

The comparison carried out for both the RDE and the scaled-up disk models, whose SCD versions have already been compared once in [Chapter 4](#) with regard to their different scales. The geometries and mesh characteristics in both 3-D, time dependent models were kept the same as the ones already presented there (refer to [Figure 4.5](#) and [Table 4.1](#)). Without deviating from the model validation investigations of [Chapter 4](#), the cathode boundary of the RDE model was described by a total applied

current $I_{l,total} = -0.565 \text{ A}$ (50 A/dm^2) and an applied electric potential $\varphi_{s,ext,init} = -5 \text{ V}$. Similarly, for the industrial-scale model the cathode boundary conditions were set at a total current $I_{l,total} = -1 \text{ A}$ and an electric potential initial value at $\varphi_{s,ext,init} = -2.5 \text{ V}$ (3.2 A/dm^2). Anode boundary conditions were set at $\varphi_{s,ext,init} = 0 \text{ V}$ for both models. The RDE model simulated deposition at $50 \text{ }^\circ\text{C}$, for 1800 s , under stagnant conditions. The scaled-up model simulated deposition at $50 \text{ }^\circ\text{C}$, for 10800 s , under stagnant conditions.

With regard to physics, in both PCD and SCD models, the current is related to the potential at the electrode surface through Equation 3.10 ($i_s = -\sigma_s \nabla \varphi_s$) and to the potential in the electrolyte through Equation 3.11 ($i_l = -\sigma_l \nabla \varphi_l$). The difference lies in the way that the electrode-electrolyte interface is described.

In the PCD model, at the electrode-electrolyte interface the electrolysis reaction is considered to be so fast that the potential difference at the boundary does not ever deviate significantly from equilibrium. Consequently, it can be characterised solely through Equation 6.1.

$$E_{eq,m} = \varphi_s - \varphi_l \quad [6.1]$$

On the other hand, in the SCD model the electrolysis reaction is assumed to present a finite rate imposing additional impedance on the boundary. As a result, the potential difference at the electrode-electrolyte interface is assumed to differ significantly from its equilibrium. Subsequently, the concept of overpotential (η_m) is introduced through Equation 3.12 ($\eta_m = \varphi_s - \varphi_l - E_{eq,m}$) and the current is described as a function of that overpotential through the Butler-Volmer equation (Equation 3.9).

While both PCD and SCD models assume uniform ionic concentration in the electrolyte, TCD models take into account concentration gradients in the electrolytic volume, alongside solution resistance (PCD) and kinetic (SCD) contributions. For this purpose, the Nernst-Planck equation (6.2) is solved for each chemical species (i)

present in the electrolyte, describing each one's mass transport through diffusion, migration, and convection.

$$\mathbf{N}_i = -\mathbf{D}_i \nabla c_i - z_i v_{m,i} F c_i \nabla \varphi_l + c_i \mathbf{u} \quad [6.2]$$

where, \mathbf{N}_i is the flux of species i ($\text{mol}/\text{m}^2 \cdot \text{s}$), \mathbf{D}_i the species diffusion coefficient (m^2/s), c_i the concentration of the ion of species i (mol/m^3), z_i the species charge number, $v_{m,i}$ ($\text{s} \cdot \text{mol}/\text{kg}$) the species mobility and \mathbf{u} (m/s) the field velocity vector.

In terms of the electrolysis reaction at the electrode-electrolyte interface, this is assumed to be transport-limited by consumption of the reactant, with kinetic expressions for the electrochemical reactions accounting for both the activation and concentration overpotentials. Consequently, the electroneutrality approximation can be applied with the condition that all ions and electroactive species in the electrolyte must be included in the model.

For the case of tertiary current distribution, the electrolyte current density does not abide by Ohm's law. The current is consequently expressed through [Equation 6.3](#),

$$\mathbf{i}_i = -F(\nabla \sum_i z_i D_i c_i) - F^2 \nabla \varphi_l \sum_i z_i^2 v_{m,i} c_i + \mathbf{u} F \sum_i z_i c_i \quad [6.3]$$

where, the diffusion terms cannot be zero since electrolyte concentration variations are taken into account. For electroneutrality, when $\sum_i z_i c_i = 0$, [Equation 6.3](#) is written as follows:

$$\mathbf{i}_i = -F(\nabla \sum_i z_i D_i c_i) - F^2 \nabla \varphi_l \sum_i z_i^2 v_{m,i} c_i \quad [6.4]$$

The current density of charge transfer reactions is expressed as a function of both the overpotential and the concentration of the electroactive species at the interface. The reaction kinetics can once more be expressed using the Butler-Volmer

model, which now incorporates the concentration dependencies through Equation 6.5,

$$i_{loc,m} = i_{0,m} \left(\frac{c_{Red}}{c_{ref}} e^{\frac{\alpha_{a,m} F \eta_m}{RT}} - \frac{c_{Ox}}{c_{Ref}} e^{\frac{-\alpha_{c,m} F \eta_m}{RT}} \right) \quad [6.5]$$

where, c_{Red} is the concentration of the species that are reduced, c_{Ox} the concentration of the species that are oxidised, and c_{ref} a reference concentration. The c_{Red} and c_{Ox} terms refer to the basic reduction reaction (Equation 6.6).

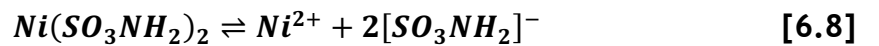


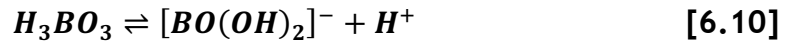
To sum everything up, the TCD interface solves for the electrolyte potential (φ_l), the electrode potential (φ_s), and the species concentrations (c_i). Equation 3.10 describes the electrode boundaries, Equation 6.4 the electrolyte domain, while Equation 6.5 constitutes the typical Butler-Volmer model expression for current density locally, at the electrode-electrolyte interface. Importantly, the reference concentration (c_{ref}) should remain the same for all species involved in a reaction to ensure that, at equilibrium, the overpotential satisfies Equation 6.2.

The last task in the development of the TCD model was to identify the ion species involved in the electrochemical system. Only nickel deposition was assumed to be taken place on the cathode surface according (Reaction 6.7), being the source of one ion species, Ni^{2+} .



Considering the electrolyte components (Table 2.1), three more ion species were identified (Reactions 6.8-6.10): $[SO_3NH_2]^-$, Cl^- , $[BO(OH)_2]^-$.





Since an aqueous electrolytic solution is used, water-based electroneutrality is assumed with two more species deriving from the dissociation of water (Reaction 6.11): H^+ and OH^- .



For the development of the model, the dissociation of every electrolyte component was assumed to be happening instantaneously and was complete (*i.e.*, 100 % dissociation). Therefore, all species were assumed to be present in their ionic form and no equilibrium reactions were taken into consideration in the electrolytic volume. The input parameters required by the software to describe each one of the ionic species involved are provided in Table 6.1.

Table 6. 1: Model input parameters describing each chemical ionic species involved.

Species	Initial Concentration ($c_{0,i} - mol/m^3$)	Charge Number (z_i)	Diffusion Coefficient ($D_{c,i} - m^2/s$)	Reference
Ni^{2+}	1632.49519	+2	6.61×10^{-10}	[14]
$[SO_3NH_2]^-$	3152.1554	-1	5.23×10^{-10}	[15]
Cl^-	112.834978	-1	2.030×10^{-9}	[16]
$[BO(OH)_2]^-$	566.06825	-1	10.996×10^{-9}	[17]
H^+	Automatically Calculated for Electroneutrality	+1	9.3×10^{-9}	Software
OH^-	Automatically Calculated for Electroneutrality	-1	5.3×10^{-9}	Software

As an initial approach to the TCD model, to simplify the model as much as possible without compromising the quality of the results but also keeping the computation time reasonably fast, only two ionic species were considered to be present in the electrolyte: Ni^{2+} and $[BO(OH)_2]^-$. This assumption was supported by the work of Hankin and Kelsall [14] reporting that, based on ion chromatography measurements, neither Cl^- nor $[SO_3NH_2]^-$ were detected in the electrolyte. Therefore, a TCD model assuming the presence of Ni^{2+} , $[BO(OH)_2]^-$, H^+ and OH^- was developed.

Figure 6.18 provides a complete comparison of the potential distribution in the electrolyte, as well as the current and thickness distributions at the cathode surface for PCD, SCD and TCD models of the RDE setup.

The visualisation in Figure 6.18 allows one to check the potential distribution in the domain and near the electrode surface as well as the current lines “travelling” towards the electrode surface. By a comparison of Figures 6.18-a, 6.18-d & 6.18-g one can observe that the potential range remains almost unaffected, and quite wide, between the PCD ($-2.02\text{ V} \leftrightarrow 0.52\text{ V}$) and SCD ($-2.25\text{ V} \leftrightarrow 0.48\text{ V}$) conditions, while it appears limited ($0.01\text{ V} \leftrightarrow 0.48\text{ V}$) for the TCD model. The maximum potential value for the PCD model coincides with the set equilibrium potential ($E_{eq} = -0.52\text{ V}$) while it is calculated slightly lower (-0.48 V) for both the SCD and TCD models.

For all three models the maximum potential values seem to appear in the electrolyte volume close to the anode surface, as it should. At the same time, the density of the current streamlines (*i.e.*, the density of the arrowheads) presents differences among the three models. For the PCD model, the current streamlines accumulate, in a disorderly manner, close to the cathode surface. In the case of the SCD model, current streamlines present an orderly distribution throughout the electrolytic domain, with a more even distribution throughout the electrolytic domain. Current distribution in the electrolyte is simulated to be even more uniform under the TCD assumption, with no areas of high current accumulation being observed anywhere.

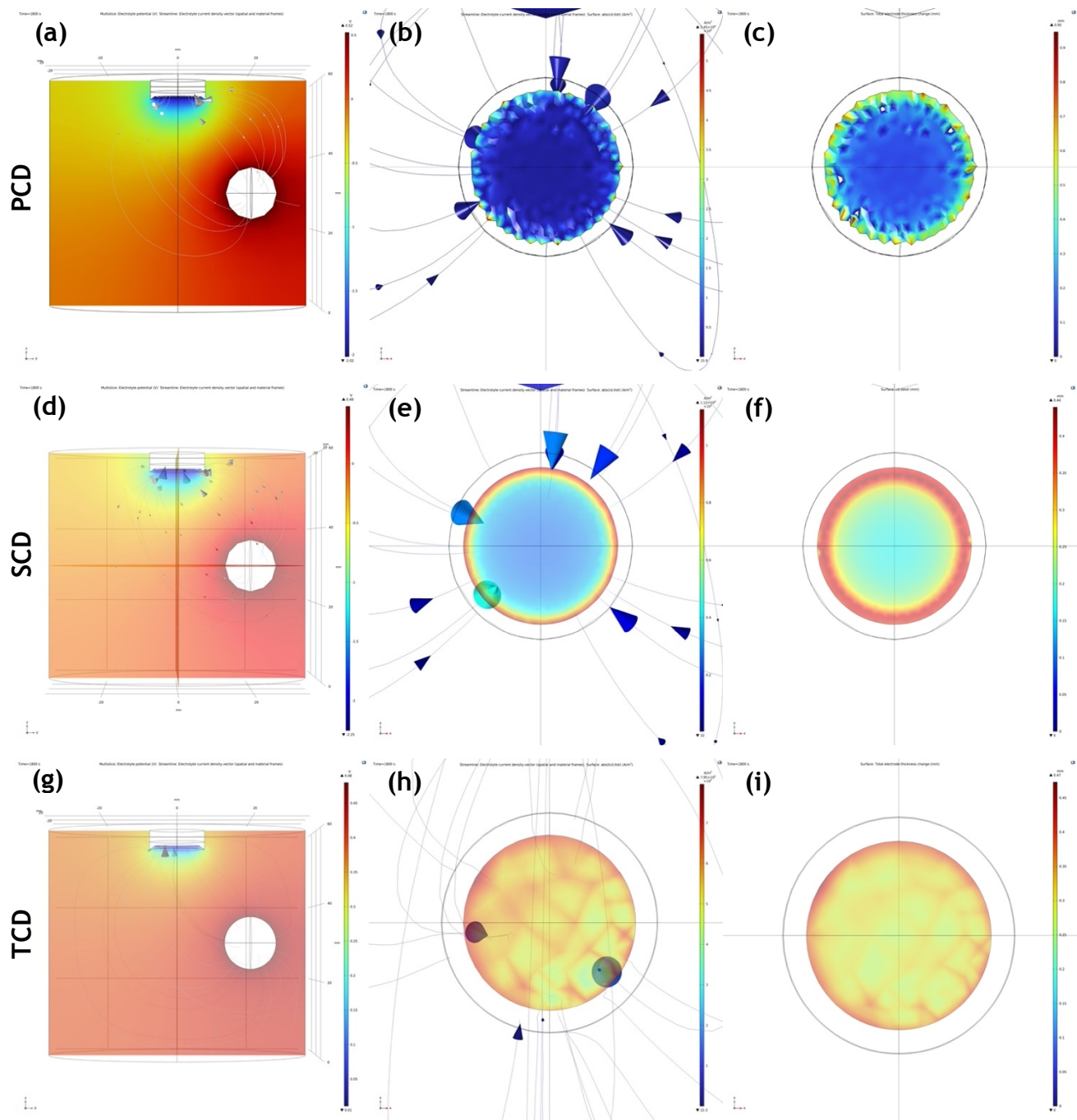


Figure 6. 18: 3-D representation of (a) the potential distribution in the electrolyte, (b) the current distribution at the cathode surface and (c) the thickness distribution at the cathode surface for the PCD RDE model.

3-D representation of (d) the potential distribution in the electrolyte, (e) the current distribution at the cathode surface and (f) the thickness distribution at the cathode surface for the SCD RDE model.

3-D representation of (g) the potential distribution in the electrolyte, (h) the current distribution at the cathode surface and (i) the thickness distribution at the cathode surface for the TCD RDE model.

The results simulate potential, current and thickness distributions for deposition processes conducted at $-0.565 A$ ($50 A/dm^2$) and $-5 V$, for $1800 s$ at $50 ^\circ C$.

The different current distributions at the cathode surface for the PCD, SCD and TCD models are shown in [Figures 6.18-b, 6.18-e & 6.18-h](#). The current behaviour at the cathode surface for each one of these cases is, consequently, depicted in the thickness distributions at the cathode simulated by the three models ([Figures 6.18-c, 6.18-f & 6.18-i](#)). As it is evident here, the PCD model produces rough results, with no detail, indicative of the predicted disorderly distribution of current at the electrode-electrolyte interface. Even though the PCD model does predict higher thickness close to the leading edge ([Figure 6.18-c](#)), the simulated thickness distribution suggested by the SCD model ([Figure 6.18-f](#)) is closer to the experimentally achieved one ($\sim 0.24 \text{ mm}$ in average). At the same time, the TCD model predicts higher thicknesses than the experimental ones, while providing more detail on what is simulated to be a non-uniform, patchy, deposition ([Figure 6.18-i](#)).

The difference among the three models, in terms of the simulated thicknesses, is more clearly presented in [Figure 6.19](#). Here it is confirmed that PCD and SCD model slightly underpredict the thickness while the TCD model slightly overpredicts it. The most important conclusion deriving from the observation of this graph, however, is the fact that TCD models are not necessarily superior to SCD ones when there are only two species in solution. The scalloped appearance of the magenta line in [Figure 6.19](#) could be attributed to convergence being forced since in the real system electroneutrality is achieved by more than two species in the electrolyte. Another interesting point is that, while the TCD model did not provide any additional detail compared to the secondary distribution case, when tertiary effects were considered, computation time was more than 133 times slower (7080 s) compared to the SCD case (53 s).

Because of the studies presented in [Chapter 4](#) suggested that the effect of scaling up can be an important consideration, the same comparison between a PCD, SCD and TCD model was also conducted for the scaled-up disk setup. In a similar manner as for the RDE studies, [Figure 6.20](#) provides a complete comparison of the potential distribution in the electrolyte, as well as the current and thickness distributions at the cathode surface for PCD, SCD and TCD models of the scaled-up disk setup.

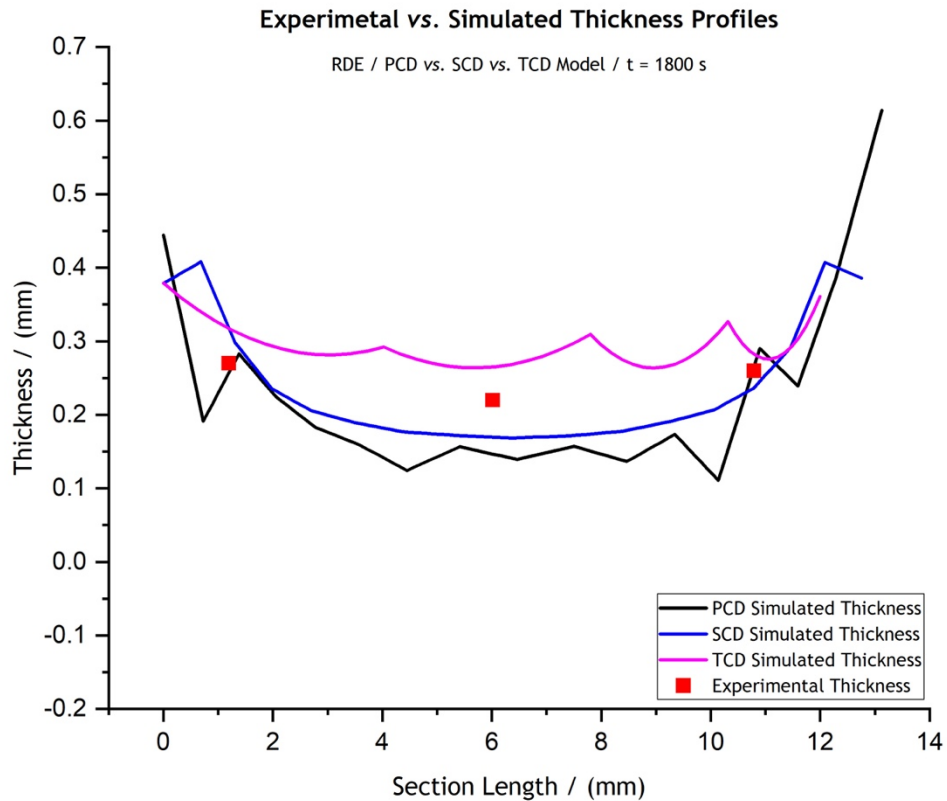


Figure 6. 19: Comparative graphs of the experimentally achieved (red data points) and the simulated thickness profiles by the PCD (black line), SCD (blue line) and TCD (magenta line) RDE setup models. The RDE deposit was produced at -5 V and -0.565 A , for 1800 s at $50\text{ }^\circ\text{C}$.

By a comparison of [Figures 6.20-a](#), [6.20-d](#) & [6.20-g](#) one can observe a similar behaviour to the one also suggested by the RDE models. The potential range remains almost unaffected between the PCD ($-0.26\text{ V} \leftrightarrow 0.52\text{ V}$) and SCD ($-0.41\text{ V} \leftrightarrow 0.48\text{ V}$) conditions, but not quite wide as it was the case for the laboratory-scale RDE models. The corresponding range for the TCD model appears once more limited ($0.2\text{ V} \leftrightarrow 0.52\text{ V}$) compared to the two other models. For all three models, the maximum potential value coincides with the set equilibrium potential ($E_{eq} = -0.52\text{ V}$) and it appears in the electrolyte volume close to the anode surface. The density of the current streamlines is, for the scaled-up model as well, predicted to be the most amplified for the TCD model ([Figure 6.20-h](#)).

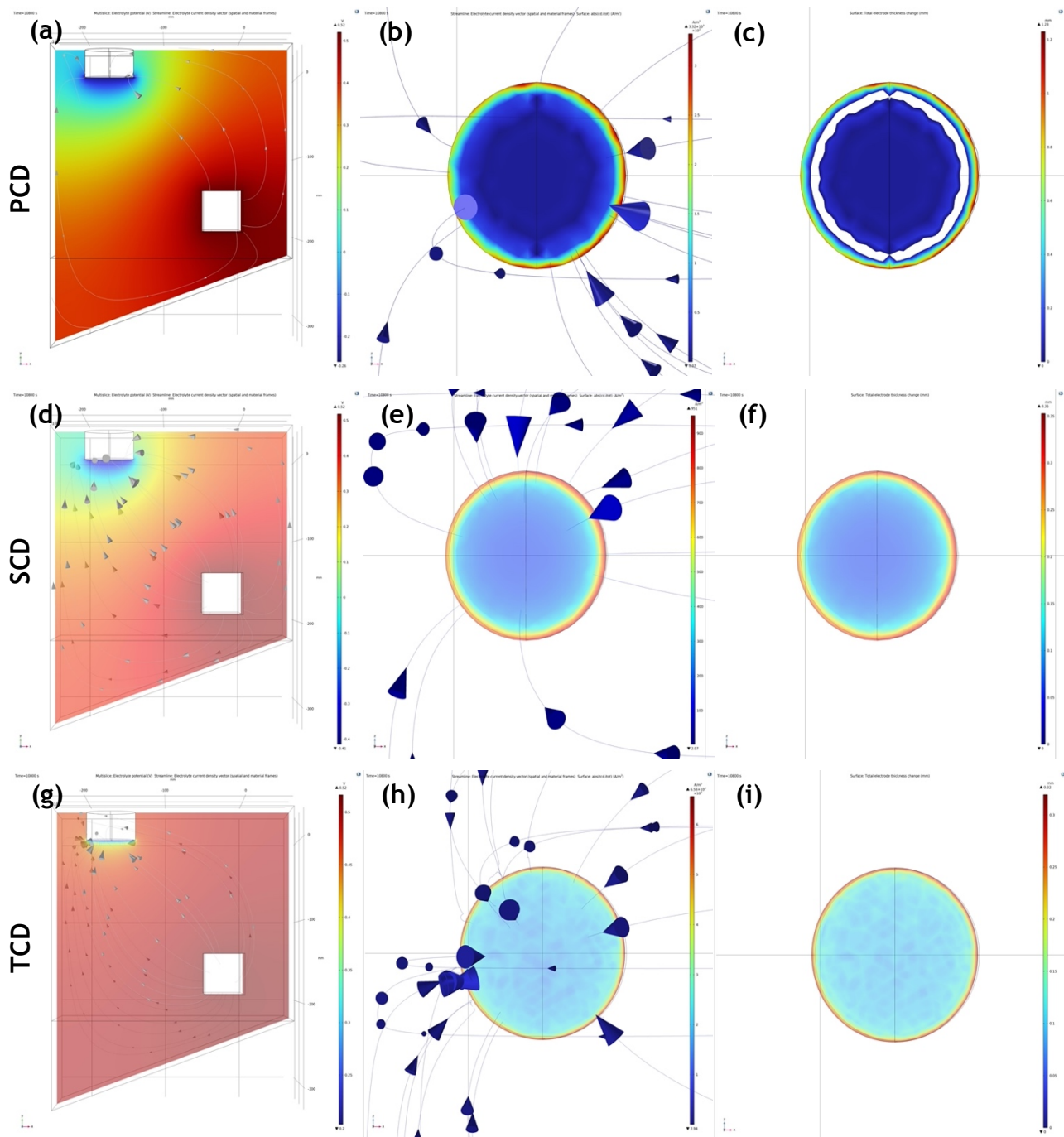


Figure 6. 20: 3-D representation of (a) the potential distribution in the electrolyte, (b) the current distribution at the cathode surface and (c) the thickness distribution at the cathode surface for the PCD scaled-up disk model.

3-D representation of (d) the potential distribution in the electrolyte, (e) the current distribution at the cathode surface and (f) the thickness distribution at the cathode surface for the SCD scaled-up disk model.

3-D representation of (g) the potential distribution in the electrolyte, (h) the current distribution at the cathode surface and (i) the thickness distribution at the cathode surface for the TCD scaled-up disk model when assuming two ionic species.

The results simulate potential, current and thickness distributions for deposition processes conducted at -1 A ($16\text{ A}/\text{dm}^2$) and -2.5 V , for 10800 s at $50\text{ }^\circ\text{C}$.

However, even though the SCD model presents, one more, the more balanced behaviour (Figure 6.20-e), the disorder of the PCD model is now significantly increased (Figure 6.20-b), with current streamlines not even reaching part of the cathode surface (indicated by the circle in Figure 6.20-a). Consequently, the PCD model suggests that a surface around the leading edge is not even deposited (white area in Figure 6.20-c).

The different current distributions at the cathode surface for the PCD, SCD and TCD models are, consequently, depicted in the thickness distributions at the cathode surface (Figures 6.20-c, 6.20-f & 6.20-i).

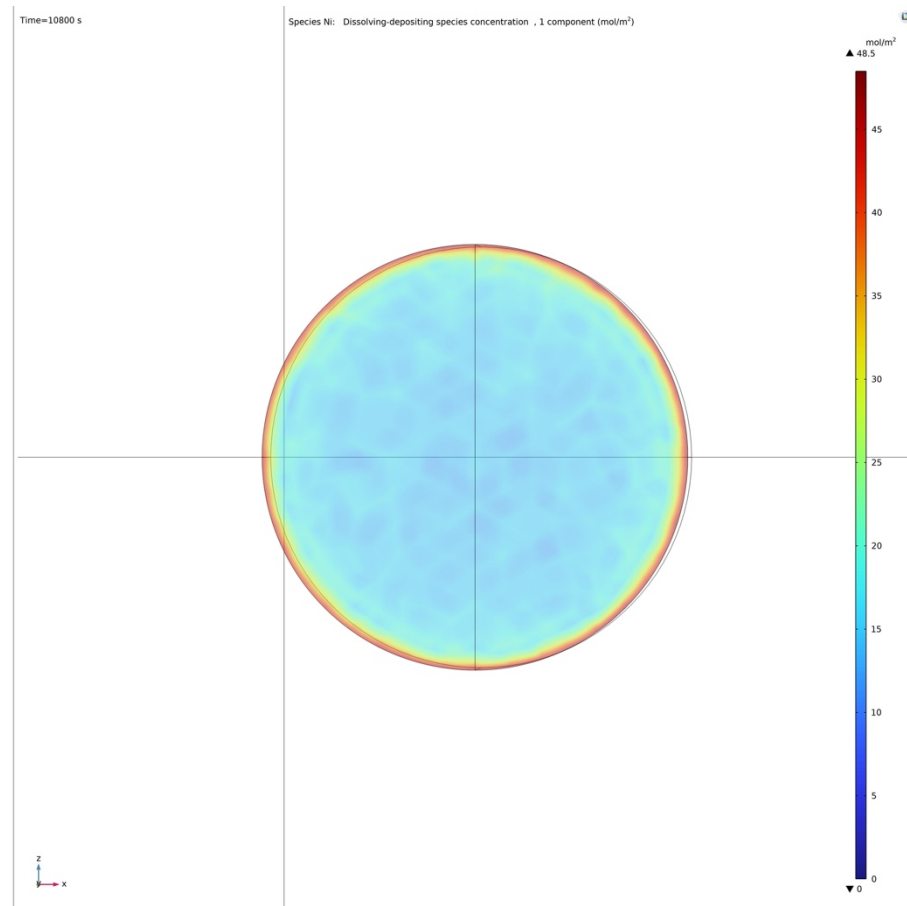


Figure 6. 21: Nickel ion concentration distribution at the cathode surface for the TCD RDE model when assuming two ionic species. The results simulate a deposition process conducted at -1 A (16 A/dm^2) and -2.5 V , for 1800 s at $50\text{ }^\circ\text{C}$.

As it was already pointed out in the previous paragraph, the PCD model produces much “rougher” results in the larger scale than those suggested for the smaller scale (RDE). The simulated thickness distribution suggested by the SCD model (Figure 6.20-f) is once much closer to the experimentally achieved one (~ 0.07 mm in average).

At the same time, the TCD model predicts slightly higher thicknesses than the experimental ones, while providing more detail on what is simulated to be a non-uniform, patchy, deposition (Figure 6.20-i). Very interestingly, it is also shown here, how this patchy thickness distribution is directly proportional to the Ni^{2+} concentration distribution across the cathode surface (Figure 6.21), being another indication that the assumption of two species being present in the electrolyte is not sufficient and forces a false convergence.

Since the working theory based on the Hankin and Kelsall paper [14] suggested higher thickness non-uniformity than the one suggested by the experimental thickness measurements, a second TCD model was developed assuming all six (Ni^{2+} , $[SO_3NH_2]^-$, $[BO(OH)_2]^-$, Cl^- , H^+ and OH^-) possible ionic species to be present in the electrolyte (Table 6.1).

Figure 6.22 shows the results for potential distribution in the electrolyte, as well as current, thickness and Ni^{2+} concentration distributions at the cathode surface for the 6-species TCD model. Very interestingly, this TCD model returned results (Figures 6.22-a & 6.22-b) simulating a system behaviour very close to the one predicted previously by the SCD model (Figures 6.20-d & 6.20-e). Even more importantly, the simulation suggested a much more uniform deposition across the cathode surface, with no patches being visible any more in terms of either the thickness or Ni^{2+} concentration distributions (Figures 6.22-c & 6.22-d) since the assumptions of six species being present in the electrolyte is a more realistic one.

The difference, in terms of the simulated thicknesses, among the four scaled-up disk models discussed so far is clearly presented in Figure 6.23. Here, as it was also the case in Chapter 4 (refer to Figure 4.7-b), it is confirmed that the SCD model is vali-

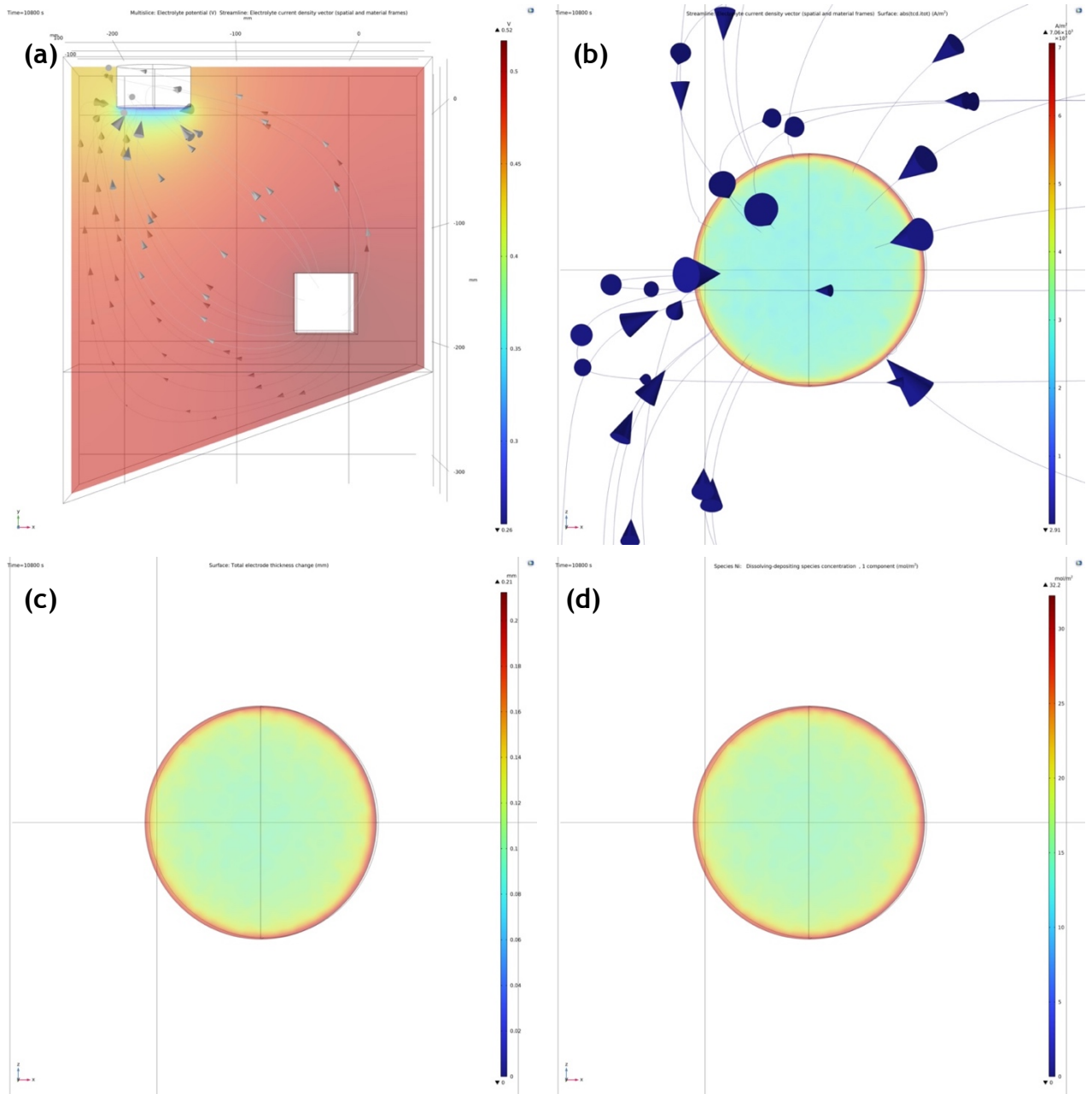


Figure 6. 22: 3-D representation of (a) the potential distribution in the electrolyte, (b) the current distribution at the cathode surface, (c) the thickness distribution at the cathode surface and (d) the nickel ion concentration distribution at the cathode surface for the TCD scaled-up disk model when assuming four ionic species. The results simulate a deposition process conducted at $-1 A$ ($16 A/dm^2$) and $-2.5 V$, for 10800 s at $50\text{ }^\circ\text{C}$.

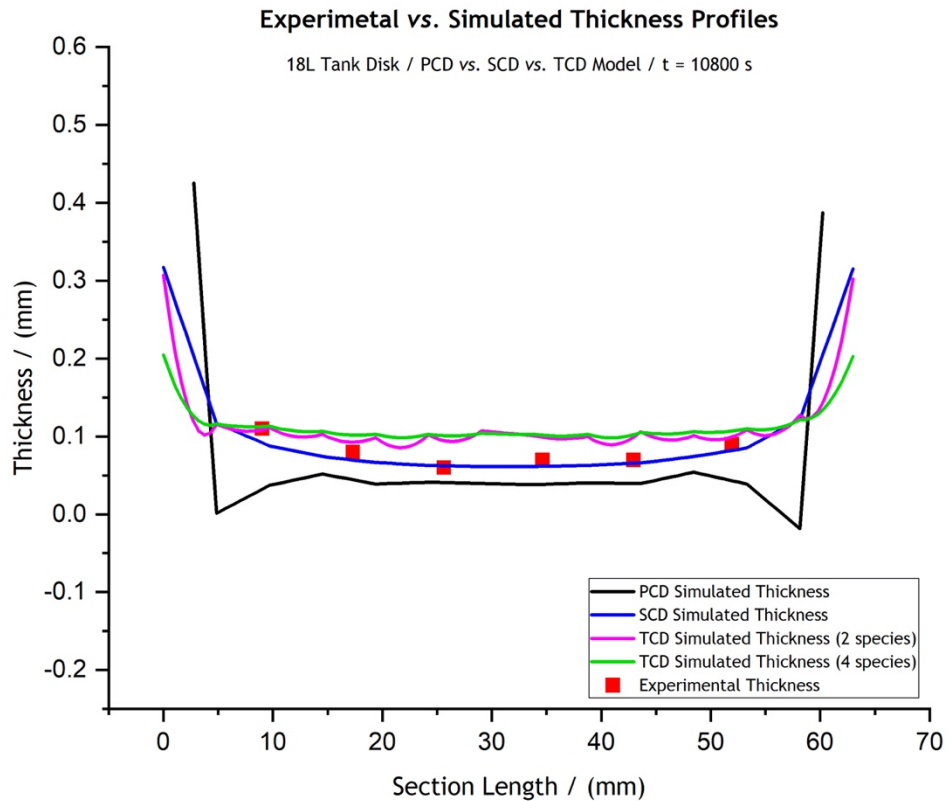


Figure 6. 23: Comparative graphs of the experimentally achieved (red data points) and the simulated thickness profiles by the PCD (black line), SCD (blue line), TCD assuming two ionic species (magenta line) and TCD assuming four ionic species (green line) scaled-up disk setup models. The scaled-up disk deposit was produced at -2.5 V and -1 A, for 10800s at 50 °C.

-dated by experimental results in the larger scale. The PCD model still underpredicts the thickness while also suggests unreasonably high current values at the leading edge, in line with the corresponding simulated disorder of the current distribution. Once more, the TCD model overpredicts the deposit thickness.

Last but not least, the comparison between the thickness profile suggested by the 2-species TCD model (magenta line) and the one suggested by the 4-species TCD model (green line) makes it clear that the latter returns results qualitatively closer to the

experimental ones (red data points), since the high non-uniformity that the 4-species TCD model suggests is not validated by the analysis of the experimentally produced deposits. However, both TCD models' results do not deviate significantly in terms of the simulated average thickness ($\sim 0.12 \text{ mm}$). These results show that TCD models are sensitive to species selected, even when they are present in small (almost negligible/undetectable) amounts in the electrolytic solution. This poses one of the main challenges in TCD since many plating solutions do not have well understood speciations.

On an important difference, the computation time for the case of the 4-species TCD model exceeded the 17 *hours* while in the case of the 6-species TCD model was more than 2 times slower (over 34 *hours*). This significant difference in computation time is attributed to the effort the model makes to solve the problem under the assumption of water-based electroneutrality. For the case when only two other species (Ni^{2+} and $[BO(OH)_2]^-$) are considered alongside the water species (H^+ and OH^-) to achieve electroneutrality (4-species TCD model), Equations 6.2, 6.4 & 6.5 are solved for two species less than for the case of the 6-species TCD model. Considering the inherent complexity of the differential equations system that needs to be solved, the addition of the two species, *i.e.*, the two additional parameters the model should solve for, requires a significantly increased computational power.

In any case, the results presented here suggest once more, even for the large scale, that SCD models may be sufficient to predict deposit thickness. TCD models may provide additional (other) information, but they need longer to converge. This may mean that SCD models for high volume metal deposition may be a reasonable approach when nearly real time solutions are needed, such as current efficiencies or potential currents etc. Additionally, as was also the case for the laboratory-scale RDE models, the computation time for the large-scale, 6-species, TCD model was more than 408 times slower (122,400 *s*) compared to the corresponding SCD case (300 *s*).

6.3 Conclusions

The objective of the studies presented in this chapter was a qualitative assessment of the *COMSOL Multiphysics*[®] models that were already validated in previous chapters. The assessment was firstly carried out in terms of the 2-D axisymmetric RDE and 3-D mechanical vane models' ability to efficiently and sufficiently simulate the effect that the use of “masks” and/or “thieves” could potentially have on the electroforming process outcomes. At a next level, a comparison of the primary, secondary and tertiary current distribution cases for both the laboratory-scale RDE and the scaled-up disk models was conducted.

In the first section of the chapter, a methodology for systematically approaching “mask”- and “thief”-related studies was laid out, and the usefulness of modelling tools in identifying such auxiliary tools that fit the purpose was showcased. Even though the relevant modelling results were not validated through practical experiments, the simulations strongly indicated that current distribution and, consequently, thickness distribution can be controlled solely by the use of “masks”. Consequently, “masks” could potentially be an important aid in the efforts to decrease dendritic growth at mandrel leading edges, just through modifications of the process setup's geometry. Specifically, the “shell mask” configuration was found to be significantly more effective than the “ring mask”, “guiding” the current much more efficiently towards the centre of the RDE and away from the edge. More importantly, the optimal distance between the “shell mask” and the cathode surface was found to be very close to the closest distance that could be achieved between the electrodes in an industrial reactor (0.5 cm). These results were consistent between the 2-D axisymmetric RDE and the 3-D mechanical vane models, revealing similar system behaviour in both scales when a “shell”-type “mask” is deployed for process optimisation purposes. Even in the case of the much more demanding mechanical vane geometry, simulations suggested that the use of a “shell”-type “mask” could optimise the thickness profile of the final product, imitating the target thickness profiles much closer than the case when no “mask” is used.

In a similar manner, even though not at all exhaustive, “thief”-related studies suggested that the use of “thieves” and “masks” would probably turn better results if used as complimentary approaches. However, finding the right combination of “thieves”, “masks” and efficient input parameters is not a trivial job. Here a “shell mask” - “ring thief” configuration was studied with the aspiration that the “ring thief” would minimise current accumulation at the leading edge, while the function of the “shell mask” focuses on guiding the current towards the centre of the RDE and away from the edge. That approach did not, however, lead to any breakthroughs in terms of the simulated current accumulation at the edge. At the same time, such results would never be enough to justify the unavoidably increased complexity of an industrial setup that follows the deployment of a “thief”.

In the second section of the chapter, the effect of the different physics in modelling results was studied for both the RDE and the scaled-up disk models. TCD models were found, in both cases, to predict very similar behaviours for the two systems under investigation compared with their SCD versions, which were successfully validated by experimental results in both scales. At the same time, TCD models also provided some additional information about the process indicating a direct correlation between the electrolyte species concentration and the deposit thickness distribution. However, the immensely longer computation times of the TCD models would not justify their use over their SCD versions.

Nevertheless, TCD models could be of assistance in cases when a correlation between the concentration of specific ionic species and current/thickness distribution is required. In that case, it is suggested that all ionic species present in the electrolyte should be declared in the model, so that it returns results in close agreement to the experimental system behaviour. If only the predominant ionic species are considered, in an effort to simplify the model, the simulations would, at least qualitatively, deviate from practice, suggesting high non-uniformity in deposition. Additionally, in the case when TCD studies are conducted under the water electroneutrality assumption, avoiding declaring all the participating ionic species would result in considerably longer computation times, due to the model being forced to balance the water

species against a fake electrolyte composition, insufficient to satisfy the working assumption.

As a general conclusion, it is once more confirmed by the results presented in this chapter that, modelling tools should always be applied after careful consideration of what model, and why, fits the purpose every time.

References

- [1] L. T. Romankiw, "Electroforming of electronic devices," *Plating & Surface Finishing*, pp. 10-16, 1997.
- [2] L. T. Romankiw, "A path: from electroplating through lithographic masks in electronics to LIGA in MEMS," *Electrochimica Acta*, vol. 42, no. 20-22, pp. 2985-3005, 1997.
- [3] S. N. Jenq, C. C. Wan and Y. Y. Wang, "The influence of self-assembled disulfide additive on the pattern shape by Cu electrodeposition through mask," *Journal of Electroanalytical Chemistry*, vol. 609, pp. 68-74, 2007.
- [4] D. Zhu and Y. B. Zeng, "Micro electroforming of high-aspect-ratio metallic microstructures by using a movable mask," *CIRP Annals - Manufacturing Technology*, vol. 57, pp. 227-230, 2008.
- [5] T. P. Moffat and H. Yang, "Patterned Metal Electrodeposition Using an Alkanethiolate Mask," *Journal of the Electrochemical Society*, vol. 142, p. L220, 1995.
- [6] E. C. Hume, W. M. Deen and R. A. Brown, "Mass Transfer Analysis of Electrodeposition Through Polymeric Masks," *Journal of the Electrochemical Society*, vol. 131, p. 1251, 1984.
- [7] W. Wang, M. R. Holl and D. T. Schwartz, "Rapid Prototyping of Masks for Through-Mask Electrodeposition of Thick Metallic Components," *Journal of The Electrochemical Society*, vol. 148, p. C363, 2001.
- [8] T. M. Braun and D. T. Schwartz, "The Emerging Role of Electrodeposition in Additive Manufacturing," *The Electrochemical Society Interface*, vol. 25, p. 69, 2016.
- [9] "Stress in electrodeposited CoFe alloy films," *Journal of Crystal Growth*, vol. 312, pp. 1262-1266, 2010.
- [10] K. Pantleon, B. V. D. Bossche, M. Purcar, P. Bariani and G. Floridor, "Simulation and experimental determination of the macro-scale layer thickness distribution of electrodeposited Cu-line patterns on a wafer substrate," *Journal of Applied Electrochemistry*, vol. 35, pp. 589-598, 2005.
- [11] K. Clauwaerta, M. Goossensa, J. D. Wildc, D. Colombarac, P. J. Dalec, K. Binnemansd, E. Matthijisa and J. Fransaerb, "Electrodeposition and selenization of brass/tin/germanium multilayers for Cu₂Zn(Sn_{1-x}Gex)Se₄ thin film photovoltaic devices," *Electrochimica Acta*, vol. 198, pp. 104-114, 2016.

- [12] H. Hafezi, A. Rosenfeld, S. Singh, J. Dukovic and M. Birang, "Copper electrodeposition on thin-seed substrates," in *207th ECS Meeting*, Quebec City, 2005.
- [13] S. Mehdizadeh, J. Dukovic, P. C. Andricacos and L. T. Romankiw, "Optimization of Electrodeposit Uniformity by the Use of Auxiliary Electrodes," *Journal of The Electrochemical Society*, vol. 137, p. 110, 1990.
- [14] A. Hankin and G. H. Kelsall, "Electrochemical recovery of nickel from nickel sulfamate plating effluents," *Journal of Applied Electrochemistry*, vol. 42, pp. 629-643, 2012.
- [15] C. J. Milora, J. F. Henrickson and W. C. Hahn, " Diffusion Coefficients and Kinetic Parameters in Copper Sulfate Electrolytes and in Copper Fluoborate Electrolytes Containing Organic Addition Agents," *Electrochemical Science & Technology*, vol. 120, no. 4, pp. 488-492, 1973.
- [16] A. C. F. Ribeiro, J. C. S. Gomes, M. C. F. Barros, V. M. M. Lobo and M. A. Estes, "Diffusion coefficients of nickel chloride in aqueous solutions of lactose at T = 298.15 K and T = 310.15 K," *The Journal of Chemical Thermodynamics*, vol. 43, no. 3, pp. 270-274, 2011.
- [17] J. E. Mackin, "The free-solution diffusion coefficient of boron: influence of dissolved organic matter," *Marine Chemistry*, vol. 20, no. 2, pp. 131-140, 1986.

Chapter 7: Conclusions

As it was extensively discussed early in this work, electroforming is increasingly gaining recognition as a promising and sustainable additive manufacturing process of *Industry 4.0*. Nickel electroforming, in particular, could play an important role in the much-desired “green” transition of lightweight manufacturing since, even within the currently available infrastructure, the same electroforming reactors can remain in use for years if properly maintained, mandrels and anode baskets are re-usable and recyclable, while process efficiency is usually close to 100%. Hazards arising from the use of nickel can easily be mitigated, while nickel recovery and recycling processes are being studied at a much faster pace to meet demand.

In that context, this project has been focusing on meeting the vision of our industry partner for large-scale / high-volume electroforming of parts to be used in aerospace applications (e.g., lipskins, mechanical vanes, erosion shields), presenting complex geometries and adhering to demanding specifications. Subsequently, the main objective of this collaboration was determined to be the bridging of the gaps among electrochemistry, chemical engineering, and manufacturing towards an optimised electroforming process demonstrating reduction in industrial and economic waste, decreased cost of operation, and reduced environmental impact.

Specifically, the objectives have been identified to be the study of the effect of physical and electrochemical parameters on electroformed parts, the development of a well-informed modelling tool based on these data and the validation of the model through carefully designed experiments. This approach was chosen for the successful identification of key engineering variables which can be used to manipulate an electroformed part. That way, the optimisation of the electroforming reactor would also be possible through the design of mandrels and reactor parts/tools to control the deposit growth rate. Eventually, an efficient scaling up of the industrial

process for volume manufacturing, using informed tool and mandrel designs, minimising the number of manufacturing trials and producing conforming parts in volume production, could be possible.

Having identified the objectives and realised the challenges, a **5-step methodology** (Figure 7.1) for systematically studying the electroforming process was laid out. The *first step* implied by the methodology involves scaling down before scaling up, focusing on the systematic electrochemical analysis of the system under investigation, in the laboratory scale, and the identification of its physical and electrochemical parameters (pH, electrolyte conductivity, limiting current, reversible and irreversible potentials, mass transfer coefficients). Moving forward, the *second step* includes the development of a well-informed model of the laboratory-scale process, before a scaled-up version of it is developed, as the *third step*. The scaled-up model should then be validated, for the *fourth step*, through deposition experiments in an industrial-scale reactor. The final, *fifth, step* is expected to be the lengthier one involving continuous cross-validation between experimental and modelling results as the process optimisation studies progress.

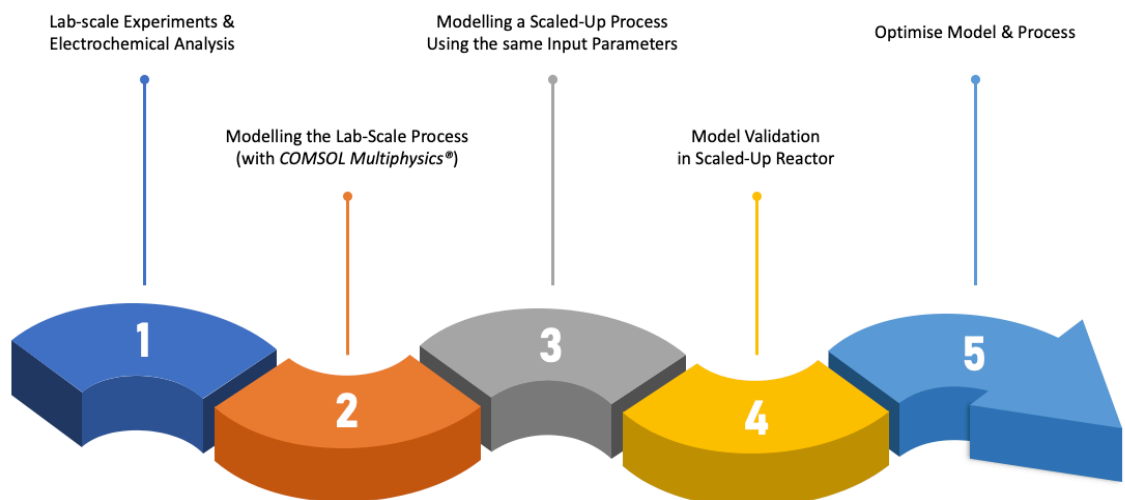


Figure 7. 1: A 5-step methodology for systematically studying the electroforming process.

The data gathered during the first phase of the project provided a complete and useful insight into the system behaviour and electrochemical characteristics. This phase proved to be essential since no complete, systematic studies of the (electro)chemistry of nickel sulphamate baths were reported before, at least not recent ones. Consequently, the system's electrochemical characterisation conducted for this work fills this gap in literature with a complete, up to date, electrochemical analysis of the nickel sulphamate system in the laboratory. In the author's opinion, the experimental approach presented for such analysis in [Chapter 2](#) should always be used before any process optimisation studies are initiated, regardless the deposited material and electrolytic bath used. [Table 7.1](#) summarises the fundamental electrochemical parameters determined for the nickel sulphamate electroforming solution.

Table 7. 1: Electrochemical parameters of the nickel sulphamate electroforming bath

Electrochemical Parameters of the Nickel Sulphamate Electroforming Bath								
pH		Conductivity		$E_{eq,Ni} \equiv E_{rev}$	α_c	α_a	i_0	i_{lim}
RT	50 °C	RT	50 °C	-0.82 V	0.194	1.806	0.42 A/dm ²	2081.38 mA/cm ²
~ 4	~ 4	55 – 61 $\frac{mS}{cm}$	88 – 104.5 $\frac{mS}{cm}$	Data gathered assuming Butler-Volmer kinetics. Laboratory analysis conducted at 50 °C, using a rotating disk electrode setup agitated at 1500 rpm. Polarisation curves obtained at a rate of 0.005 V/s and the results were corrected for ohmic drop.				

After completing the electrochemical characterisation of the system, and using the parameters of [Table 7.1](#) as input, the modelling studies of the project were initiated. Time-dependent, 3-D *COMSOL Multiphysics*[®] models were developed, designed to simulate a galvanostatically controlled electroforming process. The current at the cathode was determined, and the simulation results were validated against practical experiments in terms of the deposit thickness.

The models of three different cathode (mandrel) geometries were studied throughout this work: a rotating disk electrode (RDE) model (Figure 7.2-a), a scaled-up disk model (Figure 7.2-b) and an industrial-scale mechanical vane model (Figure 7.2-c). Samples of the deposits obtained using the three different cathode geometries are also shown here: laboratory-scale nickel disk offering a deposition surface area of $A_{RDE} = 0.0113 \text{ dm}^2$ (Figure 7.2-I), industrial-scale nickel disk offering a deposition surface area of $A_{disk} = 0.31 \text{ dm}^2$ (Figure 7.2-II), and an industrial-scale mechanical vane offering a deposition surface area of $A_{vane} = 0.9 \text{ dm}^2$ (Figure 7.2-III). The electrolytic volumes of the laboratory-scale and industrial scale models present a ration of 1 : 90.

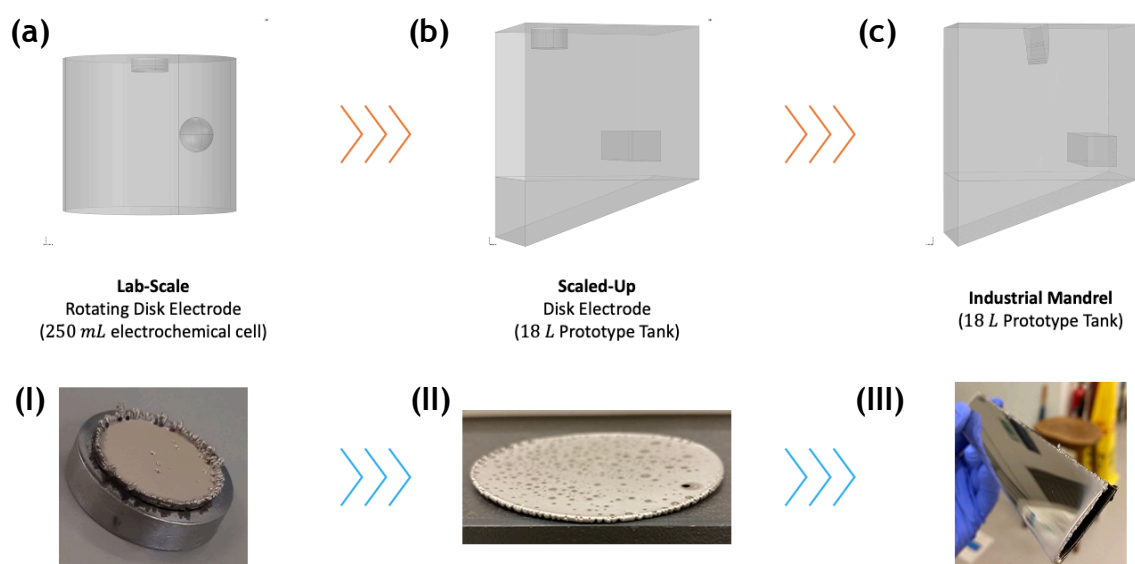


Figure 7. 2: The three geometries modelled for the purposes of the project using *COMSOL Multiphysics*[®]. (a) 3-D, laboratory-scale RDE geometry, (b) 3-D, industrial-scale disk geometry and, (c) 3-D, industrial-scale mechanical vane geometry. Samples of the deposits obtained using the three different cathode geometries are also shown here: (I) laboratory-scale nickel disk ($A_{RDE} = 0.0113 \text{ dm}^2$), (II) industrial-scale nickel disk ($A_{disk} = 0.31 \text{ dm}^2$), (III) industrial-scale mechanical vane ($A_{vane} = 0.9 \text{ dm}^2$).

For the validation practical experiments in the laboratory a standard, 250 mL electrochemical shell was used. However, for the validation practical experiment in the industrial scale, a custom, 18 L prototype electroforming reactor (Figure 7.3) was

designed, developed, and installed for the purposes of the project. All practical deposition experiments, in both scales, were conducted against 304 stainless-steel cathodes, at 50 °C, under mild agitation.

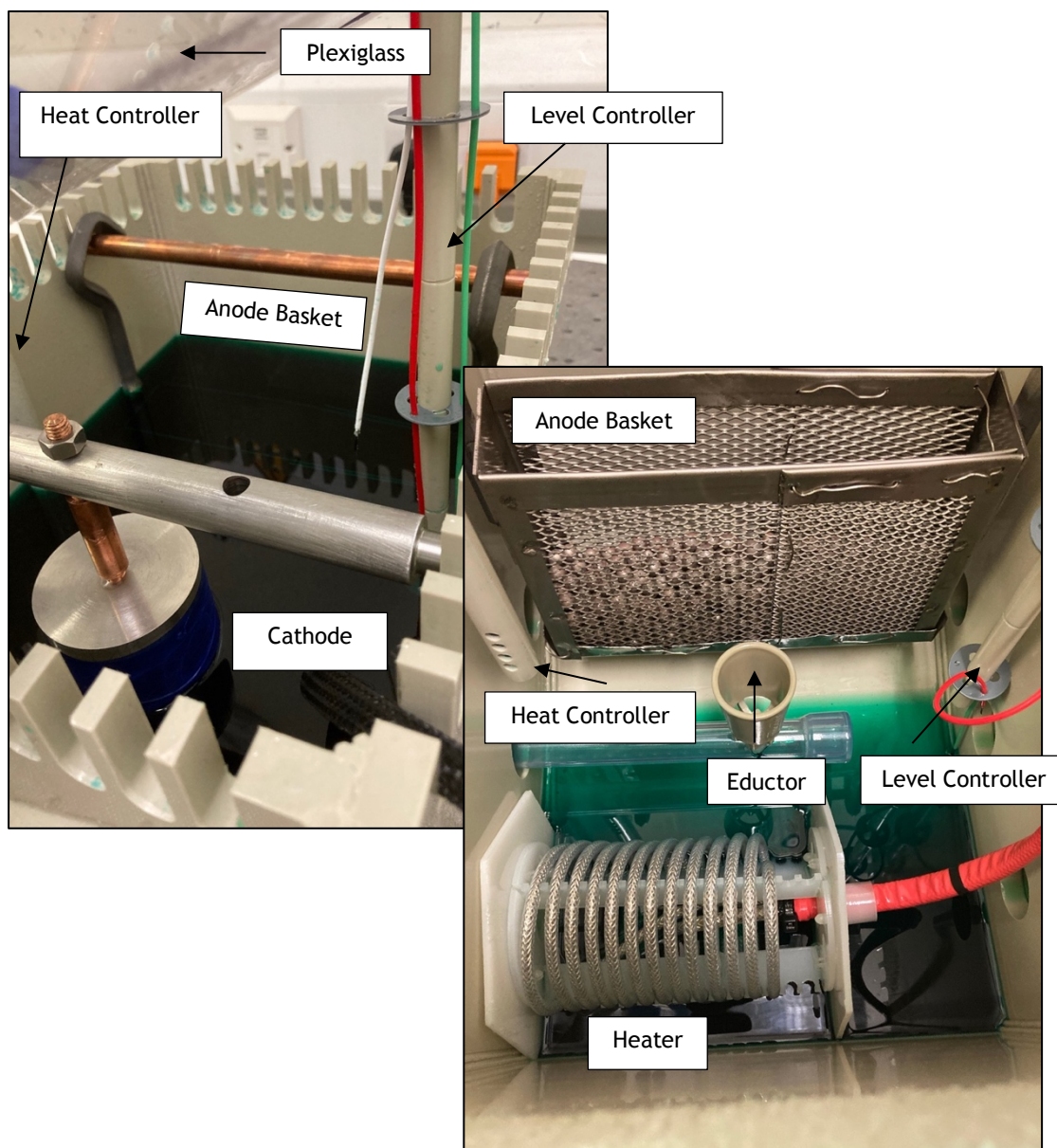


Figure 7. 3: Inside view of the custom, 18 L prototype electroforming reactor designed for the purposes of the project. The stainless-steel disk mandrel and anode basket filled with nickel pellets are shown here, immersed in the nickel sulphamate electrolytic bath. The level and temperature controllers, as well as the eductor and heater deployed, in the reactor for the large-scale experiments, are also shown lying in position in the empty tank during maintenance, with the plexiglass lid raised.

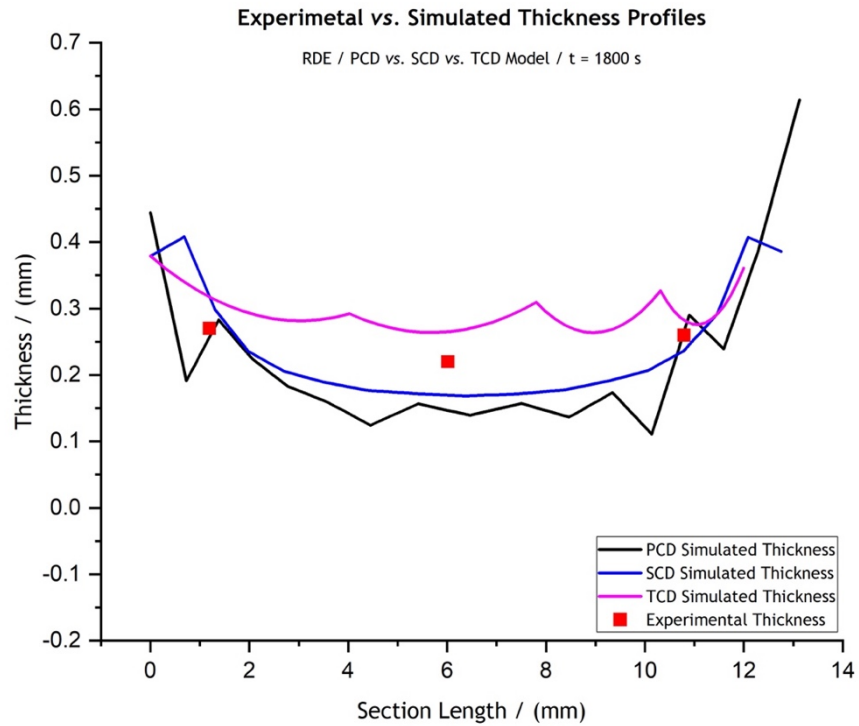
The main **novelty of the modelling work** carried out in the context of this project was the choice of the **secondary current distribution (SCD) assumption to describe the process physics**. As it has already been discussed in previous chapters, the efficiency of SCD models in modelling electrodeposition process has been strongly doubted by researchers and engineers in the past, with tertiary current distribution (TCD) models usually being preferred over their SCD versions. In effort to settle the argument, a **systematic comparative study of the primary, secondary and tertiary current distribution cases** was conducted, to support the choice of the **secondary current distribution case** as the one that **fits the purpose of modelling the nickel electroforming process**. To the author's best knowledge, this is the **first such complete comparative study ever reported in literature for nickel electrodeposition**.

Although in many cases tertiary current distribution analysis can be employed, by choosing a *Ni* electroforming system, where applied current is approximately 10 % of that dictated by mass transfer limitations, one is able to scrutinise and assess a system which should be under kinetic control. Also, the use of high-concentration electrolytes and the vigorous mixing of the electrolytic solutions are two more reasons for one to opt for secondary current distribution physics.

Indeed, TCD models were found, **regardless the process scale, to simulate similar system behaviour to the one simulated by their SCD versions**. Effectively, both SCD and TCD models were validated against practical experiments in the laboratory-scale RDE setup ([Figure 7.2-a](#)) and the industrial-scale reactor using the disk mandrel ([Figure 7.2-b](#)). For both cases, the process outcomes were predicted under both SCD and TCD assumptions to be in close agreement with the experimental data, in terms of the achieved deposit thickness ([Figure 7.4](#)).

However, **considerably longer computation times are required for TCD models to return results**. For the case of the laboratory-scale RDE model, the computation time for the TCD model was 7080 s while, for the SCD simulation computation time

(a)



(b)

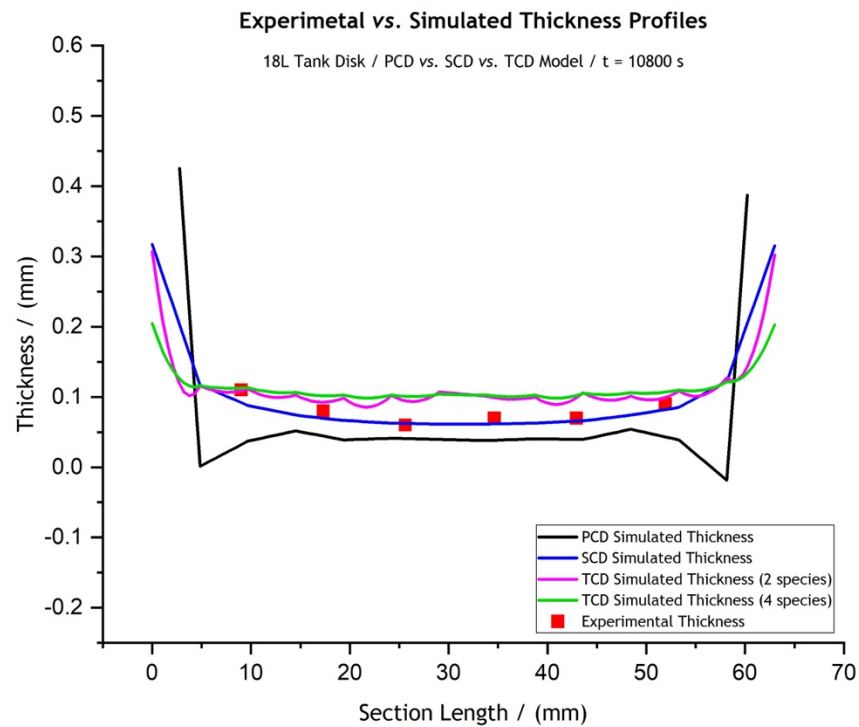


Figure 7. 4: Comparative graphs of the experimentally achieved (red data points) and the simulated thickness profiles by the PCD (black line), SCD (blue line) and TCD (magenta and green lines) models of (a) the laboratory-scale RDE setup and (b) the industrial-scale disk setup. The RDE deposited at -5 V and -0.565 A, for 1800s at 50 °C. The scaled-up disk was deposited at -2.5 V and -1 A, for 10800s at 50 °C.

was immensely decreased to 53 s. For the case of the industrial-scale disk setup, computation time was 5 min for the SCD model and over 34 h for its TCD version.

Keeping in mind that the purpose of the models developed in this project is to be used for the nickel electroforming process design and optimisation in industry, the significantly longer computation times required by the TCD models would never justify their use over their SCD versions in the fast-up industrial environment. Even if someone was to consider upgrading their hardware to increase its computational power, the requirements for modelling part geometries much more complex than the ones presented here using TCD models would call for computational power close to the one of a super-computer. At the same time, SCD models can efficiently and reasonably fast provide the desired results in a fraction of the time and computational power, working flawlessly on common professional computers.

The time efficiency of SCD models could also be utilised to counteract for the usually time-consuming mesh spacing process. Although, in the trials, mesh size determination may be slow, it is in the production setting that the current distribution model is chosen, where using an SCD may prove to be useful. In practice, the mesh size calculations have to be done prior to the actual production when it is determined if a SCD or a TCD model is a better descriptor. Once proven, the more efficient mesh is chosen for the production system and does not need to be reviewed before each run, every time that different values of current, potential etc. are studied.

As an important note, the author recognises that TCD models could be of assistance in cases when a correlation between the concentration of specific ionic species and current/thickness distribution is required. For these cases, it is suggested that all ionic species present in the electrolyte should be declared in the model, so that simulations return results in close agreement to the experimental system behaviour.

Moving on to the next important objective of the project, the two models were also used for **modelling the scaling-up of the nickel electroforming process.**

As it has already been established, the models were designed under the assumption of secondary current distribution physics and Butler-Volmer kinetics. The electrochemical parameters summarised in [Table 7.1](#) were used as input for both models. Control simulations modelled the deposition process in both scales at current values similar to those applied by the industry to determine the potential and current at the electrode surface. The results were validated by cross-checking the predicted thickness against both an electroformed disk produced in the laboratory RDE setup as well as one produced in the scaled-up electroforming reactor. The RDE deposit was found to be thinner than what was predicted by the model while, the thickness of the scaled-up disk agreed reasonably with the computed values. The deviation of the calculated thickness from the experimental RDE deposit's one was attributed to the growth of dendrites along the disk's circumference. Dimensional analysis suggests that dendritic growth at the edges should be limited for the scaled-up mandrel, which presents a larger deposition surface vs. perimeter, compared to its scaled down, RDE, replica. The two deposits have a surface area of πr^2 and a perimeter of $2\pi r$. Since the dendrites appear at the perimeter, and the remaining current with the surface area, one can assume that the current "stolen" by the edges scale as $2\pi r / \pi r^2$ or $2/r$. A corollary of this observation is that edge effects seem to influence critically the prediction of SCD models. Therefore, for model validation, the effect of scaling up should be considered to be important. **Overall, both models were validated by experimental results at a satisfactory standard.**

Having established the model's validity, **mesh sensitivity studies** were conducted to determine its inherent mesh spacing tolerance, as well as any differences observed between the two scales. For that purpose, the control meshes of both models were modified by $\pm 5\%$, $\pm 10\%$, $\pm 12\%$, $\pm 15\%$, $\pm 25\%$, $\pm 50\%$ and -75% . Regarding the RDE model, an increase of mesh element size by 12% and a decrease of 25% were found to be the thresholds after which a minor deterioration of the thickness profiles' smoothness was observed. For the electroforming reactor model, the corresponding results revealed that an increase of the element size by 15% and a decrease by 50% had a major effect on the predicted thickness profiles' smoothness. However, no significant changes in the simulated thickness were observed for either

model while the computation time increased significantly for the finest meshes in both scales. Therefore, in practice, it is suggested that mesh spacing should be optimised against computation times.

At a next level, **geometry sensitivity studies** were also conducted. A systematic investigation of the effect of the anode position on current uniformity within both the RDE and tank reactor was performed. The results suggested that **the anode position, with reference to the cathode, is “irrelevant” to the model as long as they are “far apart”**. For both scales, placing the anode frontally to the cathode, and within 10 mm of the deposition surface, resulted in increased thickness uniformity all over the electroform’s “useful” area. Outside the 10 mm proximity zone, the models suggested that changes in anode position does not affect thickness uniformity in any way. Similarly, **the reactor boundaries (i.e., reactor size) were also found to be “irrelevant” to the model**. In other words, simulations suggested that the characteristics of the final deposits are solely determined by the potential and current distributions within the part of the overall geometry that is delimited by the critical electrolytic volume between the two electrodes, regardless the overall bath volume. Only if this critical volume is considerably limited by the anode lying within 10 mm from the cathode surface an effect on thickness uniformity will be observed.

With large-scale / high-volume electroforming being the project’s industrial partner ultimate goal, these studies were of great importance in many levels. First of all, they proved that **a commercially available modelling software can be efficiently used for modelling various aspects a process optimisation operation**, starting from the development of a laboratory-scale base model, and resulting in more complex scaling-up studies in the industrial scale. At the same time, the electrochemical parameters obtained in the laboratory scale, were efficiently applied during the development of a scaled-up version of the base model, confirming the working theory that **systematic scaled-down studies play an essential role in the successful development of models simulating industrial-scale processes**. Last but not least, they provided a very important insight into the effect that system geometry might have on the final products while, they were found to be **potentially critical during reactor**

design and tooling development, dictating the most financially sustainable reactor, mandrel, and anode sizes on a case-by-case basis.

Even though the base model was already validated in two different scales, the mandrel geometries under investigation have been simple ones, of no industrial interest. Therefore, the next stage included experimental and modelling studies of a mechanical vane geometry (Figure 7.2-c), very commonly used in aerospace applications. The vane mandrel provided by *Radius Aerospace* presented a challenging geometry in terms of the target thickness profile.

Starting from the base model once more, the vane model was developed and successfully validated, in terms of deposit thickness, against deposition experiments in the prototype electroforming reactor.

First, **qualitative analysis of the experimental results suggested that deposition progresses from the sides of the cathode towards its centre, i.e.**, a faster deposition rate was confirmed at the sides of the mandrel indicating lamellar growth. The process presented **good predictability**, with the deposited nickel mass presenting an analogous relationship with both the applied current density and deposition time; between any two experiments, keeping the applied current density the same and doubling the deposition duration leads to electroforms almost double in terms of the deposited nickel mass. The same behaviour was observed if deposition duration is kept the same while the applied current density is doubled. Additionally, deposition experiments revealed a **correlation between the applied current density and the electroforms' surface finishing**, with higher current densities leading to final parts with a matte surface finishing. The same surface finishing was also observed after deposition at lower current densities for longer periods.

Regarding the modelling studies of the mechanical vane geometry, **simulations of depositions at current densities up to $\sim 5 A/dm^2$ predicted deposit thicknesses close to the experimentally achieved ones**, with higher thicknesses simulated at the “nose” and lower ones at the front and side faces of the mandrel, as expected. This agreement between experimental and simulation results was decreasing,

however, with any increase in the applied current density. **Since the vane is industrially formed at $\sim 2 \text{ A/dm}^2$, the model was proposed to fit the purpose of simulating this specific process.** However, it is suggested that further optimisation studies are of essence in order to quantitatively improve the agreement between experimental and modelling results at even higher current densities.

The last part of the mechanical vane investigations included the **structural characterisation** of the electroforms produced in the prototype electroforming reactor. Scanning electron microscopy images suggested that **pyramid-shaped nickel particles** evolve during deposition. For the first time ever, to the author's best knowledge, a **periodicity in the growth mechanism** which leads to "necklace"-like zones, $\sim 100 \mu\text{m}$ in thickness, at the "nose" area is reported. These periodic zones are suggested to probably coincide with a **periodic re-nucleation of the active NiOH_{ads} intermediate, or surfactant inclusion**, formed during the rate determining step of the nickel deposition mechanism. Elemental analysis also supports this theory since the only other element, except for the prevalent nickel, consistently present in the sample was oxygen. **Further structural investigations are believed to be necessary** to determine whether this periodic layer formation also coincides with a periodic transition between different crystallographic phases, possibly affecting the internal stresses developing in the final products.

As the final step of the qualitative assessment of the *COMSOL Multiphysics*[®] models used in this work, **the effect that the use of "masks" and/or "thieves"** could have on the electroforming process outcomes was explored. The assessment was carried out for both the 2-D axisymmetric RDE model (refer to [Chapter 2](#)) and the 3-D mechanical vane model.

A methodology for systematically approaching "mask"- and "thief"-related studies was laid out, and the usefulness of modelling tools in identifying auxiliary tools that fit the purpose was proven. Even though the relevant modelling results were not validated through practical experiments, the simulations suggested that **current and thickness distribution can be controlled solely by the use of "masks"**.

Consequently, “masks” could potentially be an important aid in the efforts to decrease dendritic growth at mandrel leading edges. A “shell mask” configuration (Figure 7.5-a) was found to be significantly more effective when compared against a “ring mask” (Figure 7.5-b), “guiding” the current much more efficiently towards the centre of the RDE and away from the edge. More importantly, the optimal distance between the “shell mask” and the cathode surface was found to be very close to the closest distance that could be achieved between the electrodes in an industrial reactor (0.5 cm).

These results were consistent between the 2-D axisymmetric RDE and the 3-D mechanical vane models, **revealing similar system behaviour in both scales** when a “shell”-type “mask” is deployed for process optimisation purposes. Even in the case of the much more demanding mechanical vane geometry, simulations suggested that the use of a “shell”-type “mask” could optimise the thickness profile of the final product, and even meet the requirements determined for highly demanding target thickness profiles as the mechanical vane one. Figures 7.5-c & 7.5-d show how the “shell”-type “mask” deployed alongside the mechanical vane mandrel “guides” the current to reach the “nose” directly and the mandrel sides indirectly, “from the top” of the “mask”. That way, a higher thickness is achieved at the “nose” and a lower one at the sides, as required.

Aspiring to further minimise, or even eliminate, current accumulation at the edge, a “ring thief” was studied alongside the “shell mask” using the 2-D axisymmetric RDE model. Even though their combination turned slightly better results in terms of thickness uniformity, no breakthroughs were observed in terms of the simulated current accumulation at the edge.

Overall, these studies suggested that both “masks” and “thieves” could, indeed, be useful aids towards the optimisation of the electroforms’ thickness uniformity. However, the involvement of “thieves” in industry would significantly increase the complexity of the process, calling for advanced power control equipment. Therefore,

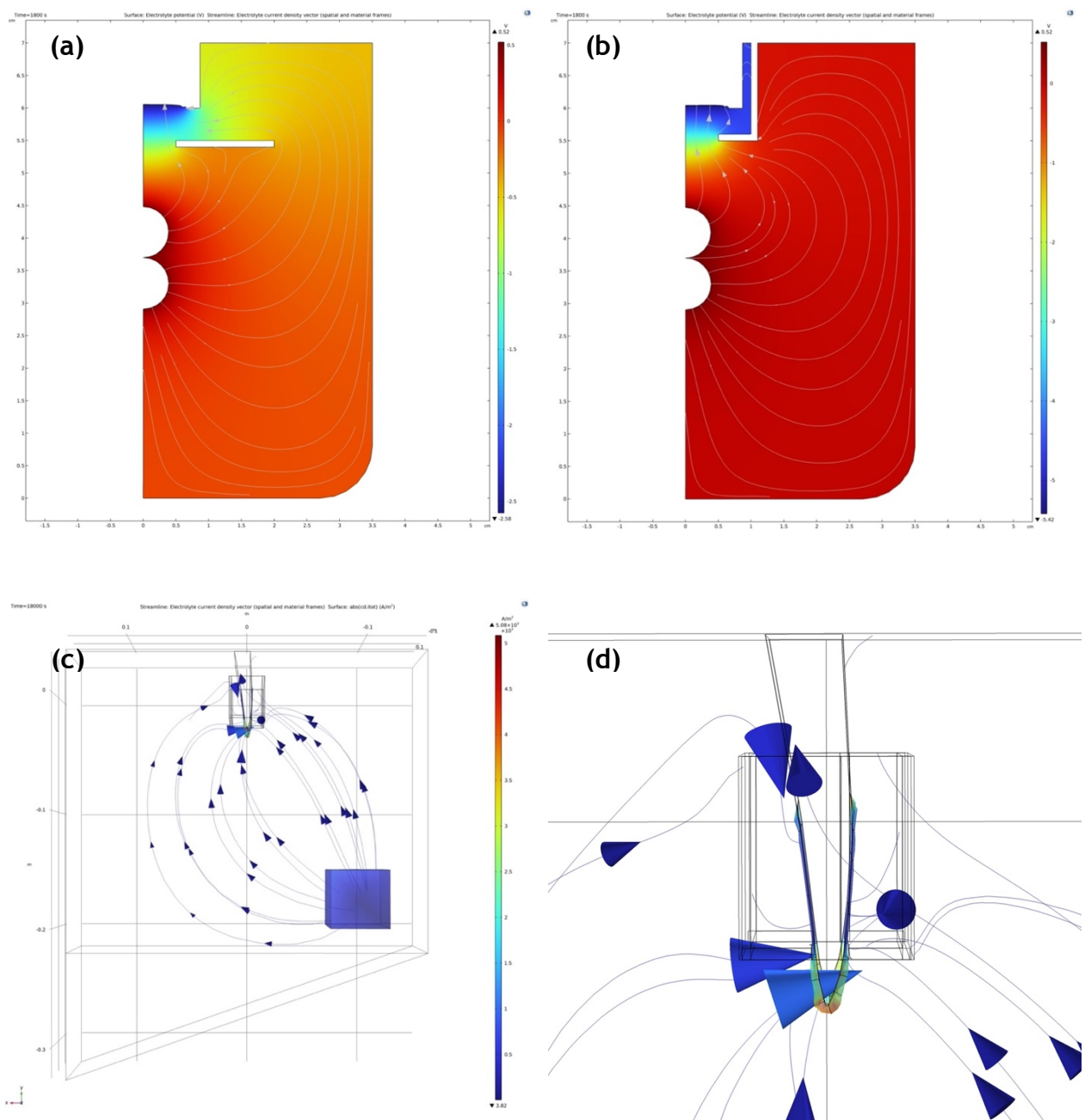


Figure 7. 5: 2-D representation of the when the effect of (a) the “ring mask” and (b) the “shell mask” was studied deploying the 2-D axisymmetric RDE model. (c) 3-D representation of the current distribution in the electrolytic volume when the effect of a “shell”-type “mask” alongside the mechanical vane mandrel was studied using the 3-D mechanical vane model. In (d) a close up of the current behaviour close to the cathode surface is provided, showing the current streamlines reaching the “nose” directly and the mandrel sides “from the top” of the “shell”-type “mask”.

every time that efficient “mask” geometries can be identified, their use should be preferred over “thieves”.

Since the identification of the proper geometry of a “mask” and/or “thief” is not a trivial task, modelling tools can be of significant help towards that direction. More importantly, the fact that **2-D axisymmetric models can qualitatively simulate current distribution as effectively as 3-D ones** could significantly reduce the time of relevant computations, allowing more candidate “mask” and “thief” configurations to be studied, in terms of their effectiveness, on a case-by-case basis.

In conclusion, the studies presented throughout this work did not only provide interesting and useful results shedding light on the electroforming’s huge potential as a promising *Industry 4.0* additive manufacturing process. But they also revealed the challenges that modellers are faced with in their effort to determine the critical parameters and key steps needed to efficiently model the process. Recent developments in computational sciences and rapid increase in computational power allow both academia and industry to develop models - which may not be representative of the process due to incorrect use of parameters, as well as inadequate validation. The authors of “*Useless Arithmetic: Why Environmental Scientists Can’t Predict the Future*” [1] aptly point out,

“... there is more to models than mathematics. There are parameters ... , and many other factors that make natural processes work. And each of the parameters is represented in a model by simplifications and assumptions. This is the point at which the mathematically challenged among us can evaluate models and even question the modelers.”

In other words, a model will always be able to calculate a result; the important question any researcher or engineer should ask themselves is, whether the input parameters are the correct ones, and how would the results be validated against independent experiments. Without such rigour, models may turn out to be sterile.

Even though the current thesis on the nickel electroforming process is by no means an exhaustive one, it constitutes a diligent piece of work, whose qualitative results and proposed methodologies could confidently be applied in industry towards the systematic study and successful optimisation of most, if not all, electrodeposition processes, regardless the scale of application.

With regards to the nickel electroforming process, specifically, this work could confidently be used as a solid starting point for the studies to follow. In the meantime, the current project's ultimate goal of initiating the bridging of the gaps among electrochemistry, chemical engineering, and manufacturing, towards an optimised nickel electroforming process, can be considered fulfilled.

References

- [1] O. H. Pilkey and L. Pilkey-Jarvis, Useless arithmetic: why environmental scientists can't predict the future, Columbia University Press, 2006.